# Thermo-responsive electrospun scaffolds for enzymatic-free passage and mammalian cell phenotype support

Floor Agnes Andrea Ruiter, BSc, MSc, AMRSC

Thesis submitted to The University of Nottingham
for the degree of Doctor of Philosophy

September 2017




*"If we knew what it was we were doing, it would not be called research, would it?"*

— Albert Einstein

# List of Publications

1. **Ruiter F.A.A.,Sidney L., Kiick K.L., Segal J.I., Alexander C., and Rose F.R.A.J.** Design of thermo-responsive polymer-peptide conjugates for human corneal stromal cell (hCSC) quiescent phenotype support. (in process)

2. **Ruiter F.A.A., Alexander C., Rose F.R.A.J., and Segal J.I.** A Design of Experiments (DoE) approach to identify the influencing parameters that determine poly-D,L-lactic acid (PDLLA) electrospun scaffold morphologies, Biomedical Materials, 12(5):055009, 2017, DOI: 10.1088/1748-605X/aa7b54

3. **Ruiter F.A.A., Alexander C., Rose F.R.A.J., and Segal J.I.** A Design of Experiments (DoE) approach to identify the key fibre morphology influencing parameter interactions of electrospun scaffolds, eCell & Materials, 32 (4):85, 2016 (TCES Conference 2016)

# Abstract

Current conventional cell culture methods for the expansion of cells to large quantities for tissue engineering and regenerative medicine application relies on the use of enzymatic digestion passaging. However, this method significantly reduces the cell viability, due to the destruction of important cell-surface proteins and therefore considered undesirable for the subsequent cell therapies [1]. Research has led to the development of thermo-responsive surfaces for the continuous culture of cells. These thermo-responsive materials properties can be used to passage cells from the surface when the cell culture temperature is reduced. Conventional cell culture is performed on a 2D platform, however this can result in undesired de-differentiation, due to lack of similarities to the natural extracellular matrix (ECM) environment. This thesis aims to develop a thermo-responsive 3D fibre-based scaffold, fabricated by electrospinning, to create an enzymatic-free 3D cell culture platform for the expansion of mammalian cells with the desired phenotype for clinical use. In particular the expansion of human corneal stromal cells (hCSCs), which have been observed to de-differentiate to their active myofibroblastic phenotype with conventional 2D cell culture methods was examined here.

Although experimentally the electrospinning method is relatively simple, at the theoretical level the interactions between process parameters and their influence on the fibre morphology is not yet fully understood. In this study a design of experiments (DoE) model was proposed to determine combinations of process parameters that result in significant effects on poly-D,L-lactic acid (PDLLA) fibre morphology. The process parameters used in this study were applied voltage, needle-to-collector distance, flow rate and polymer concentration. Data obtained for mean fibre diameter, standard deviation of the fibre diameter (stdev, measure of fibre morphology) and presence of 'beading' on the fibres (beads per $\mu m^2$) were evaluated as a measure of PDLLA fibre morphology. Uniform fibres occurred at standard deviations of $\leq$ 500 nm, 'beads-on-string' morphologies were apparent between $\pm$ 500-1300 nm and large beads were observed at $\pm$ 1300-1800 nm respectively. Mean fibre diameter was significantly influenced by the ap-

plied voltage and interaction between flow rate and polymer concentration. Fibre morphology was mainly influenced by the polymer concentration, while bead distribution was significantly influenced by the polymer concentration as well as the flow rate. The resultant DoE model regression equations were tested and considered suitable for the prediction of parameter combinations needed for the desired PDLLA fibre diameter and additionally provided information regarding the expected fibre morphology.

The thermo-responsive behaviour of the scaffolds was achieved by blend electrospinning of the thermo-responsive polymer poly(di(ethylene glycol) methyl ether methacrylate (PDEGMA) and the supportive polymer poly-D,L-Lactic Acid (PLA), which gives the support needed for cell culture. PDEGMA was synthesised by free radical polymerisation and has a lower critical solution temperature of 28°C. The optimised electrospinning process was taken forward for the fabrication of the blend electrospun PLA/PDEGMA scaffolds. Different weight (wt) % concentrations to PLA was incorporated and distribution of the PDEGMA was confirmed by fluorescent labeled PBI-PDEGMA. Initial thermo-responsive passaging method was investigated with 3T3 fibroblasts (3T3s). No significant detachment of 3T3s was observed below 10 wt% of PDEGMA in the blend electrospun PLA/PDEGMA scaffolds, while a maximum of 25% of cells detached when cooled for 30 mins at 8°C as observed for 10 wt% PDEGMA. An increase in fibre diameter from 900 nm to 2-3 μm and different cooling methods (1 and 3 h at rt and controlled cooling of -1°C per minute) did not result in an increase of 3T3 detachment. These findings indicate possible insufficient presence of the PDEGMA thermo-responsive brushes at the surface of the fibres. However, when hCSCs were cultured on these scaffolds significantly higher cell detachment was observed (approx. 100% compared to 25% for 3T3s). These findings indicate the application of the blend electrospun PLA/PDEGMA scaffolds for the culture and passaging of hCSCs.

hCSCs were observed to not adhere and proliferate on the PLA/PDEGMA scaffolds. Therefore, a peptide thermo-responsive co-polymer conjugated by photo-initiated thiol-ene chemistry was proposed. Poly(di(ethylene glycol) methyl ether methacrylate-co-poly(di(ethylene-glycol) vinyl ether (PDEGMA/ PDEGOH) was synthesised by free radical polymerisation and subsequently functionalised with a free thiol group by a

condensation reaction. The obtained poly(diethylene glycol) methyl ether methacrylate-co-poly(diethylene glycol) thiol (PDEGMA/PDEGSH) was blend electrospun and the presence of free thiols on the electrospun scaffolds were determined by ToF-SIMS and FITC labeling. These free thiol containing scaffolds were functionalised by a norbornene acid functionalised peptide sequence GGG-YIGSR by the photo-initiated thiol-ene reaction and its presence was confirmed by ToF-SIMS and ATTO labeling.

The biocompatibility of the peptide containing scaffolds was assessed by the adhesion, proliferation and immuno-staining of hCSCs. Significant increase in hCSCs adherence and proliferation was observed on the peptide containing scaffolds. Immuno-staining showed maintained expression of the desired phenotypic markers ALDH, CD34 and CD105, while showing no or low expression of the undesired phenotype expressing α-SMA marker. This desired expression was observed to be maintained after thermo-responsive passaging and observed higher when cells were cultured on PLA scaffolds with 10 wt% PDEGMA/4 mole% PDEGS-Nor-GGG-YIGSR.

In this thesis, the fabrication and application of a first generation, biocompatible thermo-responsive peptide conjugate fibrous scaffolds is described. The ease of fabrication, successful adherence and expansion of a therapeutically relevant cell type make these scaffolds a promising new class of materials for the application of cell culture expansion platforms. The scaffolds developed and reported in this thesis are believed to represent a promising contribution to the fields of biomaterials and tissue engineering.

# Acknowledgements

This work was supported by the Engineering and Physical Sciences Research Council [grant number EP/F500491/1] in the Centre of Doctoral Training in Regenerative Medicine. I would like to give a special thanks to Dr. Felicity Rose, Prof. Cameron Alexander and Dr . Joel Segal for their research expertise, supervision and support during my PhD. Big thanks to Laura Sidney, who isolated the human corneal stromal cells used in this study and helped me a lot on the cornea work. I also would like to thank Sanne Ruiter and George Joseph for their advice on the DoE approach presented in this thesis. I would like to give a special thanks to Prof. Kristi Kiick at the University of Delaware, who gave me the opportunity to work in her lab for four month and her input and expertise on the peptide conjugation work. From Kiick's lab I would like to thank Hang Lau for her daily chats, laughter and support, as well as, Tianzhi Luo and Michael Haider for their help in the peptide synthesis work and Sue Xu for lending me her electrospinning rig. I also would like to thank Prof. Pochan and Dr. Martin for letting me work in their labs while working at the University of Delaware (UD). I also like to thank Cristy Grainger-Boultby (SEM), Jiang Long (ToF-SIMS) and Teresa Marshall for their excellent technical support and from the UD ; S. Bai, P. Asare-Okai and Y. Zhao for there expertise in SEM, UPS-MS and NMR respectively. While in America I had a lovely time meeting many friends, Eugenio, Anne-Lena Willenbrink, Julie Kreibritch, Paul Kouakou, Mahmoud Sherief and Silvia Hertel, which made my stay a great experience and would like to thank them for the great time! I also would like to thank everybody in the labs B15 and A69 for their help with the chemistry work, in particularly Shaam and Rosa. Additionally, I would like to thank Michael Taylor for his help and expertise in surface analysis and Bram Zoetebier for his help in NMR interpretations.

Last but definitely not least I would like to thank Jacqueline Hicks, Anne Canning and Ivana Staka for their many funny chats and serious science discussion in our dark forgotten A09 office. Throughout my four year PhD my family has been very important and would like to thank them for putting up with me being away all the time.

# Contents

**1 Introduction** **1**

1.1 Tissue engineering (TE) and regenerative medicine (RM) . . . . . 1

1.2 *In vitro* cell expansion within the regenerative medicine field . . . . . 6

1.2.1 2D cell culture versus 3D cell culture of mammalian cells . . . . . 6

1.3 3D structure requirements . . . . . 8

1.3.1 Natural materials . . . . . 9

1.3.2 Synthetic materials . . . . . 10

1.4 3D scaffold fabrication techniques . . . . . 11

1.4.1 Hydrogels . . . . . 13

1.4.2 3D bio-printing patterns . . . . . 14

1.4.3 Electrospinning . . . . . 15

1.4.4 Electrospinning parameters . . . . . 17

1.5 Electrospun fibrous scaffolds in the regenerative medicine and tissue engineering field . . . . . 24

1.6 Enzymatic digestion vs. thermo-responsive surfaces . . . . . 29

1.6.1 Cell-sheet engineering by thermo-responsive culture . . . . . 30

1.7 Project Aims and Objectives . . . . . 35

**2 Materials and Methods** **37**

2.1 Design of Experiments (DoE) . . . . . 37

2.1.1 Design of Experiments (DoE) Theory . . . . . 37

2.1.2 Test DoE model predictions . . . . . 39

2.2 Electrospun scaffold preparation . . . . . 40

2.2.1 Polymer solution analysis . . . . . 40

2.2.2 Electrospinning . . . . . 41

2.3 Analytic techniques . . . . . 42

2.3.1 Nuclear Magnetic Resonance spectroscopy 1D and 2D analysis . 42

2.3.2 Gel permeation chromatography (GPC) analysis . . . . . 43

2.3.3 Fourier transform infra-red (FT-IR) analysis . . . . . 43

2.3.4 Measurement of polymer solution cloud points to estimate lower critical solution temperature (LCST) . . . . . 44

2.3.5 Fluorescence intensity measurements . . . . . 44

2.4 Electrospun scaffold characterisation . . . . . 45

2.4.1 Scanning Electron Microscope (SEM) . . . . . 45

2.4.2 Fibre diameters, standard deviation and number of beads per $\mu m^2$ measurements . . . . . 45

2.4.3 Tensile testing measurements . . . . . 45

2.4.4 Water contact angle measurements (WCA) . . . . . 46

2.4.5 Time-of-Flight Secondary Ion Mass Spectrometry (ToF-SIMS) sample analysis . . . . . 46

2.5 Polymer Synthesis of PDEGMA and PBI-PDEGMA . . . . . 47

2.5.1 General preparation . . . . . 47

2.5.2 Poly (di(ethylene glycol) methyl ether methacrylate) (PDEGMA) 47

2.5.3 Fluorescent labeled poly(di(ethylene-glycol)methyl ether methacrylate) (PBI-PDEGMA) **4** . . . . . 49

2.6 Thermo-responsive/peptide conjugated polymer synthesis . . . . . 52

2.6.1 Materials . . . . . 52

2.6.2 Synthesis of poly(di(ethylene glycol) methyl ether methacrylate-co-poly(di(ethylene-glycol) vinyl ether (PDEGMA/PDEGOH) **5** . . 52

2.6.3 Synthesis of poly(diethylene-glycol) methyl ether methacrylate-co-poly(diethylene-glycol) thiol (PDEGMA/PDEGSH) **6** . . . . . 54

2.6.4 Free thiol confirmation by Ellman's assay . . . . . 54

2.6.5 Free thiol presents confirmation by fluorescein-5-maleimide labeling. . . . . 55

2.6.6 Synthesis of norbornene functionalised peptide Nor-GGG-YIGSR **7** 56

2.6.7 Photo-initiated thiol-ene reaction of PDEGMA/PDEG-S-Nor-peptide or electrospun scaffolds PLA and PDEGMA/PDEG-S-Nor-peptide blend. . . . . 57

2.6.8 Peptide presence after photo-initiated thiol-ene chemistry confirmation by ATTO-NHS-ester labeling. . . . . 57

2.7 Cell Culture . . . . . 58

2.7.1 Materials . . . 58
2.7.2 Cell culture media preparation . . . 58
2.7.3 General method for cell counting by haemocytometer . . . 59
2.7.4 3T3 fibroblasts cell culture . . . 60
2.7.5 human Corneal Stromal Cell (hCSCs) culture . . . 61
2.7.6 Proliferation study of 3T3s or hCSCs on electrospun scaffolds. . . 63
2.8 Cell-electrospun scaffolds interaction studies using imunocytochemistry 64
2.8.1 Buffer preparation for immuno-staining . . . 65
2.8.2 Immuno-staining of fixed hCSCs on electrospun scaffolds . . . 66
2.8.3 Confocal microscopy . . . 69
2.9 Cell thermo-responsive detachment studies . . . 69
2.9.1 3T3 fibroblast detachment . . . 69
2.9.2 hCSCs detachment . . . 70
2.9.3 Percentage of cell detached . . . 70
2.10 Fluorescence-activated cell sorting (FACS) . . . 71
2.10.1 Immunostaining of suspended cells for Fluorescence-Activated Cell Sorting (FACS) . . . 71
2.10.2 FACS measurements . . . 71
2.11 Statistical Analysis . . . 71

**3 Optimisation of the electrospinning process 73**

3.1 Introduction . . . 73
3.1.1 DoE Model . . . 76

3.1.2 DoE approaches in literature . . . . . 80
3.2 Aims and Objectives . . . . . 82
3.3 Experimental methods . . . . . 83
3.3.1 Scaffold preparation . . . . . 83
3.3.2 DoE model output . . . . . 83
3.3.3 Scaffold characterisation . . . . . 83
3.3.4 3T3 Fibroblast behaviour on scaffolds . . . . . 83
3.4 Results & Discussion . . . . . 85
3.4.1 Fibre diameter ($Y_1$) . . . . . 86
3.4.2 Fibre morphology ($Y_2$) and Beads per $\mu m^2$ ($Y_3$) . . . . . 89
3.4.3 Test model predictions . . . . . 91
3.4.4 Cell behaviour on different electrospun scaffold morphologies . . 98
3.5 Conclusion . . . . . 104

**4 Thermo-responsive electrospun scaffolds and enzymatic-free passaging 105**

4.1 Introduction . . . . . 105
4.2 Aim and Objectives . . . . . 109
4.3 Experimental methods . . . . . 110
4.3.1 Polymer synthesis . . . . . 110
4.3.2 Blend electrospun scaffolds fabrication . . . . . 110
4.3.3 Blend electrospun scaffold characterisation . . . . . 111
4.3.4 PBI-PDEGMA distribution studies . . . . . 111
4.3.5 Cell distribution studies on the PLA/PBI-PDEGMA scaffolds . . 111

4.3.6 Cell proliferation and detachment studies . . . . . 111
4.4 Results and Discussion . . . . . 112
4.4.1 PLA/PDEGMA blend electrospun scaffolds . . . . . 112
4.4.2 PDEGMA distribution study . . . . . 117
4.4.3 3T3 proliferation and detachment studies . . . . . 121
4.5 Conclusion . . . . . 130

**5 human Corneal stromal cell (hCSCs) behaviour on the thermo-responsive fibrous electrospun scaffolds. 132**

5.1 Introduction . . . . . 132
5.2 Aims and Objectives . . . . . 136
5.3 Experimental Methods . . . . . 137
5.3.1 Polymer synthesis . . . . . 137
5.3.2 Free thiol confirmation of PDEGMA/PDEGSH polymers . . . . . 138
5.3.3 Blend electrospun scaffolds fabrication . . . . . 138
5.3.4 Blend electrospun scaffold characterisation . . . . . 138
5.3.5 Free thiol confirmation on blend electrospun scaffolds . . . . . 138
5.3.6 Peptide synthesis . . . . . 138
5.3.7 Photo-initiated thiol-ene chemistry confirmation . . . . . 139
5.3.8 Cell proliferation, phenotypic and ECM expression studies . . . . 139
5.3.9 Detachment studies . . . . . 140
5.3.10 Phenotype studies after detachment by FACS. . . . . 141
5.4 Results & Discussion . . . . . 141

5.4.1 Polymer and peptide synthesis . . . . . 147

5.4.2 PDEGMA/PDEGSH electrospun scaffolds . . . . . 158

5.4.3 hCSCs behaviour studies on the photo-initiated thiol-ene peptide derivatised electrospun scaffolds. . . . . 166

5.4.4 Thermo-responsive passaging . . . . . 176

5.5 Conclusion . . . . . 182

**6 Conclusion** **184**

**7 Future work** **186**

7.1 Electrospinning optimisation and scaffold characterisation. . . . . 186

7.2 Thermo-responsive electrospun scaffolds fibrous design. . . . . 187

7.3 hCSCs detachment studies on the fabricated scaffolds. . . . . 188

7.4 Cell specific peptide functionalisation on the fabricated scaffolds. . . . . 188

7.5 Scale-up of the fabricated scaffolds. . . . . 189

**8 References** **190**

**9 Supplementary data** **227**

9.0.1 Hydrogen Nuclear Magnetic Resonance spectroscopy ($^1$H-NMR) 227

9.0.2 Gel permeation chromatography (GPC) . . . . . 228

9.0.3 Fourier transform infra-red (FT-IR) . . . . . 228

9.0.4 Time-of-Flight Secondary Ion Mass Spectrometry (ToF-SIMS) . . 229

# List of Figures


1.1 Tissue engineering approaches are classified in three categories. . . . . 3

1.2 Schematic example of 2D cell culture versus 3D cell culture. . . . . 7

1.3 Examples of the different 3D fabrication scaffolds available. . . . . 12

1.4 Schematics of different 3D fibrous techniques for regenerative medicine purposes. . . . . 13

1.5 Different field of the application of electrospun fibres. . . . . 16

1.6 Examples of different human tissue where electrospun scaffolds are being used for tissue engineering purposes. . . . . 25

1.7 Cells connect with each other via cell-to-cell junction proteins and ECM when confluent. **A)** Enzymatic digestion disrupts these adhesive proteins and membrane receptors, while **B)** Thermo-responsive surface detachment preserves the cell-to-cell junction proteins and ECM resulting in cell sheet recovery. . . . . 30

1.8 **A)** PNIPAM and **B)** PEG containing polymers, m side chain groups number changes the corresponding LCST of the polymer. **C)** Schematic representation of the hydrophobic-hydrophilic change of thermo-responsive polymers and chemical of thermo-responsive. . . . . 32

2.1 Free radical polymerisation schematic for the synthesis of PDEGMA. . . 48

2.2 Chemistry schematic for the synthesis of fluorescent labeled PBI-PDEGMA. 49

2.3 PDEGSH synthesis schematic . . . . . 52

2.4 Schematics of cell counting by haemocymeter . . . . . 60

3.1 Electrospinning parameter interaction network. . . . . 74

3.2 Three different morphology types observed in electrospinning. . . . . 75

3.3 Schematic representing of the DoE model timeline. . . . . 84

3.4 Schematic representing the Alamar blue (AB) and cell fixing for SEM imaging timeline for cultured 3T3 fibroblast cells. . . . . 85

3.5 Histrogram and Pareto plots of most significantly impacting parameters. 88

3.6 Full and simplified predictions plotted against actual data from the test runs. . . . . 92

3.7 Schematic diagram of fibre formation. . . . . 93

3.8 **A**) Average fibre diameter, **B**) beads size, **C**) water contact angle and **D**) young modulus of different morphologies scaffolds . . . . . 96

3.9 Cell proliferation over 6 days on different fibre morphologies. . . . . 99

3.10 SEM images of fixed cells on different morphologies over 6 days proliferation. . . . . 100

3.11 4D contour predictions plots of **A)** mean fibre diameter, **B)** fibre morphology by standard deviation and **C)** number of beads per $\mu m^2$. . . . . 103

4.1 Schematic of thermo-responsive fibres and the effects on cell attachment and detachment. . . . . 109

4.2 Schematic representing the Alamar blue (AB) and cell detachment experimental timeline for cultured 3T3 fibroblast cells. . . . . 112

4.3 Cloud point hysteresis of PDEGMA and PBI-PDEGMA polymers and WCA analysis and hysteresis of PLA with different wt% PDEGMA electrospun scaffolds. . . . . 115

4.4 WCA images of changing WCA over time (40 s) at higher concentration of wt% PDEGMA present in the scaffolds. . . . . 116

4.5 PBI-PDEGMA chemical structure. . . . . 117

4.6 SEM images of different wt% percentage PDEGMA or PBI-PDEGMA. . 119

4.7 PLA/PBI-PDEGMA scaffolds representative confocal images . . . . . 120

4.8 Cell growth on different concentrations of PBI-PDEGMA/PLA scaffolds. 122

4.9 **A)** Cell proliferation on PDEGMA/PLA and PBI-PDGEMA/PLA containing electrospun scaffolds. **B)** Cell detachment at different days for different concentration PDEGMA. . . . . 124

4.10 Percentage of cell detached at **A)** different temperatures and time, **B)** difference in fibre diameter, **C)** difference in coating of scaffolds and **D)** difference in cell type. . . . . 125

4.11 Schematic example of cell adherence to fibrous scaffolds of different fibre diameters. . . . . 126

4.12 Confocal images of scaffolds in suspension at 37°C and after 1 h at rt. . . 127

5.1 Schematic of the structures of the eye and corneas six different layers. . . 134

5.2 Schematics of photo-initiated and non photo-initiated peptide scaffold labeled with fluorescein and ATTO. . . . . 139

5.3 Schematic representing the Alamar blue (AB) and immunostaining experimental timeline for cultured hCSCs. . . . . 140

5.4 Schematic representing the Alamar blue (AB) and cell detachment experimental timeline for cultured hCSCs. . . . . 141

5.5 Representative SEM images of the different electrospun fibre morphologies and corresponding proliferation of hCSC culture . . . . . 143

5.6 Representative confocal images of hCSCs on the different electrospun fibre morphologies. . . . . 144

5.7 Schematics of **A)** PDEGMA/PDEGSH synthesis and **B)** the formation of polymer-peptide derivatives electrospun scaffolds. . . . . 146

5.8 2D-NMR spectra of **A)** PDEGMA/PDEGSH and its starting product **B)** PDEGMA/PDEGOH. . . . . 149

5.9 Fluorescein staining of free thiols presence on dried PDEGMA/PDEGSH polymer. . . . . 152

5.10 Cloud point hysteresis of PDEGMA, different ratios of MA/OH and MA/SH polymers in water (2 mg/ml). . . . . 154

5.11 Chemical structure of the Nor-GGG-YIGSR peptide sequence. . . . . 155

5.12 FT-IR spectra from pure Nor-GGG-YIGSR, PDEGMA/PDEGSH and peptide functionalised PDEGMA/S-Nor-GGG-YIGSR by photo-initiated thiol-ene chemistry. Cloud point hysteresis after the photo-initiated thiol-ene reaction. . . . . 157

5.13 SEM images and Fluorescein/ATTO stained PDEGMA/PDEGSH and derivatised PDEGMA/PDEGS-Nor-GGG-YIGSR electrospun scaffolds confocal images. . . . . 160

5.14 Total intensity of the ToF-SIMS peaks of the free thiol containing scaffolds. 163

5.15 Total intensity of the ToF-SIMS peaks of peptide functionalised scaffolds by photo-initiated thiol-ene chemistry. . . . . 163

5.16 ToF-SIMS measurement of the free thiol containing scaffolds. . . . . 164

5.17 ToF-SIMS measurement of the derivatised scaffolds . . . . . 165

5.18 Different chemistry fibre structures schematics and hCSCs proliferation on these scaffolds. . . . . 168

5.19 hCSCs Phenotype expression on different chemistry fibre structures. . . 169

5.20 hCSCs morphology on different surface chemistry fibre structures schematics. . . . . 170

5.21 Representative confocal images of ECM deposition onto free thiol containing scaffolds and derivatised peptide containing scaffolds following culture of hCSCs. . . . . 172

5.22 **A)** hCSCs proliferation on different percentage derivatised PLA with PDEGM-PDEGS-Nor-GGG-YIGSR scaffolds and **B)** thermo-responsive passage cell numbers. . . . . 174

5.23 Representative hCSCs phenotype expression on scaffolds containing different percentage of bound Nor-GGG-YIGSR peptide. . . . . 175

5.24 Representative hCSCs morphology on on scaffolds containing different percentages of bound Nor-GGG-YIGSR peptide. . . . . 177

7.1 Schematic example of possible alternative AFM method to measure a more accurate Young's modulus of randomised fibrous scaffolds. **A)** Conventional AFM tip and **B)** colloid probe. . . . . 187

7.2 Schematic explanation of the co-axial electrospun fibre formation. **A)** The co-axial needle has a sheet and core needle, the thermo-responsive material will be drawn out as a sheet, while the supporting polymer PLA will be drawn out as the core of the fibre. **B)** shows the obtained co-axial fibre build up. . . . . 188

S1 Examples of Tensile test samples. . . . . 229

S2 **A)** $^{1}$H-NMR and **B)** C$^{13}$-NMR of PDEGMA . . . . . 230

S3 2D-NMR spectra of PDEGMA. . . . . 231

S4 **A)** $^{1}$H-NMR and **B)** C$^{13}$-NMR of PBI-OH . . . . . 232

S5 IR graph of PBI, PBI-OH and PBI-Br products. . . . . 233

S6 **A)** $^{1}$H-NMR and **B)** C$^{13}$-NMR of PBI-Br . . . . . 234

S7 **A)** $^{1}$H-NMR and **B)** C$^{13}$-NMR of PBI-Br . . . . . 235

S8 $^{1}$H-NMR of DEGOH . . . . . 236

S9 **A)** $^{1}$H-NMR and **B)** C$^{13}$-NMR of PDEGMA/PDEGOH monomers ratio 95:5 . . . . . 237

S10 2D-NMR spectra of PDEGMA/PDEGOH 95:5 monomer ratio . . . . . 238

S11 **A)** $^{1}$H-NMR and **B)** C$^{13}$-NMR of PDEGMA/PDEGOH monomers ratio 90:10 . . . . . 239

S12 2D-NMR spectra of PDEGMA/PDEGOH 90:10 monomer ratio . . . . . 240

S13 $^{1}$H-NMR and $C_1$3-NMR of PDEGMA/PDEGOH 80:20 monomer ratio . 241

S14 2D-NMR of PDEGMA/PDEGOH 80:20 monomer ratio . . . . . 242

S15 $^{1}$H-NMR and $C_{13}$-NMR of PDEGMA/PDEGOH 70:30 monomer ratio . . 243

S16 2D-NMR spectra of PDEGMA/PDEGOH 70:30 monomer ratio . . . . . 244

S17 FT-IR of all PDEGMA/PDEGOH and PDEGMA/PDEGSH polymers. . . 245

S18 $^{1}$H-NMR and $C_{13}$-NMR of PDEGMA/PDEGSH 98:2 ratio . . . . . 246

S19 2D-NMR spectra of PDEGMA/PDEGSH 98:2 ratio . . . . . 247

S20 $^{1}$H-NMR and $C_{13}$-NMR of PDEGMA/PDEGSH 97:3 ratio . . . . . 248

S21 2D-NMR spectra of PDEGMA/PDEGSH 97:3 ratio . . . . . 249

S22 $^{1}$H-NMR and $C_{13}$-NMR of PDEGMA/PDEGSH 96:4 ratio . . . . . 250

S23 2D-NMR of PDEGMA/PDEGSH 96:4 ratio . . . . . 251

S24 $^{1}$H-NMR and $C_1$3-NMR of PDEGMA/PDEGSH 90:10 ratio . . . . . 252

S25 2D-NMR of PDEGMA/PDEGSH 90:10 ratio . . . . . 253

S26 Ellman's assay standard curve amount of cysteine HCL mol/L. . . . . 254

S27 HPLC-MS data of A) crude-product synthesis cycle without extra washes and B) crude-product synthesis cycle with two extra washes. . . . . 255

S28 HPLC-MS data of A) purified Nor-GGG-YIGSR product peak and B) purified Nor-GGG-YIGSR shoulder of product peak. . . . . 256

S29 Representative standard curves used to determine cell number using the Alamar blue assay. . . . . 257

S30 Preliminary study performed to identify the right limitations per parameter to include all fibre morphologies into the DoE model. . . . . 258

S31 SEM images of different parameter combinations; applied voltage, distance needle to collector, flow rate and PLA polymer concentration. . . . 260

S32 Representative tensile testing graphs of different scaffold morphologies. 261

S33 Representative $^{1}$H-NMR spectra of PLA/PDEGMA blend electrospun scaffolds at different wt% PDEGMA to PLA. . . . . 262

S34 WCA images of hysteresis measurements. . . . . 263

S35 Conversion and $\ln(M_o/M)$ for ATRP polymerisation of PBI-PDEGMA. . 264

S36 GPC peaks for PDEGMA, PBI-PDEGMA(45°C) and PBI-PDEGMA(60°C) in DMF. . . . . 264

S37 Fluorescence intensity of PBI-PDEGMA(60°C) in water at different wavelengths. . . . . 265

S38 Conversion rate of RAFT polymerisation . . . . . 268

S39 Water contact angle on the different PDEGMA or PDEGMA/PDEGSH scaffolds. . . . . 269

S40 ToF-SIMS measurement of the derivatised scaffolds, -SH group falls together with -$PH_2$ from the PBS salts. . . . . 271

S41 Schematics of possible fragments of Nor-GGG-YIGSR observed by ToF-SIMS. . . . . 271

S42 ToF-SIMS peak 32 m/z overlap of signal $SH^-$ and $PH_2$. . . . . 272

# List of Tables

1.1 Summary of 3D structural fabrication techniques, their characteristics and examples per technique. . . . . 11

1.2 Electrospinning parameter category's. . . . . 17

2.1 Design of Experiments (DoE) Model Inputs, Output, and Constants Parameters and Set Limits. . . . . 39

2.2 Parameter combinations and corresponding model codes for the linear regression prediction equations of the runs used to test the DoE model.All equation parameters are represented in DoE model coding of -1,-0.8...etc. 40

2.3 Different ratios of PDEGMA/PDEGOH . . . . . 53

2.4 Details of primary, secondary antibodies and chemical staining used in immunostainings. . . . . 65

2.5 List of primary and secondary antibodies chosen for hCSCs work. . . . . 67

3.1 Different limits combination generated by MODDE 10.1 for the randomised DoE model, replica of three for all combinations and areplica of nine for the center point (N25) are not included in the table. . . . . 77

3.2 Factors that can be solved by the results of linear regression of the DoE outputs. . . . . 80

3.3 Parameter limitation levels for the DoE model . . . . . 86

3.4 Parameter combination to test DoE model. . . . . 91

3.5 Expected fibre morphologies and number of beads. . . . . 94

4.1 Mean fibre diameter and standard deviation for PLA with different wt% percentage PDEGMA or PBI-PDEGMA scaffolds. . . . . 117

4.2 GPC data of PDEGMA, PBI-PDEGMA (45°C) and PBI-PDEGMA (60°C) in DMF. . . . . 118

5.1 GPC data of PDEGMA/PDEGOH polymers in THF. . . . . 148

5.2 Ellman's assay on PDEGMA/PDEGSH polymers. . . . . 151

5.3 Cloud-points of all different PDEGMA, PDEGMA/PDEGOH and PDEG MA/PDEGSH polymers ratios. . . . . 153

5.4 Ellman's assay after photo-initiated thiol-ene reaction of MA/SH (96:4) and Nor-GGG-peptide . . . . . 156

5.5 Representative range, average and standard deviation (SD) of the different scaffolds fibre diameters. . . . . 158

5.6 Flow cytometry % of cell population of keratocyte phenotype expression. 178

S1 DoE model parameter combinations with corresponding average of replicated FD, Stdev, number of beads per $\mu m^2$. . . . . 259

S2 Optimum electrospinning parameters for different % PDEGMA with 25 w/v% PLA. . . . . 262

S3 WCA hysteresis values of PLA with different wt% PDEGMA scaffolds. . 263

S4 Two-way ANOVA values for different %wt PDEGMA or PBI-PDEGMA proliferation studies. . . . . 266

S5 Two-way ANOVA values for different %wt PDEGMA and PBI-PDEGMA proliferation studies compared per day. . . . . 267

S6 Calculated percentage of OH in co-polymer vs. observed percentage free thiol after condensation reaction. . . . . 268

S7 Negative and Positive secondary ions reported from the electrospun scaffolds of different chemical composition. . . . . 270

S8 Flow cytometry Y-mean and X-mean cell population of keratocyte phenotype expression . . . . . 273

S9 ANOVA value of Y-mean and X-mean of FACS. . . . . 274

S10 Total percentage of cell population expression CD34, CD105, ALDH or α-SMA . . . . . 274

S11 Total percentage of cell population expression CD34, CD105, ALDH or α-SMA, two-way ANOVA values. . . . . 275

# Abbreviations

**2D** two-dimensional

**3D** three-dimensional

**Ac** Acetone

**ANOVA** Analysis of Variance

**approx.** approximately

**atm P** Atmospheric Pressure

**ATTO** 3,6-bis(dimethylamino)-10-4-[(2,5-dioxopyrrolidin-1-yl)oxy]-4-oxobutylacridinium perchlorate

**ATRP** Atom transfer radical polymerisation

**Boc** tert-butyl carbamates

**c*** Critical Overall Concentration

**$C_e$** Entanglement Concentration

**cm** centimetre

**$C^{13}$-NMR** Carbon Nuclear Magnetic Resonance spectroscopy

**CNS** Central nervous system

**co** Co-polymer

**conc.** Concentration

**CS** Chitosan

**CRC** Colorectal cancer cells

**DCM** Dichloromethane

**DEGMA** di(ethylene glycol) methyl ether methacryalate

**DEGOH** di(ethylene glycol) vinyl ether

**DMF** Dimethylformamide

**DoE** Design of experiments

**dof** Degrees of freedom

**ECM** Extracellular matrix

**ECs** primary epithelial cells

**EDTA** Ethylenediaminetetraacetic acid

**EE** Equisetum arvense extract

**ESCs** Embryonic stem cells

**FD** Fibre Diameter

**FDA** United States Food and Drug Administration

**Fmoc** Fluorenylmethyloxycarbonyl

**FT-IR** Fourier transform infrared

**GelMA** Gelatin methacryloyl

**GMP** Good manufacturing practice

**GPC** Gel permeation chromatography

**H** Humidity

**HBSS** Hank's Balanced Salt Solution

**hCECs** Human corneal epithelial cells

**hCSCs** Human corneal stromal cells

**HPLC** High pressure liquid chromatography

**HPLC-MS** High pressure liquid chromatography mass spectrometry

**HQCS** Heteronuclear single-quantum correlation spectrometry

**hMSC** Human mesenchymal stem cells

$^{1}$**H-NMR** Hydrogen nuclear magnetic resonance spectroscopy

**HSG** Human submandibylar salivary gland

**hSMCs** Human vascular smooth muscle cells

**hTSPC** Human tendon progenitor stem cell

**HUVECs** Human umbilical vein endothelial cells

**kV** Kilovoltage

**LCST** Lower liquid critical solution temperature

**MAA** Methacrylic acid

**mag.** Magnification

**MALLS** Multiangle laster light scattering

**mESCs** Mouse embryonic stem cells

**ml/hr** Millilitre per hour

**mPEGA** Poly(ethylene glycol) methyl ether acrylate monomer

**mPEGMA** Poly(ethylene glycol) methyl ether methacrylate monomer

**MW** Molecular Weight

**n** Number of technical repeats

**NGF** nerve growth factor

**nHA** nanohydroxyapatite

**nm** nanometre

**Nor-GGG-YIGSR** Peptide sequence glycine-glycine-glycine-tyrosins-isoleucine-glycine-serine-arginine with norbornene acid N-terminal group

**PA-6** Polyamide-6

**PAN** Polyacrylonitrile-co-methylacryalate

**PANI** Polyaniline

**PC12** Pheochromocytoma 12

**PCL** Polycaprolactone

**PCNA** Proliferating cell nuclear antigen

**PDEAM** poly(poly(N,N-diethylacrylamide)

**PDEGMA** Poly(di(ethylene glycol)) metyhl ether methacrylate

**PDEGMA/PDEGOH** poly(diethylene glycol) methyl ether methacrylate-co-poly(diethylene-glycol) vinyl ether

**PDEGMA/PDEGSH** Poly(diethylene glycol) methyl ether methacrylate-co-poly(diethylene-glycol) thiol

**PDEGMA/PDEG-S-Nor-GGG-YIGSR** UV-cured poly(diethylene-glycol) methyl ether methacrylate-co-poly(diethylene-glycol) thiol with peptide sequence glycine-glycine-glycine-tyrosins-isoleucine-glycine-serine-arginine with norbornene acide N-terminal group

**PDLLA** Poly-D-L-lactic acid

**PEG** Polyethylene glycol

**PEGMA** Poly(ethylene glycol) metyhl ether methacrylate

**PEI** Polyethylenimine

**PEO** Polyethylene oxide

**PET** polyethylene terephthalate

**pFA** Para-formaldehyde

**PGA** poly (glycolic acid)

**PGS** poly(glycerol sebacate)

**PLA** Poly-lactic acid

**PLLA** Poly-L-lactic acid

**PLGA** Poly-co-lactic-glycolic acid

**PMMA** Poly (methyl methacrylate)

**PMO** poly($MEO_2MA$-co-OEGMA)

**PNIPAM** Poly(N-isopropylacrylamide)

**PNS** Peripheral nervous system

**polyHEMA** poly(2-hydroxyethylmethacrylate)

**PPGMA** Poly(propylene glycol) methacrylate

**PS** Polystyrene

**PVP** Polyvinylpyrrolidone

**Pyr.** Pyridine

**SA** Stearyl acrylate

**SD** Standard deviation

**SEM** Scanning electron microscopy

**SLS** Sodium lauryl sulfate

**SMA** Smooth muscle actin

**SPAN60** Sorbitan stearate

**rt** Room temperature of 20°C

**RI** Refraction index

**T** Temperature

**TCPS** Tissue culture polystyrene

**THF** Tetrahydrofuran

**ToF-SIMS** Time-of-flight secondary ion mass spectrometry

**RAFT** Reversible addition fragmentation chain transfer polymerisation

**UV** Ultraviolet

**UV-Vis** Ultraviolet–visible

**VIC** Valvular interstitial cells

**VIPS** Vapour-induced phase separation

**wt** Weight

**w/v** Weight per volume

**WCA** Water contact Angle

**QbD** Quality by Design

**YIGSR** Tyrosins-isoleucine-glycine-serine-arginine peptide sequence

# Chapter 1

# Introduction

Currently patients with severe organ injury or damage are treated with organ or tissue transplants. However, these treatments face many complications, such as organ shortages or quality, the necessity for life long immuno-suppression and organ/tissue rejection, due to immune response [2]. In addition, organ transplants are in increased demand for the treatment of chronic diseases such as diabetes, renal failure, liver cirrhosis, stroke and muscular dystrophy. Hence the need for scientists to look elsewhere for the solution to treat these diseases. Within the medical community regenerative medicine (RM) is of increasing interest to overcome these complication. This medical treatment is based around the replacement or regeneration of human tissues and organ functions [3]. This field combines multidisciplinary fields, such as cell therapies, tissue engineering, gene therapy and medical devices.

## 1.1 Tissue engineering (TE) and regenerative medicine (RM)

The term regenerative medicine was first used by Kaiser [4] and was later considered the right term for the broad field of tissue engineering (TE), stem cell research, cell transplantation, biochemistry and biotechnology [5, 6]. However, the concept of tissue engineering is much older and was first reported by Bisceglie [7] in 1933. They reported mouse tumour cells survival when seeded and wrapped in a polymer mem-

brane and implanted into the abdominal cavity of a pig. No immuno response of the pig immune system was observed after implantation. Several decades later, Chick et al. [8] observed the release of insulin in response to glucose concentration change when pancreatic beta cells from neonatal rats were cultured on synthetic capillaries perfused with media. The actual term tissue engineering was implemented in 1988 when Fung [9] used the term 'tissue' to describe the living organisms between cells and organs. The term was later expanded to the interdisciplinary field of applying engineering and life science principles towards the manufacturing of biological replacement that restores, maintains or improves the aimed tissue function [10]. Currently there are three different approaches in the tissue engineering field: 1) cell therapies with the use of isolated cells, 2) bio- materials or synthesised materials for induced tissue engineering, and 3) the combination of cells with the support of bio-material scaffolds (see Figure 1.1). Many criteria need to be considered to achieve an effective, long-lasting treatment or repair of damaged tissue and gene therapy. To start with a sufficient amount of cells are required. Additionally, cells must either be maintained or differentiated in the desired phenotype. When 3D structures are used cells must be adaptable to the structural support and produce ECM. Furthermore cells obtained *in vitro* must be compliant with native cells in structure and mechanical properties and need to be able to integrate with the native cells, which reduces the risk of immunological rejection. In general associated biological risks must be minimised [2, 11, 12].

Cells used in cell therapies can be classified into four groups 1) autologous cells, 2) allogeneic cells, 3) xenogenic cells and 4) stem cells. Cells harvested from the patient's own body rather than a donor are autologous cells. These autologous cells have the advantage of resulting in no or lower immune rejection when used as clinical treatment. However, these cells are not always harvested in the quantity or quality needed or show limited proliferation capacity when expanded, mainly due to the tissue end-stage failure *in vitro* [2, 13, 14]. Moreover, the harvest of autologous cells is costly and has high batch to batch variation, which makes them unsuitable for universal large scale clinical use. Instead, cells from a healthy donor can be used [15], these cells are classified as allogeneic cells. An example of clinically used allogeneic cells is the use of human paneatic islet cells for the treatment of type I diabetes [16]. This transplan-

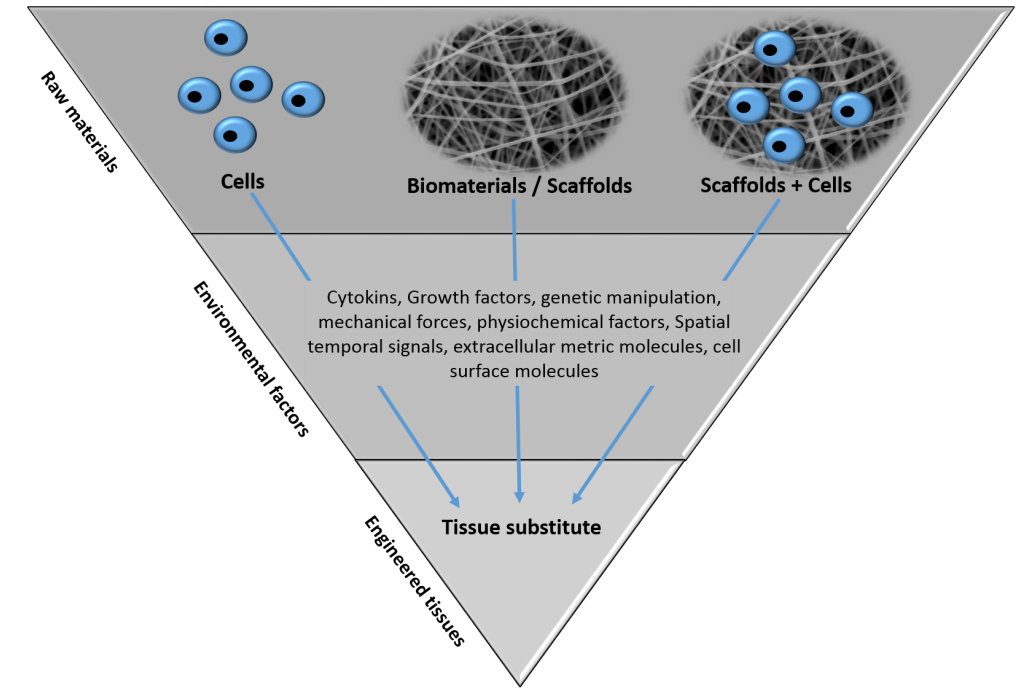



**Figure 1.1:** Tissue engineering approaches are classified in three categories. 1) cells on it own, 2) scaffolds and 3) combination of scaffolds and cells. Environmental factors can be used to enhance their implementation as tissue substitute.

tation results in the reduction of insulin injection dependency of the patient. Major advantages of the use of allogenic cells include uniformity, standardized production, cost-effective and increased quality control [2]. However, one main drawback is the change of immune response of the recipient's body. This risk can be reduced by screening donors for gene compatibility and in many cases relatives of patients are selected as cell donors to reduce the risk of immune response. A well known treatment with relative's allogeneic donor cells is the treatment of leukemia [17] . Cells from different species or xenogenic cells are another possible cell source. These cells have been used for the delivery of specific chemicals within the engineered tissue with the impaired function [18]. For instance insulin dependent diabetic kidney transplant patients were successfully treated by transplanting foetal porcine islet-like cell clusters. This resulted in positive staining of insulin and glucagon [19]. However, existing treatments require

prolonged treatment of immuno- suppressants to avoid xenogenic graft rejection of the human body [20]. In contrast, primary cells from original tissues do not show any immuno response due to their immunological compatibility. Nevertheless, the use of primary cells has major drawbacks such as limited lifespan and insufficient cell expansion numbers. Furthermore, de-differentiation can occur when cultivated *ex vivo*, resulting in inappropriate phenotypes. Examples include articular chondrocytes expressing fibrocartilage, instead of the hyaline cartilage observed *in vivo* [21] and human corneal stromal cell differentiation to myofibroblasts [22]. In addition, some cell phenotypes, such as spinal cord neurons, are practically impossible to harvests from living patients and donors [12]. Whereas, multipotent stem cells have the ability to expand in high numbers and are able to be differentiated in different phenotypes. However, this cell differentiation is a costly and complex process [23]. Moreover, this differentiation *ex vivo* is challenging due to risk of contamination when cells are isolated, instability of maintaining their desired cell type *in vitro* [24] and low reproducibility of observed results [25]. Another possible cell source is embryonic stem cells (ESCs), mainly derived from discarded non-transferable human embryos using immuno-surgical techniques. These ESCs have been observed to grow much faster than adult stem cells. However, political, ethical and religious opposition have resulted in a biased view on the use of these cells. This has resulted in preferred use of allogenic mature cells or adult stem over ESCs.

In many cases, an initial expansion of harvested patient's cells by 2D *in vitro* cell culture is required to obtain a reasonable amount of cells. These large quantities of cells are subsequently seeded onto the 3D scaffold of interest which provides tissue formation support due to the bio-mechanical environment. These scaffolds can be made of permanent scaffolds in which the bio- composite will be implanted, while degradable materials can be used as implants to provide support when tissue forms and slowly degrade to make room for the newly developed tissue. In all cases, the implanted materials must be able to survive, restore normal function and integrate with the surrounding tissues without the undesired inflammatory response [26, 27]. This initial expansion of harvest cells is most commonly done on 2D cell culture on tissue culture plastic polystyrene (TCPS) within specially formulated cell media with animal serum

for cell growth. Depending on the purpose of the cells the media can be formulated to stimulate differentiation of the cell to the required phenotype. Although 2D cell culture works for most robust cell lines (i.e. fibroblast), many other cell types require a different approach to maintain their specific phenotype (i.e. corneal stromal cells, stem cells and cancer cell lines).

The natural extracellular matrix (ECM) in the body promotes proliferation, survival, migration and differentiation of the cells. However, 2D cell culture does not mimic this ECM environment resulting in undesired differentiation or no cell differential response. Therefore, an increased interest has developed in the manufacturing of 3D ECM mimicking scaffolds from either natural or synthetic materials as cell culture expansion templates besides the use as tissue substitute for implantation methods for these different cell types [26]. Mechanical strength, structures and materials of these scaffolds play a key role in the support of cell attachment, growth, differentiation and function on these structures. Moreover, these scaffolds need to be bio-compatible and biodegradable at a controlled rate when used as transplant, or non or slowly biodegradable when used for *in vitro* cell expansion.

Engineering scaffolds have the potential for complex tissue reconstruction. However, there are still many challenges to resolve. These challenges include stem cell differentiation, phenotypic support, scaffold compatibility, cell expansion drawbacks, scaffold design, cost of manufacturing of these scaffolds and scale-up possibilities. This review describes *in vitro* 3D scaffold support systems for cell expansion designed for the use in regenerative medicine application. This leads to the main aims and objective for the research project presented in this thesis.

## 1.2 *In vitro* cell expansion within the regenerative medicine field

### 1.2.1 2D cell culture versus 3D cell culture of mammalian cells

*In vitro* cell culture platforms are utilized to investigate the cell and tissue physiology and pathophysiology of mammalian cells outside of the body. Traditionally cells are cultured on 2D tissue culture polystyrene (TCPS) surfaces [28]. Although, TCPS cell culture approaches are appropriate for routine cell culture they do not represent an accurate representation of the native 3D ECM tissues. Cells grown in 2D culture are observed to be flatter and more stretched than their native morphology *in vivo*. Cells are attached to the flat surface and neighbouring cells with a small portion of their membrane, while most of the cell's membrane is exposed to the bulk cell culture media. Consequently many biological mechanisms (such as differentiation and tissue morphogenesis) are observed as different compared to the *in vivo* native organs or tissues [29, 30]. Within the native tissue, cells are connected with each other as well as to the extracellular matrix (ECM). Cell surface receptors interact with their neighbouring cells, the surrounding ECM and other exogenous factors. The 3D ECM provides mechanical support and is involved in the regulation of intracellular complex signaling process. This process influences phenotypic fate by changing the gene, resulting in protein expression and in the case of stem cells influences the self-renewal or differentiation to adult cell types [23, 26, 31, 32]. This shows the importance of implementing 3D environments when cells are cultured *ex vivo*. For this reason, the main challenge in 3D scaffold manufacturing is to mimic the structure and biological function of the natural ECM [30, 33–35].

Many cell culture studies have observed significant difference in cell growth, morphology and population when cultured on 3D environmental structures [29, 36]. Difference in proliferation rate between 3D and 2D culture have been observed and are cell type and matrix dependent. Many cell lines exhibit reduced proliferation rates in 3D culture compared to 2D [29]. This is due to structural hindrance for the cells to migrate

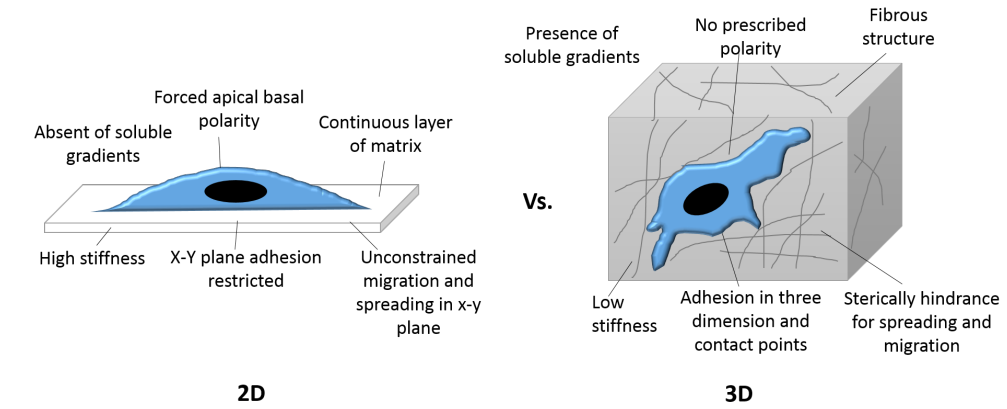



**Figure 1.2:** Schematic example of 2D cell culture versus 3D cell culture. Cells spread and flatten onto 2D cell culture plastic, while different cell morphologies are present within the 3D structure due to more cell binding sites and larger surface areas provided.

and spread out (see Figure 1.2). For example, decreased expression of the proliferating cell nuclear antigen (PCNA) protein marker and reduced cell numbers was observed when endometrial cancer cell lines Ishikawa, RL95-2, KLA and EN-1078D were cultured on 3D reconstituted basement membranes compared to 2D culture [37]. Other cell lines that have been shown to proliferate more slowly are human submandibylar salivary gland (HSG) cells ( cultured on Matrigel) [38], human embryonic kidney (HEK) 293 cells (collagen I microspheres) [39], colorectal cancer cells (CRC), CACO-2, DLD-1, HT-29, SW480, LOVO, COLO-206F (cultured on laminin-rich-extracellular matrix) [40], and human mammary epithelial cells MCF10A (cultured on complex 3D silk scaffolds and Matrigel)[41]. In contrast, JIMT1 breast cancer cells were observed to grow 1.86 fold faster on Matrigel than in 2D culture. However, this same cell line was observed to grow 7.2 fold slower when cultured on poly(2-hydroxyethylmethacrylate) (polyHEMA) 3D scaffolds [42]. These findings suggest that the structure and materials of the 3D models have a direct impact on the proliferation rate of the cells. In addition researchers have shown the cells in 3D structures differ in gene, protein and cell receptor expression from 2D culture. 3D environmental cell culture platforms provide a much larger surface area and more binding sites for the cells compared to 2D

TCPS (see Figure 1.2). Cell adhesion complexes and cellular cytoskeleton play a key role in the molecular signaling pathways and are therefore mainly influenced with the surrounding substrate adherence [43]. For example, Kiss et al. [44] observed cell morphology changes and up-regulation of CXCR4 and CXCR7 in prostate cancer cell lines PC3, Du145, and LNCaP when cultured in the cell-ECM like 3D culture (Matrigel). In contrast, Pineda et al. [45] found higher levels of cytoskeletal elements and ECM proteins when embryonic cells were cultured in 2D compared to grown in 3D structures. This is due to the difference in Young's modulus of the 2D to 3D structures, which significantly impacts the response of the cells [46]. Mabry et al. [46] revealed that the substrate stiffness had a significant impact on valvular interstitial cells (VIC) gene expression. More gene expression changes, such as cytoskeletal, contractility, and matrix remodeling genes, were observed when cultured on 2D TCPS, while less changes were observed on the less stiff hydrogels.

## 1.3 3D structure requirements

To mimic the native ECM environment many factors must be taken into account to obtain a functional, structural and mechanical equal or better scaffold then the native tissue. These include porosity, stiffness of material, fibre diameters, structure scaffold and material used. 3D scaffolds need to be designed to meet the needs of nutritional and biological binding of the specific cells [2]. Porosity of the scaffolds controls the continuous exchange of nutrients, oxygen and waste metabolites, as insufficient exchange can lead to aggregation nutrients or waste products and can result in cell death. Beside mass transfer porosity supplies increased binding sites for the cells [47]. Mechanical properties should match the native ECM and depends on the cell type and origin in the body [45, 46]. For example, bone cell lines have been observed to prefer stiffer materials [48], while cells from cartilage, heart, nerves, skin and ganglion require much softer environments [49]. Engler et al. [50] observed post-infarct fibrotic scars when cardiomyocytes heart cells were cultured on stiff substrates. This was due to overstraining of the cells which resulted in no beating. However, when these same cells

were cultured on an elastic substrate the cells were observed to beat. In the case of stem cells the modulus of the substrate has a direct impact on their differentiation. For instance, Saha et al. [51] observed neurons when cultured on soft hydrogels (100-500 Pa), while harder gels (1 000-10 000 Pa) resulted in glial cells. It is therefore important to investigate the origin of the desired cells before designing the 3D structures. Native ECM is built of large fibril protein that forms a fibrous structure and consequently give mechanical support [52]. This fibrous structure is therefore considered desirable in 3D ECM mimicking structures. Additionally, the materials used must be bio-compatible and show bio- activity to promote cell adherence and migration. Two types of materials have been used in 3D manufactured scaffolds. These are 1) natural materials and 2) synthetic materials.

### 1.3.1 Natural materials

Naturally derived materials have the advantage of their biological recognition and are susceptible to cell-triggered protealytic degration and remodeling [53]. Due to biocompatibility, ECM native proteins have been commonly used in the tissue engineering field. These include collagen [54], hyaluronic acid [55], chitosan [56], elastin [57] and gelatin [58]. Collagen is found in various connective tissues and is the main structural protein in the human body. Collagen type I(skin and bone tissue), type II(cartilage) and type III(blood-vessels) are the most commonly used material in bio- materials. Collagen is FDA approved and has been successfully used for the treatment of wound healing for burns and chronic wounds [25, 59, 60]. Burke et al. [25] created an artificial skin of fibroblast seeded collagen scaffolds for the treatment of extensive burn injury, which to date are still utilized. Beside body derived materials, nature derived materials are also commonly used. Examples include silk [61] produced by insect larvae to form cocoons and alginate [62] derived from algae. Although natural materials are biocompatible these materials have complex sourcing, processing and purification steps before being able to be used. Additionally, they have been shown to have limitations in low mechanical strength, a malleable structure, lack of consistency and have the risk of immunogenicity and possible disease transmission [12, 13, 63].

### 1.3.2 Synthetic materials

Synthetic materials have the advantage over natural materials due to their reproducibility, adjustable chemistry, mechanical strength, lower cost of production and absence of infection transmission. They can be classified into three different materials; 1) bio-inert, 2) resorbable and 3) bioactive materials. Bio-inert material stainless steel has been widely use as artificial hips. However, these materials have been observed to provoke scar tissue formation. Nonetheless, polyethylene terephthalate (PET) non-degradable polymer has been observed to show no undesired response. Ma et al. [64] has demonstrated this by the observation of spreading, proliferation and phenotype support when cultured on methacrylic acid (MAA)-grafted PET electrospun nanofibrous. In contrast, the resorbable materials are biodegradable and will eventually dissolve generating harmless dissolution products. The most common degradable polymers used are the poly (α-hydroxy) acid polymers. These polyesters are low in toxicity, biocompatible and are FDA-approved. Furthermore, they are easy to shape and have high tensile properties. These polymers include poly (lactic acid) (PLA) [65, 66], poly (glycolic acid) (PGA) [67], co-polymer PLGA [68] and polycaprolactone (PCL) [69]. Degradation and strength of these polymers can be controlled by their molecular weight, copolymer ratio and chemical structure and can be altered to obtain the desired degradation rate and strength required. Examples of successful application of these synthetic polymers in 3D cell cultures are Yao et al. [58] who observed successful adherence and osteogenic differentiation when human mesenchymal stem cells (hMSC) were seeded on 3D electrospun PLA/PCL nanofibrous scaffolds. Evrova et al. [70] also showed successful adherence and differentiation on PLGA:PEO electrospun scaffolds. Although these polymers have many advantages they do not have any biological interaction with the cells. This can be resolved with the use of a combination of natural and synthetic polymers [43, 71]. Bioactive materials [72] stimulate a biological response beside a structural support. In addition, increased research has been conducted into functionalisation of polymers with chemically signaling factors, proteins or peptides for better biological interaction [73].

## 1.4 3D scaffold fabrication techniques

Many different fabrication techniques are utilized to fabricate 3D structures. Examples are hydrogels, 3D bio-printing, foam scaffolds, self assembly, micro-particles and electrospinning (see Figure 1.3). A summary of the different 3D structures and their structural characteristics can be found in Table 1.1. To translate these product scaffolds to the clinic it is critical that the fabrication technique is suitable for scalable manufacturing to good manufacturing practice standard (GMP) [74]. As previously mentioned native ECM is built up of a porous fibrous environment and therefore this section is focused on the fabrication of fibrous scaffolds. These are hydrogels, 3D bio-printing and electrospinning 3D fabrication technique (see Figure 1.4). The fabrication technique electrospinning is explained in more detail as this technique was as identified most suitable for the aim of the project.

**Table 1.1:** Summary of 3D structural fabrication techniques, their characteristics and examples per technique.

| Technique | Particles | Porous | Fibrous | Examples |
|---|---|---|---|---|
| **Micro-particles** | x | x | - | Functionalised solid particle or porous hydrogels |
| **Foam scaffolds** | - | x | - | High pressure processing |
| **Self-assembly** | x | x | x | Nano-particle aggregation |
| **Hydrogels** | x | x | x | Particles or structures |
| **3D printing** | - | x | x | Customised structures |
| **Electrospinning** | - | x | x | Random or Aligned fibre mats |

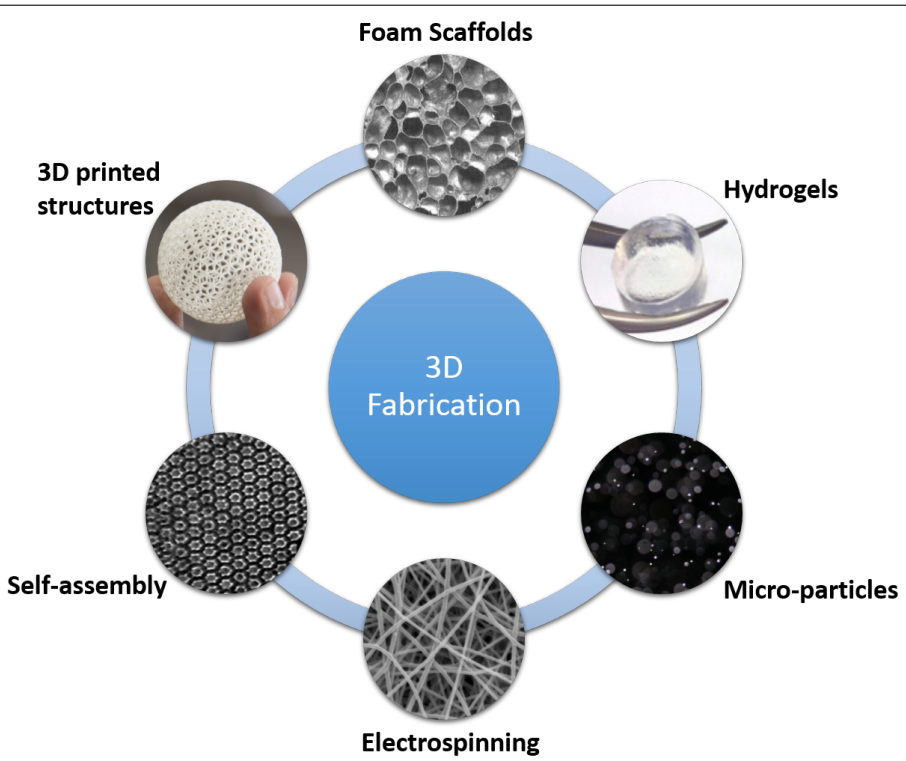



**Figure 1.3:** Examples of the different 3D fabrication scaffolds available.

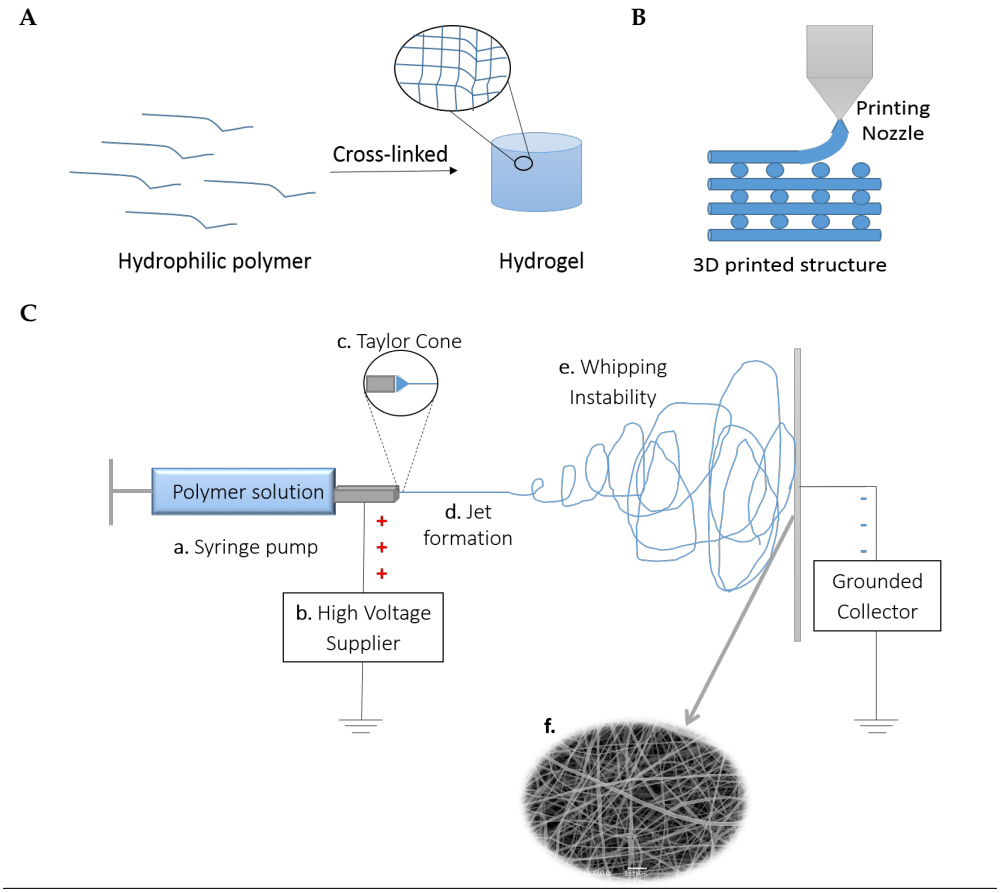



**Figure 1.4:** Schematics of different 3D fibrous techniques for regenerative medicine purposes. **A)** Hydrogels, **B)** 3D bio-printing and **C)** Electrospinning. **a**) A polymer/solvent solution is pushed through a needle at a set flow rate by a syringe pump. **b**) A voltage is applied into the polymer/solvent solution. Due to the oppositely charged liquid and collector a **c**) Taylor Cone with **d**) extracting jet is formed. **e**) Instability occurs due to electrostatic repulsion which results in an unstable and rapid whipping fibre jet ejection from the Taylor cone, **f**) resulting in solid fibre deposit on the grounded collector.

### 1.4.1 Hydrogels

Hydrogels are mostly built of synthesised hydrophilic polymers or natural products, such as collagen I [75], matrigel (bone marrow like biomatrix) [38], gelatin [76], or alignate [34]. Hydrogels are based on polymer chain networks which are extensively

swollen with water (see Figure 1.4A) [77, 78]. These cross-linked polymeric networks have the ability to swell and retain a significant fraction of water within their structure, due to hydrophilic functional groups attached to the back bone of the polymer. Hydrogels retain their structure and do not dissolve due to the cross-linking network of the polymer. This water retention characteristic shows similarities with natural ECM which contains large volumes of water and are therefore considered suitable for *in vitro* 3D ECM mimicking cell culture platforms. Incorporation of cells within the hydrogel structure are also reported. For example, Nichol et al. [76] reported the use of cell-laden photopolymerised micro-patterned hydrogels of gelatin methacrylate (GelMA). Human umbilical vein endothelial cells (HUVEC) incorporated in the hydrogel were observed to bind to, proliferate, elongate and migrate in the microfabricated GelMA gels. However, these hydrogels have low shelf lives, due to dehydration and have low mechanical strength.

### 1.4.2 3D bio-printing patterns

3D bio-printing utilizes a layer-by-layer build up method to deposit materials within a predefined structure, which mimic the ECM fibril structures, tissues or organs (see Figure 1.4B). The main bio-printers used for the deposition and patterning of 3D structures are inkjet [79, 80], micro-extrusion [81] and laser-assisted printers [82]. Beside the printing of material structure, the bio-printing of cell containing printing materials has also been reported as successful [79, 80, 83]. For example, a recent study by Costantini et al. [84] reported the use of 3D bio-printed hydrogel aligned fibers laden with muscle precursor cells (C2C12). Enhanced myogenic differentiation and the formation of parallel aligned long- range myotubes were observed *in vitro* and *in vivo* (back of immuno-compromised mice). These studies have shown the potential of these 3D printed cell containing hydrogels for skeletal muscle tissue engineering and human clinical application. Although, 3D-printing has the potential in the tissue engineering field, this novel process is still in development with many process related issues still needing to be addressed.

### 1.4.3 Electrospinning

Electrospinning is a well-established technique used for over a century to produce controlled fibres of specific diameters and porous structures [85]. The first record of the "electrostatic spraying" phenomenon goes back to 1628 [86], which reported the formation of a cone shape and small droplet ejection when an electrically charged piece of amber was brought near to a water droplet. Centuries later in 1887 Boys [87] reported the formation of fibres by "electrical spinning" from multiple materials (shellac, sealing-wax, gutta-percha, beeswax and collodion). Two decades later in 1902 the electrospinning process was patented by Cooley [88] and Morton [89]. Further development of the electrospinning process for commercial use were made and patented by Anton [90] in 1934 and 1944 [91] for the fabrication of textile yarn. From that point the use of electrospun fibrous mats has been implemented in many different fields (see overview Figure 1.5).

The electrospinning process has been considered a suitable method for the production of fibrous scaffolds, due to the cost effective and reproducible production of fibres with diameters in the range of micro-metres and nano-metres [92]. Furthermore, a vast range of polymers (natural and synthetic) can been used for the fabrication of fibrous scaffolds. Electrospinning parameters can be changed to control the resultant shape, size and porosity of the electrospun fibres [93]. The obtained fibrous structures show similarities with the natural extracellular matrix (ECM) resulting in cell penetration through the pores. Therefore, electrospun scaffolds are considered a potential platform for *in vitro* cell culture which mimic *in vivo* environment characteristics. Consequently electrospinning is widely used for tissue engineering in the regenerative medicine field [85, 94, 95].

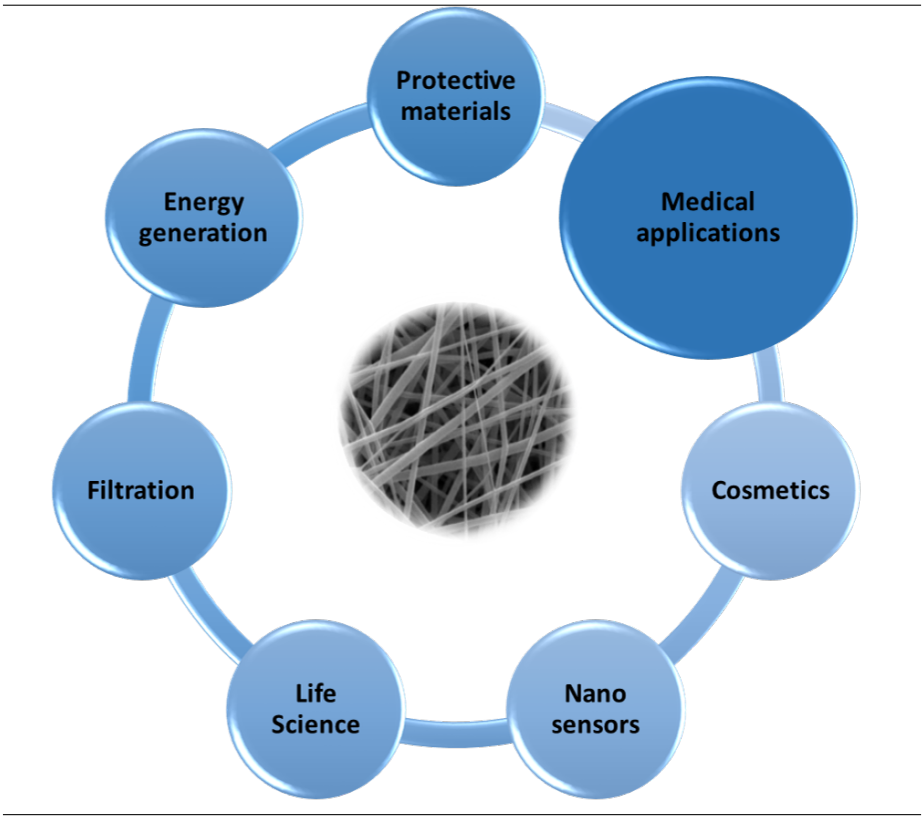



**Figure 1.5:** Different field of the application of electrospun fibres.

### The electrospinning process

The electrospinning set-up consists of a syringe pump, which ejects the polymer solution at a controlled rate, connected to a conductive spinneret (needle). A positive voltage is applied to the spinneret in the range of 0 to 30 kV, while a negative voltage or no voltage is applied to the collector (flat or rotating mandrel of metallic material). This collector with opposite polarity is placed at a defined distance from the spinneret to collect the fibre mat, as shown in Figure 1.4C. The electric field applied to the spinneret will result in a build up of charge on the polymer solution droplet surface. When the electric field exceeds the surface tension of the droplet this leads to a change of the rounded meniscus solution drop to a conical shaped droplet with ejecting fibre jet. This phenomenon is called the Taylor cone (see Figure 1.4Cc). Instability of the ejected fibre jet occurs due to electrostatic repulsion which results in an unstable and

rapid whipping fibre jet, which is accelerated towards the collector of opposite polarity. Polymer-jet elongation, thinning and solvent evaporation occurs while the fibre jet travels through the atmosphere. This leads to the deposition of non-woven solid polymer fibres on the collector plate [96].

**Table 1.2:** Electrospinning parameter category's.

| Category | Parameters |
|---|---|
| **Solution** | 1. Viscosity |
| | 2. Concentration |
| | 3. Molecular weight polymer |
| | 4. Elasticity |
| | 5. Surface tension |
| | 6. Solvent |
| | 7. Conductivity |
| **Processing** | 1. Flow rate |
| | 2. Applied voltage |
| | 3. Collecting distance |
| **Ambient** | 1. Temperature |
| | 2. Humidity |
| | 3. Atmospheric Pressure |

### 1.4.4 Electrospinning parameters

Process parameters can greatly affect fibre formation and morphology. For a reproducible electrospinning process these parameters must be known and kept constant. These process parameters can be separated into three categories; 1) solution, 2) processing, and 3) ambient parameters (see Table 1.2).

#### Solvent Parameters

The polymer solution parameters significantly influence the resultant fibre formation. The concentration and polymer characteristics highly affect the solution's viscosity and

subsequently the electrospinning jet stability, fibre formation and diameter. Higher viscosities will result in an increase in fibre diameter, due to less stretching of the jet during the whipping stage. Molecular weight (MW) of the polymer also greatly influences the viscosity of the polymer solution. Fortunato et al. [97] showed a linear increase in fibre diameter with increasing MW of PolyEthylene Glycol (PEG; 550, 1550, 10 000, 20 000 and 100 000 g/mol) from 500 nm to 1200 nm. Tao and Shivkumar [98] and Koski et al. [99] saw the same increase of fibre diameter when increasing the MW at a given polymer concentration. Beside polymer MW and solvent, additives have been observed to influence the viscosity as well. Jun et al. [100] investigated the influence of viscosity and conductivity on the fibre diameter and fibre morphology. This study showed beading at lower viscosities and a decrease of beading when the conductivity of the solution was increased by adding pyridinium formiate, which subsequently increased the total solution viscosity. Viscosity is therefore directly related to the polymers MW, concentration, structure of the polymer, additives and solvent [101]. Most electrospinning research uses polymer concentration as an independent parameter whilst not taking into account the viscosity. By using viscosity as a parameter it is possible to compare different polymers by keeping the viscosity constant [102, 103].

Molecular weight (MW) of the polymer not only affects the viscosity of the solution, but can result in core-sheath fibre formation when using a mixture of polymers. For example, Zhang et al. [104] and Wei et al. [105] developed core-sheath nanofibres of a PEG/chitosan (CS) polymer mixture by using different average MWs (from 3000 to 200.000 g/mol). They found that the MW of CS, the weight ratio of the two polymers and the spinning temperature mainly affected the core-sheath formation. PEG core fibres were formed due to their lower MW compared with CS. These low MW polymers have increased mobility due to rheological factor, small dimensions and low degree of chain entanglements and therefore higher solubility is implied. This results in movement to the jet core during the rapid drying process of the jet, followed by the drawing process of the fibre. Higher MW polymers will stay in the sheath of the jet as movement is hindered due to the polymer chain entanglements [97].

The occurrence of chain entanglement depends on the concentration and structure

of the polymer. For example, branched polymers will result in higher entanglement concentration then linear polymers. McKee et al. [106] investigated the implication of semidilute un-entanglement (branched polymers) and semidilute entanglement (linear polymers) concentration regimes on the electrospinning process using a series of linear and branched PET-co-polyethyleneimine (PEI) polymers. They observed an increase in entanglement concentration ($C_e$) when the branched polymer PEI was used compared to an equivalent MW linear PEI. This is due to the higher segment density of the branched polymer chains, which hinders chain overlap and entanglement. This results in beaded nanofibres at minimum $C_e$ and uniform, defect-free fibres at $C_e^{2-2.5}$. Therefore, defining the entanglement concentration of the polymer-solvent solution before electrospinning could cut down the time used to optimise the electrospinning parameters.

Although many studies suggest the importance of the solution's viscosity no significant correlation was observed. Basu et al. [107] hypothesised the importance of the elastic storage energy of the polymer solution. This energy storage stabilised the polymer extension, due to the entanglement of the polymer network formed. Therefore, resulting in continued drawing of the ejected jet without breakage. While loss of entanglement of the polymer network results in elastic stretching and subsequently fragmentation of the jet [108]. Yu et al. [109] investigated the influence of the degree of elasticity on the fibre morphology after electrospinning with the use of Boger fluids, which are fluids of constant viscosity whose degrees of elasticity can be altered. An increase in degree of elasticity was observed to eliminate the formation of beaded fibres. While lack of elasticity was observed to prevent fibre formation, instead droplets and beads-on-strings (big beads with small strings) structures were formed. This is due to the Rayleigh instability which is driven by the surface tension forces. However, polymer concentration well above the critical overall concentration $c^*$ showed more uniform fibre formation. When the fluid relaxation time exceeds growth of instability the capillary forces activate the elastic response, resulting in a delay of jet break-up. Therefore, the use of an elastic polymer is highly recommended for the formation of uniform fibres.

Electrospinning solvents have an effect on the electrospinning solution by influencing their surface tension, conductivity, and viscosity. Casasola et al. [101] investigated the effect of pure and binary-solvent systems of different solvents on the formation of electrospun fibre morphology. Besides the influence of the solvent on the viscosity of the solution, they observed the formation of uniform fibres when highly conductive solvent systems were used (acetone/DMF; 2.8 µS/cm[1]). Furthermore, the solvent evaporation rate was also observed to influence the fibre diameter and morphology. Quick solvent evaporation resulted in the formation of thicker fibre diameters and porous structure on the surface. Due to the quick evaporation rate a local cold area occurs on the jet's surface. This cold area traps condensed water drops from the air, which evaporate when fibres are collected. This leaves a drop shaped porous surface morphology [110]. This highlights the importance of carefully considering the solvent or solvent system used. When choosing a solvent the toxicity should be kept to a minimum as possible traces of solvent within the scaffolds fibres could interfere with the cells [111].

The polymer-solution surface tension also influences the electrospinning process. Cohesive forces among liquid molecules means that each molecule is pulled equally by neighbouring liquid molecules in every direction resulting in a net force of zero. The applied voltage during electrospinning overcomes these forces, resulting in the phenomenon of the Taylor cone with ejecting jet. Casasola et al. [101] showed that the surface tension varies by solvent type such that they should be taken into account in parameter selection before electrospinning. Wei et al. [105] investigated the fibre morphology of blended polymer mixtures pointing out that the surface tension is the third parameter with the most impact on the fibre formation. High surface tensions resulted in bead formation, due to the minimisation of the surface area, while polymer solutions with lower surface tensions resulted in bead free fibres [97].

Conductivity of the electrospinning solution results in a surface charge or current which is overcome by the Coulomb force between charges and the force due to the external applied voltage, resulting in a Taylor cone. This Coulomb force can be varied by changing the conductivity of the solution [112]. Therefore, the conductivity of the solution has a direct link to the stability of the electrospinning Taylor cone. Additives, such

as salt, can be used to improve the conductivity of the electrospinning solution [113]. Angammana and Jayaram [112] investigated the effect on the electrospinning process and fibre morphology with poly(ethylene oxide) (PEO)/water of different conductivities. This showed an increase of jet current with increase of solution conductivity up to $\pm$ 200 µs/mm, thereafter the jet current decreased gradually with the increased conductivity. A power law relationship was observed; and fibre diameter decreases when the conductivity increases. Too low or high conductivity resulted in no Taylor cone formation. Multi-jets were also observed with an increased conductivity of the polymer solution [85, 96, 114]. Jun et al. [100] investigated the fibre diameter and morphology with respect to viscosity, surface tension and conductivity of the polymer solution. Pyridine formiate was added to the dichloromethane (DCM)/PLA solution to improve the conductivity of the solution, resulting not only in an increase of conductivity but also an increase in the viscosity. However, no significant increase in surface tension was observed. More uniform fibre formation and a decrease in fibre diameter was observed with the addition of pyridine formiate. Therefore, conductivity of the solution most not be overlooked and be taken into account when optimising the process.

**Process Parameters**

Their are three main process parameters; applied voltage, flow rate and needle-to-collector distance. As mentioned before, the external applied voltage overcomes the surface tension and current of the polymer solution droplet to form a Taylor cone. The voltage results in a large electrostatic force near the exit of the nozzle which stretches the jet significantly and triggers the viscoelastic response. Subsequently, jet formation and thinning occurs. Applied voltage during electrospinning should be adjusted to obtain a steady state jet, in a way that the pulling rate is not too fast or slow to cause jet interruption and whipping instability. Fallahi et al. [115] stated that for a stable process the rate in which the fluid is forced into the drop must be equal to the fluid carried away by the jet, which is generated by the applied voltage. The impact of different voltage on the electrospinning process of polyacrylonitrile (PAN) solution with a constant flow rate were investigated [115]. Two jet regimes were observed; stable jet at

low voltage, where the jet flow rate was lower then the flow rate and a fluctuating jet regime were the jet flow rate was higher then the flow rate. Also a increase in jet current was observed with increase of applied voltage. Samatham and Kim [116] observed beads-to-string fibres during the fluctuation jet regime and bead-free fibres at the stable regime. Therefore, getting a good balance between the flow rate and the applied voltage is an important step for bead-free fibre formation [117].

Besides the direct correlation of the flow rate with the Taylor cone, jet formation and jet and whipping stability, it also influences the fibre diameter. An increasing flow rate results in a significant increase in the fibre diameter [118]. Tang et al. [119] saw an exponential-like increase in fibre diameter when the flow rate was increased from 1 ml/hr to 2.5 ml/hr. Nonetheless, if bead-free fibres are desired the applied voltage should be increased with increased flow rate, to produce a stable jet [115].

Distance between collector and needle influences the whipping and stretching time of the jet resulting in decrease of fibre diameter when distance is increased and vice versa. However, this parameter effect has been observed less profound than other process parameters [120]. Needle-to-collector distances of 5 to 25 cm are most commonly reported in literature. Hekmati et al. [121] observed an increase in polyamide-6 (PA-6) nanofibre diameters with a decreasing needle-to-collector distance. Generally, too small a distance results in insufficient solvent evaporation time resulting in fibre flatting due to insufficient drying [120], as well as bead formation [122]. While too great a distance results in little whipping on whipping instability [120].

#### Ambient Parameters

When the polymer jet whips through the air to the collector the ambient environment plays a role in the solvent evaporation and solid fibre formation. The ambient temperature influences two main parameters in the electrospinning process; the solvent evaporation rate and the viscosity of the polymer solution. Solvent evaporation increases with an increase in temperature, while viscosity decreases with increasing temperature [123]. Chen et al. [124] reported not only a decrease in viscosity (1.2 to 0.4 Pa·s),

but also of surface tension (87 to 35 mN/m) and an increase in conductivity (0.35 to 1.14 ms/cm) when increased temperature was used from 20 $^{\circ}C$ to 100 $^{\circ}C$. De Vrieze et al. [123] saw the same decrease in viscosity when increasing the temperature. Subsequently, this change in viscosity and solvent evaporation rate resulted in a difference of fibre diameter. Hardick et al. [125] reported a correlating reduction of viscosity with an increase in temperature, due to a reduction of melt enthalpy of the solution. Therefore, it's important to control the temperature in order to control the reproducibility of the electrospinning process.

The ambient humidity also influences solvent evaporation and viscosity of the polymer solution [126]. Hardick et al. [125] saw an increase in melt enthalpy of the polymer solution with increase of humidity and consequently an increase in viscosity which showed a significant increase in fibre diameter. Besides difference in fibre diameter, atmospheric humidity influences the fibre morphology. De Vrieze et al. [123] reported absorption of water on the jets surface at higher humidities, because of higher partial pressure of water in the air. This causes a deposit of a water transparent film, which disturbs complete drying of the polymer solution jet during the time of flight resulting in fused fibres on the collector. High humidity is therefore not desired. Cai and Gevelber [127] looked at Taylor Cone formation in correlation with an increase of humidity. They observed an increase in Taylor cone volume with an increase in ambient humidity (20% to 60%). To replicate the same Taylor cone volume at different humidities an increased applied voltage was required. This was concluded to be due to the decrease in current (56 nA to 35 nA) of the solution (12 wt% polyvinylpyrrolidone(PVP)/ethanol) when the ambient humidity was increased. Diaz-Gomez et al. [103] observed fibre breakages at low humidity ($\leq$ 50%), which they proposed to be due to increased stretching of the jet during whipping after solvent evaporation. At high humidity ($\geq$ 50%) the presence of surface pores was observed, caused by vapour-induced phase separation (VIPS). Firstly, water vapour absorbs into the jet to the water-miscible solvent. Phase separation occurs when the hydrophobic polymer precipitates out of the solution, creating polymer-rich and polymer-poor regions within the jet. Finally, phase-separated geometry are locked in by rapid evaporation of the highly volatile solvent, resulting in fibres with pores on the surface. Casper et al. [128] also reported porous fibres with an

increase in pores on the fibre surface when increasing the ambient humidity.

The ambient pressure of below atmospheric pressure is not commonly used. This is due to poor electrospinning stability at lower pressures. When pressure below atmospheric pressure was used, the polymer solution in the syringe was observed to flow out of the needle, causing unstable jet initiation. Moreover, decreased pressure results in rapid bubbling of the solution due to uncontrolled rapid solvent evaporation. Furthermore, very low pressures were observed to make electrospinning impossible due to direct discharge of the electrical charge [93].

## 1.5 Electrospun fibrous scaffolds in the regenerative medicine and tissue engineering field

Electrospun fibrous scaffolds are of increased interest in the use of tissue engineering due to the multitude of polymers that can be used [129] and unique cell guiding and supporting architecture (non-woven fibrous scaffolds in range of μm to nm fibre diameters) [130]. These scaffolds were firstly implemented as biomedical scaffolds in 1978 by Annis et al. [131]. They electrospun polyurethane (PU) elastomers to produce elastomeric vascular prothesis with the use of a rotating mandrel to form tubes of electrospun PU. These tubes were investigated *in vivo* as replacement for thoracic aorta in 42 mini-pigs. Although these tubes were observed to only withstand pressures under 800 mmHg these grafts were observed viable even without initial cell seeding [131]. This encouraged the application of electrospun scaffolds in many different tissue engineering applications, in which choice of materials, fibre orientation, porosity, fibre surface porosity and modifications were carefully chosen. Examples of tissue types where the use of these scaffolds are considered are: vascular vessels, wound dressings,cornea, muscles, neurons, cartilage/bone, heart and urethral regeneration (see overview of implementation of electrospun scaffolds for human tissues Figure 1.6).

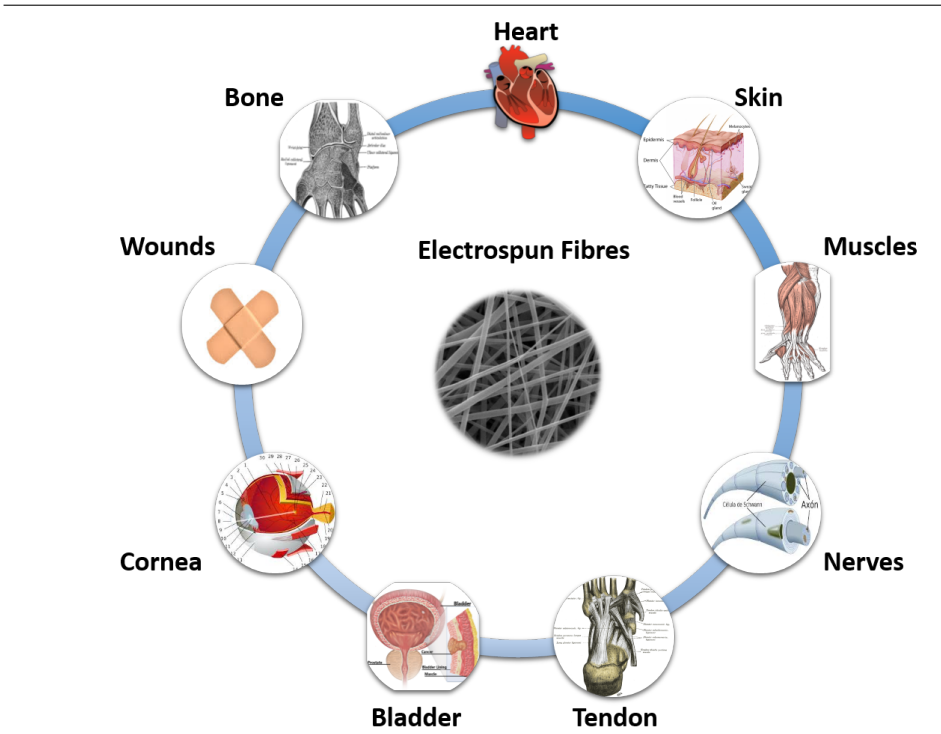



**Figure 1.6:** Examples of different human tissue where electrospun scaffolds are being used for tissue engineering purposes.

Zhou et al. [132] demonstrated the use of aligned PLLA microfibres with a porous fibrous surface for blood vessel tissue engineering. They observed favorable cellular responses of human vascular smooth muscle cells (hSMCs), resulting in increased cell adherence, alignment and proliferation. Cells were observed to express desired vascular matrix protein and maintained the desired contractile phenotype. This was concluded due to the porous fibrous surface which enhanced the anisotropic wettability of the fibres and contributed to increased protein adsorption (up to 17.69 $\mu g\ mg^{-1}$). Another study, Wang et al. [133] demonstrated the use of crosslinked PU/PEGMA hybrid nanofibres as potential substitute for artificial vascular scaffold. The incorporation of PEGMA significantly enhanced the PU scaffolds mechanical strength as well as their hydrophilicity. This resulted in more favorable scaffolds for the adhesion and proliferation of human umbilical vein endothelial cells (HUVECs) compared to the pure PU scaffolds. Similarly, He et al. [134] demonstrated good biocompatibility of PLA fibrous

electrospun scaffolds for the culture of HUVECs. They observed a confluency of 75%, while maintaining their differentiated phenotype.

Electrospun fibres are also implemented as wound healing dressing. Rho et al. [59] demonstrated the use of cross-linked collagen nanofibres coated with ECM proteins for early-stage wound healing. Human keratinocyte adherence when transplanted *in vivo* (rats) was observed on the coated scaffolds, making them a good candidate for biomedical application. A more recent study by Yao et al. [58] proposed the use of a bilayer membrane electrospun nanofibrous scaffold as potential wound dressing. This multilayer was composed of a commercially available PU wound dressing (HeraDerm®) as outer layer and an electrospun gelatin/keratin nanofibrous mat as inner layer. These bilayer membranes were observed to increase cell adherence, spreading and migration within the gelatin/keratin nanofibrous mat. Moreover, *in vivo* animal studies observed an increase in the number of blood vessels developed, reduction of the wound area after 4 days and complete wound healing after 14 days. A thicker epidermis and multiple newly formed hair follicles were observed in the healed area. Therefore, these bilayer scaffolds are concluded to be a successful scaffold for the complete regeneration of the wounded skin tissue. Another area where electrospun scaffolds are implemented is the regeneration of cardiac tissue. For example, Kenar et al. [135] produced blend electrospun poly(3-hydroxybutyrate-co-3-hydroxyvalerate) (PHBV), poly(L-D,L-lactic acid) (P(L-D,L)LA) and poly(glycerol sebacate) (PGS) aligned fibre mats and observed effective cell alignment and penetration of mesenchymal stem cells (MSCs) from the human umbilical cord matrix cells. Similary, fibronectin-coated chitosan electrospun fibres demonstrated cellular attachment and spreading of neonatal rat cardiomyocytes when co-cultured with fibroblasts. The structural morphology of these cylindrical fibrous scaffolds was observed to be retained in long-term cell culture, concluding the potential of these scaffolds in the heart tissue regeneration [136].

The ability of fabricating aligned fibrous scaffold morphology has encouraged the use of electrospun scaffolds in neural tissue engineering for the regeneration of peripheral nervous system (PNS) and central nervous system (CNS) injuries. These aligned fibres provide directional cues for neuron cell orientation and extension [123]. For example,

Wang et al. [137] investigated the response of Swann cells on aligned fibrous scaffolds with different fibre diameters. Neurite extension was observed to be guided along the aligned fibres of all fibre diameters. However, smaller fibre diameters (293 $\pm$ 65 nm) resulted in shorter neurite lengths of 42% and 36% compared to intermediate (759 $\pm$ 179 nm) and larger fibre diameters ( 1325 $\pm$ 383 nmm) substrates. Therefore, suggesting the importance of careful consideration of the fibre diameters when constructing nerve regenerative electrospun scaffolds. Zhang et al. [138] also observed this cell orientation to co-axial electrospun polyaniline (PANI) and poly(L-lactic acid-co-3-caprolactone)/silk fibroin aligned fibres incorporated with nerve growth factor (NGF). The NGF present in the fibres supported much higher cell numbers and differentiation of rat pheochromocytoma 12 (PC12) cells with neurite outgrowth.

Another tissue area of interest for the implementation of electrospun fibres is the cornea. The main part of the cornea (stroma) is built up of aligned collagen fibres. Phu et al. [139] developed collagen I electrospun scaffolds to mimic the native environment of the cornea and investigated the impact of aligned or random fibres on the expression of the undesired αsmooth musle actin (α-SMA, upregulated in hazy corneas) of rabbit-derived corneal fibroblast. They observed reduced myofibroblast phenotype expression of the cells on the electrospun scaffolds compared to the TCPS. Moreover, significantly more down-regulation of the α-SMA was observed on the aligned fibre scaffolds compared to the random fibre scaffold. Beside desired down regulation of the undesired phenotype reduced light scattering of the scaffolds was observed. This is important for the implementation of these scaffolds in the cornea, as transparency is required. A more recent study by Kong et al. [140] incorporated aligned PLGA fibres in a collagen gel hybrid compressed construct to improve their mechanical properties. To improve the desired light transmittance these constructs were laser-perforated resulting in 72 $\pm$ 1.8% transmittance from the scaffold after 7 days immersed in PBS. These hybrid constructs were demonstrated to support human corneal epithelial cells (hCECs) and human cornea stromal cells (hCSCs) adherence, proliferation and desired phenotype. These studies suggest the viability of electrospun scaffolds or combination of electrospun and hydrogels for the replacement of corneal tissues.

Furthermore, electrospun scaffolds are shown to support cartilage and bone tissue development. For instance, Shin et al. [141] observed cell adherence, proliferation and ECM matrix formation of MSCs derived from neonatal rats on highly porous PCL electrospun nanofibrous scaffolds. Moreover, mineralisation and type I collagen were detected after 4 weeks of of culture. Similarly, osteogenic differentiation and mineralisation of human adipose tissue-derived MSCs was observed when cultured on PLA electrospun nanofibres containing equisetum arvense extract (EE) and nanohydroxyapatite (nHA) for 3 weeks. While less mineralization of about 1.8 and 3 times lower were observed when cultured on PLA/nHA or TSCP control surface, respectively [66]. The micro-structural similarities of the fibrous scaffolds with the native collagen matrix utilizes the support of chondrogenesis of human bone marrow-derived MSCs. In addition, aligned PLLA fibrous scaffold can be used to promote human tendon progenitor stem cell (hTSPC) adherence, guides alignment and enables tendon-specific gene expression [142].

Other areas that electrospun scaffolds have been used is the regeneration of urethral and female reproductive system (anterior pelvic floor). Derakhshan et al. [143] demonstrated the support of human bladder smooth muscle cells adherence, proliferation and alignment when cultured on PLLA fibrous. Similarly, an *in vivo* study of PLGA fibrous scaffold with autologous bladder cells were observed to sufficiently repair urinary flow rate and bladder tissue after implantation into five boys with urethral defects [144]. Human clinical trials were also conducted successful for the reconstruction of anterior pelvic floor. Poly(L-lactic-co-caprolactone) and fibrinogen blend electrospun fibrous mesh were observed to improve the patients symptoms and resulted in significantly greater improvement of the pelvis floor regeneration compared to the polypropylene electrospun fibrous mesh [145]. Finally, electrospun scaffolds have been observed to show potential in the regeneration of oesophageal tissue. PCL/PS electrospun fibrous scaffolds were observed cytocompatible for primary epithelial cells (ECs), promoting adherence and proliferation of these ECs. When these PCL/PS scaffolds were coated with oesophageal basement membrane proteins the metochondrial activity of the ECs was greatly improved and therefore, BM protein coated PCL/PS scaffolds were reported suitable for the promotion of epithelium regeneration [146].

## 1.6 Enzymatic digestion vs. thermo-responsive surfaces

To obtain large quantities of viable cell numbers, cells need to be detached from their cell culture platform when confluent. Current enzymatic digestion utilises disruption of cell-substrate and cell-cell interactions (see schematic explanation Figure 1.7A). This is done with a mixture of protease enzymes, such as trypsin, collagenase, dispase and pronase [147–149] and chelating agents, such as ethylenediaminetetraacetic acid (EDTA). Cell-cell interaction and cell-substrate interaction is mediated by various adherence proteins (integrins and ECM proteins like fibronectin and vitronectin). These protein interactions are strengthened with the use of divalent cationic metals. For example calcium ($Ca^{2^+}$) encourage fibronectin-integrin interaction. Proteolysis by protease proteins disrupt this interaction and chelating agent EDTA chelates the divalent cationic metals. This brings about damage of cell-membrane proteins, such as growth-factor receptors and ion channels [150, 151]. Additionally, enzymatic digestion can cause internal cell damage by degradation of polyribosomes [1]. Furthermore, enzymatic digestion by dispase was observed to damage desmosomes of keratinocytes. However, alternative passaging by thermo-responsive surfaces was observed to show no damage of the same desmosomes [1]. Therefore, over the last decade many studies have been focused on the development of enzymatic-free detachment systems, to maintain cell viability and functions to obtain viable cells for clinical use [152–156]. Mainly they are evolved around thermo-responsive materials [157–165].

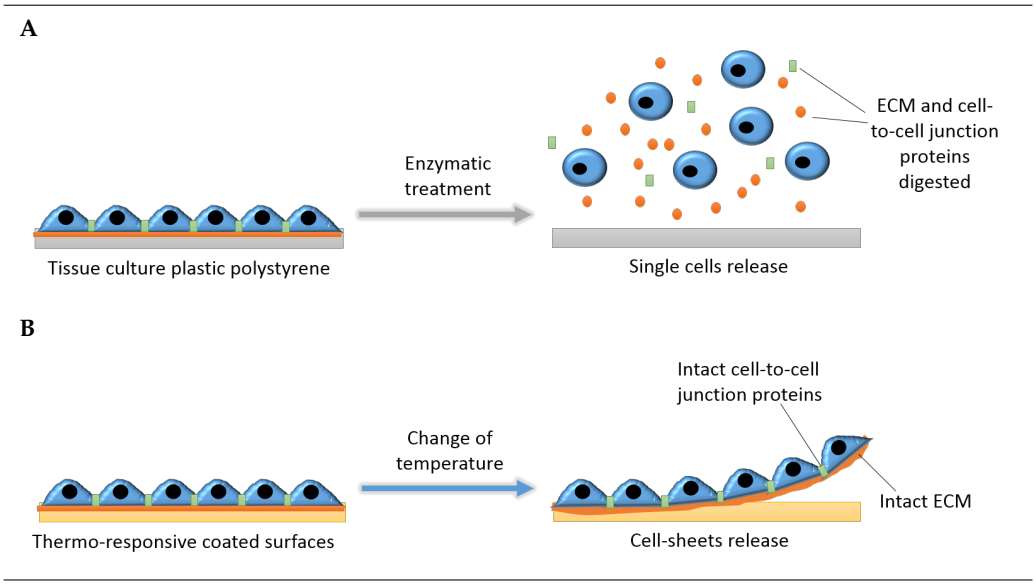



**Figure 1.7:** Cells connect with each other via cell-to-cell junction proteins and ECM when confluent. **A)** Enzymatic digestion disrupts these adhesive proteins and membrane receptors, while **B)** Thermo-responsive surface detachment preserves the cell-to-cell junction proteins and ECM resulting in cell sheet recovery.

### 1.6.1 Cell-sheet engineering by thermo-responsive culture

Thermo-responsive polymers undergo chain deformation, due to the transformation from hydrophobic to hydrophobic interaction. This transformation is temperature dependent and is defined as the lower liquid critical solution temperature (LCST, see Figure 1.8C). The chain deformation to hydrophilic state has been observed to support cell detachment and is therefore considered as a potential alternative application for *in vitro* cell culture expansion for tissue engineering and regenerative medicine.

Thermo-responsive polymers show the potential of cell-sheet engineering as an alternative approach in the tissue engineering field. This method involves the non-invasive harvest of cultured cells and cells sheets (see schematic explanation Figure 1.7B) [166]. These 2D cell-sheets can then be transferred to other culture-dish surfaces or direct implantation in the host tissue. Examples include skin, corneal epithelium, bladder urothelium and periodontal ligament. Poly(n-isopropylacrylamide) (PNIPAM, see Fig-

ure 1.8A) has been widely investigated as a smart surface coating for cell-sheet recovery [167, 168]. Kushida et al. [168] demonstrated the successful release of bovine aortic endothelial cell sheets from PNIPAM (LCST of 32°C) grafted TCPS. The cells were harvested without the disruption of cell-cell junctions and cell-surface/receptor damage observed when detached by enzymatic digestion method. Deposition and accumulation of fibronectin expressed by the cells was observed on the PNIPAM surface and was detected to stay adhered to the cell sheets after detachment. These cell sheets with intact ECM can function as a natural substance to attach these sheets onto other surfaces or structures [169] and are observed to be suitable for *in vivo* tissue regeneration. For example, primary hepatocytes cell sheets were successfully recovered from PNIPAM grafted surface and were observed to form 2D en-grafted hepatic tissue when transplanted into a subcutaneous space. These cell sheets formed new tissue structure and were shown to be stable for longer than 200 days, exhibiting liver-specific functionalities and were therefore concluded suitable for *in vivo* liver repair [170]. Miyahara et al. [171] also showed the successful application of cell sheet as *in vivo* tissue repair. MSCs cell sheet monolayers recovered from responsive culture dishes were transplanted *in vivo* onto scarred myocardium four weeks after coronary ligation. These sheets gradually grew to form en-grafted thick tissue layer with undifferentiated and few cardiomyocyte cells. These MSCs cell sheets were observed to significantly improve cardiac function (compared to fibroblasts cell sheets) in rats with myocardial infarction and reversed wall thinning in the scarred tissue. Beside the successful recovery of viable cell-sheets this non-invasive cell-sheet recovery result in minimal effect in cell phenotype changes [172]. A very recent study by Malheiro et al. [172] reported the successful harvest of pre-polarised macrophages from PNIPAM-grafted plates with minimal cell phenotype changes observed.

The use of cell-sheet engineering was observed to be significantly effective for the recovery of corneal tissues. Nishida et al. [173] reported the use of normal rabbit corneal epithelial cell cell-sheets recovered from PNIPAM grafted dishes for the treatment of corneal erosion. *In vivo* transplantation of these cell-sheets into rabbits were observed to be well-accepted within the injured tissue after three weeks implantation. Additionally, cell-sheets of human corneal endothelial cell sheets released from PNIPAM grafted

dishes were observed to show morphologies and functionalities similar to the native corneal endothelium *ex vivo* [174]. Furthermore, *in vivo* xenograft transplantation in rabbits resulted in stromal hydration properties of these cell sheets. Therefore, cell-sheets recovered from thermo-responsive surfaces were considered a possible clinical application for ocular reconstructive surgery.

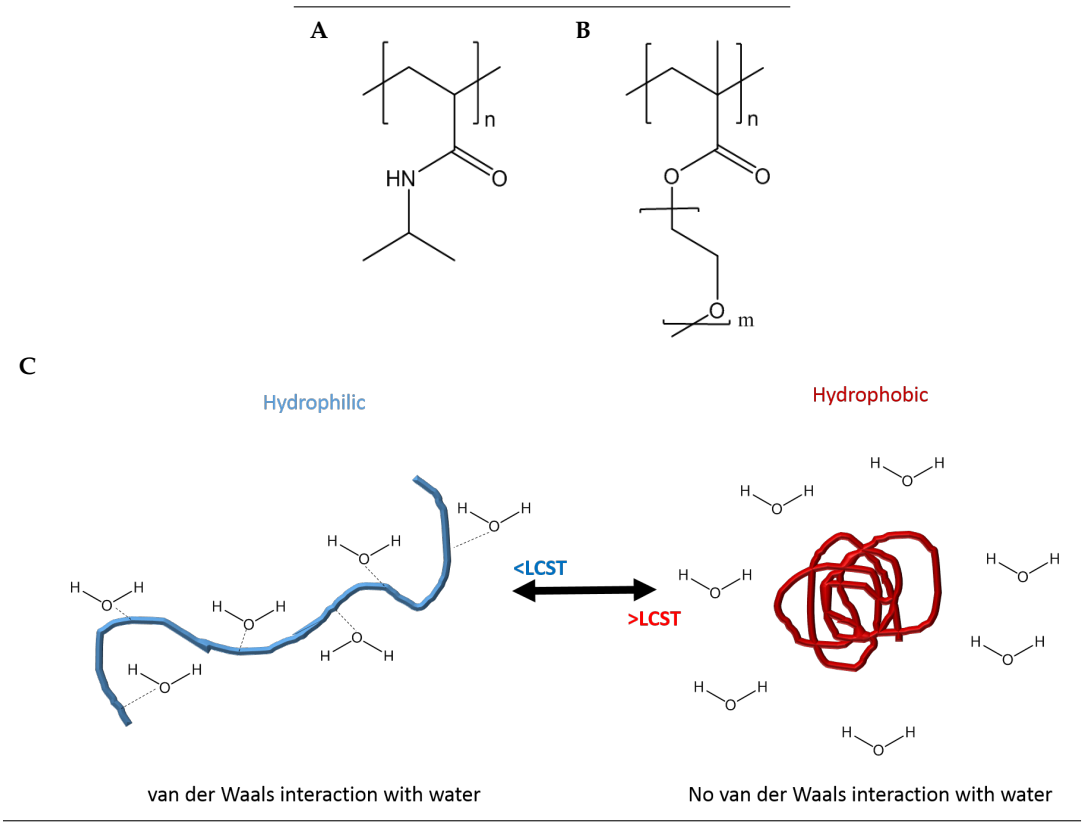



**Figure 1.8: A)** PNIPAM and **B)** PEG containing polymers, m side chain groups number changes the corresponding LCST of the polymer. **C)** Schematic representation of the hydrophobic-hydrophilic change of thermo-responsive polymers and chemical of thermo-responsive.

Additionally, these 2D cell-sheets can also be used to construct a complex stratified tissue structure of stacked cell-sheets, for the purpose of tissue replacement, such as cardiac, liver, kidney, periodontal or blood vessels construction [175–179]. For example, Haraguchi et al. [177] observed spontaneous and simultaneous pulsing of two layers of cardiomyocyte cell-sheets recovered from PNIPAM-grafted dishes. Beside synchronised pulsation of the two layered cell-sheets, immunohistology analysis showed

the formation of gap junction between the two cell-sheet layers. This demonstrated successful construction of electrically communicative 3D cardiac constructs for cardiac tissue repair. A later study by the same group [180] demonstrated the *in vivo* cardiac repair applying a cardiomyocyte four layered cell-sheet construct in nude rats. The construct was transplanted in the dorsal subcutaneous tissues of nude rats. After three week post-transplantation a surface electrogram and spontaneous beating of the transplanted graft was observed. Beside only cell-sheet layered constructs, a synthetic structure can be added for extra mechanical support. Iwata et al. [179] incorporated a PGA membrane sheet in a three-layered cell-sheet of periodontal ligament primary derived cells. This construct was transplanted *in vivo* (canine) to a dental root surface with three-wall periodontal defects. The transplanted cell sheet construct regenerated both the cone and cementum of well-oriented collagen fibrils. Significantly less bone regeneration was observed for the control group without cell-sheet contruct transplantation.

Many cell types were successfully cultured and harvested from PNIPAM 2D coated surfaces, these include cardiac myocytes, mouse embryonic stem cells, human smooth musle cells, vaculas endothelial cells, human corneal endothelial cells, and keratinocytes. However, irreversible phase transition [181], possible van der Waals binding of the PNIPAM amide group with polyamides of the proteins [182] and recently observed toxicity on endothelial cells [183] have led to doubt in the use of PNIPAM for tissue engineering applications.

Other polymers have been observed to show thermo-responsive behaviour. These side chain poly (ethylene glycol) (PEG) containing branch polymers are bio-compatible and water soluble (see Figure 1.8B). The LCST of these thermo-responsive materials are easily tunable with the length of the PEG side groups [184, 185]. The polymers are easy to synthesise with the use of (methyl)acrylate by either anionic addition, free-radical, or controlled radical polymerisation [184], which enables many variations of PEG containing polymers. Sefcik et al. [162] observed adherence, detachment and no gene expression change of fibroblasts on poly($MEO_2$MA-co-OEGMA) (PMO) polymer substrates. Similarly, Dey et al. [163] demonstrated successful culture and subsequent passaging over 10 cycles of mouse embryonic stem cells (mESCs) on plasma-polymer

grafted PMO glass slides. Likewise, Wischerhoff et al. [186] saw similar adherence and deadherence of L929 mouse fibroblasts on PMO modified gold substrate. All these studies are built around the use of a thin layer of thermo-responsive material in 2D culture. However, as discussed before 3D substrates are preferred over 2D platforms.

Different 3D structures with incorporated thermo-responsive polymers have been observed to show successful cell culture and cell adherence. These include fibrous, microparticles and hydrogels. For instance 3D non-woven poly(propylene) (PP) grafted PNIPAM scaffolds were observed to show thermal cell release of HC04 and HepG2 hepocytes after 2 h of temperature reduction [187]. Micro-particles of poly(ethylene glycol) methacrylate (PEGMA) and poly(propylene glycol) methacrylate (PPGMA) were observed to form aggregates that entrap mouse myoblast cells (C2C12) during cell culture temperature (37°C), while aggregates collapsed and detached cells when cooled [188]. The production of electrospun fibrous scaffolds with thermo -responsive behaviour have also been reported [133, 189, 190]. Despite the unique supporting architecture these fibrous scaffolds have poor cell penetration due to small porosity, which makes them ideal for cell culture expansion and cell-sheet recovery methods. Cells grown on these electrospun scaffolds form cell-sheets on the surface of the scaffold, resulting in easy thermo-responsive harvest of these cell-sheets. The 3D structure supports better nutritional supply and large surface area compared to 2D grafted thermo-responsive platforms. Examples include the production of poly((3-mercaptopropyl) methylsiloxane)/ PNIPAM [189], N-isopropylacrylamide and stearyl acrylate (PNIPAM/SA) [190] and PEGMA/PU [133] containing electrospun fibrous scaffolds. Cell adhesion and proliferation have been demonstrated on these thermo-responsive electrospun fibrous scaffolds. Only one cell release study has been conducted to date [191].

To conclude, the use of a thermo-responsive electrospun scaffolds for the expansion of mammalian cell culture (human corneal stromal cells (hCSCs) has been proposed for this study. The aim of this study is further described below in the aims and objectives of this research project.

## 1.7 Project Aims and Objectives

Cell therapies and tissue engineering based treatment require large quantities of cells of the desired phenotype. However, conventional 2D cell culture has been observed inappropriate for many cell types to maintain their phenotypic characteristics when grown in large quantities. 3D substrates have been proven to be a more suitable alternative to obtain large quantities of cells while supporting desired phenotypes. This is due to their 3D culture environment which shows similarities with native ECM. Beside the use of 3D environmental culture platforms, incorporation of smart materials, such as thermo- responsive polymers, can eliminate the use of enzymatic digestion for cell passaging. Enzymatic digestion has been reported to cause cell membrane damage and risk of contamination can render the cells unsuitable for clinical use. Responsive surfaces have been reported to induce significantly less damage to cells when passaged and therefore result in increased quality of cells expanded.

The project aim of this study is to develop a cell culture expansion platform for the expansion of mammalian cells to large quantities. For this reason the chosen scaffold needed to utilise a 3D environment without the cell being trap between the 3D construct for ease of cell sheet detachment. This was achieved by creating 3D electrospun thermo-responsive fibrous scaffolds that mimic the native fibrous ECM environment with a porous size to small for cells to penetrate through. Electrospinning has been proven to be a reliable method to fabricate controlled fibre diameters, morphologies, porosity and provides a cost-efficient scalable process for possible up-scaling. In addition to the similarities of the native ECM, the fibrous scaffolds show good mechanical support, providing large surface areas for cell attachment. The cell will be grown on top of this scaffolds, having the feel of a 3D environment, while keeping a sheet formation which can be detached by the thermo-responsive behaviour of the scaffolds incorporated polymer.

For the thermo-responsive behaviour of the scaffolds poly (di(ethylene glycol) methyl ether methacrylate (PDEGMA) was considered, due to it's lower critical solution temperature (LCST) of 28°C and FDA-approved material composition (oligo (ethylene gly-

col) monomers) [192]. Poly-D-L-lactic acid (PDLLA) was used as a supportive material within the electrospun scaffold. These two polymers were blend electrospun to obtain fibrous scaffold for mammalian cell culture, in particular primary human corneal stromal cells (hCSCs).

The project aim was achieved through the following objectives:

1. Optimise the electrospinning process and significantly impacting parameter interactions on fibre morphologies with the use of a Design of Experiment (DoE) optimisation model.
2. Investigate the attachment and proliferation of 3T3 fibroblast (3T3s) on different electrospun scaffolds morphologies.
3. Produce blend electrospun PLA/PDEGMA scaffolds and investigate the thermoresponsive behaviour of these scaffolds with the use of 3T3s.
4. Investigate the use of the optimised PLA/PDEGMA scaffolds for the support of human corneal stromal cell phenotype (hCSCs) when cultured and after thermoresponsive detachment.

# Chapter 2

# Materials and Methods

## 2.1 Design of Experiments (DoE)

### 2.1.1 Design of Experiments (DoE) Theory

A design of experiments approach of 4 factors and 3 levels was used (see DoE factors and levels in Table 2.1). From 25 different process parameters combinations, 81 scaffolds, including triplicate samples and 9 replicates of middle point, were generated. A "randomisation strategy" was used to reduce variability. In addition, a one single operator approach was used to avoid unnecessary variability in the model. Linear regression, ANOVA and data analysis were performed in MODDE 10.1.1 and Minitab 17.2.1 software. The following linear regression equation (Eq. 2.1.1) was used to identify the most significant impacting parameters ($X_1$,$X_2$,$X_3$,$X_4$) on the fibre diameter, standard deviation and beads per $\mu m^2$ ($Y_1$,$Y_2$,$Y_3$).

$$Y_i = \beta_0 + \sum_{j=i}^{m} \beta_i X_i + \sum_{i=1}^{m}\sum_{j=i}^{m} \beta_{ij} X_i X_j + \sum_{i=1}^{m}\sum_{j=i}^{m}\sum_{k=j}^{m} \beta_{ijk} X_i X_j X_k + \sum_{i=1}^{m}\sum_{j=i}^{m}\sum_{k=j}^{m}\sum_{l=k}^{m} \beta_{ijkl} X_i X_j X_k X_l + \varepsilon \quad (2.1.1)$$

The linear regression output was fitted for each Y output of the experimental data to obtain an "ordinary least square" linear estimation for $Y(X_1, X_2, X_3, X_4)$. This is a third order complete model with $X_i, X_j, X_k$, and $X_l$ the independent electrospinning parameters (applied voltage, distance, flow rate and polymer concentration) that influence the response $Y_i$ (mean fibre diameter, stdev or number of beads per $\mu m^2$. The $\beta_0$ is the model constant; $\beta_i$ is the linear coefficient representing the influence factor of individual independent parameters on $Y_i$. $\beta_{ij}$ is the cross 1st order interactions, product coefficients representing the influence factor of two independent parameter interactions on $Y_i$. $\beta_{ijk}$ is the 2nd order interactions, product coefficients representing the influencing factor of three independent parameter interactions on $Y_i$. $\beta_{ijkl}$ is the cross 3rd order interaction coefficient representing the influencing factor of all independent parameter interactions on $Y_i$ and $\varepsilon$ is the error. The higher the $\beta$ coefficient, the more influence it has on $Y_i$. Using this approach, the most important individual or combinations of independent parameters can be identified.

**95% confidence interval for estimates (CI) of DoE Prediction Equations**

The models 95% confidence interval for estimates were calculated by the following equations. Firstly the standard error was calculated by Eq. 2.1.2 which can be used to find the 95% confidence interval for estimates (CI) Eq. 2.1.3.

$$\text{standard error} = \sqrt{\Sigma(\text{predicted} - \text{actual})^2}/\text{sample size} \tag{2.1.2}$$

$$\pm\ 95\%\ \text{CI} = \text{predicted} - \text{degree of freedom} * \text{standard error} \tag{2.1.3}$$

**Table 2.1:** Design of Experiments (DoE) Model Inputs, Output, and Constants Parameters and Set Limits.

| **DoE Inputs Parameters** | | | | | |
|---|---|---|---|---|---|
| **Parameter** | $X_s$ | **unit** | **Low Level (-1)** | **Centerpoint (0)** | **High Level (1)** |
| Polymer Concentration | $X_1$ | w/v% | 15 | 20 | 25 |
| Applied Voltage | $X_2$ | kV | 10 | 15 | 20 |
| Flow Rate | $X_3$ | mL/hr | 1 | 3 | 5 |
| Needle/ Collector Distance | $X_4$ | cm | 15 | 17.5 | 20 |
| **DoE Outputs** | | | | | |
| **Parameter** | $Y_S$ | **unit** | | | |
| Fiber Diameter | $Y_1$ | nm | | | |
| Standard deviation | $Y_2$ | nm | | | |
| Number of beads per $\mu m^2$ | $Y_3$ | | | | |
| **DoE Constant Parameters** | | | | | |
| **Parameter** | | **unit** | **value** | | |
| Rotation speed mandrel | | rpm | 50 | | |
| Temperature | | $^{\circ}C$ | 20 | | |
| Humidity | | % | 44 | | |
| PLA MW | | kDA | $115 \pm 69$ | | |

### 2.1.2 Test DoE model predictions

The model was tested by electrospinning three scaffolds of random combinations inside the model limits, in which flow rate and concentration levels were different from

the levels used to "train" the DoE model. For example, a flow rate of 2 mL/hr and 4 mL/hr were used in run B and C (Table 2.2), while flow rate of 1, 3, and 5 mL/hr were used in training the model (see Table 2.1). Full and simplified predictions of the fibre diameter, standard deviation and number of beads per $\mu m^2$ were performed with the corresponding model code. Confidence intervals (CI) 95% for estimates were calculated. The smaller the 95% CI the more in agreement the predictions from the equation are with the data generated from the experiments; when this experimental data falls within the 95 % CI the model is therefore considered predictive.

**Table 2.2:** Parameter combinations and corresponding model codes for the linear regression prediction equations of the runs used to test the DoE model.All equation parameters are represented in DoE model coding of -1,-0.8...etc.

| **Targeted Run** | **Applied Voltage [kV]** | **Model code** | **Needle-to-collector distance [cm]** | **Model code** | **Flow rate [mL /hr]** | **Model code** | **Polymer Concentration [w/v%]** | **Model code** |
|---|---|---|---|---|---|---|---|---|
| **A** | 20 | *0* | 20 | *1* | 1 | *-1* | 23 | *0.6* |
| **B** | 20 | *0* | 20 | *1* | 2 | *-0.5* | 17 | *-0.6* |
| **C** | 20 | *0* | 20 | *1* | 4 | *0.5* | 20 | *0* |

## 2.2 Electrospun scaffold preparation

### 2.2.1 Polymer solution analysis

#### Materials

A Acetone (Ac) and dimethylformamide (DMF) were purchased from Sigma-Aldrich, Switzerland. Medical grade poly-D,L-lactic acid ( PDLLA; Mw: 115 kDa, Mn: 69 kDa, Đ: 1.7, isomer composition ratio of 70:30) was purchased from Evonik Industries, Germany, Essen. PDEGMA, PBI-PDEGMA and PDEGMA/PDEGSH were synthesized

(see methods section 2.5 and 2.6.3).

#### Rheometeric analysis

All polymer solutions were prepared and stirred overnight at room temperature (20°C, rt). The rheological properties of the polymer solutions were determined using a Modular Compact Rheometer (MCR302, Anton Paar GmbH, Austria) with pressure control chamber. Viscosity and thickening/thinning behaviour were observed over the shear rate of 0.07 to 3000 $s^{-1}$. Visco-elastic behaviour was observed by oscillatory shear test, with varying frequencies between 0. 01 and 15 Hz, and an applied shear rate of 2 Pa.

### 2.2.2 Electrospinning

#### Production of PLA electrospun scaffolds

Electrospun solutions were prepared, the day before the planned experiment, in Ac:DMF (1:1) with the desired concentration of PLA dissolved by stirring at rt overnight (approx. 16 h). Obtained scaffolds were fabricated using a Climate Control EC-CLI platform with rotating target collector EM RTC electrospin unit (IME Technologies, the Netherlands, Geldrop) with a 0.8 mm internal diameter (21 gauge) flat tip needle. The conducting surface was reduced to a width of 5 cm (approx. 100 $cm^2$ surface area) by covering either side of the rotating mandrel (7.5 cm diameter) with parafilm. The climate control system was started 30 mins before the run to obtain constant temperature and humidity of 20°C and 44% respectively. A total volume of 2 mL polymer solution per run was used in the spinning process for each scaffold batch. Applied voltage, needle-to- collection mandrel distance and flow rate were adjusted according to the DoE combinations (see Table 2.1 and Table S1). The tubing and needle were carefully rinsed with acetone to remove any of the previous samples prior to every electrospinning run.

**Production of blended PLA with (PBI)PDEGMA or PLA with PDEGMA/PDEGSH electrospun scaffolds**

Electrospun solutions were prepared, the day before the planned experiment, in Ac:DMF (1:1) with PLA 25 w/v% and the desired weight percentage of (PBI) PDEGMA or PDEGMA/PDEGSH (2.5, 5, 10, 15 and 20 wt%) at rt by stirring. Obtained scaffolds were fabricated using a Climate Control EC-CLI platform with rotating target collector EM RTC electrospin unit (IME Technologies, the Netherlands, Geldrop) with a 0.8 mm internal diameter (21 gauge) flat tip needle. The conducting surface was reduced to a width of 5 cm (approx. 100 $cm^2$ surface area) by covering either side of the rotating mandrel (7.5 cm diameter) with parafilm. The climate control system was started 30 mins before the run to obtain constant temperature and humidity of 20°C and 44% respectively. A total volume of 2 mL polymer solution per run was used in the spinning process for each scaffold batch. Applied voltage, needle-to-collection mandrel distance and flow rate were set to 19 kV, 17.5 cm and 0.5 mL/hr respectively. The tubing and needle were carefully rinsed with acetone to remove any of the previous samples prior to every electrospinning run.

## 2.3 Analytic techniques

### 2.3.1 Nuclear Magnetic Resonance spectroscopy 1D and 2D analysis

**1D 1-Hydrogen and Carbon-13 NMR analysis ($^1$H-NMR and C$^{13}$-NMR)**

$^1$H-NMR and C$^{13}$-NMR spectra were recorded on a Bruker Avance III 400 spectrometer at 399.8 MHz ($^1$H) and 100.5 MHz (C$^{13}$) in deuterium chloroform ($CDCl_3$). MestReNova 11.0 software was used to analyse the obtained spectra. All chemical shifts are reported in part per million (ppm) relative to $CDCl_3$ (7.24 ppm for $^1$H-NMR and 77.2 ppm for C$^{13}$-NMR) or tetramethylsolane (TMS). Full explanation of the analysis techniques can be found in Supplementary section 9.0.1.

**2D-NMR Heteronuclear Single-Quantum Correlation spectroscopy analysis (HQSC)**

HSQC 2D-NMR spectra was recorded on a Bruker Avance III 400 spectrometer at 399.8 MHz in deuterium chloroform ($CDCl_3$). MestReNova 11.0 software was used to analyse the obtained spectra. All chemical shifts are reported in part per million (ppm) relative to $CDCl_3$ (7.24 ppm for $^1$H-NMR and 77.2 ppm for $C^{13}$-NMR).

### 2.3.2 Gel permeation chromatography (GPC) analysis

Molar masses of polymer were measured in tetrahydrofuran (THF) or dimethylformamide (DMF) eluents. THF samples were measured using a 1) Waters GPC ( Milford, MA) with two Water Styragel (HR1 and HR4) columns, a Waters 2695 auto-sample pump and a refractive index (RI) detector (Waters 410). Samples were eluted at 40°C at a flow rate of 1.0 mL/min. DMF samples were measured using a 2) Agilent/Polymer Laboratories GPC-50 instrument with triplet detection (viscometry, refractive index (RI), and multiangle laster light scattering (MALLS)). Separations were achieved using Polargel L columns (eluent-(DMF)). Calibration for both different eluents (DMF and THF) were performed using linear poly(methyl methacrylate) (PMMA) standards (Polymer Laboratories) in the molecular weight range 1- 1200 kDa. Molecular weights and dispersity values were calculated using Cirrus GPC 3.0. Full explanation of the analysis technique can be found in Supplementary section 9.0.2.

The samples were dissolved in THF or DMF in a concentration of 10 mg/mL and filtered through 0.45 µm filters to remove any big particles and unwanted impurities.

### 2.3.3 Fourier transform infra-red (FT-IR) analysis

Sampels were measured using a Agilent FT-IR spectrometer, Agilent Technologies, UK. Solid samples were put on top of the diamond, pressure was applied and spectras was measured. Solid electrospun scaffolds result in not enough interaction with the diamond detecto and therefore were dissolved in acetone, dropped on the diamond and dried to form a sheet of electrospun scaffolds on the diamond detector. Full explanation

of the analysis technique can be found in Supplementary section 9.0.3.

### 2.3.4 Measurement of polymer solution cloud points to estimate lower critical solution temperature (LCST)

A 2 mg/mL thermo-responsive polymer solution was prepared in $dH_2O$ and cooled on ice to dissolve the polymer. The solutions were kept on ice to avoid polymer aggregation. 1 mL of solution was added into a ultraviolet-visible (UV/VIS) cuvet and placed into the UV/VIS equipment. The chamber was cooled to 5°C before measurement using a Quantum Northwest Peltier-Controlled Cuvette Holder (Quantum Northwest Inc, WA, USA). UV absorbance was measured by Agilent Technologies Cary 60 UV/VIS (Santa Clara, CA, USA) at 550 nm wavelength while the solution was heated at 60°C in a rate of 1°C/min. The solution was left at 60°C for 5 minutes before measurement of the UV absorbance at 550 nm wavelength while cooling down the solution to 5°C again at the same rate of 1°C/min. A approximation of the LCST was determined at the solution cloud point temperature when non-linearly increase of the absorbance was observed.

### 2.3.5 Fluorescence intensity measurements

The fluorescence labeled PBI-PDEGMA (see synthesis method 2.5.3) fluorescence intensity in water was measured by Tecan Spark® equipment (Tecan, Männedrof, Switzerland). Polymer was dissolve in water (2 mg/mL), added into a 24 well plate (1 mL per well, n=3 wells) and placed in the plate reader. The 24 well plate was exposed to different wavelengths from 400 to 800 nm increasing 2 nm/min and fluorescent intensity of the solution was measured at the different wavelength points. Subsequently fluorescent intensity to wavelength was plotted by GraphPad Prism 7.01 software.

## 2.4 Electrospun scaffold characterisation

### 2.4.1 Scanning Electron Microscope (SEM)

For each obtained scaffold a 1x1 cm sample was cut out of the centre, mounted on a pin stubs (12.5 mm) with carbon tabs (12 mm) and gold sputter coated for 300s at 25 mA (EM SCD005, Leica Microsystems). All scaffolds were analysed by SEM (JSM-6060LV, Jeol LtD Japan) at x1000, x2000, and x5000 magnifications (mag.) with six different fields of view captured for each scaffold.

### 2.4.2 Fibre diameters, standard deviation and number of beads per $\mu m^2$ measurements

Fibre diameter measurements were performed with ImageJ 1.48v software, six SEM images were taken at x5000 mag. with 20 measurements per image (120 in total). Beads were included in the measurements and measured on the widest point of the bead. Mean fibre diameter and standard deviation of the measurements were calculated by GraphPad Prism software. Number of beads per $\mu m^2$ measurements were performed with ImageJ 1.48v software on three x2000 magnification SEM images. Beads per image were counted and beads per $\mu m^2$ were calculated.

### 2.4.3 Tensile testing measurements

Tensile testing was performed by applying 5 g pull force on 3 x 1 cm (ht x wd) scaffolds strips for the different scaffolds (TA.HDplus Texture Analyser, Stable Micro Systems, UK). Blue role was wrapped around the top and bottom of the scaffold strips to improve the grip of the Tensile tester clamps (see Figure S1). Corresponding force curves were used to calculate the Young's modulus by measuring the slope of the deformation curve.

### 2.4.4 Water contact angle measurements (WCA)

#### Static WCA

Static WCA measurement were performed on commercial contact angle goniometer (KSV CAM 200). A $dH_2O$ drop was added to the surface of the scaffold and a picture was made. The WCA software calculated the resultant WCA of the $dH_2O$ drop. For each scaffold 36 measurements on different parts of the scaffold were performed and the average was calculated by Graphpad Prism 7.01.

#### WCA hysteresis

Hysteresis is the difference between WCA of an increased and reduced waterdrop on the surface of the scaffold. This was done by adding the initial water drop size as set for static measurements and leaving the needle in the drop. Increased WCA was obtained by adding slight more water to the initial drop. Hereafter, the drop was reduced by aspirating the water slightly until a more tear drop form was obtained. With this measurement more information can be observed about the WCA taking in account the roughness of the surface.

### 2.4.5 Time-of-Flight Secondary Ion Mass Spectrometry (ToF-SIMS) sample analysis

ToF-SIMS measurements were performed by Jiang Long. Scaffolds of different chemical combinations were attached to a glass slide by double tap. Samples were put into the ToF-SIMS and set under vacuum the night before measurement to obtain a stable vacuum. Negative and positive spectra were collected using a ION TOF, ToF-SIMS IV instrument (Münster, Germany) equipped, with a bismuth liquid metal ion gun (LMIG). A voltage of 25 kV and $Bi_3{}^+$ primary ion source were used. The beam was directed at a 45° angle to the sample with a beam spot of 1-2 μm in the high current bunched mode. Three different points of the scaffolds of interest of a surface area of

500 μm by 500 μm were taken with 256 x 256 pixels, 15 scans (1 shot per pixel). Spectra obtained were analyzed and relevant peaks identified by IONTOF GmbH SurfaceLab 6 Software, Germany. Full explanation of the analysis technique can be found in supplementary section 9.04.

Spectra were normalised to total ion count and calibrated with m/z= 1 ($H^+$), 15 ($CH_3^+$), 31 ($CH_3O^+$), 55 ($C_3H_3O^+$), 57 ($C_3H_5O^+$) and 99 ($C_5H_7O_2^+$) for positive spectra and m/z= 1 ($H^-$), 12 ($C^-$), 13 ($CH_2^-$), 14 ($CH_3^-$) and 15 ($CH_4^-$) for negative spectra.

## 2.5 Polymer Synthesis of PDEGMA and PBI-PDEGMA

### 2.5.1 General preparation

#### Materials

All chemicals were purchased from Sigma-Aldrich Co Ltd, Switzerland.

#### Recrystallisation of AIBN

Azobisisobutyronitrile (AIBN) was recrystallised in methanol. 4 g AIBN was added to an 100 mL erlenmeyer flask, in a separated beaker 50 mL methonal was heated to 50°C and added to the erlenmeyer with AIBN. When all the AIBN was dissolved reaction contents was left in the fridge for 1 h to allow crystals to form. The resulting crystals were recovered by filtration and dried under vacuum. The product (melting point 102-105°C) was sorted in the freezer (-8°C) until required.

### 2.5.2 Poly (di(ethylene glycol) methyl ether methacrylate) (PDEGMA)

#### Synthesis of poly(di(ethylene glycol) methyl ether methacrylate) (PDEGMA) 1

Di(ethylene glycol) methyl ether methacrylate (11 mL, 6 mmol), 2-butanone (20 mL), 1-dodecanethiol (0.088 mL) and recrystalised AIBN (see method section 2.5.1, 72 mg)

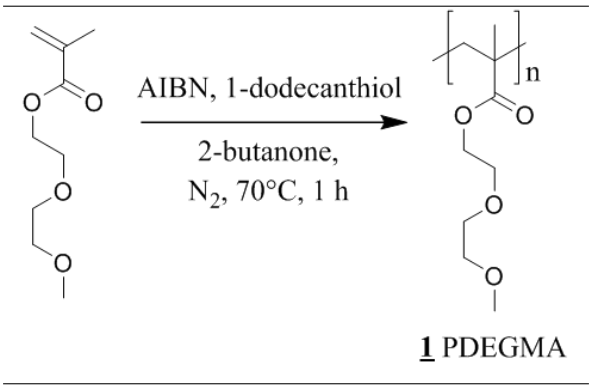



**Figure 2.1:** Free radical polymerisation schematic for the synthesis of PDEGMA.

were added to a dry 50 mL round bottom flask. The reaction contents were degassed for 25 mins by $N_2$, closed with parafilm and heated to 70°C for 1 h. The mixture was cooled to room temperature (rt, 20°C) and added to hexane (500 mL) drop wise while stirring. The precipitated polymer was re-suspended in 2-butanone and dropped into 500 mL hexane. This was repeated 3 times. The resultant polymer was dried overnight and the identity of the products were evaluated by spectroscopic methods (see supplementary data Figure S2 and Figure S3).

$^{1}$H-NMR (400 MHz, $CDCl_3$): δ(pm) = 0.8-1.0 (d, 3H, $CH_3$), 1.0-1.1 (s, 3H, $CH_3$), 1.8-2.1 (d, 2H, $CH_2$), 3.4 (s, 3H, $CH_3$), 3.45-3.5 (s, 2H, $CH_2O$), 3.5-3.6 (s, 2H, $CH_2O$), 3.6-3.7 (s, 2H, $CH_2O$), 4.0-4.1 (s, 2H, $CH_2O(C{=}O)$). $C^{13}$-NMR (100 MHz, $CDCl_3$): δ(ppm) = 16-17 ($CH_3$ backbone), 33 (C(C=O)), 46 (C backbone), 52-54 ($CH_2$ backbone), 59 ($OCH_3$), 67 ($CH_2O(C{=}O)$), 68-72 (3C, $OCH_2$), 176 (C=O).

### 2.5.3 Fluorescent labeled poly(di(ethylene-glycol)methyl ether methacrylate)-2-methyl-propanoyl)oxy]ethoxy)ethyl)-perylene-3,4,9,10-tetracarboxylic acid bisimide (PBI-PDEGMA) 4

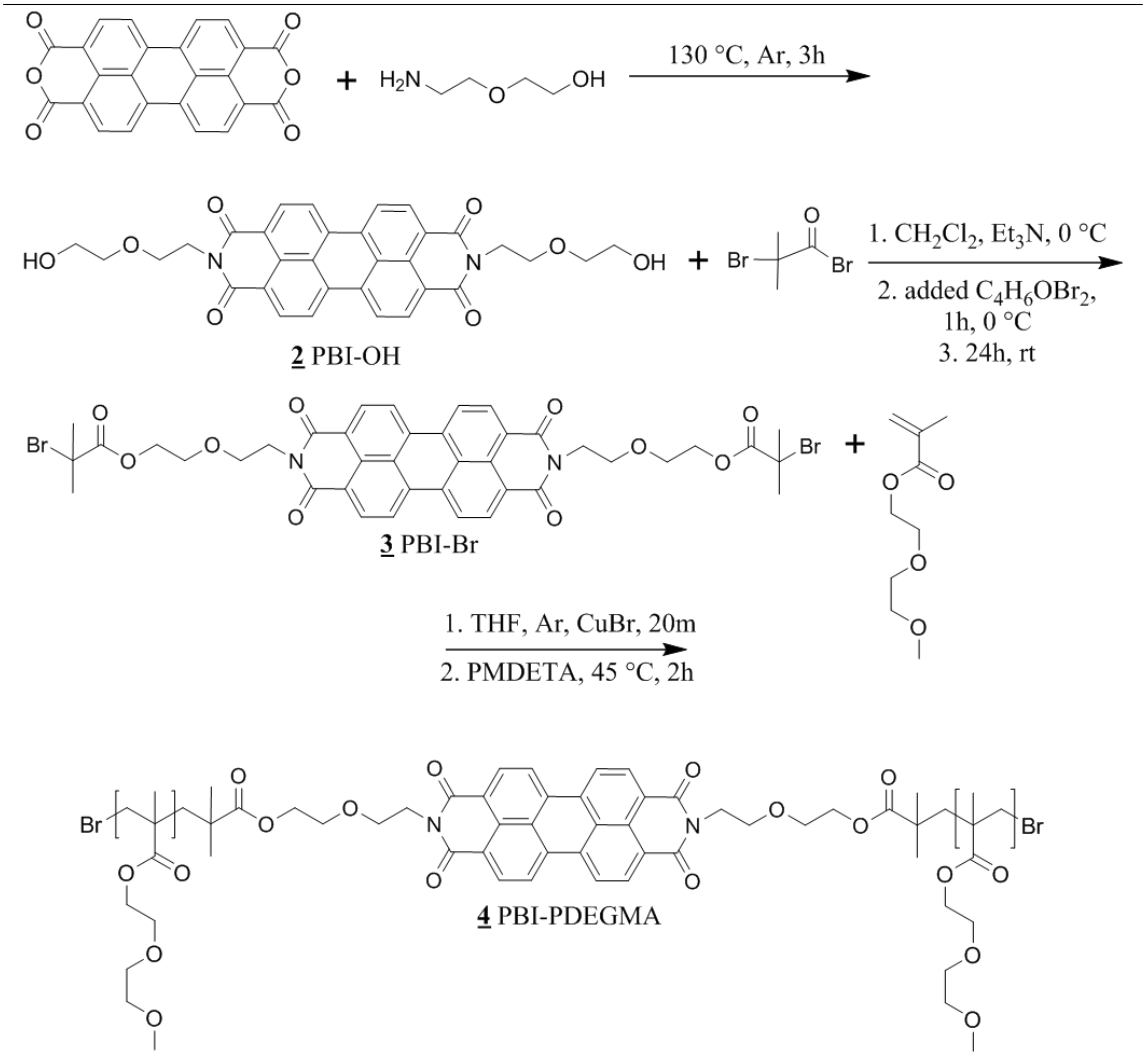



**Figure 2.2:** Chemistry schematic for the synthesis of fluorescent labeled PBI-PDEGMA.

**Synthesis of N,N-Bis(2-[2-hydroxyethoxy]ethyl)perylene-3,4,9,10-tetra carboxylic acid bisimide (PBI-OH) 2**

Perylene-3,4,9,10-tetracarboxylic acid dianhydride (785 mg, 2 mmol) and 2-(2-amino-ethoxyl) ethanol (1.5 mL) were added to a dry round bottom flask and degassed with Ar. The mixture was heated 130°C under argon for 3 h, cooled down to rt and diluted into MeOH (20 mL). The suspension was centrifuged and the obtained precipitate was washed with MeOH (4 x 20 mL). The product was obtained after drying under vacuum as a dark red powder, dried in vacuum and confirmed by $^{1}$H-NMR, C$^{13}$-NMR (see supplementary data Figure S4) and FT-IR (see supplementary data Figure S5).

$^{1}$H-NMR (400 MHz, $CDCl_3$): δ(ppm) = 3.54 (t, 4H, $CH_2$), 3.95 (t, 4H, $CH_2$), 3.73 (t, 4H, $CH_2$), 4.05 (t, 4H, $CH_2$), 8.65 (s, 4H, ArH), 8.71 (d, 4H, ArH). C$^{13}$-NMR (100 MHz, $CDCl_3$): δ(ppm) = 40 ($CH_2N$), 61 ($CH_2OH$), 70 and 72 ($CH_2O$), 120 (=C(C=O)), 140 (C=C), 162 (C=O). FT-IR: $cm^{-1}$ = 1650 (C=O amide stretching, strong), 1750 (C=O ester stretching, strong), 2840-2900 (C-H alkane stretching, medium), 3000-3100 (C-H aromatic alkene stretching, medium).

**Synthesis of N,N-Bis(2-bromo-2-methylpropanoyl)oxy]ethoxy)ethyl) perylene-3,4,9, 10-tetracarboxylic acid bisimide (PBI-Br) 3**

The obtained product (PBI-OH, 570 mg, 1 mmol) of the condensation reaction was suspended in dry $CH_2Cl_2$(150 mL) and $Et_3N$ (0.4 mL, 3 mmol) and cooled down to 0°C. 2-bromoisobutyryl bromide (0.69 g, 3 mmol) in dry $CH_2Cl_2$ (10 mL) was added drop-wise into the mixture for 1 h while stirring. When all of the solution was added the mixture was left while stirring for 24 h at rt (20°C). The resultant triethylamine hydrobromide ( $(C_2H_5)_3N\bullet HBr$) and unreacted N,N′-bis(2-[2-hydroxyethoxy]ethyl)perylene-3,4,9,10-tetracarboxylic acid bisimide were removed by filtration and $CH_2Cl_2$ was removed by rotary evaporation (atmospheric pressure (1013 mbar), 40°C waterbath). A silica gel column with $CHCl_3$/10% MeOH as eluent was performed to purify the N,N′-bis(2-(2-bromo-2- methylpropanoyl)oxy]ethoxy) ethyl) perylene-3,4,9,10-tetracarboxylic acid bisimide (PBI-Br) product. Initiator structure was confirmed by $^{1}$H-NMR, C$^{13}$-NMR

(see supplementary data Figure S6) and FT-IR (see supplementary data Figure S5).

Resultant product was a dark red solid, $^{1}$H-NMR (400 MHz, $CDCl_3$): δ(ppm) = 1.84 (s, 12H, $CH_3$ ), 3.54 (t, 4H, $CH_2$), 3.95 (t, 4H, $CH_2$), 3.73 (t, 4H, $CH_2$), 4.35 (t, 4H, $CH_2$), 8.65 (s, 4H, ArH), 8.71 (d, 4H, ArH). $C^{13}$-NMR (100 MHz, $CDCl_3$): δ(ppm) = 33 ($C_3$), 40 ($CH_2N$), 51 (C), 63 ($CH_2OH$), 65 and 70 ($CH_2O$), 175 (OC(C=O)). FT-IR: $cm^{-1}$ = 1650 (C=O amide stretching, strong), 1750 (C=O ester stretching, strong), 2840-2900 (C-H alkane stretching, medium), 3000-3100 (C-H aromatic alkene stretching, medium).

**Synthesis of poly(di(ethylene-glycol)methyl ehter methacrylate)-2-methyl propano yl)oxy]ethoxy)ethyl)-perylene-3,4,9,10-tetracarboxylic acid bisimide (PBI-PDEGMA) 4**

The PBI-Br (100 mg, 0.12 mmol), PMDETA (41.6 mg, 0.24 mmol) and PEGMA (2.0 g, 4.21 mmol) were dissolved in 10 mL of THF and added into a Schlenk tube. The solution was purged with argon for 20 min and sealed with parafilm. Subsequently, in a second Schlenk tube a CuBr(II) (34.6 mg, 0.24 mmol) was added and the solution was purged for 20 min as well and sealed with parafilm. The purged PBI-Br solution was added to the Schlenk tube containing CuBr via cannula using an argon gas line. When all the solution was added Schlenk tube was sealed and heated to 45°C or 60°C using an oil bath for 6 hours. NMR samples were taken at 2h, 4h and 6h to follow the polymerisation. The resultant mixture was diluted in THF at a reaction mixture/THF volume ratio of 1:3. The catalyst was removed from the mixture with the use of a neutral alumina column. The product was concentrated by removing the solvent THF by rotation evaporation (22 mBar, 35°C) precipitated using a large amount of ethyl ether and dried under vacuum. The crude product was purified by dialysis in water for 48 hours. The PBI-PDEGMA product was recovered after freeze-drying and confirmed by $^{1}$H-NMR and $C^{13}$-NMR (see supplementary data Figure S7).

$^{1}$H-NMR (400 MHz, $CDCl_3$): δ(ppm) = PBI: 3.95 (t, 4H, $CH_2$), 3.73 (t, 4H, $CH_2$), 4.35 (t, 4H, $CH_2$), 8.65 (s, 4H, ArH), 8.71 (d, 4H, ArH) PDEGMA: 0.8-1.0 (d, 3H, $CH_3$), 1.0-1.1 (s, 3H, $CH_3$), 1.8-2.1 (d, 2H, $CH_2$), 3.4 (s, 3H, $CH_3$), 3.45-3.5 (s, 2H, $CH_2O$), 3.5-

3.6 (s, 2H, $CH_2O$), 3.6-3.7 (s, 2H, $CH_2O$), 4.0-4.1 (s, 2H, $CH_2O(C{=}O)$). $C^{13}$-NMR (100 MHz, $CDCl_3$): $\delta$(ppm) = PBI: 26 ($CH_3$), 37 ($CH_2N$), 46 (C), 65 ($OCH_2$). PDEGMA: 16-17 ($CH_3$ backbone), 33 (C(C=O)), 46 (C backbone), 52-54 ($CH_2$ backbone), 59 ($OCH_3$), 67 ($CH_2O$(C=O)), 68-72 (3C, $OCH_2$), 176 (C=O).

## 2.6 Thermo-responsive/peptide conjugated polymer synthesis

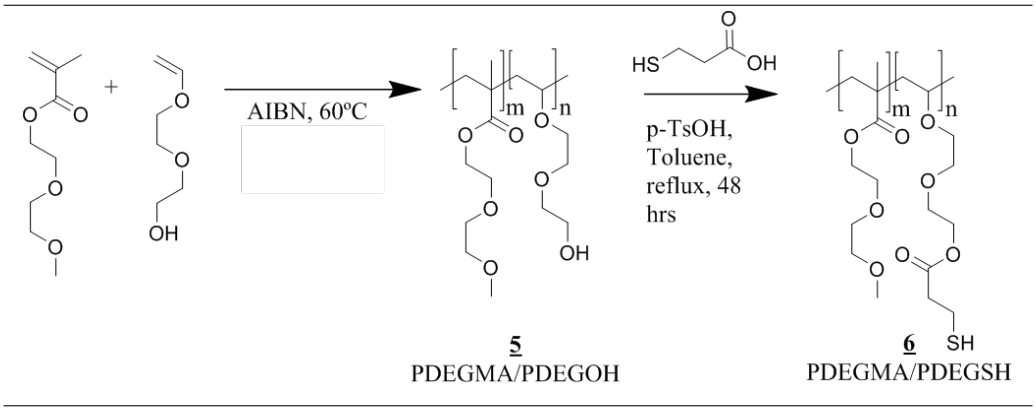



**Figure 2.3:** PDEGSH synthesis schematic

### 2.6.1 Materials

Hexane was purchased from Fisher Scientific, USA. Fmoc-alanine, Fmoc-glysine, Fmoc-isoleucine, Fmoc-valine, Fmoc-Tyrosin(t-butyl), Fmoc-arginine(Boc), Fmoc-lysine(Boc), and Fmoc-serine(t-butyl) were purchased from ChemPep. All other materials were purchased from Sigma-Aldrich, Switzerland.

### 2.6.2 Synthesis of poly(di(ethylene glycol) methyl ether methacrylate-co-poly(di(ethylene-glycol) vinyl ether (PDEGMA/PDEGOH) 5

Di(ethylene glycol) methyl ether methacrylate and di(ethylene glycol) vinyl ether were added in different ratios (see Table 2.3), 2-butanone (20 mL), 1-dodecanethiol (0.088 mL) and AIBN (recrystallised, see method section 2.5.1, 72 mg) were added to a dry 50

mL round bottom flask. The reaction contents were degassed for 25 mins by $N_2$, closed with parafilm and heated to 70°C for 1 hour. The mixture was cooled to room temperature (rt) and added to hexane (500 mL) drop wise while stirring. The precipitated polymer was re-suspended in 2-butanone and dropped into 500 mL hexane. This was repeated 3 times. The resultant polymer was dried overnight and the identity of the products were evaluated by spectroscopic methods, $^1$H-NMR, C$^{13}$-NMR and 2D-NMR (see supplementary data Figure S8-S16) and FT-IR (see supplementary data Figure S17).

$^1$H-NMR (400 MHz, $CDCl_3$): $\delta$(ppm) = 0.8-1.0 (d, 3H, $CH_3$), 1.0-1.1 (s, 3H, $CH_3$), 1.4 (s, 2H, $CH_2$ of OH backbone), 1.8-2.1 (d, 2H, $CH_2$), 3.4 (s, 3H, $CH_3$), 3.45-3.5 (s, 2H, $CH_2O$), 3.5-3.6 (s, 2H, $CH_2O$ and s, 1H, CH from OH backbone), 3.6-3.7 (s, 2H, $CH_2O$), 3.7-3.8 (t, 2H, $CH_2-OH$), 4.0-4.1 (s, 2H, $CH_2O(C=O)$). C$^{13}$-NMR (100 MHz, $CDCl_3$): $\delta$(ppm) = 16-17 ($CH_3$ backbone), 33 (C(C=O)), 46 (C backbone), 52-54 ($CH_2$ backbone), 59 ($OCH_3$), 61 ($CH_2OH$), 67 ($CH_2O$(C=O) and CH from OH backbone), 68-72 (6C, $OCH_2$), 176 (C=O). IR: $cm^{-1}$= 1163-1210 (C-O ester stretching, strong), 1375-1450 (C-H alkane methyl group bending, medium), 1735-1750 (C=O ester stretching, strong), 2700-3000 (C-H alkane stretching, medium), 2700-3000 (O-H intermolecular bond stretching, weak).

**Table 2.3:** Different ratios of PDEGMA/PDEGOH

| %PDEGMA:PDEGOH | DEGMA [mL; mmol] | DEGOH [mL; mmol] |
|---|---|---|
| 100 : 0 | 11 ; 6.1 | 0 ; 0 |
| 95 : 5 | 10.45 ; 5.7 | 0.55 ; 0.4 |
| 90 : 10 | 9.9 ; 5.3 | 1.1 ; 0.8 |
| 80 : 20 | 8.8 ; 4.8 | 2.2 ; 1.6 |
| 70 : 30 | 7.7 ; 4.3 | 3.3 ; 2.4 |

### 2.6.3 Synthesis of poly(diethylene-glycol) methyl ether methacrylate-co-poly(diethylene-glycol) thiol (PDEGMA/PDEGSH) 6

PDEGMA/PDEGOH (2.5 g, 4.4 mmol) was added to 200 mL toluene, and an excess amount of 3-mercaptopropanoic acid (2.3 g, 2.2 mmol), p-TSA (0.33, 1.76 mmol) and DTT (0.34 g, 2.2 mmol). This solution was reflux for 48 hours at 135°C. Water resulting from the condensation reaction was collected by a Dean stark trap as result of azeotropic distillation. Toluene was removed by rotary evaporation under reduced pressure and the resulting PDEGMA/PDEG-SH was precipitated in cold ether for three times. The resultant polymer was dried under vacuum and the characterised by spectroscopic methods $^{1}$H-NMR, C$^{13}$-NMR and 2D-NMR (see supplementary data S18-S25) and FT-IR (see supplementary data Figure S17).

$^{1}$H-NMR (400 MHz, $CDCl_3$): δ(ppm) = 0.8-1.0 (s, 3H, $CH_3$), 1.0-1.1 (s, 3H, $CH_3$), 1.4 (s, 2H, $CH_2$ of OH backbone), 1.8-2.1 (d, 2H, $CH_2$), 2.3 (t, 2H, $CH_2-C=O$ of SH group), 2.9 (t, 2H, $C\underline{H_2}-SH$ of SH group) 3.4 (s, 3H, $CH_3$), 3.45-3.5 (s, 2H, $CH_2$), 3.5-3.6 (s, 2H, $CH_2$ and s, 1H, CH from OH backbone), 3.6-3.7 (s, 2H, $CH_2$), 4.0-4.1 (s, 2H, $CH_2$ and s, 2H, $C\underline{H_2}-O-C=O$ of SH group). C$^{13}$-NMR (100 MHz, $CDCl_3$): δ(ppm) = 16-17 ($CH_3$ backbone), 33 (C(C=O)), 33 ($CH_2$(C=O)), 34 ($CH_2SH$), 46 (C backbone), 52-54 ($CH_2$ backbone), 59 ($OCH_3$), 68-72 (3C, $OCH_2$), 176 (C=O). IR: $cm^{-1}$= 1163-1210 (C-O ester stretching, strong), 1375-1450 (C-H alkane methyl group bending, medium), 1735-1750 (C=O ester stretching, strong), 2550-2600 (S-H stretching, weak), 2700-3000 (C-H alkane stretching, medium).

### 2.6.4 Free thiol confirmation by Ellman's assay

The presence of free thiols was confirmed by Ellman's assay. When free thiols are available, they react with the Ellman's reagent (5,5'-Disulfanediylbis(2-nitrobenzoic) acid (DNTB)) disulfide bond; cleaving this disulfide bond results in 2-nitro-5-thiobenzoate ($TNB^-$) product. The $TNB^-$ ionises to the yellow coloured $TNB^{2-}$ dianion in water at neutral and alkaline pH. The amount of free thiols can be calaculated by quantifying the amount of $TNB^{2-}$, by measuring the absorbance of visible light at 412 nm.

Ellman's assay reaction buffer was prepared using 0.1 M Sodium phosphate and 1 mM EDTA (pH of 8.4). Cysteine hydrochloride monohydrate standard curve solution of final concentrations of 0, 0.25, 0.5 to 1.5 mM were prepared and Ellman's reaction solution (4 mg in 1 mL reaction buffer) were prepared freshly before every assay. 250 μL of cysteine standard curve solution was added to 2.5 mL reaction buffer and 50 μL Ellman's solution. This solution was mixed and incubated for 15 min at room temperature. UV absorbance was measured by Agilent Technologies Cary 60 UV-Vis (Santa Clara, CA, USA) at 412 nm wavelength. A standard curve was fitted ($R^2$=0.99), in the resulting equation Abs =1.108 * amount of free thiols was used as reference for amount of free thiols in the PDEGMA/PDEGSH solution samples (see standard curve supplementary data Figure S26).

PDEGMA/PDEGSH polymer samples of 2 mg/mL were prepared. 250 μL polymer solution was added to 2.5 mL reaction buffer and 50 μL Ellman's reagent solution, incubated for 15 min at rt, and UV absorbance measured at 412 nm. Percentage free thiol were calculated by the following equation. Percentage free thiols= (mmol polymer/mmol free thiols) * 100.

### 2.6.5 Free thiol presents confirmation by fluorescein-5-maleimide labeling.

All PDEGMA/PDEGSH different ratio polymers were dissolved in acetone at 4 mg/mL. One drop of 100 μL was dried on a glass slide. The dried polymers on the glass slides or electrospun PLA and PDEGMA/PDEGSH blend scaffold (see method section 2.2.2) were emerged in 3 mL PBS (5 mM EDTA). 30 μL of 0.1 mg/mL tris-(2-carboxyethyl) phosphine (TCEP, 10 equivalent (eq.)) was added to reduce the possible disulfide bonds formed when free thiol reacted together and incubated for 30 min at rt. A stock solution of 0.01 mg/mL fluoresceince-5-maleimide was prepared and was added to the glass slide in a 1:1 ratio, SH:maleimide group, incubated for 30 min at rt in a dark environment and washed 3 times with PBS and imaged under confocal, images where enhanced to observed lower signals on the fibres.

### 2.6.6 Synthesis of norbornene functionalised peptide Nor-GGG-YIGSR 7

DMF, Fmoc deprotection agent piperazine, activator N,N'-Diisopropylcarbodiimide (DIC), and activator base Oxyma were purchased from Fisher Scientific (Pittsburgh, PA, USA). Norbornenene funcitonalised peptide Nor-GGG-YIGSR was synthesised on a Rink Amide Resin (ChemPep, Wellington, FL) with a Liberty Blue$^{TM}$ Peptide Synthesizer (CEM Corporation, UK). Fmoc-alanine, Fmoc-glysine, Fmoc- isoleucine, Fmoc-valine, Fmoc-Tyrosin(t-butyl), Fmoc-arginine(Boc), Fmoc-lysine(Boc), and Fmoc-serine(t-butyl) were used to build up the peptide sequence. Amino coupling cycles were as followed: Fmoc-deprotection, 4x washing, coupling, coupling, 2 x washing. The N-terminus of the peptide was functionalised with a norbornene acid end group using the same coupling cycle. This norbornene functionalised peptide sequence was cleaved off the resin in a strong acid solution of 95% trifluoracetic acid (TFA), 2.5% deionised $H_2O$, and 2.5% triisopropylsilane under shaking for 4 h. Cleaved resin was filtered off, TFA was evaporated until 20% of the volume was left, and obtained product was precipitated three times in 30 mL cold ethyl ether and centrifuged down. Product was re-suspended in 80% water and 20% acetonitrile (ACN), frozen in liquid nitrogen, and lypholised. Dried peptide was then reconstituted in the same water/ACN ratios and purified by preparative-scale reverse-phase high performance liquid chromatography (RP-HPLC) using a Waters Xbridge BEH130 Prep C-18 column. The mobile phase comprised gradients of degassed, deionised water with 0.1% TFA and ACN with 0.1% TFA, at a flow rate of 21 mL/min. Peptide presence was detected by UV absorbance at 214 nm, fractions were collected and lypholised. Molecular weight of the purified peptide sequence was verified by electrospray ionization mass spectrometry (ESI-MS, AutospecQ, VG Analytical, Manchester, UK) (see obtained MS spectra supplementary data Figure S27 and Figure S28).

### 2.6.7 Photo-initiated thiol-ene reaction of PDEGMA/PDEG-S-Nor-peptide or electrospun scaffolds PLA and PDEGMA/PDEG-S-Nor-peptide blend.

10 mg PDEGMA/PDEGSH polymer was dissolved in PBS to a concentration of 1 mg/ μL, 10 eq. TCEP was added and left on a shaker in a cold room (8°C) to avoid precipitation of the thermo-responsive polymer. 10 mg Nor-GGG- YIGSR was dissolve in 100 μL DMSO and added to the polymer TCEP solution. 55 μL LAP solution of 13.4 μg/ μL in PBS was added and left under a 365 nm Mercury spot UV lamp (Blak-Ray® B-100 AP High Intensity UV Lamp, "UVP) at a strength of 6 mW/cm$^2$ in an ice bath (to avoid polymer precipitation). Sample was left for 15 min and a small sample was taken every 5 min to observed the reaction ratio of the thiol-ene click reaction. These polymer-S-peptide samples were warmed up until polymer precipitated and centrifuged down, dissolved in cold water and precipitated out by warming up of the sample for 3 times. These polymer-S-peptides were dried overnight and characterised by Ellman's assay and IR measurements.

In case of the electrospun scaffolds the scaffold was emerged in 1 mL PBS (5 mM EDTA, 7.4 pH), 10 eq. TCEP was added shaken for 30 min in a cold room (8°C) to obtain complete free thiol formation. Nor-GGG-YIGSR (10 eq.) and LAP solution (55 μL) was added. This was UV exposed under a 365 UV lamp at a strength of 6 mW/cm$^2$ for 90 seconds. Scaffolds were washed with de-ionised water and dried overnight before IR measurements were taken.

### 2.6.8 Peptide presence after photo-initiated thiol-ene chemistry confirmation by ATTO-NHS-ester labeling.

All PDEGMA/PDEGSH different ratio polymers were dissolved in acetone at 4 mg/mL. One drop of 100 μL was dried on a glass slide. The dried polymers on the glass slides or electrospun PLA and PDEGMA/PDEGSH blend scaffold were emerged in 3 mL PBS (5 mM EDTA). 30 μL of 0.1 mg/mL tris-(2-carboxyethyl)phosphine (TCEP, 10 eq.) was added to reduce the possible disulfide bonds formed when free thiol reacted together

and incubated for 30 min at rt. Nor-GGG-YIGSR (10 eq.) and LAP solution (55 µL) was added. This was exposed to UV (to initiated the thiol-ene reaction) under a 365 UV lamp at a strength of 6 mW/cm$^2$ for 90 seconds. Scaffolds were washed with de-ionised water a stock solution of 0.01 mg/mL ATTO-NHS-ester was prepared and was added to the glass slide in a 1:1 ratio, peptide:ATTO group, incubated for 30 mins at rt in a dark environment and washed 3 times with PBS and imaged under confocal.

## 2.7 Cell Culture

### 2.7.1 Materials

DMEM, Trypsin, PBS, 2% gelatin stock, Antiboitic-Antimycotic (AB/AM) buffer were purchased from Sigma-Aldrich Co Ltd., Switzerland. Trypan Blue Solution (0.4 v/v%) was purchased from Thermo Fischer Scientific, UK. Foetal Bovine Serum (FBS), Alamar Blue, TrypLE dissociation reagent, DMEM/F-12 + Glutamax, KnockOut Serum Replacement (KSR), FGF-basic (bFGF), MEM Non-Essential Amino Acids (NEAA) were purchased from Gibco Life Technologies, UK. Human Leukaemia Inhibitory Factor (hLIF) was purchased from Cell Signalling Technologies, the Netherlands.

### 2.7.2 Cell culture media preparation

#### DMEM containing 10 v/v% FBS (DMEM10) for 3T3 fibroblasts

From a 500 mL DMEM media bottle 55 mL was removed and stored in a separate centrifuge tube for any work with required antibiotic and serum free media. FBS (50 mL) and 5 mL AB/AM (100 units/mL penicillin, 100 $\mu$g/mL streptomycin (Sigma-Aldrich Poole, UK)) were defrosted and added to the DMEM media bottle.

**Stem Cell Medium (SCM) for human Corneal Stromal Cells (hCSCs)**

Previously aliquoted Knock-out serum (KSR, 100 mL), 4x bFGF aliquots (50 μL, 10 μg/mL of sterile distilled water), 1x hLIF aliquot (50 μL, 5 μg/mL of PBS (0.1% BSA)) and 1 mL AB/AM was defrosted in the fridge (4°C). From a 500 mL DMEM/F11 + GlutaMAX 110 mL was removed and saved for Alamar blue assay serum-free medium. A 100 mL KSR (20 v/v%), bFGF aliquots (0.04 w/v%), hLIF aliquot (0.01 w/v%), AB/AM (0.2 w/v%) and 5 mL MEM Non-essential Amino Acids (NEAA, 1 w/v%) was added. The SCM was aliquoted in 50 mL falcon tubes (40 mL per tube) and stored in freezer (-20°C). When required the aliquots were defrosted in the fridge (4°C) overnight and syringed through a 0.2 μm filter before use. Defrosted aliquots were used up to 7 days after defrost and kept in fridge. Medium aliquots were not used after this period as the bFGF and hLIF rapidly lose their activity.

### 2.7.3 General method for cell counting by haemocytometer

A glass Neubauer haemocytometer with coverslip was used. Both parts were cleaned with IMS. The coverslip was moistered with water and affix to the haemocytometer. Before centrifuging the cell suspension 100 μL of cell suspension was removed. Trypan Blue (100 μL of 0.4%) was added (final concentration 0.2% Trypan Blue). Trypan Blue will penetrate through the membrane of dead cells, while is not taken up by living cells. 100 μL of Trypan Blue-treated cell suspension gently applied to both chambers of the haemocytometer. Using a inverted microscope the grid lines of the haemocytometer were put in focus using the 10x objective. The living unstained cells were counted in one set of 16 squares of the heamocytometer with the use of a hand tally counter (see Figure 2.4 for schematic of haemocytometer). Cells were only counted when present within the square or on the right-hand and bottom boundary lines. All 4 sets of 16 corners were counted and cells/mL was calculated using Eq. 2.7.1. Stained cells (dead) were counted if present to estimate the cells viability.

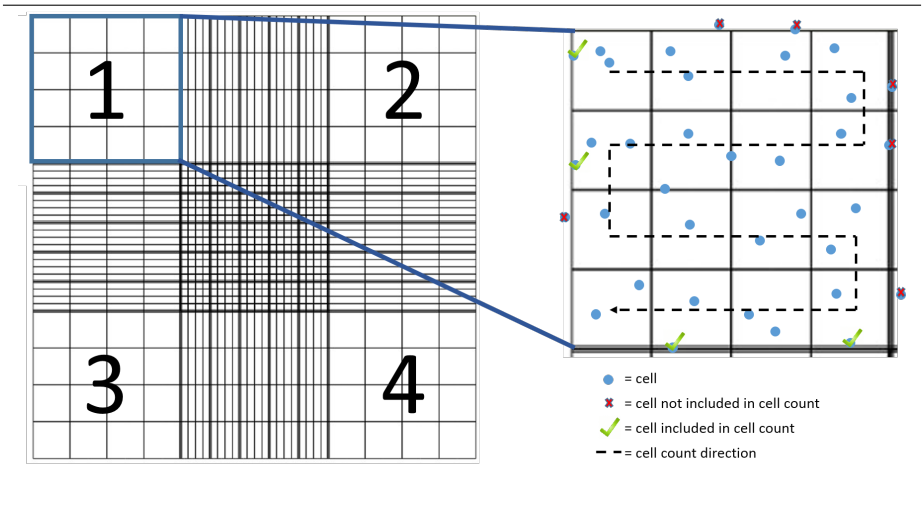



**Figure 2.4:** Schematics of cell counting by haemocymeter. Cells were counted which fall within the 4 corner squares of 16 squares. Only cells present on the right and bottom borderlines were included.

$$\text{Amount of cells/mL} = \frac{\text{Total cell count}}{\text{Amount of corner squares}} * \text{Dilution factor} \tag{2.7.1}$$

$$\text{Total cells in pellet} = \text{Amount of cells/mL} * \text{Total volume cell suspension} \tag{2.7.2}$$

### 2.7.4 3T3 fibroblasts cell culture

#### 3T3 cell revival from cryo-store

Genetically modified red fluorescent protein expressing 3T3 fibroblast were modified in-house by Dr. James Dixon. Red fluorescence expressing 3T3 fibroblast were defrosted from cryo-store in a waterbath at 37°C. Diluted in 50 mL DMEM10 (10 v/v% FBS), 50 µL was removed for cell counting, centrifuged and DMEM10 was aspirated of leaving the pellet of cells. By cell counting (see method section 2.7.3) the amount of DMEM10 to obtain 250.000 cells/mL was calculated, solution was prepared and 1 mL per T75 cell culture flasks was added with 11 mL of DMEM10. The cells were incubated

at 37°C, 5% $CO_2$.

#### 3T3 cell culture and passaging

Every 2-3 days a media change was performed. Spent media was aspirated, cells were washed with PBS (3 x 5 mL) and 11 mL DMEM10 was added. PBS and DMEM10 were pre-warmed in a waterbath at 37°C. When cells were 80% confluent (6-7 days culture) the cells were washed with PBS (3 x 5 mL) and 3 mL Trypsin was added and incubated for 5 mins at 37°C. The trypsinised cells in the flask were gently tapped to make sure all cells were detached from the T-flasks surface. DMEM10 (7 mL) was added and gently mixed over the cell culture surface and added to a centrifuge tube, centrifuged (5 mins at 500 g) and reseeded in the necessary density using cell counting by haemocytometer (see method section 2.7.3) for the required experiment.

#### Preparation of 3T3 cryo-store samples

All steps were the same as in previous section. However, the obtained pellet was re-suspended in a 10% DMSO to FBS ratio resulting in $1x10^6$ cells per mL and added to the 1 mL cryo tubes. These tubes were frozen overnight at controlled gradual decrease in temperature (1°C per min at - 80°C in a Mister Frosty) before being placed in the liquid nitrogen ($N_2$) long term storage's. Tubes were labeled with the cells type, passage number, cell density and date of preparation. All cells were cryo-stored at passage number 72.

### 2.7.5 human Corneal Stromal Cell (hCSCs) culture

#### 0.1 v/v% gelatin coating of 2D cell culture surfaces

T75 and 24 well plates were used as positive controls and were coated with 0.1 v/v% gelatin in PBS to improve attachment. 0.1 v/v% gelatin in PBS was made up by adding 1 mL gelatin stock (1 v/v% gelatin) in 19 mL PBS. This solution filter sterilised through

a 0.2 μm filter to sterilise. Solutions were freshly prepared when needed. 200 μL or 3 mL, 24 well or T75 flask respectively was added, agitated to insure complete coverage of the solution on the surface and incubated for 2 h at 37°C. Excess gelatin solution was removed before cell seeding. Coated T75 flasks were kept in 3 mL PBS in the fridge at 4°C for up to a week, when cell seeding was not performed on the same day as the coating.

**hCSCs isolation**

hCSCs were isolated from corneal rims (donor number=E2840/41) in-house by Laura Sidney Academic Opthamology, Division of Clinical Neuroscience, Queen's Medical Centre Campus. The excess sclera was removed and the epithelium and endothelium were gently detached. Resulting in the remaining stromal tissue. This was divided into small pieces and digested in 1 mg/mL collagenase Type IA (Sigma Aldrich) for 7 h at 37°C. Cell digests solution was filtered (40 μm cell strainer), centrifuged, resuspended in SCM, culture, and cryo-preserved at passage number 2 [193, 194].

**hCSCs cell revival from cryo-store**

Laura Sidney provided the hCSCs cryovials for all studies. All vials contained hCSCs at passage number 2. hCSCs were defrosted from cryo-store in a waterbath at 37°C. Diluted in 50 mL SCM (10 v/v% FBS), 50 μL was removed for cell counting, centrifuged and SCM was aspirated of leaving the palette of cells. By cell counting (see method section 2.7.3) the amount of SCM medium to obtain 250.000 cells/mL was calculated, solution was prepared and 1 mL per T75 cell culture flasks was added with 11 mL of SCM medium. The cells were incubated at 37°C, 5% $CO_2$.

**hCSCs cell culture and passaging**

Every 2-3 days a media change was performed. Spent media was aspirated, cells were washed with PBS (3 x 5 mL) and 11 mL SCM medium was added. PBS and SCM

medium were pre-warmed in a waterbath at 37°C. When cell were 80% confluent (7-9 days culture) the cells were washed with PBS (3 x 5 mL) and 2 mL TripLE was added and incubated for 5-10 mins at 37°C. The trypsinised cells in the flask were gently tapped to make sure all cells were detached from the T-flasks surface. DMEM10 (serum containing media, 3 mL) was added and gently mixed over the cell culture surface and added to a centrifuge tube, centrifuged (5 mins at 500 g) and reseeded in the necessary density using cell counting by haemocytometer (see method section 2.7.3) for the required experiment.

### 2.7.6 Proliferation study of 3T3s or hCSCs on electrospun scaffolds.

**Scaffold preparation and sterilisation.**

Electrospun scaffolds were cut into 1.5 cm by 1.5 cm squares which were fixed in the Cell CROWN® inserts and transferred to a non-tissue culture plastic 24 well plate. These transwells were sterilised for 10 mins under UV light at 800 energy level and incubated for 2 h at 37°C in 1 mL of DMEM containing 10 w/v% AB/AM (100 units/mL penicillin, 100 μg/mL streptomycin). The solution was removed and scaffolds were washed with PBS (3 x 1 mL) to removed any traces of media.

**Cell seeding**

Cells were passaged from T75 flasks and 3T3 (passage number 74) or hCSCs (passage number 4) were seeded onto the scaffolds at 60.000 cells/mL in DMEM10 or SCM medium respectively. Per scaffold 1 mL media was added and incubated at 37°C, 2% $CO_2$. Media was changed every 2 to 3 days culture.

**Proliferation study by cell viability assay Alamar blue**

Alamar blue cell viability reagent, resazurin, is used to assess the viability of the cells. Resazurin, is non-toxic and can penetrate the cell membrane. When the cell is metabol-

ically active the cytosol of the cell is reduced. This reduced environment results in the reduction of resazurin into the highly fluorescent compound resorfin. A calibration curve of known cell numbers (30 000, 60 000, 120 000, 240 000, 480 000, 960 000, and 1 920 000 3T3s or hCSCs cells) were obtained and resultant fluorescence was compared to obtain the amount of viable cells on the electrospun scaffolds. See corresponding calibration curves for 3T3s and hCSCs cells (see supplementary data Figure S29).

A stock solution of 10 w/v% Alamar blue in serum free DMEM was prepared. Scaffolds were rinsed with warm Hank's Balanced Salt Solution (HBSS, pre-warmed in a waterbath 37°C) for 3 times to remove any traces of FBS, which can interfere with the assay. 500 µL of the Alamar blue solution was added to scaffolds, plus 3 wells with cells without scaffold as positive control and unseeded scaffolds for negative control. The Alamar blue and scaffolds were incubated for 90 min at 37°C and flourescence intensity was analysed by plate reader (TECAN, infinite® M200, Männedrof, Switzerland at excitation wavelength and bandwidth of 560 nm; 9 nm, emission wavelength and bandwidth of 590 nm; 20 nm, number of flashes 25 and integration time 20 µs). Gain were set to 64 and 87 for 3T3s and hCSCs respectively. Alamar blue assays were performed at day 0, 2, 5 and 7 of culture for 3T3s and for hCSCs at day 0, 2, 5, 7 and 9 of culture. In case of day 0 the cells were left to attach after seeding for 6 h. Samples were assayed in-triplicate to be statistically reliable.

## 2.8 Cell-electrospun scaffolds interaction studies using imunocytochemistry

Para-formaldehyde (PFA), Bovine Serum Albumin (BSA), Glycine, Triton X-100, Donkey Serum were purchased from Sigma-Aldrich Co Ltd., Switzerland. 4',6-diamidino-2-phenylindole (DAPI) was purchased from Santa Cruz Biotechnology. Alexa-FLour 488-conjugated phalloidin was purchased from New England Biolabs. Antibodies details can be found in Table 2.4.

**Table 2.4:** Details of primary, secondary antibodies and chemical staining used in immunostainings.

| Antigen | Clone | Source (Catalog No.) | Host | Conjugates |
|---|---|---|---|---|
| | | **Primary anitbodies** | | |
| **Vimentin** | V9 | Vecto Labs (VPV684) | Mouse | - |
| **CD34** | QBEND10 | Sigma (SAB4700736) | Mouse | - |
| **CD105** | Polyclonal | R&D Systems (AF1097) | Goat | - |
| **ALDH3A1** | Polyclonal | Abcam (Ab76976) | Rabbit | - |
| **α-SMA** | 1A4 | LSBio (LS-C210475) | Mouse | - |
| **Lumican** | Polyclonal | R&D Systems (AF2846) | Goat | - |
| **Collagen I** | Polyclonal | Abcam (Ab34710) | Rabbit | - |
| | | **Secondary anitbodies** | | |
| **Mouse IgG**[a] | Polyclonal | Life Technologies (A-21202) | Donkey | AF[b]-488 |
| **Goat IgG**[a] | Polyclonal | Life Technologies (A-11056) | Donkey | AF[b]-546 |
| **Rabbit IgG**[a] | Polyclonal | Life Technologies (A-10040) | Donkey | AF[b]-546 |
| | | **Chemical staining** | | |
| **Phalloidin** | - | Thermo-Fisher (A12379) | - | AF[b]-488 |
| **DAPI** | - | Thermo-Fisher (D1306) | - | - |

[a] IgG, immunoglobulin; [b] AF, Alexa Fluor

### 2.8.1 Buffer preparation for immuno-staining

#### Permeabilisation Buffer

For the permeabilisation buffer 100 µL of Triton-X100 was dissolved into 100 mL PBS (0.1% Triton-X100) using a magnetic stirrer and flea. This buffer was stored in the fridge at 8°C.

#### Wash Buffer

For the wash buffer, 2 g Bovine Serum Albumin (BSA, 1% BSA) and 4.5 g glycine (0.3M glycine) to 200 mL PBS and stirred using a magnetic stirrer and flea. This buffer was

stored in the fridge at 8°C.

**Blocking Buffer**

The blocking buffer was prepared, 150 µL of donkey serum to 5 mL wash buffer (3% donkey serum) and stirred using a magnetic stirrer and flea. This buffer was prepared the day on which the immuno-staining was performed and only the required volume was made up at a time.

### 2.8.2 Immuno-staining of fixed hCSCs on electrospun scaffolds

To observe the phenotype expression of the hCSCs on the different electrospun scaffolds the cell were immuno-stained for the following markers, see Table 2.5 for primary and secondary antibodies used.

Three different immuno-staining combinations were selected, see Table 2.5. For immuno-staining combinations **B** and **C** membrane permeabilisation was required. While immuno-staining combination **A** are cell surface antigens and so permeabilisation of the cells was not required.

**Fixing Cells for SEM or immuno-staining**

To observe their adherence and proliferation of the cells and there interaction with the electrospun scaffolds. Cells were fixed on the scaffold by 2 w/v% paraformaldehyde (pFA) in PBS at day 0, 2, 5, 7 and 9. Media was removed and scaffolds was rinsed with PBS. pFA 1 mL per scaffolds were added and incubated for 10 min at room temperature. Subsequently, the scaffolds with fixed cells were washed with PBS for 3 times. Fixed samples were stored in PBS at 4°C for up to a 1 month if microscopes were not available.

**Table 2.5:** List of chosen primary and secondary antibodies and their counter combinations for **A)** and **B)** phenotype marker expression, **C)** morphology staining and **D)** ECM expression of fixed hCSCs cells to confirm the phenotype of the cells in interaction with the elctrospun scaffolds. Ratio of μL of antibody to μL wash buffer is presented in the brackets. m= mouse, g= goat, r= rabbit.

| **Double staining sample code** | **Primary antibodies** | **Secondary antibodies** | **Primary antibodies** | **Secondary antibodies** | **Cells Permeabilised (Yes/No)** |
|---|---|---|---|---|---|
| **A** | CD34-m (1:200) | AF488-m (1:300) | CD105-g (1:200) | AF546-g (1:300) | No |
| **B** | ALDH3A1-r (1:100) | AF488-r (1:300) | α-SMA-m (1:200) | AF594-m (1:300) | Yes |
| **C** | - | Phalloidin AF488 (1:60) | Vimentin-m (1:100) | AF594-m (1:300) | Yes |
| **D** | Collagen I-r (1:100) | AF488-r (1:300) | Lumincan-g (1:100) | AF546-g (1:300) | Yes |

### Permeabilisation

Following storage, the PBS was removed from the scaffold with fixed cells are stored in was removed 200 μL of permeabilisation buffer was added per scaffold for immuno-staining combinations **B**, **C** and **D** and incubated for 10 mins at room temperature. Permeabilitisation buffer was removed and scaffolds were washed with PBS for three times, each wash lasting 5 mins.

### Blocking

Blocking was performed to prevent non-specific binding of the primary antibodies. After samples with permeabilised membranes were performed the blocking step was performed to all immuno-staining combinations. 200 μL of blocking buffer was added

per scaffold and incubated for 1 h at room temperature.

**Primary antibody incubation**

200 µL of primary antibody solution was added according to the immuno-staining combination per scaffold at the required dilution factor prepared in wash buffer (see Table 2.5). Samples were incubated at 4°C overnight for about 16 h. Negative controls were incubated in wash buffer only.

**Secondary antibody incubation**

The primary antibody solutions were removed and the scaffolds were rinsed with wash buffer for 3 times, each wash lasting 5 minutes. Work was moved to a dark room to protect the fluorescent secondary antibodies. 200 µL secondary antibodies were added per scaffold, including negative controls. This was incubated for 1 h at room temperature in the dark (covered in foil). Subsequently, the scaffolds were washed 3 times with PBS, each wash lasting 5 mins.

**Phalloidin counterstain**

The actin cytoskeleton of combination **C** was stained by phalloidin counterstain. After washing with wash buffer in previous step the scaffolds of combination **C** were incubated for 20 mins in the dark in 200 µL actin solution (see dilution ratio, Table 2.5). Subsequently, they were washed once in wash buffer.

**DAPI or Hoechst counterstain**

All fixed cells nuclea were stained with DAPI (hCSCs) or Hoechst (3T3). 200 µL DAPI or Hoechst solution (5 µL of 250 µg/mL stock solution in 5 mL wash buffer (1:1000)) was added per scaffold and incubated for 10 mins at room temperature in the dark.

DAPI solution was removed and samples were washed 3 times by PBS, each wash lasting 5 mins.

### 2.8.3 Confocal microscopy

Scaffolds were observed to stay fixed in position of Cell CROWN® insert into a basket kind of structure. To obtain flat scaffolds for imaging the immunostained scaffold sides were cut off. These were mounted in fluorescence mounting medium (Dako) and sealed with colourless nail-polish. When imaging on the Zeiss Elyra S.1 Super Resolution Confocal Miscroscope, slides were imaged upside down, as the scaffolds are opaque. For 3T3s on scaffolds with PBI-PDEGMA, 10x and 64x water lens were used for imaging on the Zeiss Elyra S.1 using ZEN 2.3 SP1 software (Black, Zeiss). Images were captured at wavelength 405 nm, 488 nm and 561 nm for Hoechst, PBI-PDEGMA and red fluorescent protein expression of genetically modified 3T3 respectively. In case of the hCSCs immunostaining, 4x and 20x lens were used in case of the upright fluorescence microscope (BX51, Olympus) with images captured with a black and white camera (XM-10, Olympus) and Cell ˇ F software (Olympus). Samples were measured upright in this case, with no coverslip. Wavelength of 405 nm, 488 nm and 566 nm for DAPI, CD34 or ALDH or Actin and CD105 or α-SMA or Vimentin, respectively.

## 2.9 Cell thermo-responsive detachment studies

### 2.9.1 3T3 fibroblast detachment

Scaffolds were moved from the Cell CROWN® and place in a new non-treated 24 well plate and submerged in 1 mL DMEM10. This well plate was moved out of the incubator and cooled to rt or 8°C in the fridge for different times. This will change the scaffold to hydrophilic characteristics which detach the cells. Scaffolds were vigorously agitated in the DMEM media by holding it with a tweezer. Subsequently, the DMEM10 with detached cells were placed into a cell culture treated 24 well plate and incubated for 6 hour before performing the Alamar blue viability assay (see method section 2.7.6). The

remaining scaffolds were left in the well plate and fresh DMEM10 1 mL was added and incubated for the same amount of time and subsequently Alamar blue viability, to see if any cells were remaining on the scaffold after detachment.

### 2.9.2 hCSCs detachment

Scaffolds were moved from the Cell CROWN® and place in a new non-treated 24 well plate and submerged in 1 mL SCM. This well plate was moved to the fridge for 30 min at 4°C. This will change the scaffold to hydrophilic characteristics which detach the cells. Scaffolds were vigorously agitated in the DMEM media by holding it with a tweezer. Subsequently,, the SCM with detached cells we placed into a cell culture treated 24 well plate and incubated for 6 hour before performing Alamar blue viability assay (see method section 2.7.6). The remaining scaffolds were left in the well plate and new SCM 1 mL was added and incubated for the same amount of time and subsequently Alamar blue viability, to see if any cells were remaining on the scaffold after detachment.

In case of the cells detached for FACS the cells were centrifuge down and re-suspended in PBS and immunostained, see method section 2.8.

### 2.9.3 Percentage of cell detached

All detachment data is presented in percentage of cells detached. This is calculated by subtracting the amount of cell on the scaffold left after passaging with the initial amount of cells before the passaging. This number was then defined by initial amount of cells and multiplied by 100. Obtained number represent percentage of cells detached.

## 2.10 Fluorescence-activated cell sorting (FACS)

### 2.10.1 Immunostaining of suspended cells for Fluorescence-Activated Cell Sorting (FACS)

Instead of fixing cells on scaffolds the hCSCs were detached from the scaffolds (see method section 2.9.2), re-suspended in 2 w/v% pFA and fixed for 30 min, centrifuged (5 mins at 500 g) and re-suspended in PBS. Samples were stained in combinations **A** and **B** (see Table 2.5) with the sample method (see method section 2.8.2). As cells were in suspension, cells were washed between every step by centrifugation (3x for 5 mins at 300g each washing step). Positive control were samples CD34, CD105, ALDH and α-SMA on their own and negative control were the secondary antibodies without the primary antibodies present. Cells were stored for 2 days in 4% pFA after the secondary antibody step. Number of cells stained were measured by FACS to quantify cell populations expressing certain markers of interest (see method section 2.10).

### 2.10.2 FACS measurements

Cell were immuno-stained in two different combination in suspension 2.10.1. Samples were stored in 4 w/v% pFA solution and analysed with MoFLo® Astrios$^{TM}$ (Beckman Coulter, USA) flow cytometry equipment. Samples were agitated before analysis to assure single cells in the solution. Data obtained were analysed by Kaluza Analysis software and obtained X-means and Y-means were analysed with two-way ANOVA by GraphPad Prism 7.01 software.

## 2.11 Statistical Analysis

Statistical significance of all cell studies were determined by one or two-way ANOVA followed by the Tukey's multiple comparisons test using GraphPad Prism 7 software. Results were presented as means ± standard deviation (SD). Significant differences

were considered when $p < 0.05$. All significant difference are indicated by *=<0.05, **=<0.01, ***=<0.001, and ****=<0.0001.

# Chapter 3

# Optimisation of the electrospinning process

## 3.1 Introduction

Electrospinning is widely used in the manufacture of biologically relevant scaffolds for cell culture, enabling the formation of micro or nanoscale fibres and porous matrix structures [85]. Scaffolds produced by this method exhibit similarities in physical and material properties to the native extracellular matrix (ECM), facilitating their application in regenerative medicine and tissue engineering as *in-vitro* culture platforms for mammalian cells [27, 85, 94, 95, 195–199]. In the electrospinning process, a polymer solution or melt is accelerated through a charged needle towards a grounded or opposite polarity collector. A high voltage is applied to the needle, which acts on the meniscus solution droplet at the tip. The rounded droplet extends to form a conical shape known as a Taylor cone [200], in which the electric field exceeds the surface tension of the droplet resulting in a fibre jet being ejected from the Taylor cone towards the collector. Solvent evaporation occurs while the fibre jet travels through the atmosphere, leading to solid polymer fibre deposition on the collector [96]. Flat or rotating mandrel collectors are commonly used [199]. Although electrospinning can produce well-defined fibres, process parameters can greatly affect fibre morphology.

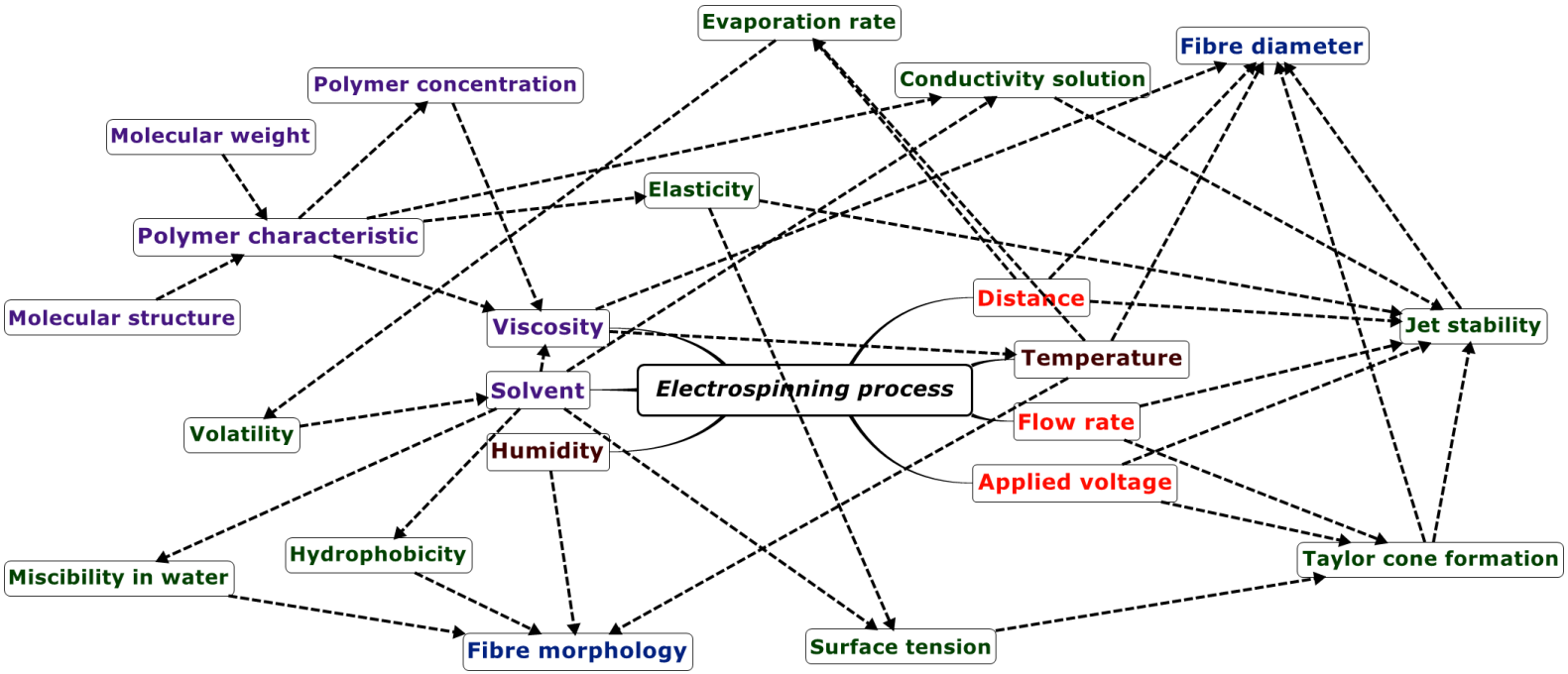



**Figure 3.1:** Presentation of the complex interactions between electrospinning process parameters (red), polymer solution characteristics (purple), underlying influencing variables (green), ambient factors (brown) and electrospun scaffold characteristics (blue); based on published literature between 2006 and 2016 [101, 107, 112, 123, 201–205].

Many parameters may change the resultant fibre morphologies; these factors include applied voltage, collector plate distance from the needle, polymer solution concentration, solvent type and flow rate. The interaction between these process parameters is complex, with variation of one factor often altering another, as shown in Figure 3.1 [101, 107, 112, 123, 201–205]. It is therefore challenging to investigate each individual parameter experimentally and the resultant procedure is time-consuming. For reproducible electrospinning to occur, the key process parameters must be identified and stably controlled.

In general, three fibre morphologies can arise from electrospinning; uniform fibres, 'beads- on-strings' and 'big beads' (see Figure 3.2). The occurrence of beading is thought to be as a result of flow rate or polymer concentration [102, 118, 206] , with beading impacting upon the reproducibility, biological significance and downstream cell viability of the scaffolds [68]. As a result, much effort has been invested to identify process parameters that will yield uniform fibres. Although bead formation is a common phenomenon, the understanding of the parameter combinations resulting in beaded morphologies is still unclear. Electrospinning process optimisation is a common topic in published literature as researchers attempt to understand the specific effect of multiple variables [97, 111, 118, 119, 121, 205, 207].

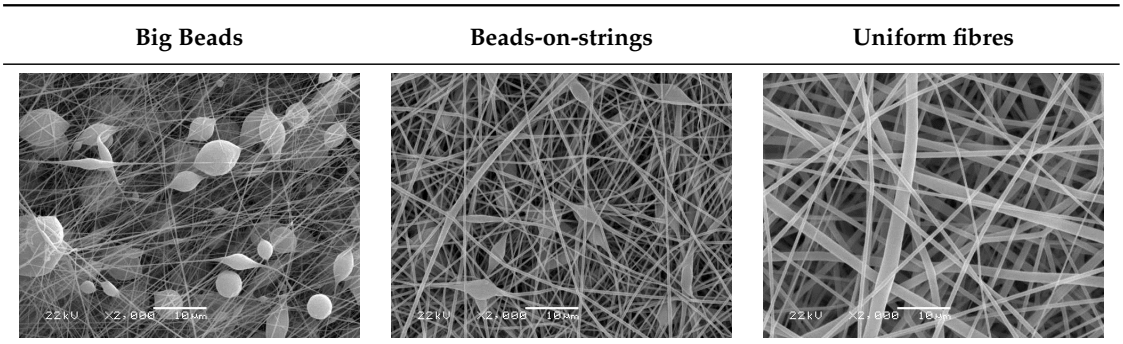



**Figure 3.2:** SEM images of the three common fibre morphologies observed in electrospun fibrous scaffolds (and as used in this study). **A)** Big beads (SD $\pm$ 1406 nm), **B)** Beads-on-strings (SD $\pm$ 1297 nm), and **C)** uniform fibres (SD $\pm$ 433 nm). (n=18, 3 scaffolds, 6 SEM images per scaffolds, 20 fibre measurements per SEM images.) Scale bar is 10 µm.

Much research has been reported on the impact of such parameters (on fibre diameter for example), however little is known about the interaction between these parameters (i.e. how they influence each other). To date, experimental design towards understanding process parameter effects has mostly involved one factorial approaches (see more info in Supplementary data Figure S30). This singular focus excludes the interrelationship between interacting parameters and as mentioned above, results in time consuming optimisation experiments. Design of experiments (DoE) or quality by design (QbD) approaches use fractional design to identify the most influential parameters. This method takes into account the interaction of parameter interrelationship, using linear regression and analysis of variance (ANOVA) mathematical models [208], identifying the significantly impacting factors and parameter interactions on the resultant fibre characteristics. Different combinations of the factors (parameters, such as applied voltage etc.) levels (high or low values of the parameter settings, example for applied voltage 10, 15 and 20 kV) are tested and resultant outputs (such as, fibre diameter etc) are used to define factor combination interactions. Building on the understanding of parameter interaction and interdependence, the DoE approach contributes to the overall understanding of the electrospinning process as a manufacturing technique.

### 3.1.1 DoE Model

A DoE model gives information of the process inputs cause-and-effect relationship with the outputs. Inputs are set to higher and lower levels and are combined in different combinations. For example in this study, a full four factor, three level fractional design with replication of 3, was used giving $3^{4_{factors}}_{levels} = 81$ runs (Table 3.1) of different combinations) or in this case electrospinning runs(a.k.a. degrees of freedom - *dof* - in statistical parlance). Collecting such a large dataset has the benefit of, 1) increased accuracy of statistical estimates and 2) confidence intervals, which are crucial for a systematic and comprehensive investigation of the electrospinning parameters [209]. Most DoE are performed in a "randomisation strategy" for uncontrolled parameters to reduce variability. In addition, a one single operator approach is recommended to avoid unnecessary variability in the model ("blocking strategy" of operator effect). Lin-

ear regression is thereafter used to identify the factor or interacting factors with the most impact on the process output.

**Table 3.1:** Different limits combination generated by MODDE 10.1 for the randomised DoE model, replica of three for all combinations and a replica of nine for the center point (N25) are not included in the table.

| Run | Voltage ($X_1$) | Distance ($X_2$) | Flow rate ($X_3$) | Polymer Concentration ($X_4$) |
|---|---|---|---|---|
| N1 | -1 | -1 | -1 | -1 |
| N2 | 1 | -1 | -1 | -1 |
| N3 | -1 | 1 | -1 | -1 |
| N4 | 1 | 1 | -1 | -1 |
| N5 | -1 | -1 | 1 | -1 |
| N6 | 1 | -1 | 1 | -1 |
| N7 | -1 | 1 | 1 | -1 |
| N8 | 1 | 1 | 1 | -1 |
| N9 | -1 | -1 | -1 | 1 |
| N10 | 1 | -1 | -1 | 1 |
| N11 | -1 | 1 | -1 | 1 |
| N12 | 1 | 1 | -1 | 1 |
| N13 | -1 | -1 | 1 | 1 |
| N14 | 1 | -1 | 1 | 1 |
| N15 | -1 | 1 | 1 | 1 |
| N16 | 1 | 1 | 1 | 1 |
| N17 | -1 | 0 | 0 | 0 |
| N18 | 1 | 0 | 0 | 0 |
| N19 | 0 | -1 | 0 | 0 |
| N20 | 0 | 1 | 0 | 0 |
| N21 | 0 | 0 | -1 | 0 |
| N22 | 0 | 0 | 1 | 0 |
| N23 | 0 | 0 | 0 | -1 |
| N24 | 0 | 0 | 0 | 1 |
| N25 | 0 | 0 | 0 | 0 |

**Regression Model**

A regression model is fitted for each $Y_i$ output of the experiment data to obtain a "ordinary least square" linear estimation for Y($X_1$, $X_2$, $X_3$, $X_4$), which is a second-order complete model (Eq. 3.1.1) with $y_i$, where $X_i$, $X_j$, $X_k$, and $X_l$ are the independent variables that influences the response y. $\beta_0$ is the model constant, $\beta_i, \beta_j, \beta_k$, and $\beta_l$ are the linear coefficients $\beta_{ij}, \beta_{ik}, \beta_{il}, \beta_{jl}$, and $\beta_{kl}$ are the cross, $1^{st}$ order interactions, product coefficients. $\beta_{ijk}$ is the cross, $2^{th}$ order interactions, product coefficients, $\beta_{ijkl}$ is the cross, $3^{th}$ order interaction coefficient, m is the number of X (in this case 4 factors) and $\varepsilon$ is the error.

$$\begin{aligned} y_i =& \beta_0 + \sum_{i=1}^{m=4} \beta_i X_i + \sum_{i=1}^{m=4} \sum_{j=i}^{m=4} \beta_{ij} X_i X_j + \sum_{i=1}^{m=4} \sum_{j=i}^{m=4} \sum_{k=j}^{m=4} \beta_{ijk} X_i X_j X_k \\ &+ \sum_{i=1}^{m=4} \sum_{j=i}^{m=4} \sum_{k=j}^{m=4} \sum_{l=k}^{m=4} \beta_{ijkl} X_i X_j X_k X_l + \varepsilon_i \end{aligned} \tag{3.1.1}$$

This equation can be rewritten to give the $\varepsilon_i^2$, given by Eq. 3.1.2, in which n is the amount of data points (in this case 81).

$$\begin{aligned} \varepsilon_i^2 =& y_i - \beta_0 - \sum_{i=1}^{m=4} \beta_i X_i - \sum_{i=1}^{m=4} \sum_{j=i}^{m=4} \beta_{ij} X_i X_j - \sum_{i=1}^{m=4} \sum_{j=i}^{m=4} \sum_{k=i}^{m=4} \beta_{ijk} X_i X_j X_k \\ & \sum_{i=1}^{m=4} \sum_{j=i}^{m=4} \sum_{k=j}^{m=4} \sum_{l=k}^{m=4} \beta_{ijkl} X_i X_j X_k X_l \end{aligned} \tag{3.1.2}$$

This can be used in the least square function L, given by Eq. 3.1.3, which will be used to estimate the $\beta$ values.

$$
\begin{aligned}
L &= \sum_{i=1}^{n} \varepsilon_i^2 \\
&= \sum_{i=1}^{n} \left( y_i - \beta_0 - \sum_{i=1}^{m=4} \beta_i X_i - \sum_{i=1}^{m=4} \sum_{j=i}^{m=4} \beta_{ij} X_i X_j - \sum_{i=1}^{m=4} \sum_{j=i}^{m=4} \sum_{k=i}^{m=4} \beta_{ijk} X_i X_j X_k \right. \\
&\quad \left. - \sum_{i=1}^{m=4} \sum_{j=i}^{m=4} \sum_{k=j}^{m=4} \sum_{l=k}^{m=4} \beta_{ijkl} X_i X_j X_k X_l \right)^2
\end{aligned} \tag{3.1.3}
$$

The parameters $\beta_0, \beta_i, \beta_{ij}, \beta_{ijk}$ and $\beta_{ijkl}$ were estimated by minimising the least square functional L. Herefore, the L was differentiate with respect to each of the parameters and set the derivative to zero.

These least square estimation of the regression coefficients $\beta_i, \beta_{ij}, \beta_{ijk}$,and $\beta_{ijkl}$ can be filled into the general linear regression equation, giving the following full estimated equation (Eq. 3.1.4):

$$
\begin{aligned}
Y =& \widehat{\beta}_0 + \widehat{\beta}_1 X_1 + \widehat{\beta}_2 X_2 + \widehat{\beta}_3 X_3 + \widehat{\beta}_4 X_4 + \widehat{\beta}_{12} X_1 X_2 + \widehat{\beta}_{13} X_1 X_3 \\
&+ X_3 \widehat{\beta}_{23} X_2 X_3 + \widehat{\beta}_{14} X_1 X_4 + \widehat{\beta}_{24} X_2 X_4 + \widehat{\beta}_{34} X_3 X_4 \\
&+ \widehat{\beta}_{123} X_1 X_2 X_3 + \widehat{\beta}_{234} X_2 X_3 X_4 + \widehat{\beta}_{124} X_1 X_2 X_4 \\
&+ \widehat{\beta}_{134} X_1 X_3 X_4 + \widehat{\beta}_{1234} X_1 X_2 X_3 X_4
\end{aligned} \tag{3.1.4}
$$

The following factors (see Table 3.2) can be filled in with the parameter (X) levels (-1, 0, 1) and the Y value generated from the DoE runs analysis, after which matrix inversion can give the values for $\beta_i, \beta_{ij}, \beta_{ijk}$, and $\beta_{ijkl}$.

As Seyedmahmoud et al. [209] cites by using code variables the role of each parameter is normalised so that ranking [$\beta_i, \beta_{ij}, \beta_{ijk}$, and $\beta_{ijkl}$] immediately renders the relative importance of each parameter. The design is orthogonal so each parameter [$\beta_i, \beta_{ij}, \beta_{ijk}$,and $\beta_{ijkl}$] can be estimated separately and dropped if not significant.

Meaning the higher the $\beta$ value the more it has an impact on the electrospinning, while low $\beta$ values are negligible. To decide the statistical significance of the each parameter their $p$-value is calculated. $p$-value defines the probability of observing a certain value by chance against a reference statistical distribution. In practice, an effect or interaction is non-significant and negligible when the $p$-value associated to a $C$-coefficient is higher than the significance level value chosen. In most cases a significance level of 5% is used. These calculations are done by ANOVA. $t$-value represents the standardised effect of the parameter or interacting parameters. Therefore, the higher the $t$-value the more impact it has on the electrospinning. $t$-test can be used to find the most significant parameter combinations. Using a 5% significance level, which will vary by the amount of *dof* or in this case the amount of runs in the DoE. Coefficient of determination $R^2$ is used to indicate the goodness of fit of the model and is represented by the percentage of the variation in Y that is explained by the regression model. As the $R^2$ value increases with the number of parameters $p$ in the model, it is appropriate to consider the $R^2$-adj which is less than $R^2$ and is defined with Eq. 3.1.5.

**Table 3.2:** Factors that can be solved by the results of linear regression of the DoE outputs.

| **Factors filled in by DoE results** | | |
|---|---|---|
| $y_i$ | $X_1$ | $X_2$ |
| $X_3$ | $X_4$ | $X_1X_2$ |
| $X_1X_3$ | $X_1X_4$ | $X_2X_3$ |
| $X_2X_4$ | $X_1X_2X_3$ | $X_1X_2X_4$ |
| $X_1X_3X_4$ | $X_2X_3X_4$ | $X_1X_2X_3X_4$ |

$$R^2_{adj} = 1 - (1 - R^2)\frac{p}{n - p - 1} \tag{3.1.5}$$

In which, p is the total number of explanatory variables in the model and n is the sample size. This adjusts the $R^2$ for the number of predictors relative to the number of data point in regression models encompassing two or more terms.

### 3.1.2 DoE approaches in literature

Currently there is limited research focusing on DoE approaches in electrospinning [210–216]. Desai and Sung [217] described a DoE approach using a two level frac-

tional design of four factors. Polymer concentration and needle-collector distance, individually and in combination, were observed to have a significant impact on the fibre thickness and bead density (number of beads) of fibres fabricated from polyaniline/ poly (methyl methacrylate) (PANI/PMMA). Cui et al. [218] used a three level fractional design of six factors to investigate the effect of parameters (voltage, polymer conc., molecular weight (MW), solvent system, flow velocity, and nozzle size) on the mean fibre diameter and percentage of beading of PDLLA fibres. A significant impact of MW and concentration of the polymer on the fibre diameter was observed. Likewise, a significant effect of MW, concentration and solvent system used, on the percentage of beading was identified. A more recent and larger DoE investigation by Seyedmahmoud et al. [209] used different polymer MWs as a variable while keeping the polymer concentration constant (12 w/v%), to fabricate bead-free poly-L-lactic acid (PLLA) fibres. This DoE was proposed by the authors to be more robust due to the size of the model: 5 factors, 3 levels and replicated runs (96). A significant impact of polymer MW on the fibre diameter was observed. To date, there are few published studies using DoE models to identify parameters that would yield uniform fibre formation with little to no beading. When embarking upon a new DoE approach for electrospinning, an initial optimisation phase is performed to identify the key parameter values to be selected for the model. Most chosen parameters are selected based on the production of uniform fibres whilst excluding the 'undesirable' morphologies of bead formation that can be observed in the electrospinning process. In adopting this 'trial and error' approach, there is a lack of understanding of the impact of process parameters on the different fibre based morphologies. Investigating these features (such as 'big beads' and 'beads-on-strings'; see Figure 3.2), in addition to uniform fibres, would provide a better understanding of which parameters lead to which morphologies. This should reduce optimisation time and give an indication of the most appropriate process parameter window required to achieve the desired fibre morphology. A DoE model can also provide a linear regression equation that can be used to predict the fibre diameter and the chance of bead formation within the chosen set of parameters.

In this chapter, a DoE method is presented which focuses on finding the parameters that significantly influence the fibre diameter, morphologies and bead distribution ob-

served in electrospinning of PDLLA fibres. A simple three level design of four factors and three input levels (high; 1, middle; 0 and low; -1) in combination was performed. Scaffold produced for cell culture purposes have focused on the behaviour of cells on uniform fibre orientations [95, 132, 137, 198, 219–224]. However, very few studies have compared the different fibre morphologies for cell proliferation [225]. The scaffolds with different fibre morphologies obtained by the DoE model were tested for the proliferation capacity of 3T3 fibroblasts (more information supplementary data Figure S30 and Figure S31).

## 3.2 Aims and Objectives

The aim of the study presented in this chapter is the investigation of the impact of parameter interactions in the electrospinning process on the resultant fibrous morphology. This is done by the use of a Design of Experiments approach. The fibrous morphology scaffolds obtained were mechanically tested and used to investigate 3T3 proliferation on these different scaffolds.

This study aim was achieved through the following objectives:

1. Identify parameter limitations for the DoE model.
2. Produce scaffolds of different parameter combinations of the DoE model, measure average fibre diameter, standard deviation and beads per $\mu m^2$.
3. Process DoE outputs and investigate the significant parameters interactions.
4. Test DoE model linear regression equation outputs predictions against real data.
5. Analyse mechanical properties (water contact angle (WCA) and Young's modulus) of the scaffolds with different fibre morphologies.
6. Observe 3T3 proliferation and viability on the different morphology scaffolds using scanning electron microscopy (SEM) and Alamar blue assay.

## 3.3 Experimental methods

### 3.3.1 Scaffold preparation

The scaffolds were electrospun with DoE parameter combinations (see method section 2.2.2 and Table 3.1), SEM images were taken (see method section 2.4.1) and FD, SD and beads per $\mu m^2$ were calculated using ImageJ software (see method section 2.4.2) .

### 3.3.2 DoE model output

Obtained FD, SD and beads per $\mu m^2$ per scaffolds were added into DoE software MODDE 10.1 and outputting linear regression formulas, paretto plots and 4D response contour plots were analysed and concluding were drawn (see method section 2.1 and Figure 3.3).

### 3.3.3 Scaffold characterisation

Water contact angle (see method section 2.4.4) and strength of scaffolds were analysed (see method section 2.4.3).

### 3.3.4 3T3 Fibroblast behaviour on scaffolds

3T3 fibroblast were seeded onto the scaffolds at 60 000 cells/mL (n=12 scaffolds per different morphology, see method section 2.7.6), proliferated for 6 days and cell numbers on different time points were calculated with the use of Alamar blue assays on 6 of the 12 scaffolds (see method section 2.7.6). One scaffold per morphology per day was fixed for SEM imaging (see method section 2.8.2). See schematic of the experimental timeline in Figure 3.4.

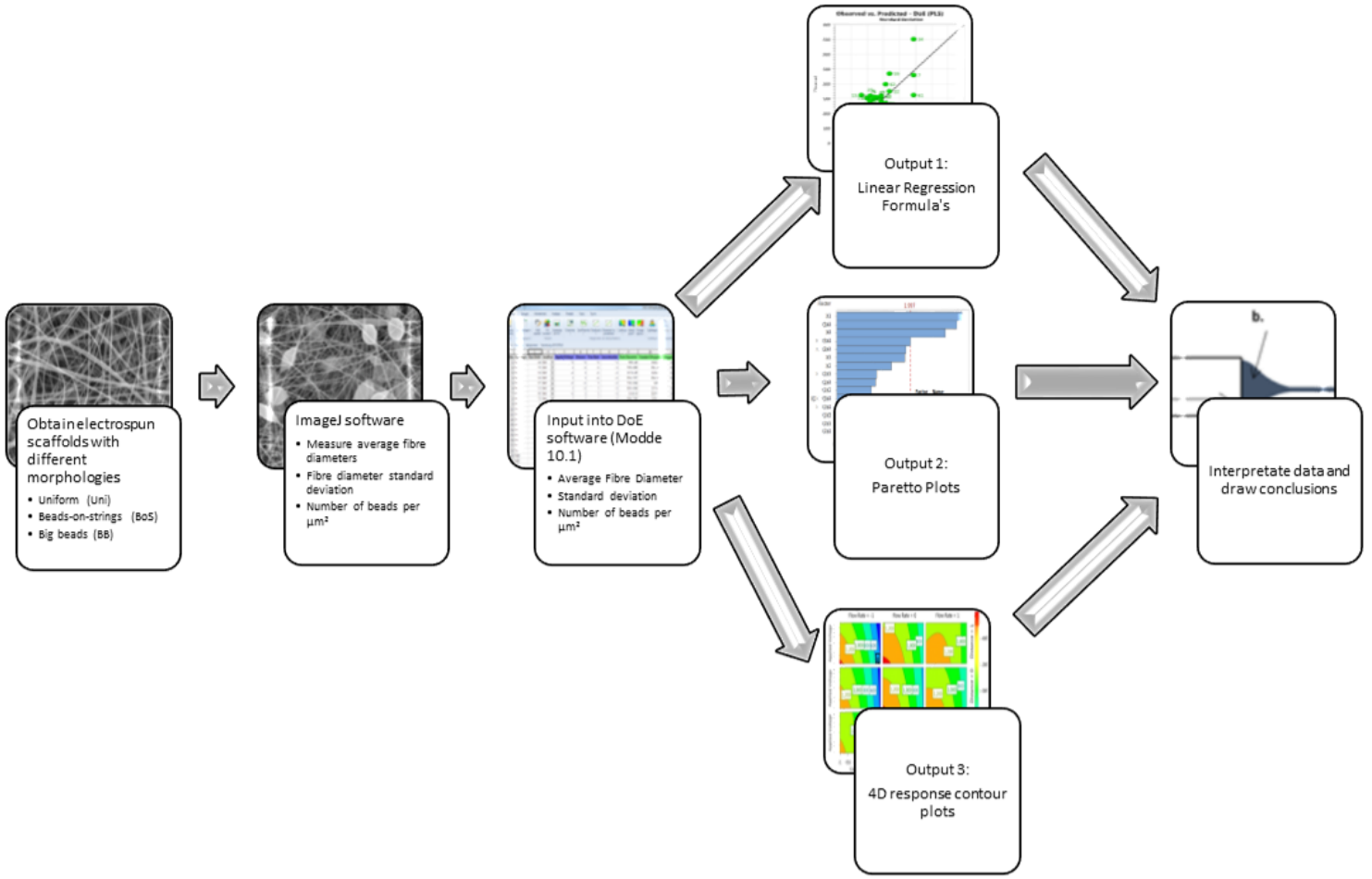



**Figure 3.3:** Schematic representing of the DoE model timeline.

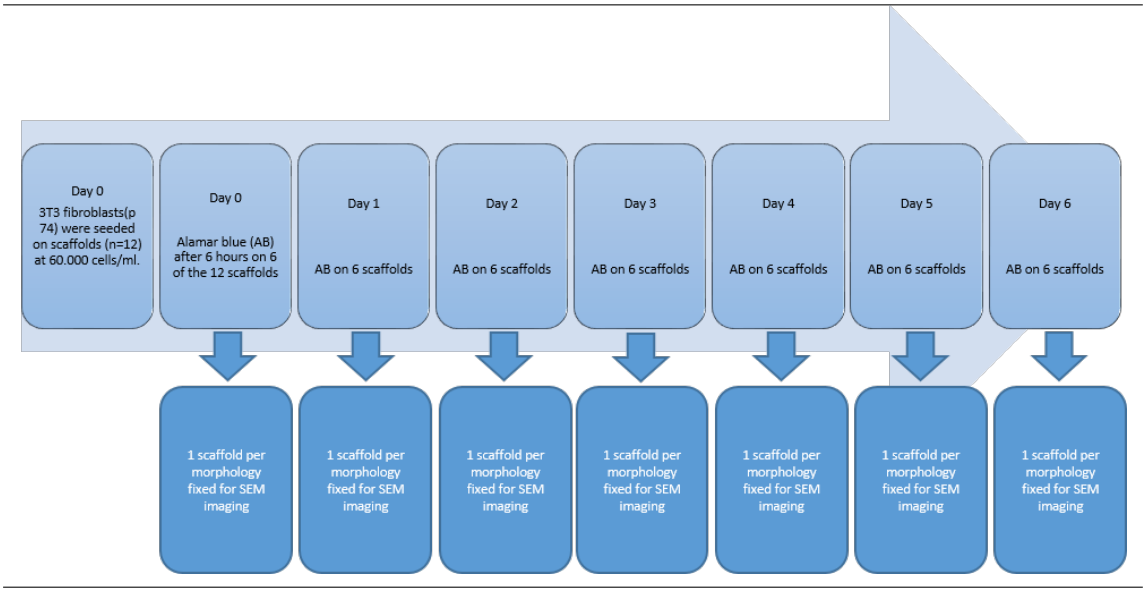



**Figure 3.4:** Schematic representing the Alamar blue (AB) and cell fixing for SEM imaging timeline for cultured 3T3 fibroblast cells over 6 days on the different electrospun fibre morphology scaffolds (n=12 per different scaffold).

## 3.4 Results & Discussion

A DoE approach can identify the parameters with the most significant impact on the resulting PDLLA fibre morphology. As difference in isomeric properties of PLA has been investigated intensely through existing literature [226–228], this work is exclusively focused on PDLLA polymer. A preliminary study, supplementary data; Figure S30, identified the sets of parameter levels (see Table 3.3) for the DoE model used to produce fibres of all three morphologies. From these sets, a DoE model of 4 factors, 3 levels and 3 replications was considered suitable, resulting in 81 electrospinning runs in total (25 different parameter sets, 3 replicates for each parameter set, 9 replicate of middle point). The preliminary study identified a correlation between the variation of fibre diameters over the different morphologies observed in the electrospinning process. These three different morphologies were termed 'big beads', 'beads-on-strings' and 'uniform fibres' (see Figure 3.2). Although the standard deviation gives an indi-

cation of morphology, it does not give a measure of the number of beads. Therefore, number of beads per $\mu m^2$ was included in the DoE model. The significant parameters that influenced mean fibre diameter, standard deviation and number of beads per $\mu m^2$ were identified by the DoE model. Parameter combinations and corresponding average fibre diameter, standard deviations and number of beads per $\mu m^2$ are shown in supplementary data; Table S1.

**Table 3.3:** Parameter limitation levels for the DoE model per parameter set by preliminary study and used outputs.

| **Parameter Inputs** | $X_s$ | **Unit** | **-1** | **0** | **1** |
|---|---|---|---|---|---|
| **Voltage** | $X_1$ | kV | 15 | 20 | 25 |
| **Distance** | $X_2$ | cm | 15 | 17.5 | 20 |
| **Flow rate** | $X_3$ | ml/hr | 1 | 3 | 5 |
| **Concentration** | $X_4$ | w/v% | 15 | 20 | 25 |
| **DoE Model Outputs** | | | | | |
| **Mean fibre Diameter** | $Y_1$ | nm | | | |
| **Standard deviation** | $Y_2$ | $\pm$ nm | | | |
| **Beads per $\mu m^2$** | $Y_3$ | number of beads | | | |

### 3.4.1 Fibre diameter ($Y_1$)

A normal distribution was observed throughout the data with a mean of 871 $\pm$ 189 nm (see Figure 3.5A). Linear regression was observed (see corresponding linear regression equation 3.4.1). A pareto plot (see Figure 3.5B) showed applied voltage as the most significant influencing parameter ($X_1$), followed by the flow rate and polymer concentration combined ($X_3X_4$), on the mean fibre diameter and the polymer concentration on its own ($X_4$).

$$
\begin{aligned}
Y_1 =& 872.5 - 72.4X_1 + 31.5X_2 - 39.3X_3 - 62.5X_4 - 21.2X_1X_2 \\
&+ 9.4X_1X_3 + 23.7X_1X_4 + 8.2X_2X_3 - 1.7X_2X_4 - \\
&73.6X_3X_4 + 24.4X_1X_2X_3 - 9.7X_1X_2X_4 + 45.0X_2X_3X_4 \\
&+ 42.3X_2X_3X_4 - 12.0X_iX_jX_kX_l
\end{aligned} \tag{3.4.1}
$$

The corresponding linear regression equation can be simplified to include only the significant impacting factors in the regression equation, as the non-significant impacting factors will generate a small change in the outcome Y of the equation due to their low $\beta$ factor (see Eq. 3.4.2). The 95% confidence interval (CI) for estimates was calculated giving a 95% CI of $\pm$ 32 nm for a full prediction and a 95% CI of $\pm$ 35 nm for the simplified prediction.

$$
Y_1 = 872.5 - 72.4X_1 - 62.5X_4 - 73.6X_3X_4 \tag{3.4.2}
$$

For a stable electrospinning process, the force (flow rate) required to push the polymer solution into the Taylor cone must be equal to the force generated by the jet pull rate that carries the solution away. This jet pull rate is created by the difference in electrical potential [115]. A good balance between the flow rate and the applied voltage is therefore important [117] (see Figure 3.7A). Polymer concentration has a direct impact on the whipping and stretching of the polymer jet. A decrease in whipping occurs with increasing polymer concentration due to the physical weight of polymer and polymer/solvent interaction within the jet. This results in an increase in fibre diameter and explains the significant interacting effect of flow rate and polymer concentration on the resultant fibre diameter observed here as well as the significant impact of applied voltage (see Figure 3.5B).

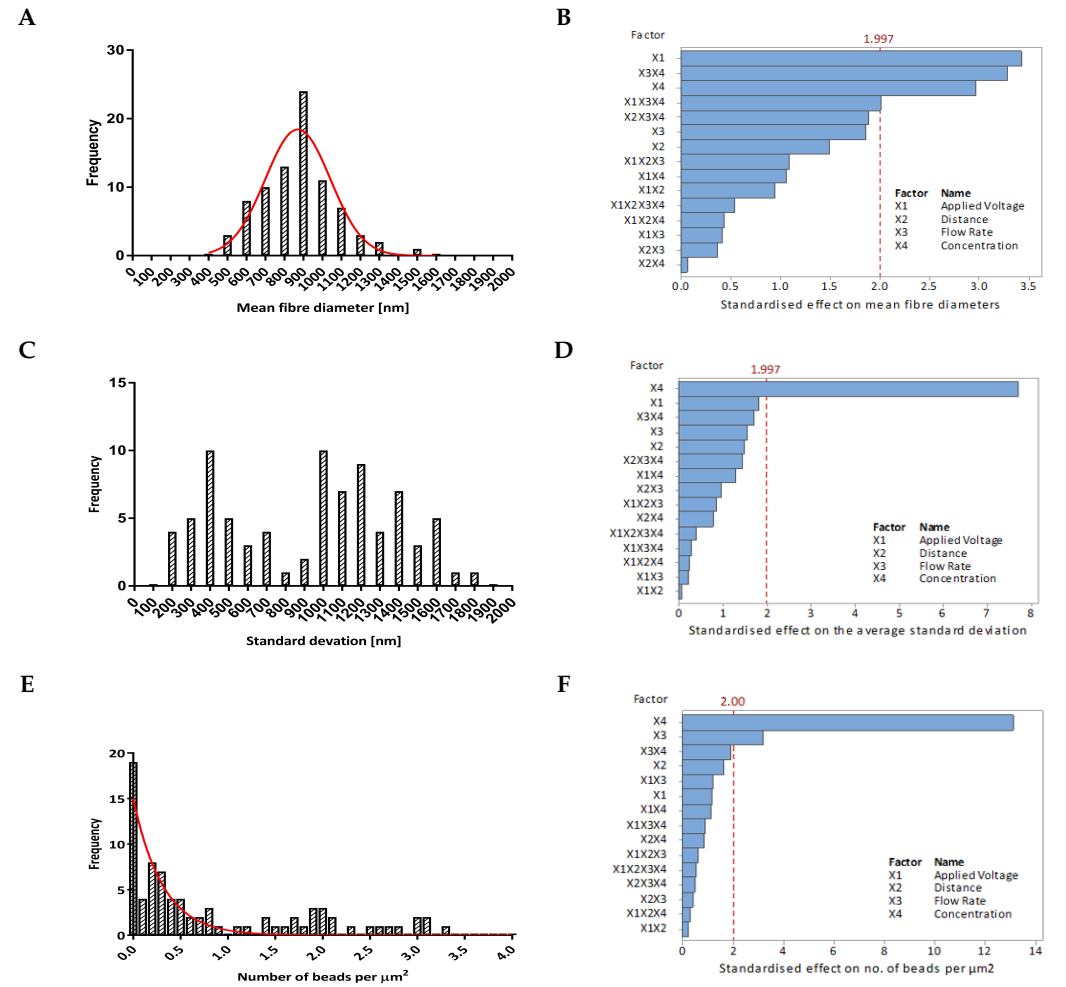



**Figure 3.5:** Histogram of distribution (81 scaffolds, n=120 fibre measurements per scaffold; bead count on three mag. x2000 SEM images per scaffold) and Pareto plots of most influencing parameter/parameter interactions of **A**), **B**) mean fibre diameter, **C**), **D**) fibre morphology, and **E**), **F**) number of beads per $\mu m^2$. Parameters with standardised effect over $t_0$ (0.05) = 2 or 1.997 have a significant impact on the scaffold's characteristics.

### 3.4.2 Fibre morphology ($Y_2$) and Beads per $\mu m^2$ ($Y_3$)

Standard deviations (SD) in the range of $\pm$ 200 to $\pm$ 1800 nm were observed throughout the DoE. Figure 3.5C shows $\pm$ 400-500 nm and $\pm$ 1000-1200 nm as the most frequently observed standard deviations. SEM images with SD ranges $\leq$ 500 nm showed scaffolds with uniform fibres. Beads-on-strings formation was observed between 500-1300 nm and large beads were observed within the range of $\pm$ 1300-1800 nm. Therefore, SD was concluded to be an appropriate measure of fibre morphology. A pareto plot showed a significant influence of only the polymer concentration ($X_4$; see Figure 3.5D) on the corresponding fibre morphology. Linear regression was observed (see corresponding full and simplified linear regression equations 3.4.3 and 3.4.4); 95% CI was calculated giving a 95% CI of 359 nm for a full prediction and a 95% CI of 358 nm for the simplified prediction.

$$\begin{aligned} Y_2 =& 929.6 - 83.1X_1 + 67.7X_2 + 70.6X_3 - 352.5X_4 - 2.8X_1X_2 \\ & - 10.5X_1X_3 + 62.4X_1X_4 + 46.5X_2X_3 + 37.9X_2X_4 \\ & + 83.2X_3X_4 + 41.1X_1X_2X_3 - 10.8X_1X_2X_4 + 13.9X_2X_3X_4 \\ & + 69.8X_2X_3X_4 - 18.7X_1X_2X_3X_4 \end{aligned} \tag{3.4.3}$$

$$Y_2 = 929.6 - 352.5X_4 \tag{3.4.4}$$

The number of beads per $\mu m^2$ had a direct correlation with the SD ranges observed for the fibre diameters. More beads per $\mu m^2$ were observed at higher standard deviations for big bead morphologies ($\pm$ 1-3 beads per $\mu m^2$), the beads-on-string morphology correlated to $\leq$ 1 beads per $\mu m^2$, while uniform fibres correlated with 0-0.2 beads per $\mu m^2$ (Figure 3.5E). No beading was observed at the highest polymer concentration 25 w/v% PDLLA at the lowest flow rate (1 mL/hr). The highest number of beads (3 beads per $\mu m^2$) was observed for the lowest concentration 15 w/v% PDLLA and the highest flow rate of 5 mL/hr. The pareto plot showed a significant impact of polymer concentration ($X_4$) and flow rate ($X_3$) on the number of beads per $\mu m^2$ (see Figure 3.5F and Eq. 3.4.5 and 3.4.6).

$$
\begin{aligned}
Y_3 =& 0.8793 + 0.0880X_1 + 0.1220X_2 + 0.2393X_3 - 0.9754X_4 + 0.0181X_1X_2 \\
&- 0.0968X_1X_3 - 0.0873X_1X_4 + 0.0303X_2X_3 - 0.0660X_2X_4 \\
&- 0.1510X_3X_4 - 0.0493X_1X_2X_3 - 0.0263X_1X_2X_4 + 0.0715X_2X_3X_4 \\
&+ 0.0376X_2X_3X_4 + 0.0421X_1X_2X_3X_4
\end{aligned} \tag{3.4.5}
$$

$$
Y_3 = 0.8793 + +0.2393X_3 - 0.9754X_4 \tag{3.4.6}
$$

The three observed fibre morphologies corresponded to particular SD ranges due to including the bead diameters in the fibre diameter measurements. By including the beads in the measurement the standard deviation increased when the scaffold was heterogeneous in diameter (due to this beading) and decreased when the fibres were uniform and more homogenous. Therefore, lower standard deviations corresponded to uniform fibres (homogenous morphologies) while larger standard deviations corresponded to large bead formation (heterogeneous morphologies). More uniform fibres were observed for high concentrations of PDLLA (25 w/v%). An increase in beading was observed when the PDLLA concentration was reduced to both 20 and 15 w/v%. The DoE results confirmed this observation showing that the fibre morphology was only significantly affected by the polymer concentration ($X_4$; see Figure 3.5D). The number of beads per $\mu m^2$ value had a direct correlation with the SD ranges observed for the fibre diameters. The amount of beading was observed to increase at the lowest concentration of PDLLA and the highest flow rate, whilst no beading was observed for higher concentrations of PDLLA and lower flow rates. This observation was confirmed by the DoE output showing a significant impact of polymer concentration ($X_4$) and flow rate ($X_3$) on the number of beads per $\mu m^2$ (see Figure 3.5F). This is attributed to the instability of the Taylor cone. As mentioned before, Taylor cone interruption resulted in bead formation (i.e. electro-spraying rather than electrospinning) , which increased when a high flow rate was used with a low polymer concentration solution [115] (see Figure 3.7B). The number of beads per $\mu m^2$ was therefore directly correlated with the flow rate used.

### 3.4.3 Test model predictions

The predictive equations 3.4.1, 3.4.2, 3.4.3, 3.4.4, 3.4.5 and 3.4.6 were tested by choosing different random combinations of parameters within the boundary of the DoE model (see Table 3.4) and testing the resulting prediction against measurements generated from scaffolds fabricated using those test parameters.

**Table 3.4:** Parameter combinations and corresponding model codes used for the linear regression prediction equations of the runs used to test the model. All equation parameters are represented in DoE model coding of -1,-0.8...etc.

| Run | Applied Voltage [kV] | Model Code | Needle-to-collector distance [cm] | Model Code | Flow rate [mL/hr] | Model Code | Polymer conc. [wt%] | Model Code |
|---|---|---|---|---|---|---|---|---|
| **A** | 20 | 0 | 20 | 1 | 1 | -1 | 23 | 0.6 |
| **B** | 20 | 0 | 20 | 1 | 2 | -0.5 | 17 | -0.6 |
| **C** | 20 | 0 | 20 | 1 | 4 | 0.5 | 20 | 0 |

The obtained fibre diameters of the test runs were within the 95% CI of the predicted mean fibre diameters for all test runs (Figure 3.6A). A much higher 95% CI was observed for the SD and number of beads per $\mu m^2$. This was due to the inability to control the unstable Taylor cone, which made the prediction of the exact size of the beads and number of beads per $\mu m^2$ less accurate. However, as stated earlier, different ranges of SD and number of beads per $\mu m^2$ corresponded to the different morphologies (see Table 3.5). Beads-on-strings formation was observed (Figure 3.6D-F) when morphology SD predictions fell within the beads-on-strings SD ranges (see Table 3.5). The number of beads per $\mu m^2$ data showed the same correlation of the predicted number of beads ranges to SD ranges. A more appropriate way to predict fibre morphology and beading was to group the calculated SD or number beads per $\mu m^2$ to the corresponding morphology, i.e. the extent of beading (see Table 3.5).

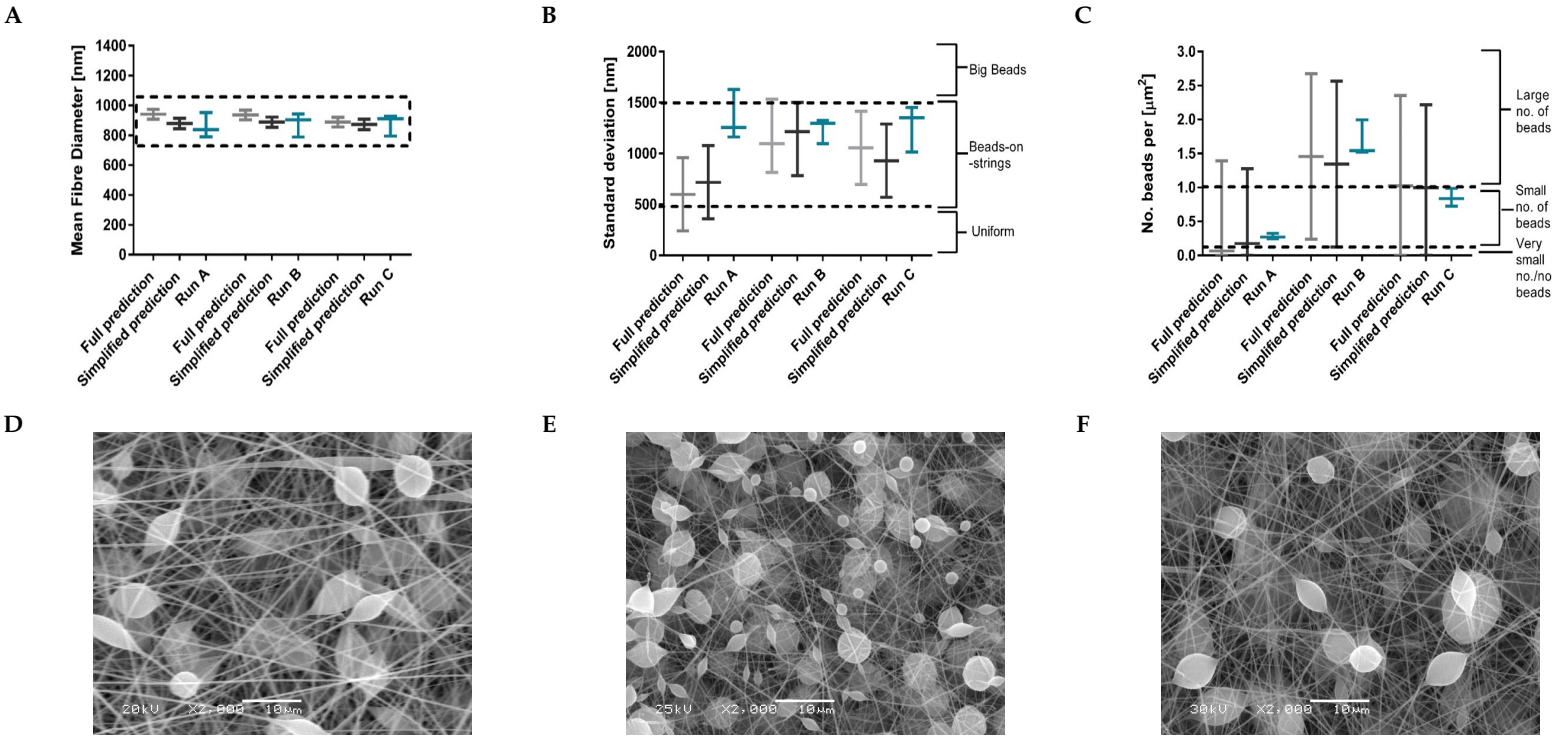



**Figure 3.6:** Full and simplified predictions plotted against actual data from the three test runs for **A**) the mean fibre diameter, **B**) standard deviation and **C**) beads per $\mu m^2$ and corresponding SEM images from the test runs. **D**) Run A, **E**) Run B and **F**) Run C. All test runs fall within the 95% confidence intervals for estimates of the prediction equations. Morphologies observed in the SEM images shown are in correspondence to where the observed range the predictions fall, see **B**) and **C**). (n=18, 3 scaffolds per run, 6 SEM images per scaffold, 20 measurements per SEM images, error bars=SD)

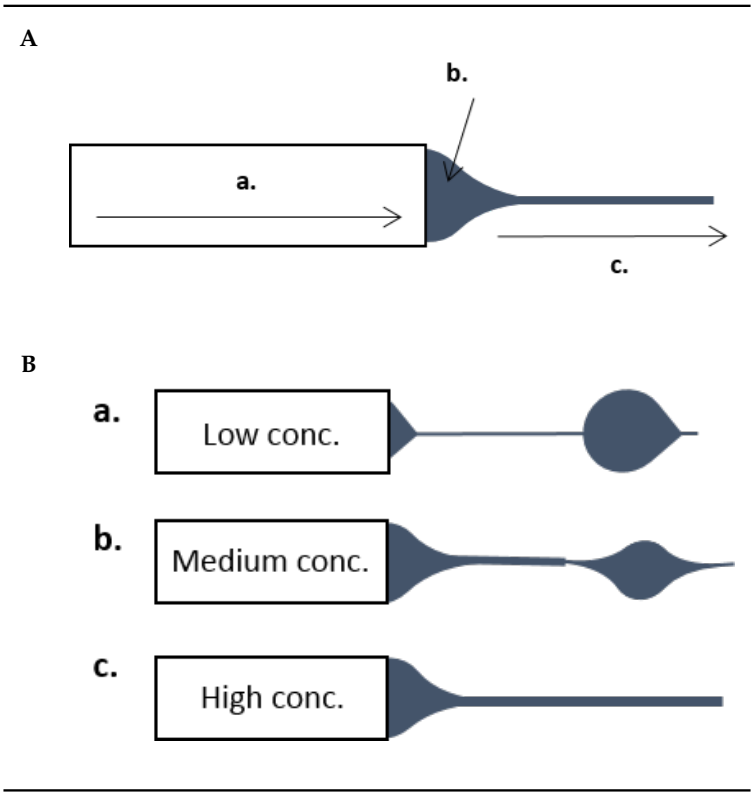



**Figure 3.7:** Schematic diagram of fibre formation. **A)** Applied voltage and polymer concentration have an impact on a) flow rate, b)Taylor cone stability and c) jet pull rate. This influences fibre formation and therefore the mean fibre diameter. Flow rate and pull rate must be equal for a stable electrospinning process (i.e. a=c), while a<c and a>c results in the formation of an unstable jet and fibre interruption resulting in bead formation. Schematic of polymer concentration effect on fibre formation. **B)** Increased polymer concentration results in an increased amount of polymer in the Taylor cone which in turn increases the stability of the cone. a) Low conc. polymer solutions result in breakage of the Taylor cone causing bead formation. b) Medium conc. polymer solutions result in less Taylor cone breakage but the Taylor cone is unstable and leads to the beads-on-string morphology. c) Higher conc. polymer solutions result in the formation of a stable Taylor cone and hence uniform fibres are produced.

**Table 3.5:** Expected fibre morphologies and number of beads as predicted by the DoE model for standard deviation and beads per $\mu m^2$.

| **Fibre Morphology** | **Uniform fibres** | **Beads-on-strings** | **Big beads** |
|---|---|---|---|
| **Standard deviation** | $\leq$ 500 nm | 500-1300 nm | $\geq$ 1300 nm |
| **Beads per $\mu m^2$** | 0-0.2 | 0.2-1 | $\geq$ 1 |

A stable/uninterrupted Taylor cone has a direct effect on the stability of the polymer jet. The concentration of the polymer solution significantly affects Taylor cone stability, as observed in the DoE, with low polymer concentrations leading to jet instability. This is because polymer concentration influences the viscosity of the solution which in turn affects Taylor cone stability. Higher polymer concentrations will stabilise the Taylor cone when the electric field pulls away the polymer jet. At lower polymer concentrations, a weaker Taylor cone forms and is subsequently interrupted resulting in beading when a voltage is applied. Besides the amount of polymer required to stabilise the Taylor cone, the flow rate used has to be sufficient to yield a continuous Taylor cone (see Figure 3.7B). The viscosity of the polymer solution is directly related to the molecular weight of the polymer [97, 99, 100, 212], structure of the polymer, additives (such as addition of salts) and solvent system used [101]. The effect on the solution viscosity must therefore be considered when changing the polymer or solvent system [102, 103]. A previous study observed a correlation between polymer entanglement concentration ($C_e$ ; i.e. the extent of interaction between polymer chains) and bead formation [106]. Beading was generated at a minimum $C_e^1$, while uniform and defect free fibres were observed at $C_e^{2-2.5}$. Entanglement concentration increases with higher polymer concentrations. This explains the decrease in beading observed when increasing the polymer concentration since the lower concentrations are below the entanglement concentration of the PDLLA solution.

No difference in fibre diameter was observed for big beads and beads-on-string fibre morphologies (Figure 3.8), while a significantly higher fibre diameter was observed for uniform fibres. This is due to the beads holding most of the polymer, so the fi-

bres between the beads were possibly stretched more during the whipping stage of the electrospinning process (see Figure 1.4C). Due to the significantly different topographic roughness of the surface between the scaffolds morphologies, a significantly higher WCA was observed for the big beads morphology (see Figure 3.8). This relationship of higher WCA when the surface is rougher has previously been observed in literature [229–233]. Water contact measurement on porous surfaces can result in two different effects: 1) the Cassie and 2) Wenzel state. The Cassie state is when air is trapped underneath the drop between the fibres, resulting in a higher WCA [234]. The Wenzel state is when the water droplet emerges between the fibres decreasing the WCA of the surface [235]. The topography of the surface of the scaffolds may increase the energetic barrier of the water droplet to separate the Cassie state to the Wenzel state resulting in a higher water repellence (hydrophobicity to the interfaces) [229, 236]. To reduce the influence of the Cassie effect on the WCA measurement, contact hysteresis can be used, which is the difference between the advancing (increase the droplet size) and receding (decreasing droplet size) contact angle [237, 238].

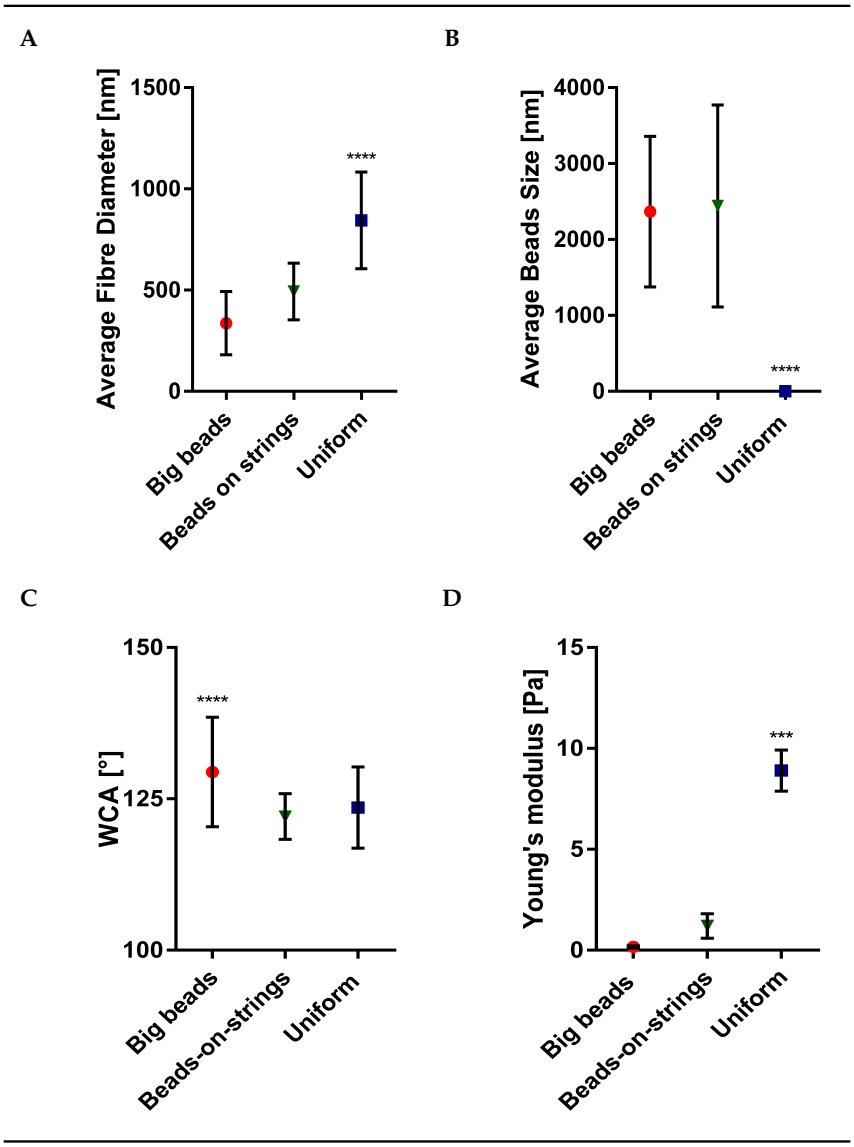



**Figure 3.8:** **A**) Average fibre diameter in nm for the three different morphologies. Beads were not included in the measurement. Significantly higher fibre diameters were observed for the uniform fibres. While the big beaded morphology showed a very small average fibre diameter. **B**) Beads size of the different morphologies were similar for the beads-on-string and big bead morphologies. **C**) Summary of the mean WCA and standard deviation are plotted in graph. Significantly higher WCA were observed for big beaded fibres. **D**) Tensile testing Young's modulus results are plotted. Scaffold consisting of uniform fibres have significantly higher Young's modulus those consisting of big beads and beads-on-string morphology. (n=3 scaffolds, Two-way ANOVA, ***=<0.001, ***=<0.0001, error bars=SD)

A lower Young's modulus was observed for the big beads morphology scaffold than for the beads-on-strings morphology. This may be because, unlike the big beads morphology, the larger fibre diameter and more stretched beads allows initial stretching of the fibres without resulting in their breakage (see Figure S1 and Figure S32). Tensile testing is performed by applying a vertical pull force on two sides of the scaffolds while this method is well established for aligned fibre materials, its accuracy for measuring the young's modulus for random fibre arrangements is limited. This is due to variation between batches and on how the sample is cut, due to changes in the orientation of the fibres. A few studies have focused on the use of atomic force microscopy (AFM) as an alternative method to measure the mechanical properties of electrospun fibres [239, 240]. Using this technique, single PCL fibres were manipulated either by pushing the fibre down [240] or sideways [239], and generating information on the Young's modulus, energy loss, and elasticity of this single fibre. Although these methods give information on the properties of singular fibres, no studies have yet focused on possible bulk fibre scaffold analysis by AFM, which may be a more accurate representation on what the cells experience when they bind to the scaffold surface. Initial experiments (data not shown) of these scaffolds by AFM resulted in loss of contact of the AFM needle to the fibres and subsequently no workable force curve. This is probably due to the small diameter of the fibres, round nature of the fibres and multiple layers of fibres. This results in no support for the fibre and subsequently in bending of the total fibre into the porous structure below the fibre. Liang et al. [241] explored this limitation by using a deposit of 2D xanthan fibres on a flat surface resulting in successful measurement of Young's modulus of the fibres. However, it is debatable if this is a good representation of the actual forces cells experience on a fibrous scaffold of different layers of fibres. More optimisation is needed to get a better representation of the scaffolds Young's modulus. However, this was considered to be outside of the scope of this work.

### 3.4.4 Cell behaviour on different electrospun scaffold morphologies

Fibre diameters were measured excluding the beads to observe actual diameter of the fibre between the beads. A significantly higher average fibre diameter was observed for uniform fibres of 844 $\pm$ 239 nm (see Figure 3.8D), while smaller average fibre diameter were observed for the big beads and beads-on-strings morphology (BB; 493 $\pm$ 140 nm and BoS; 337 $\pm$ 157 nm). However, no significant difference in bead size was observed between big beaded and beads-on-string morphologies with sizes ranging from 2000 to 2500 nm (see Figure 3.8B).

Static water contact angle (WCA) measurements showed a significantly higher WCA for the big beaded morphology compared to uniform and beads-on-strings morphologies (see Figure 3.8C). Tensile testing resulted in a significantly lower Young's modulus and low elongation for the big beaded scaffold observed (see Figure 3.8E and Figure S1). On the other hand, deformation with high elongation was observed for beads-on-strings morphology.

Cell proliferation studies resulted in no significant difference observed between uniform fibres and beads-on-strings morphology. However, significantly higher cell growth is observed for the big beads morphology at day 6 as indicated by the increasing cell number (see Figure 3.8B and Figure 3.9).

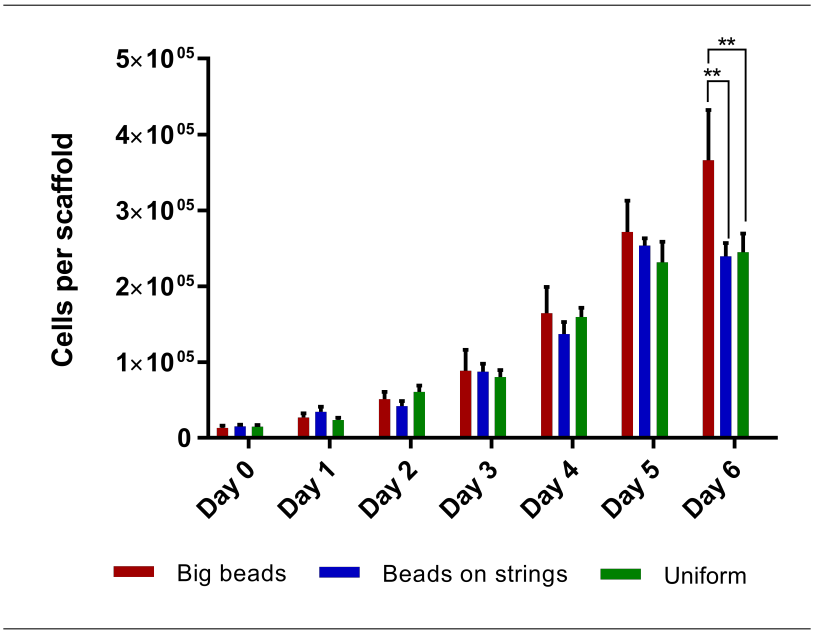



**Figure 3.9:** Cell proliferation over 6 days on different fibre morphologies. (n=3 scaffolds, two-way ANOVA **=0.01, error bars=SD)

This could be due to the change in WCA and Young's modulus compared to the other two morphologies. This may be due to the more hydrophobic and softer scaffold characteristic. No difference in cell proliferation was observed for the uniform and beads-on-strings morphology scaffolds. The SEM images show no preference in cell attachment on either beads or fibres present in the scaffolds (white arrows, see Figure 3.10). Therefore, the presence of beads-on-strings defects seems to have no effect on the cell attachment to the scaffolds, as observed from SEM images (white arrows, see Figure 3.10).

The current limited knowledge of the effects of interacting electrospinning process parameters on fibre morphology requires further understanding of the relationship between those parameters and bead formation. Understanding this relationship will make optimisation easier and less time consuming without having to perform many experiments where a single parameter is tested in turn. From the DoE model, it is evident that the concentration of the polymer solution significantly influences the fibre morphology whereas polymer concentration and flow rate both significantly influence

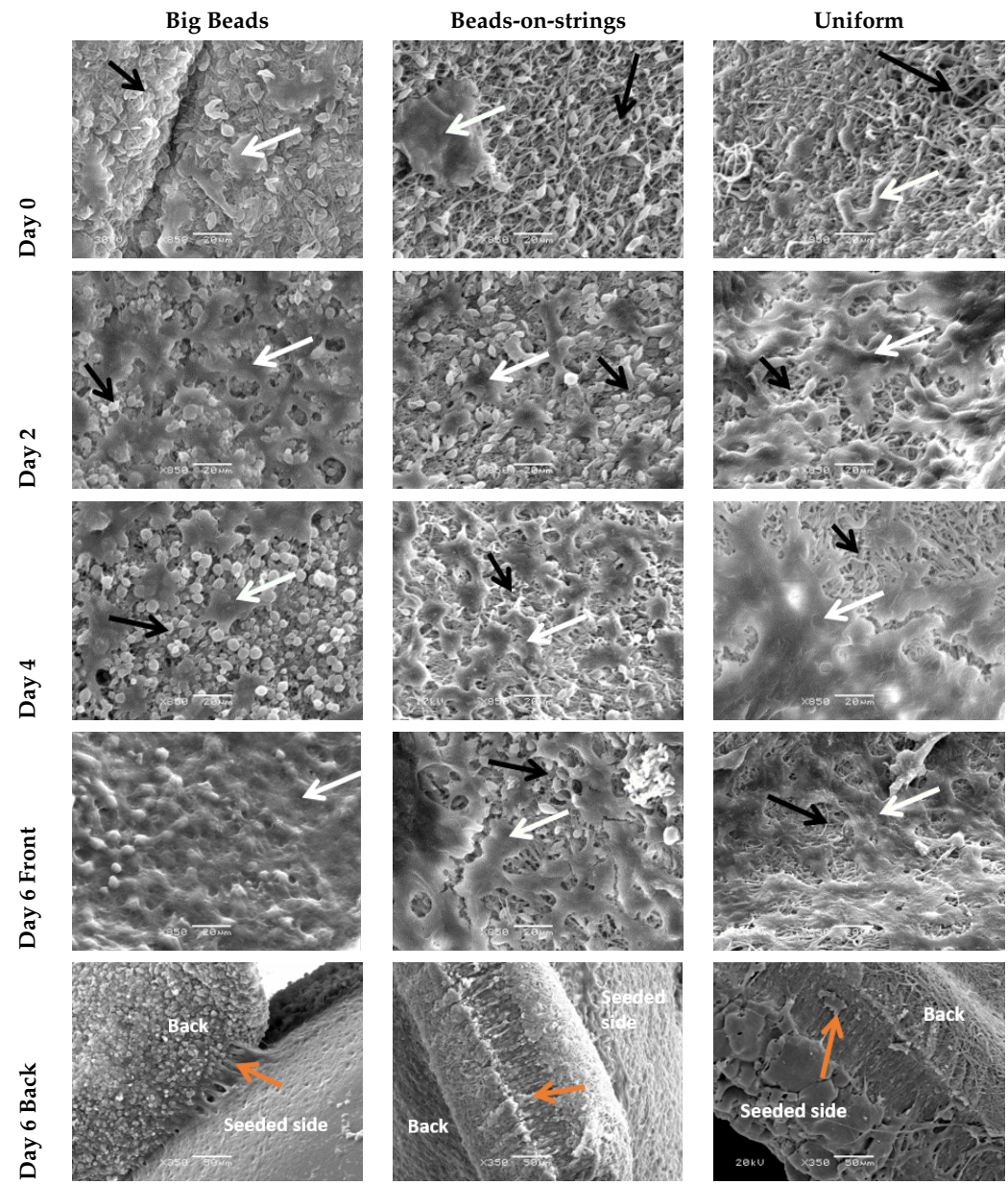



**Figure 3.10:** SEM images of fixed cells on different morphologies over 6 days proliferation. Complete cell coverage of the scaffolds surface was observed at day 6 for all morphologies. White arrows are part of the scaffolds fibre morphology, the black arrow indicate cells on the scaffolds and the orange arrows show cells moving from front to the back over the scaffolds etch. Scale bar first four rows = 20 μm and last row = 50 μm.

the number of beads in the scaffold. A previous study on PLLA fibres [242] showed that only polymer concentration had a significant impact on the extent of bead formation which is in contrast to the findings reported here. This could be due to the lower levels of polymer concentrations explored by Patra and colleagues (4 and 7 w/v% compared to 15 and 25 w/v% in this study), a difference in the solvent system used (DCM:DMF compared to Ac:DMF in this study) and the size of the DoE of only 30 runs (compared to 81 runs in this study). In this study, mean fibre diameter was mostly influenced by the applied voltage and the interaction between polymer concentration and flow rate. These findings are not fully in agreement with previous DoE studies. For example, Coles et al. [243] observed a significant impact of polymer concentration on the resultant PLA average fibre diameter with applied voltage and distance having much lower impact on the fibre diameters. However, their study excluded data from experiments which resulted in no fibre formation, thus reducing the range of morphologies considered by their model. Other studies using different polymers saw the same significant impact of polymer concentration on the fibre diameter with no significant impact of the voltage and flow rate/polymer concentration as. Again, this could be due to selected data sets being considered in the prior studies rather than the whole sets of fibres, including the 'imperfect' ones. Differences in the previous work include the exclusion of fibre defect formation [244, 245], using only visual observation as a measure of beading formation [246], not including flow rate in the DoE [246–248], not factoring in the difference in the characteristics of the polymers [244–246, 249, 250] and solvents used [248]. For example, Senthil and Anandhan [250] looked at the impact of polymer concentration, applied voltage and flow rate (µl/min) on the average fibre diameter of styrene-acrylonitrile copolymer (SAN) using DMF as solvent. Clearly, even if using a similar solvent (DMF to Ac/DMF in this study), the electrospinning of a polymer such as SAN with very different physical properties to the PDLLA in this study, would greatly affect the viscosity, conductivity and surface tension of the electrospinning solution. Therefore, this model has limited application to other polymer/solvent systems, due to the impact of solvent differences (such as, volatily, permittivity) and polymer characteristics (such as molecular weight) within the electrospinning system [98, 101, 111, 251]. However, this DoE model could be expanded with more parameters such as solvent

systems to investigate the impact further.

4D contour prediction plots were produced from the data generated in this study and from the observed interactions in the DoE model (see Figure 3.11). These prediction plots show that uniform fibres or fibres with a very small number of defects could be obtained with mean fibre diameters between 600 and 1000 nm when using the highest polymer concentration (25 w/v%; see Figure 3.11A). Fibre mats with a small number of beads per $\mu m^2$ were observed at the highest flow rate (5 mL/hr), at a PDLLA concentration of 25 w/v% and a collector plate distance of 20 cm (see Figure 3.11B-C). Although this resulted in more defects, these parameters generated scaffolds with the lowest mean fibre diameters (650-700 nm; Figure 3.11i). When defect-free fibres were apparent, the range of fibre diameters was found to increase to between 700-1000 nm (see Figure 3.11D). An increased number of beads will occur at high flow rates and low polymer concentrations, with the highest number of beads observed at very low or high voltages and larger collector plate to needle distances (see Figure 3.11B-C). Higher mean fibre diameters will be observed when using low applied voltages. When defect-free fibres are required, a compromise must therefore be made as the mean fibre diameter will increase, whilst for smaller fibre diameters a small number of defects are likely to occur (see Figure 3.11D, i-ii). It may therefore be appropriate to set tolerance limits for such beading defects with the knowledge that these will be unavoidable.

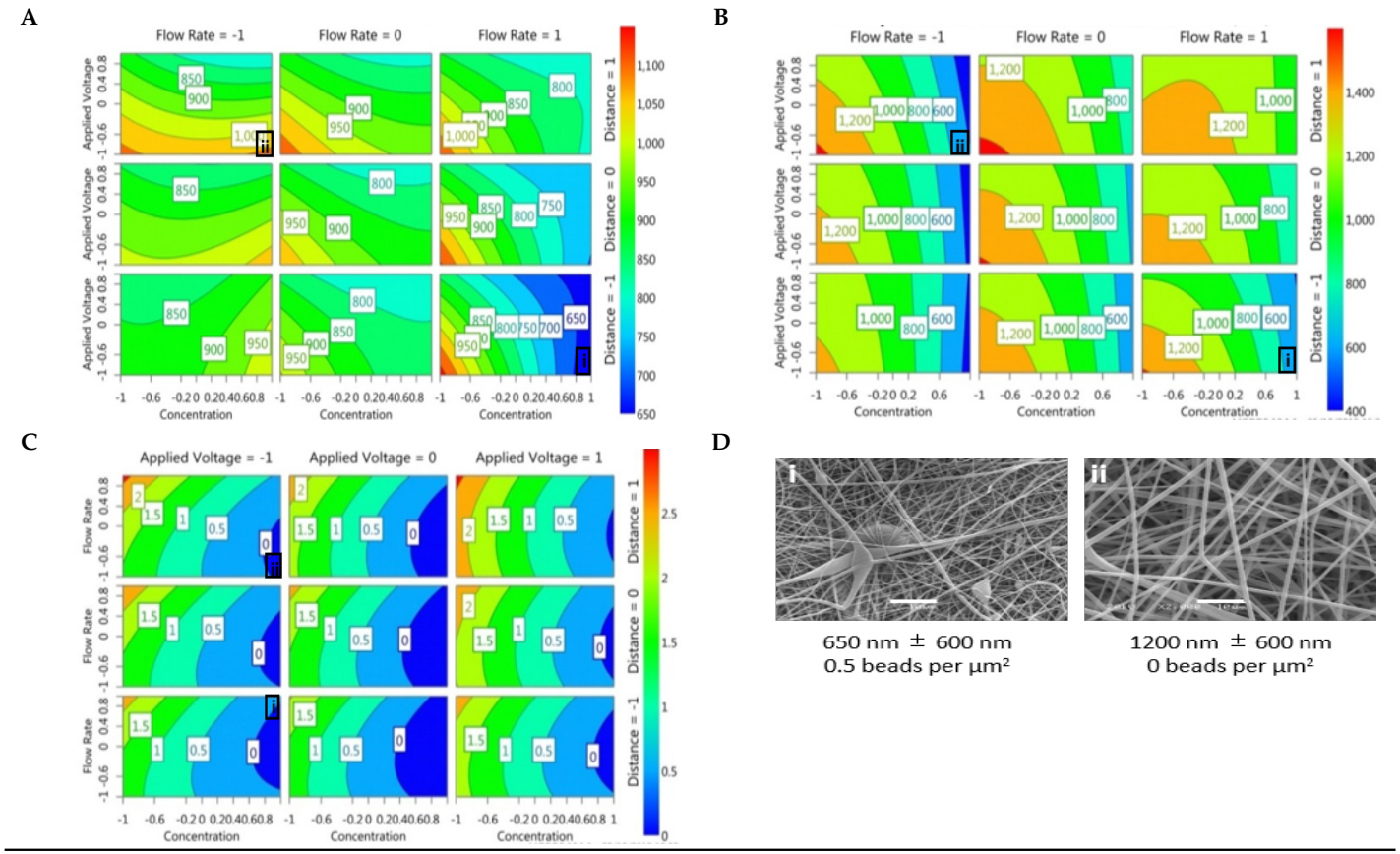



**Figure 3.11:** 4D contour predictions plots of **A)** mean fibre diameter, **B)** fibre morphology by standard deviation and **C)** number of beads per $\mu m^2$. Most significant impacting parameters are positioned in axes X and Y. Parameter values are concentration (1) 25 w/v%, (0) 20 w/v%, (-1) 15 w/v%; applied voltage (1) 25 kV, (0) 20 kV, (-1) 15 kV; flow rate (1) 5 mL/hr, (0) 3 mL/hr, (-1) 1 mL/hr and distance of collector plate from the needle (1) 20 cm (0) 17.5 cm, (-1) 15 cm. D) Contour plots show that if i) lowest fibre diameters are required some beading will occur. While ii) uniform fibres with small standard deviation will result in a higher mean fibre diameter.

## 3.5 Conclusion

A DoE model is an effective approach to identify the most significantly impacting parameters and the effects of parameter interactions on resultant electrospun PDLLA scaffold characteristics. Identifying these significant parameters can streamline optimisation experiments thus reducing the time spent on preliminary studies to find the required parameter combination for the desired fibres. By separating the morphological characteristics of the fibre scaffolds, it was clear that polymer concentration plays a vital role in influencing the final fibre morphology and extent of beading. Polymer concentration plays a more interacting role with the flow rate in terms of influencing fibre diameter. Applied voltage also had a significant effect on the fibre diameter, which confirms the importance of the formation of a stable polymer jet and Taylor cone during the electrospinning process. Matrix inversion on the regression equations as well as interpretation of the 4D contour plots (see Figure 3.11) reported by the DoE can be used as guidance to identify the most appropriate parameter combination for the desired scaffold morphology and fibre diameter. For example, when uniform fibres are required, high polymer concentrations and low (1 mL/hr) to medium (3 mL/hr) flow rates are recommended. Production of fibre mats composed of small fibres of $\leq 700$ nm in diameter will result in a small number of fibres exhibiting the 'beads-on-strings' morphology. In this way, these regression equations give the parameters needed to result in the desired fibre diameter and provide a valuable indication of expected bead formation, or avoidance, as well as morphology. Slight defects of the fibrous morphology of beads-on -strings did not result in a different response of the 3T3s cell proliferation. However, big beads significantly changed the scaffolds strength and WCA. Hereby, it can be concluded that small defects (beads-on-strings) within the scaffold will not result in a significant difference in cell attachment and proliferation.

# Chapter 4

# Thermo-responsive electrospun scaffolds and enzymatic-free passaging

## 4.1 Introduction

Current cell culture relies on the use of enzymes such as trypsin, collagenase and pronase to detach cells by the digestion of cell adherence proteins [148]. However, this results in damage of the cell membranes surface, which occurs through hydrolysis of membrane-associated protein resulting in apoptosis signaling due to membrane receptor damage [151, 252, 253]. Huang et al. [150] observed a significant up-regulation of cell death supporting proteins expression and a down-regulation of cell adherence/ proliferation proteins expression of the cells after the use of trypsin. This digestion-induced damage is very time dependent [254] and unsuitable for more enzymatic-sensitive cell lines such as RAW264.7 [255]. Over the last decade many studies have focused on developing an enzymatic-free detachment method through responsive materials, which maintains the cell viability and function after passaging [152–156]. The vast majority involves the use of thermo-responsive polymers to attach and detach

cells [157–163, 165, 256, 257]. The detachment of cells from thermo-responsive surfaces occurs due to changes in polymer chain hydration as the polymer under goes an sharp volume transitions from extended hydrophilic states at lower temperature to collapsed hydrophobic states when reaching across their Lower Critical Solution Temperature (LCST)[183] or visa versa when the polymer exhibits a Upper Critical Solution Temperature (UCST)[258, 259]. This transition is entropy driven and dependent on the solvent-interaction with the ratio of polar and apolar groups in the polymer structure. The progressive exclusion of the water solvent on reaching temperatures above its LCST creates an entropically driven hydrophobic self-association. For example, the is hydrophilic amides interacts with water molecules by van der waals interaction in cold conditions. However, when heated the hydrophobic collapsed backbone and isopropyl result in the interruption of these H-bondings in which the water molecules are released to the bulk solution and the polymer collapses and aggregates when in solution. This aggregation when in solution can be used to identify the thermo-responsive polymer's LCST or UCST. This is done by measuring the light transmittance of the thermo-responsive polymer in solution when heated. When the polymer reaches it's LCST or UPST the polymer will aggregate resulting in an cloudy solution, which reduces the light transmittance of the solution. The LCST or UPST can be estimated from this change of transparent to cloudy solution [260–262].

Poly(N-isopropylacrylamide) (PNIPAM) is the most commonly used thermo-responsive material. Achiha et al. [167] were the first to propose the use of the thermo-responsive material PNIPAM as a cell culture passaging substrate. PNIPAM has a LCST of 32°C, making the polymer hydrophobic at cell culture temperatures (37°C) and hydrophilic when cooled to temperatures lower than the LCST and is therefore suitable for cell culture and detachment. It is hypothesised that this hydration ruptures the cellular anchors (the ECM laid down by the cells onto the surface), this rupture results in cellular detachment in cell sheet formation [183]. This thermo-responsive cell sheet harvest has been observed to be less damaging for the cells and their ECM than enzymatic digestion and mechanical dissociation passage methods. For example, Canavan et al. [263] compared the removal of bovine aortic endothelial cells (BAEC) monolayer via three different methods; 1) thermo-responsive PNIPAM surfaces, 2) mechanical dis-

sociation and 3) enzymatic digestion. Immuno-assays after detachment showed non-destructive harvest of cell sheets and most underlying ECM when harvested via the thermo-responsive method, while damage of the cells and ECM were observed for both the enzymatic and the mechanical dissociation method [263]. Although, PNIPAM is commonly used, recent literature suggests possible cytotoxicity of the polymer [264]. Cooperstein and Canavan [264] investigated the cytotoxicity of the PNIPAM on four different cell types (endothelial, epithelial, smooth muscle and fibroblast cells). No cytotoxity was observed at low concentrations (below 5 mg/mL) and contact time (below 24 h). However, endothelial cells showed decreases of viability after 48 h exposure of the PNIPAM (above 5 mg/mL). This was explained as being due to the more sensitive cells reaction on impurities left from the PNIPAM synthesis. Besides the cytotoxicity of PNIPAM in solution other studies have suggested a toxic effect of PNIPAM's monomer to neural tissue. However, they observed no toxic effect when the polymerised to PNIPAM on cells or tissue. Therefore, toxicity seems to be highly related to impurities of the polymerisation or trashes of the monomer.As this study aims to develop a cell culture platform for the highly sensitive human corneal stromal cells, PNIPAM was considered unsuitable.

Poly (ethyl glycol) (PEG) based polymers are a promising alternative showing similar hydration effects when cooled under the LCST ( different depending on the length of the side brushes) [163, 256, 265–267]. For instance, Dey et al. [163] observed successful multiple passage cycles (10 cycles) without differentiation of mouse embryonic stem cells when cultured on poly ( methoxyethoxyethylmethacrylate-co-oligoethyleneglycol methacrylate) (poly(MEO(2)MA-co-OEGMA)) grafted glass slides. Voss et al. [256] also observed successful detachment of PaTu 8988t cells from the PEG based polymer poly(di(ethylene glycol) methyl ether methacrylate (PDEGMA) coated monolayer when cooled to 25°C for several minutes (LCST of 28°C). A recent study reported the cytotoxicity of PEG-based monomers mPEGMA-500 (IC50 values of 4.7 mg/mL for HeLa cells and 5.3 mg/mL for L929 cells) and mPEGA-480 (0.2 mg/mL for Hela cells and 0.1 mg/mL for L929 cells) [268]. No reports have been found of the toxicity of PDEGMA's monomer, as well as, previous research in our group has demonstrated no cytotoxic response to the PDEGMA polymer[269]. Therefore, PDEGMA was consid-

ered as a suitable thermo-responsive polymer for this study.

A significant challenge in bioengineering is translating phenotypic control of the cell by substrate chemistry into a 3D platform. This might be achieved through innovative manufacturing methods, such as 3D-printing, topographic patterning, microparticles and electrospun fibres. However, most of the thermo-responsive polymers studies are based around a deposited polymer in thin layers on a 2D TCPS surface [154, 157, 158, 163, 164, 183, 219], which shows no similarities with the ECM structure within the body, as the native ECM is a 3D mesh of instructive cues. Only a few studies have focused on the incorporation of 3D topographic features with thermo-responsive properties [159, 219, 270]. For example, Tsai et al. [161] reported successful detachment of confluent NIH3T3 fibroblast sheets from electrospun PNIPAM microgel patterned polystyrene (PS) substrates. Oh et al. [271] also observed detachment of human fibroblast from PNIPAM-grafted nanofibres, while PNIPAM-grafted PS dishes showed decreased detachment. Moreover, the nanofibrous structure not only resulted in cell detachment but also enabled improvement of the fibroblast attachment, spreading and cell growth. For these reasons, an electrospun fibrous scaffold with incorporated PDEGMA thermo-responsive polymer was investigated in this study, which combines the benefits of a 3D environment, including increased cell adherence and non-invasive cell detachment. The thermo-responsive polymer behaviour is used to detach the cells from these electrospun scaffolds.

This chapter is focused on the production of thermo-responsive electrospun scaffolds and their ability to adhere and proliferate 3T3 fibroblast cells. The thermo-responsive change of hydrophilicity of PDEGMA when cooled will be used to detach the 3T3 fibroblast cells from the 3D structure when confluent (see Figure 4.1).

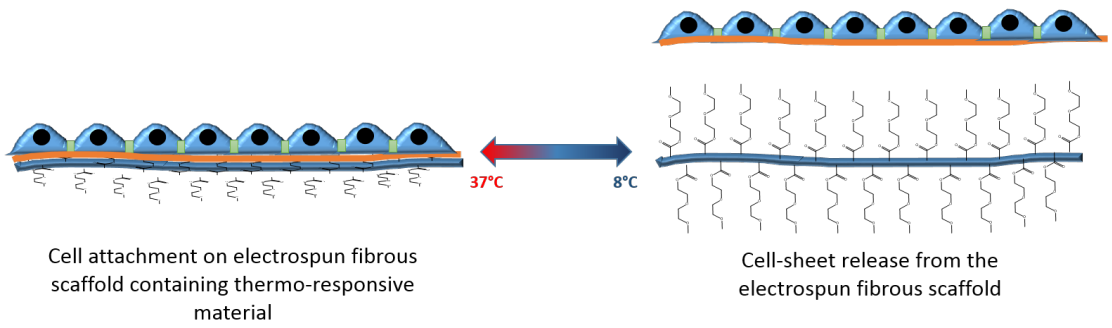



**Figure 4.1:** Schematic of thermo-responsive fibres and the effects on cell attachment and detachment.

## 4.2 Aim and Objectives

The aim of the study presented in this chapter is the preparation of thermo-responsive electrospun scaffolds and to investigate their application as supports for a cell culture platform with enzymatic-free passage of 3T3 fibroblasts (3T3s).

This was achieved through the following objectives:

1. The synthesis of poly(di(ethylene glycol) methyl ether methacryalate (PDEGMA).
2. The preparation of different concentration PDEGMA and PDLLA electrospun scaffolds.
3. Investigation of the attachment and detachment of 3T3 fibroblasts on different wt% PDEGMA containing electrospun scaffolds.
4. Identification of the concentration needed of thermo-responsive PDEGMA in scaffold, resulting in the best adherence, proliferation and detachment of 3T3 fibroblasts.
5. The synthesis of fluorescent labeled PDEGMA, poly(di(ethylene-glycol) methyl

ether methacrylate)-2-methyl propanoyl)oxy]ethoxy)ethyl)-perylene-3,4,9,10 -tetracarboxylic acid bisimide (PBI-PDEGMA).

6. Investigation of the distribution of the PBI-PDEGMA within the scaffolds and the 3T3 fibroblast behaviour.

7. Investigation of the influence of fibre diameter on the thermo-responsive passage behaviour.

## 4.3 Experimental methods

### 4.3.1 Polymer synthesis

The thermo-responsive polymer poly(di(ethylene glycol) methyl ether methacrylate (PDEGMA) and poly(di(ethylene-glycol) methyl ether methacrylate)-2-methyl-propan oyl)oxy]ethoxy)ethyl)-perylene-3,4,9,10-tetracarboxylic acid bisimide (PBI-PDEGMA) were synthesised by RAFT and ATRP polymerisation respectively, see methods section 2.5.2 and 2.5.3. Polymer structures were determined by $H^1$-NMR and $C^{13}$-NMR (see method section 2.3.1). Molecular weights were measured using GPC (see method section 2.3.2) and thermo-responsive behaviour was determined by cloud point measurements (see method section 2.3.4).

### 4.3.2 Blend electrospun scaffolds fabrication

PLA polymer was blend electrospun with PDEGMA or PBI-PDEGMA in different weight percentages (2.5, 5, 10, 15 and 20 wt%, see method section 2.2.2). $^1$H-NMR (see method section 2.3.1) was performed to confirm wt% present in resultant fibres as well as to observe any trace of the toxic electrospun solvent DMF used during the electrospinning process.

### 4.3.3 Blend electrospun scaffold characterisation

Scaffold morphology was analysed using SEM (see method section 2.4.1). Average FD and SD were calculated using ImageJ software (see method section 2.4.2). Static and hysteresis WCA were analysed, as well as a static WCA of 40 s time period to determine the thermo-responsive behaviour of the scaffolds, see method section 2.4.4.

### 4.3.4 PBI-PDEGMA distribution studies

Confocal imaging was performed to analyse the distribution of the fluorescent labeled PBI-PDEGMA in different wt% of the blend electrospun scaffolds (2.5, 5, 10, 15 and 20 wt%), see method section 2.8.3.

### 4.3.5 Cell distribution studies on the PLA/PBI-PDEGMA scaffolds

Red fluorescent expressing 3T3s (p=74) were seeded at 60 000 cells/ml on the different wt% scaffolds (n=3 per different wt% scaffolds) and cultured for 7 days , see method section 2.7.6. Cells were fixed at day 7 (see method section 2.8.2) and cell nuclei were stained with Hoechst (see method section 2.8.2). Fixed and counter-stained cells distribution on the scaffolds were analysed using confocal imaging, see method section 2.8.3.

### 4.3.6 Cell proliferation and detachment studies

Red fluorescent expressing 3T3s (p=74) were seeded at 60 000 cells/ml onto the scaffolds (n=12 scaffolds per different morphology, see method section 2.7.6), proliferated for 7 days and cell numbers at different time points were calculated with the use of Alamar blue assays on 6 of the 12 scaffolds (see method section 2.7.6). The other 6 scaffolds were used for detachment studies at day 6. Scaffolds were imaged using confocal imaging (see method section 2.8.3) in PBS at 37°C, subsequently cells were detached (see method section 2.9.1) and imaged again using confocal imaging. Cells left

attached on the scaffolds and detached cell numbers were calculated with the use of Alamar blue assay and percentage detached were calculated, see method section 2.7.6 and 2.9.1. See schematics of experimental timeline in Figure 4.2.

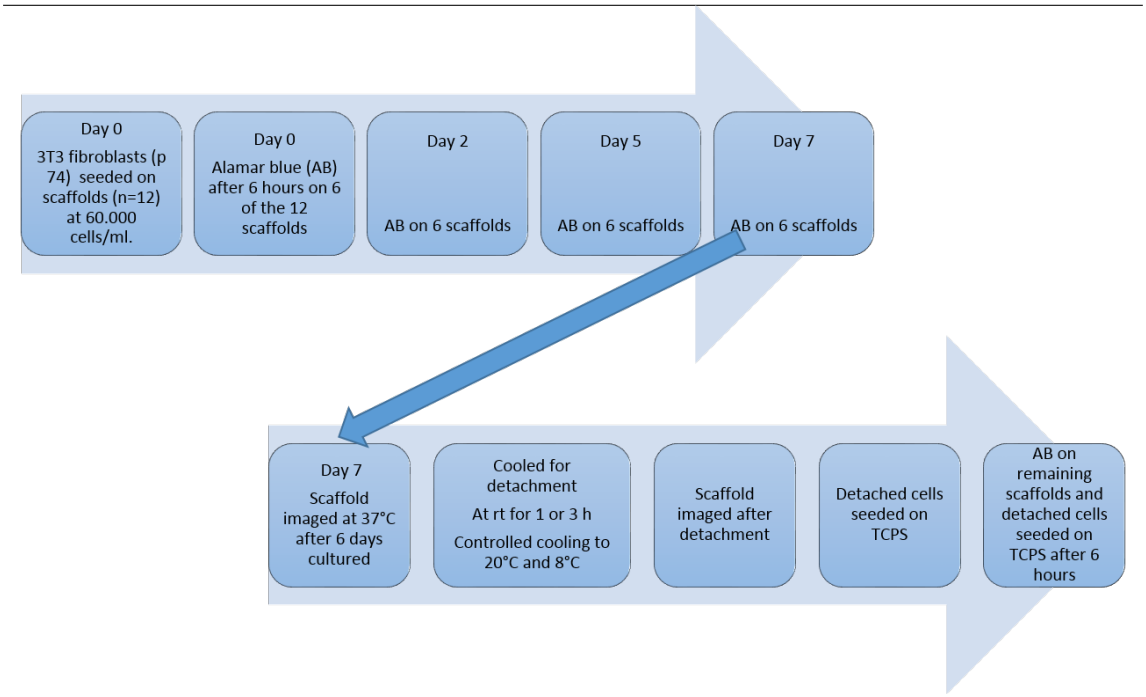



**Figure 4.2:** Schematic representing the Alamar blue (AB) and cell detachment experimental timeline for cultured 3T3 fibroblast cells over 6 days on the different electrospun fibre morphology scaffolds (n=12 per different scaffold).

## 4.4 Results and Discussion

### 4.4.1 PLA/PDEGMA blend electrospun scaffolds

The thermo-responsive polymer PDEGMA was successfully synthesised and characterised by $^{1}$H-NMR, C$^{13}$-NMR and 2D-NMR (see Figure S2, S3 and corresponded peaks section 2.5.2). The Lower Critical Solution Temperature (LCST) was estimated by measuring the cloud point of the polymer in aqueous solution (see method section 2.3.4). The purified polymer after synthesis was dissolved in an aqueous solution and heated

to 60°C. The solution became cloudy as the polymer chains associated above LCST and formed aggregates, whereas cooling the solution resulted in a phase change to a transparent solution. A difference in cloud point was observed with a LCST of 28°C when heated and shifted to 20°C when cooled (see Figure 4.3A). This observed difference in cloud point from heated to cooled and cooled to heated (also known as the cloud point hysteresis) is a commonly observed phenomenon, which is driven by the rate of aggregate formation or deformation and is temperature, concentration and time dependent [256, 257, 272]. For example, previous studies on the kinetics of the dissolving and resolving of PiPAAm/water solution show a reversible molecular change if the temperature remains less than ca 6-8°C above the LCST for less then a few minutes [273]. However, when left at higher temperatures for a longer time, the deformation time of the formed polymer aggregates increases significantly [274].

The thermo-responsive fibrous scaffolds of PLA with PDEGMA were fabricated. The obtained PDEGMA was blend electrospun with PLA in different wt% PDEGMA (2.5 to 20 wt%) to PLA (25 w/v%) in Ac:DMF (1:1). See Table S2 and Figure 4.6 for optimum parameters and corresponding fibre SEM images of different wt% PDEGMA to PLA scaffold formation. $^{1}$H-NMR spectra confirmed percentage of PDEGMA to PLA as well as no traces of the toxic solvent DMF observed after electrospinning (see $^{1}$H-NMR spectra Figure S33). To investigate the thermo-responsive behaviour of the scaffolds water contact angle measurements were performed (see method section 2.4.4). A water contact angle (WCA) of below 90° can be identified as a surface with hydrophilic properties. Scaffolds were heated to 37°C and cooled to rt (as well as the WCA liquid) and WCAs were measured upon contact of the drop with the scaffolds' surface. Thermo-responsive behaviour was observed for scaffolds containing 10 to 20 wt% PDEGMA (see Figure 4.3B). However, no significant difference was observed between the wetting behaviour as a proxy for polymer phase transition behaviour between scaffolds of 10 to 20 wt% PDEGMA. When measuring the WCA over a period of 40 s (temperature was left constant at rt, 20°C), a change in WCA was observed on scaffolds with 10, 15 and 20 wt% PDEGMA (see Figure 4.3C and supplementary data Table S3). The time studies demonstrated difference in the WCA droplet shape on the different scaffolds (see Figure 4.4). As discussed in chapter 3, topographic roughness has a significant in-

fluence on surface wettability [229–233]. Two different wetting transitions can occur on a rough topographic surface when measuring the WCAs, which occur due to air being trapped between the topography and droplet (Cassie state). These two wetting transitions are as follows; 1) the bottom of the droplet is pinned and the drop falls in between the topography while keeping its round shape, or 2) the droplet is de-pinned and displaced laterally [229]. The first wetting transition was observed for the scaffold with 15 wt% PDEGMA, while the second transition was observed for the scaffolds with 10 and 20 wt%. Therefore, the topography of the electrospun scaffolds has an impact on the resulting WCA. To reduce this topographic effect, WCA hysteresis measurements were performed. This is done by measuring the difference between an advancing and reducing waterdrop on the surface of the scaffold (see method section 2.4.4). A significantly higher hysteresis was observed for the 20 wt% PDEGMA scaffolds (see Figure 4.3D). Smaller hysteresis was observed for all other PDEGMA concentrations, while the PLA on its own showed the lowest hysteresis. This gives an indication that the thermoresponsive polymer concentration in the fibres changes the wettable behaviour of the scaffolds. This could be due to insufficient PLA to PDEGMA distribution resulting in difference of surface chemistry. This results in macroscopicpatches of high WCA and others with low WCA, which subsequently increases the hysteresis. In case of the 20 wt% scaffolds loss of droplets was observed while trying to measure the reducing WCA, due to very hydrophilic macroscopicpatches of scaffold (see Figure S34). This uneven distribution probably occurred during the electrospinning process. When a mixture of polymers are blend electrospun, heterogeneity of the polymer solution has a significant impact on the distribution of the polymers within the formed fibres of the scaffold. The brush like structure of the PDEGMA may hinder even mixing of the polymer within the electrospinning solution, resulting in uneven distribution when electrospun.

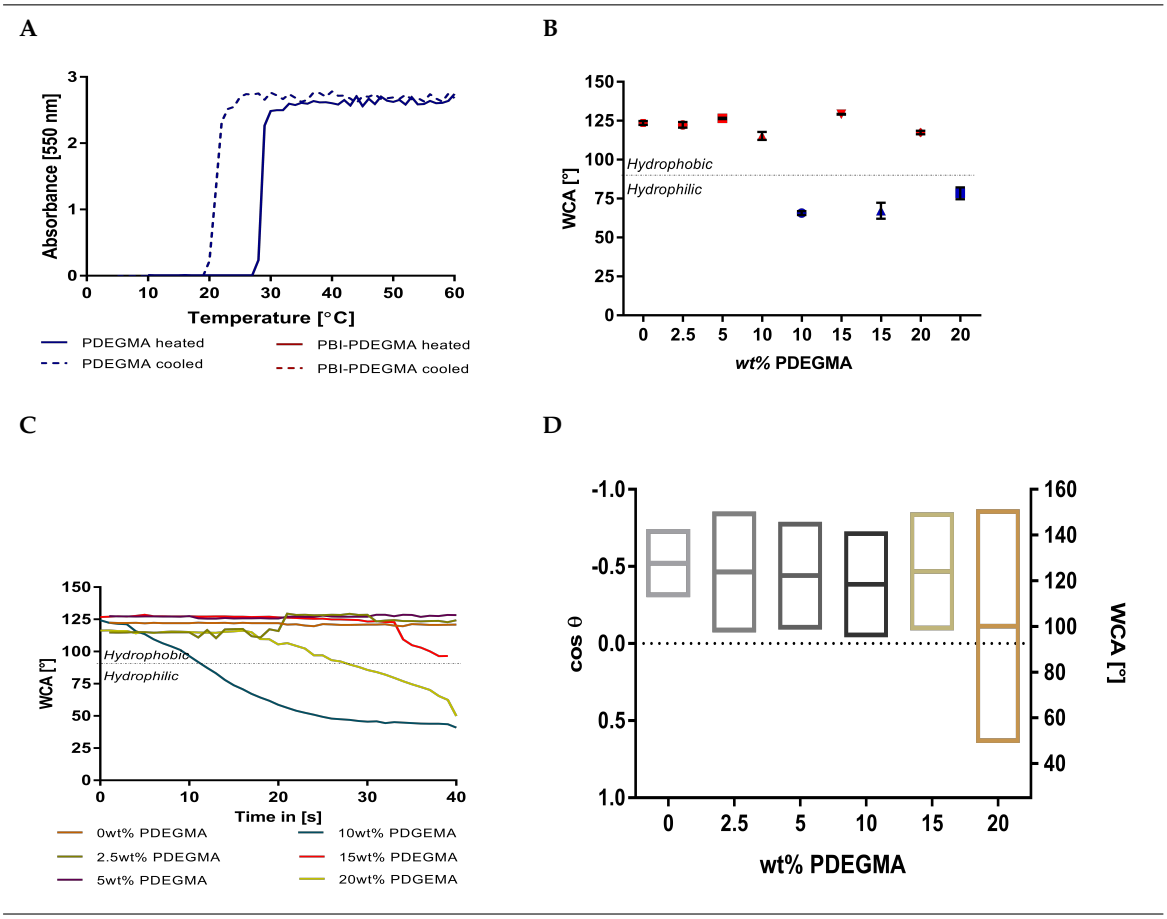



**Figure 4.3: A)** Cloud point hysteresis of PDEGMA and PBI-PDEGMA and WCA **B)** static analysis, **C)** static WCA over 40 s and **D)** WCA hysteresis of PLA with different wt% PDEGMA scaffolds. Error bars = SD.

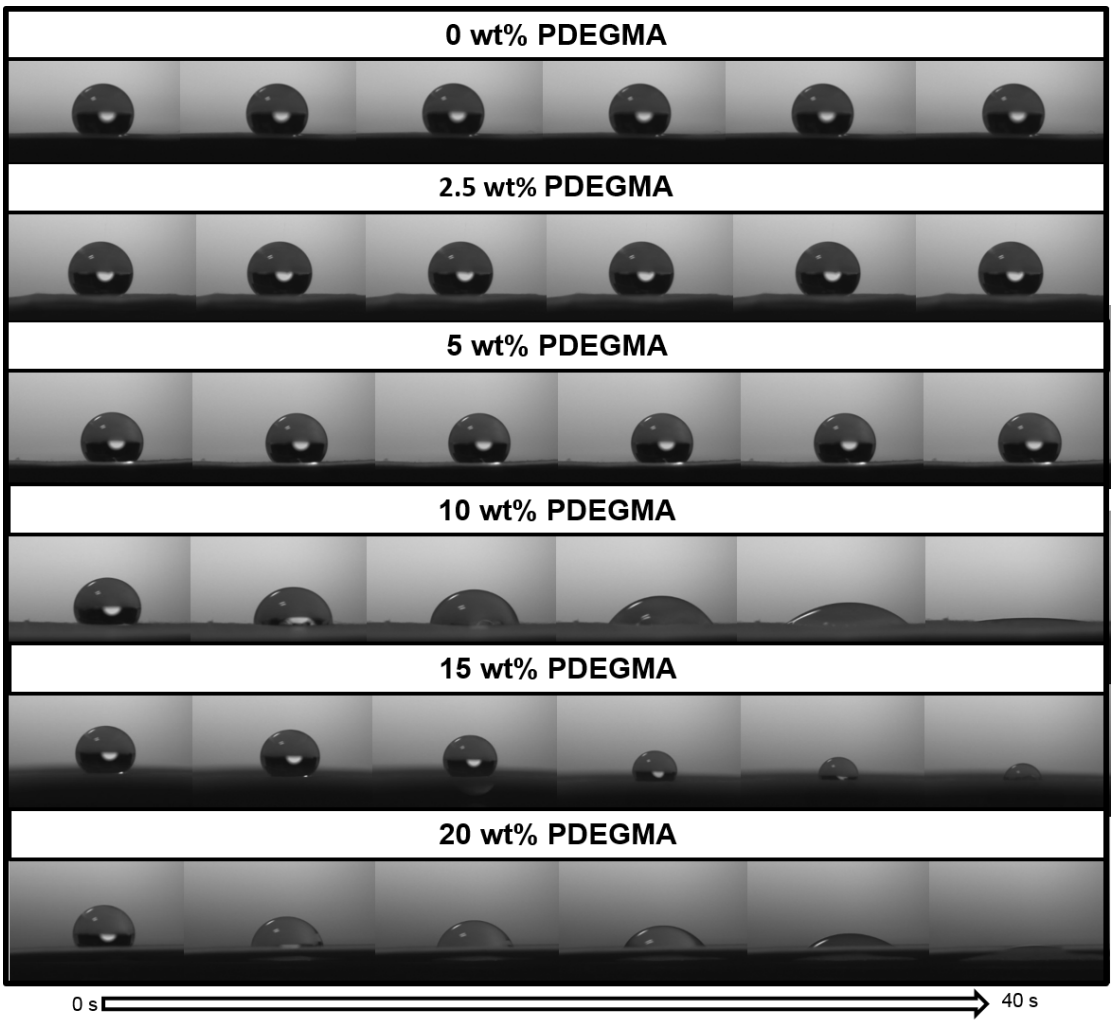



**Figure 4.4:** WCA images of changing WCA over time (40 s) at higher concentration of wt% PDEGMA present in the scaffolds.

**Table 4.1:** Mean fibre diameter and standard deviation for PLA with different wt% percentage PDEGMA or PBI-PDEGMA scaffolds.

| | PDEGMA | | PBI-PDEGMA | |
|---|---|---|---|---|
| **%** | **Mean fibre diameter [nm]** | **SD [nm]** | **Mean fibre diameter [nm]** | **SD [nm]** |
| **0** | 870 | 348 | 789 | 219 |
| **2.5** | 834 | 755 | 729 | 385 |
| **5** | 899 | 740 | 863 | 688 |
| **10** | 759 | 402 | 853 | 678 |
| **15** | 1032 | 393 | 811 | 385 |
| **20** | 1228 | 758 | 857 | 338 |

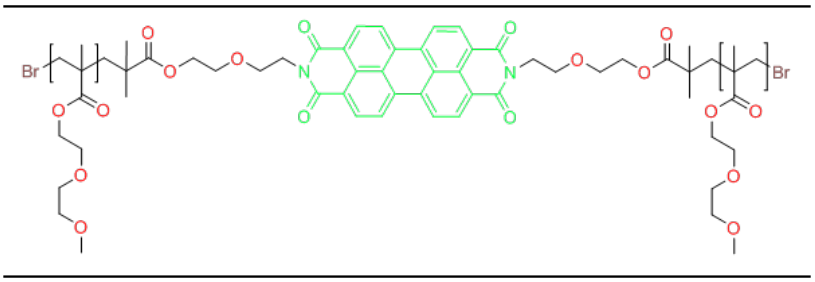



**Figure 4.5:** PBI-PDEGMA chemical structure, part of structure that causes the fluorescence response is coloured green.

### 4.4.2 PDEGMA distribution study

To test this hypothesis of uneven distribution of the PDEGMA in the scaffold a fluorescent labeled poly(di(ethylene- glycol) methyl ether methacrylate)-2-methylpropanoyl) oxy]ethoxy)ethyl)perylene-3,4,9,10-tetracarboxylic acid bisimide (PBI-PDEGMA, Figure 2.2) was synthesised. The linear asymmetric structure of the PBI-PDEGMA polymer was considered preferable, due to the small difference in structure of the fluorescent labeled PDEGMA to the original PDEGMA structure (see Figure 4.5). This is essential to avoid difference in behaviour during the electrospinning process, such as viscosity and electrospinning solution homogeneity. The original ATRP polymerisation [275] was performed at 45°C. However, this was observed to be unsuitable due

to low conversion rates of 22% (see Figure S35) and high molar mass distribution of 5.2 (see Figure S36). The method was optimised to 60°C, which resulted in a significantly higher conversion of 60% after 4 h (see Figure S35). GPC analysis showed a significantly lower molar mass distribution of 2.2 for PBI- PDEGMA (60°C) compared to the PBI-PDEGMA (45°C, see Table 4.2). Lower Mn and Mp were observed for PBI-PDEGMA ( 60°C) compared to the PDEGMA polymer. However, due to the lower PD and average molecular weight nearer to the PDEGMA Mw, PBI-PDEGMA (60°C) the polymer was concluded to be suitable for the distribution studies. Fluorescence intensity studies of the PBI-PDEGMA (60°C) in water indicated high fluorescence intensity (9000 a.u.) in the low blue-green range (425-510 nm), while lower intensities (90 a.u.) were observed in the green to far red range (510-700 nm, see supplementary data Figure S37 and method section 2.3.5). PBI-PDEGMA (60°C) was successfully blend electrospun with PLA at different wt% at the same electrospinning parameters used for PLA with PDEGMA scaffolds (see Table S2 and Figure 4.6). Fibre diameters of the 2.5 to 20 wt% PBI/PDEGMA to PLA were observed to be in a similar range to the PDEGMA scaffolds, between 750-1000 nm (see Table 4.1). However, some defects were observed. As discussed in chapter 3 small defects did not result in a significant difference in the proliferation of the 3T3 fibroblast and were therefore considered acceptable within the fibrous structures. Confocal imaging at 488 nm of the blend electrospun PLA with PBI-PDEGMA (60°C) showed even distribution of the PDEGMA throughout the fibres from 10 wt% PBI-PDEGMA (60°C).

**Table 4.2:** GPC data of PDEGMA, PBI-PDEGMA (45°C) and PBI-PDEGMA (60°C) in DMF.

| Polymer | Mn [kDa] | Mp [kDa] | Mw [kDa] | Đ |
|---|---|---|---|---|
| **PDEGMA** | 41 | 27 | 44 | 1.7 |
| **PBI-PDEGMA (45°C)** | 73 | 44 | 277 | 5.2 |
| **PBI-PDEGMA (60°C)** | 15 | 13 | 31 | 2.2 |

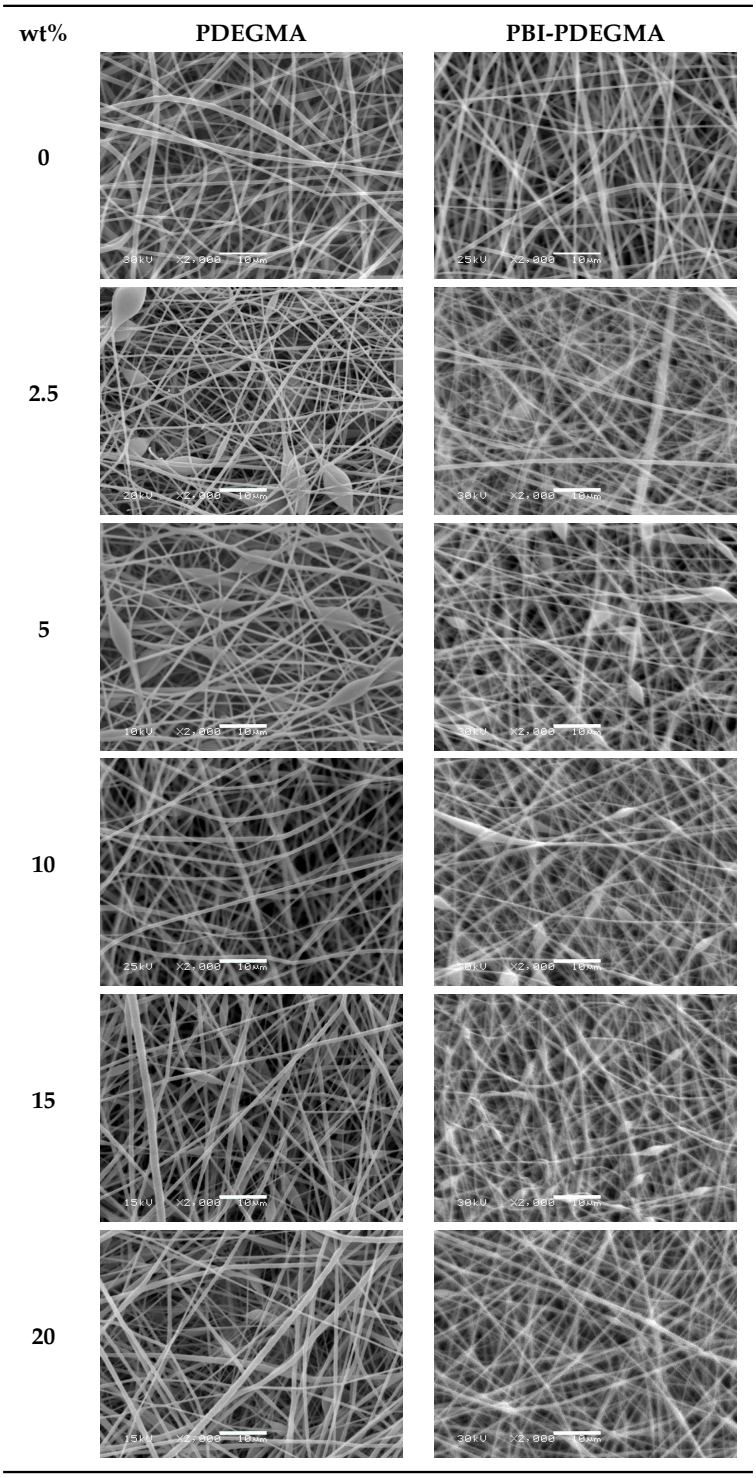



**Figure 4.6:** SEM images of different wt% percentage PDEGMA or PBI-PDEGMA.

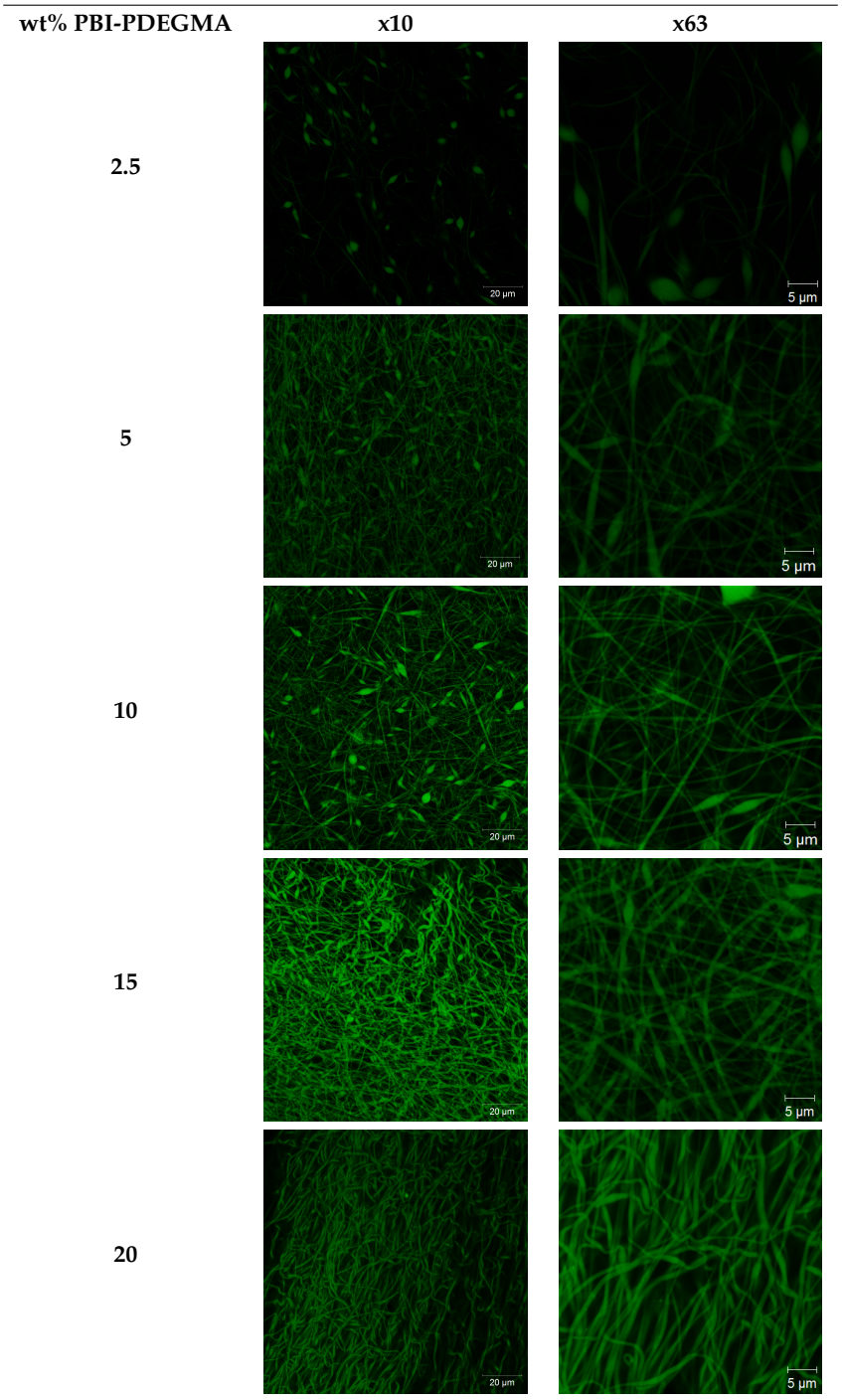



**Figure 4.7:** Representative confocal imaging of different PBI-PDEGMA percentage to observe PDEGMA distribution in the electrospun scaffolds. Imaging taken with 488 nm filter channel. Scale bar for x10 and x63 = 20 µm and 5 µm respectively.

However, at the lowest concentration the PBI-PDEGMA (60°C) was contained in the beads within the fibrous beads-on-string structures, which explains the higher WCA observed for these scaffolds (135° compared to 110° for 10 wt% and higher, see Figure 4.3B). Therefore, even coverage of the PDEGMA within the blend electrospun fibres is concentration and fibre morphology dependent and shows even distribution at concentration above 10 wt%. The observed hysteresis of the WCA is therefore highly unlikely due to the heterogeneity of the PDEGMA but is more topography dependent.

### 4.4.3 3T3 proliferation and detachment studies

Genetically modified red fluorescent protein (RFP) expressing 3T3 fibroblast cells were successfully cultured on the different PDEGMA and PBI-PDEGMA scaffolds for 7 days (see Figure 4.9A and supplementary data Table S4). Lower cell numbers were observed for scaffolds with more then 10 wt% PBI-PDEGMA (see Figure 4.9A), indicating possible cytotoxicity of the PBI-PDEGMA at higher concentrations. Confocal images of scaffolds with PBI-PDEGMA (60°C) observed background fluorescence from the PBI-PDEGMA polymer in the red channel (561 nm). However, when channels were overlapped the cells were easily identified. Images showed no change of cell morphology and large patches of cell attachment on the PBI-PDEGMA (60°C) containing scaffolds, while clusters of cells were observed on the PLA controls. Increased cell spreading was observed for all PBI-PDEGMA containing scaffolds, however no complete coverage was observed. This could be due to the hydrophobic nature of the PLA polymer in the electrospun scaffolds, resulting in difference in cell adherence protein attachment and subsequently cell adherence to the scaffold [276]. Hydrophilic surfaces promote sufficient cell adherence proteins from the media and result in better cell distribution attachment. The presence of the PDEGMA or PBI-PDEGMA in the scaffolds results in a decrease of hydrophobic, resulting in increased protein adherence and therefore increased cell adherence and distribution on the scaffolds.

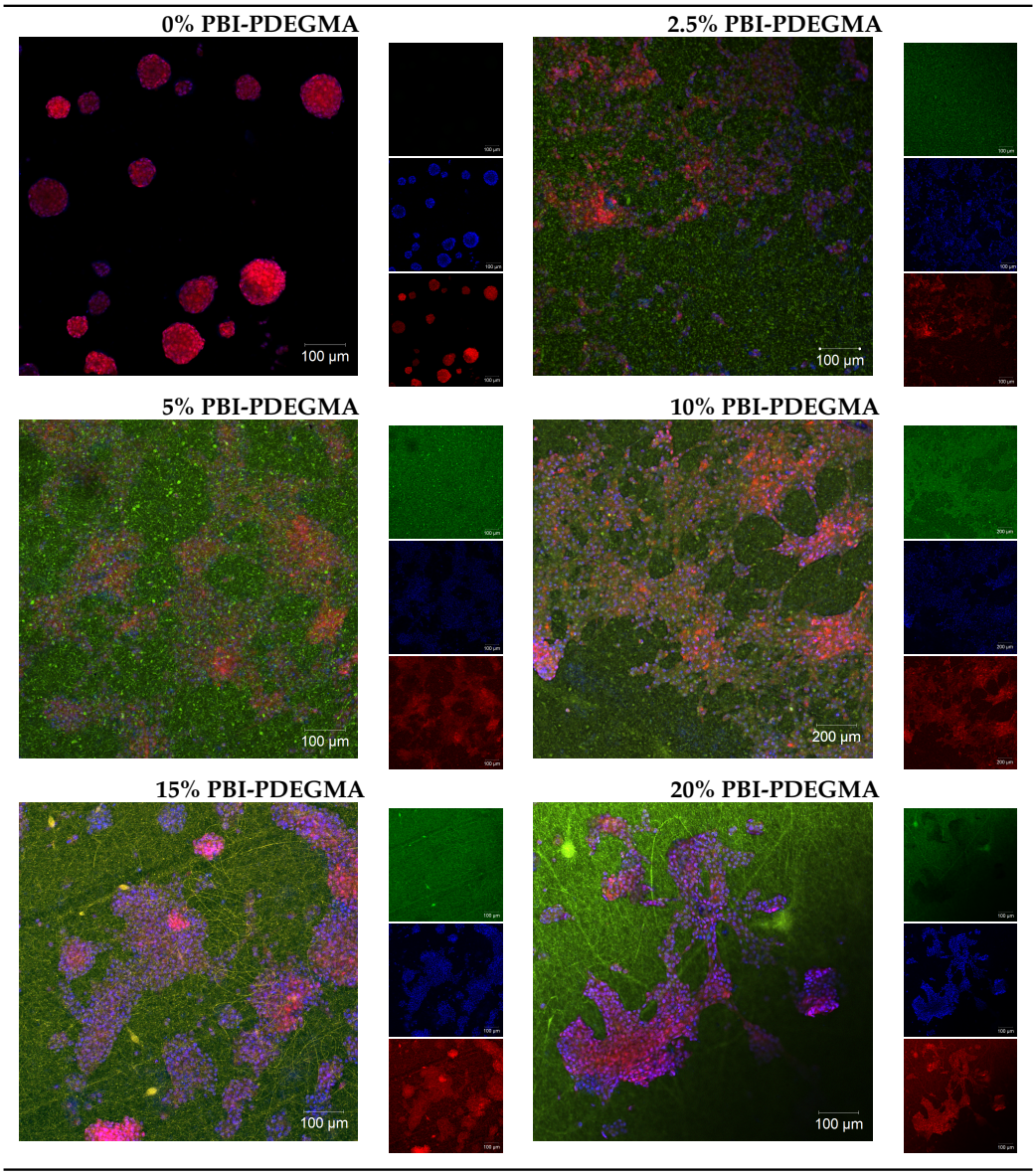



**Figure 4.8:** Representative confocal images of cell growth distribution on different PBI-PDEGMA containing electrospun scaffolds. Cell nuclei stained with Hoechst and genetically modified 3T3 fibroblast with red fluorescent protein expression. Scale bar = 100 µm. (better contrast images can be found in the electronic version.)

To investigate the thermo-responsive passaging abilities of the fibrous scaffolds, scaffolds at day 0, 2, 5 and 7 of cell culture were cooled for 1 h at rt (20°C). The number of cells on the scaffolds before and after thermal cycling above and below the PDEGMA's phase transition temperature were calculated by Alamar blue assay. No significant cell detachment was observed for scaffolds with 2.5 and 5 wt% PDEGMA for all days, which correlates with the uneven distribution of the PBI-PDEGMA observed (see Figure 4.9B and supplementary data Table S5). Significant detachment was observed at day 2 and 7 for 10 and 15 wt%; and 10 and 20 wt% respectively(see Figure 4.9B); indicating insufficient detachment for most scaffolds. Therefore, a time dependent study was performed. Scaffolds were cooled for 1 or 3 h at rt or cooled at a controlled 1°C/min till reaching 20°C. As the initial detachment study showed no significant difference in percentage detached from scaffolds with 10 to 20 wt%; 10 wt% PDEGMA PLA scaffolds were taken forward for all other thermo-responsive studies. Percentage of detached cells (day 7 of cell culture) for passages at 1 or 3 h at room temperature (20°C) and controlled cooling were calculated. Less cell detachment was observed after 3 h (approx. 15%), while only 25% of cells were observed detached from the scaffolds when cooled to rt for 1 h (see Figure 4.10A) Even less detachment of max 5% was observed when cooled in a controlled temperature change of 1°C per minute to 20°C in the -80°C freezer (stored in a freezing container with IPA for controlled cooling). This indicates that leaving the scaffold for a longer time or exposure to colder environments does not increase their thermo-responsive cell detachment behaviour and may have a negative effect on the cell metabolism, due to increased stress on the cells inducing metabolic changes. Therefore, detachment in cold conditions should neither take too long nor be performed at too low temperatures (around 0°C) [94]. This finding concludes that best cell detachment was observed at shorter times (1 h). However, a higher percentage of cell detachment is preferable.

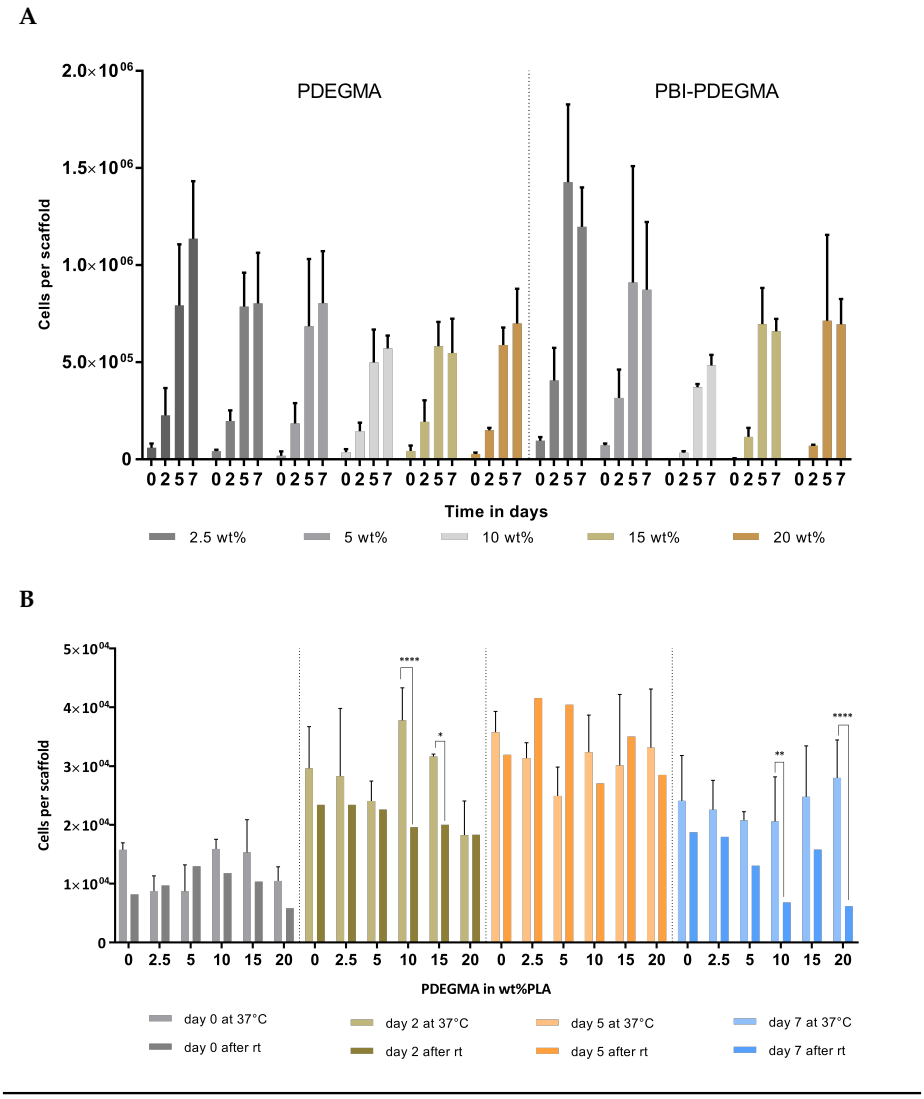



**Figure 4.9: A)** Cell proliferation on PDEGMA/PLA and PBI-PDGEMA/PLA containing electrospun scaffolds over 7 days on different wt% PDEGMA and different wt% PBI-PDEGMA compared to control of 10 wt% PDEGMA. **B)** Cell detachment at different days for different concentration PDEGMA. (n=3 scaffolds, two-way ANOVA, *=<0.05, **=<0.01, ****=<0.0001, error bars=SD).

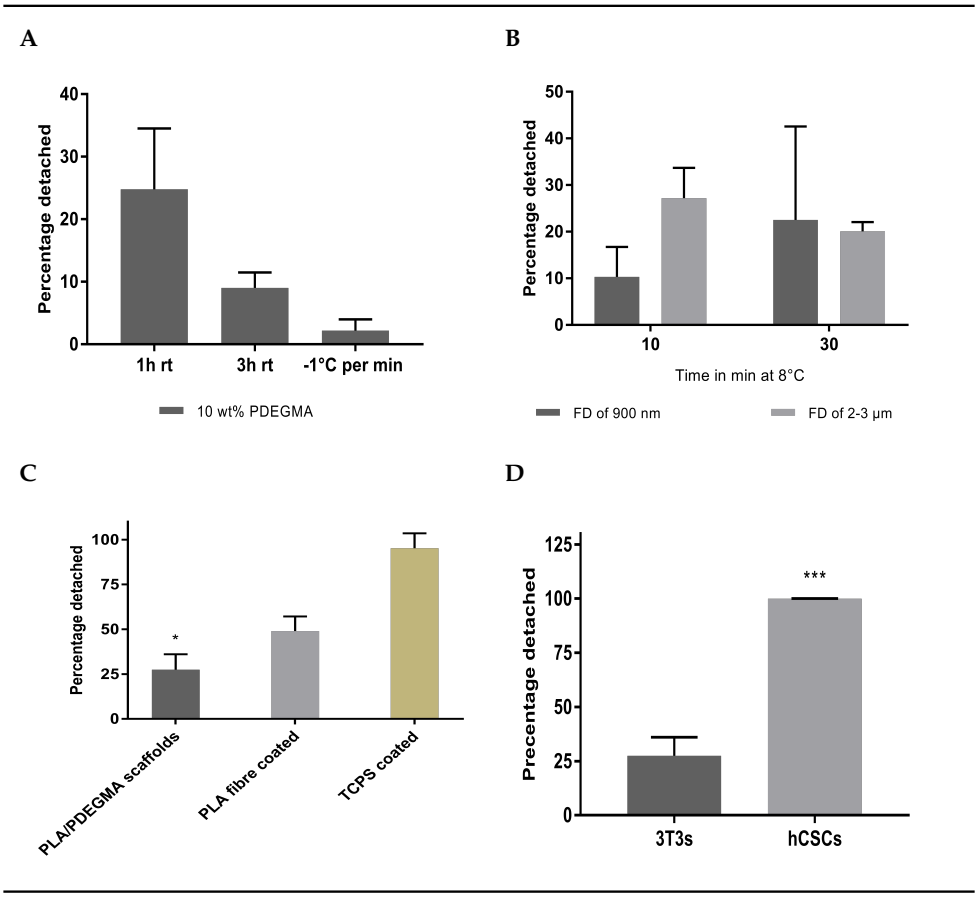



**Figure 4.10:** Percentage of cell detachment at **A)** 1 and 3 h at rt (20°C) or control cooling conditions. **B)** cells cultured on two different fibre diameters and **C)** cultured on coated PLA scaffolds with PDEGMA, blend scaffolds PLA/PDGEMA and PDEGMA coated on 2D tissue culture (TCPS) plastic. **D)** 3T3 fibroblasts (3T3s) vs human corneal stromal cells (hSCSs) percentage detached. (n=3 scaffolds, two-way ANOVA Tukey's multiple comparison for A and B, on-way ANOVA Tukey's multiple comparison for C and unpaired t-test for D. *=<0.05, ***=0.001, error bars=SD)

Confocal imaging of the scaffolds in suspension showed small clusters of cells detached from the scaffolds after cooling (see Figure 4.12). Previous research within the group [269] observed significant detachment of 3T3s of PLGA 10 wt% PDEGMA scaffolds when cooled for 10 mins at 8°C. Cells were observed to detach in sheets, due to the cell adherence between the cells not being disrupted during the thermo-responsive method [263]. This differs from the current finding, which could be due to the differ-

ence in cell interaction with the scaffolds surfaces, due to the difference in base polymer of PLA to PLGA in the previous study. The cells show a patching morphology on the scaffolds surface, see Figure 4.12, which could result in small cells cluster detached instead of a cell sheet. Besides difference in cell behaviour on the scaffolds, the previous study has differences in fibre diameter used (2-3 µm to 900 nm in this study), cell seeding number (100.000 cells/ml to 60.000 cells/ml in this study) and different passage method (10 mins at 8°C to 1 h at rt in this study). Therefore, another possible reason for the low detachment observed on the scaffolds may be the lower FD used (900 nm), giving the cells more surface anchor point to hold on to resulting in lower detachment [277] (see Figure 4.11 for schematic description).

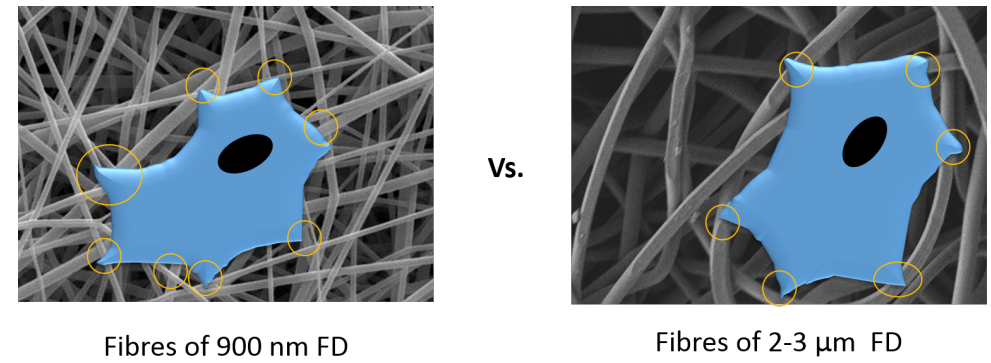



**Figure 4.11:** Schematic example of cell adherence to fibrous scaffolds of different fibre diameters. Fibre diameters of 900 nm results in many more anchor points for the cell to hold on to, while larger fibre diameters result in less anchor points for the cells to attach.

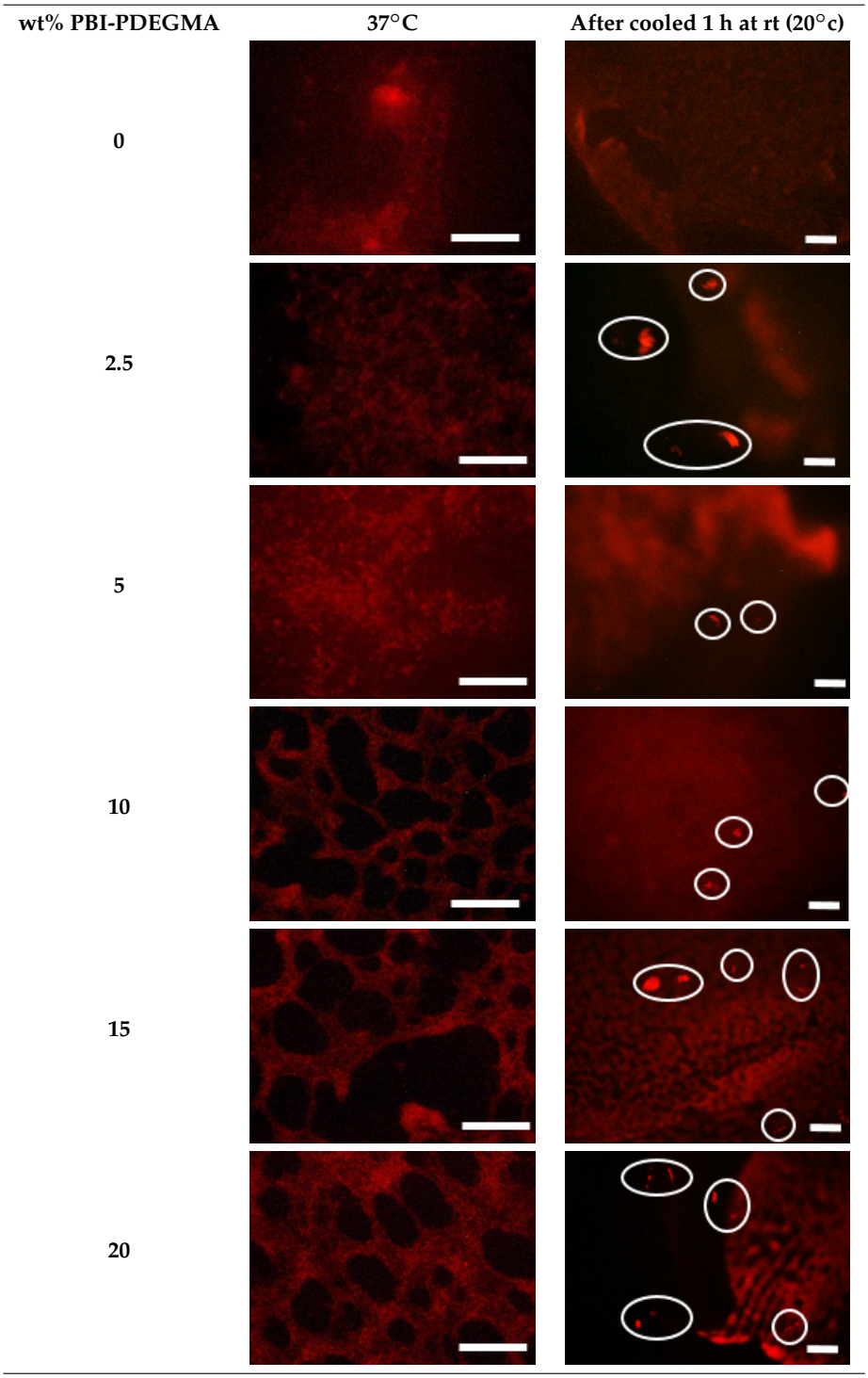



**Figure 4.12:** Representative confocal images of scaffolds in suspension before and after 1 hr at rt, after 7 days of genetically modified 3T3 fibroblasts culture. Scale bar at 37°C is 300 µm and scale bar after 1 h at rt is 1 mm. Cell clusters observed detached are circled on images.

Hence, a detachment study of two different fibre diameter scaffolds was performed. A passage method of lower detachment temperature of 8°C for 10 mins of the previous study was implemented to eliminate differences [269]. Approximately 10 and 20% cell detachment from the fibres of 900 nm and 2-3 μm diameter respectively were observed. A slightly lower cell detachment percentage was obtained for the 900 nm FD. However, no significant difference was observed. When cooled for 30 mins, cell detachment increased to 25% for the 900 nm FD scaffolds, while lower detachment of 20% was observed for 2-3 μm FD scaffolds. This concludes that the fibre diameter does not play a significant role in the cell detachment, while length of cooling resulted in increased detachment from the 900 nm FD scaffolds.

Another possible reason for the lower cell detachment could be due to the location of the thermo-responsive brushes of the polymer within the fibres. Although, even distribution through the fibres was confirmed by fluorescent labeling. The PDEGMA brushes may be hidden away under the PLA in the fibres, resulting in hindrance of the brushes to expand under cooled conditions. To confirm this hypothesis a detachment study of PLA/PDEGMA scaffolds, coated PLA fibres and PDEGMA coated on tissue culture (TCPS) plastic was performed. Significantly lower detachment of 25% was observed on the blend electrospun PLA/PDEGMA scaffolds. While no significant difference was observed between PDEGMA coated PLA fibres and coated TCPS. This finding gives an indication that the PDEGMA blended during the electrospinning may not be predominantly present on the fibres' surface. Thermo-responsive brushes may have moved inwards during the electrospinning process resulting in a lower amount of thermo-responsive brushes available on the surface of the fibres. A possible way to overcome this problem is by bringing the PDEGMA to the outside of the fibres with the use of co-axial electrospinning [69], in which a sheath of PDEGMA can be formed on the outside of a PLA core fibre. This is further discussed in more detail in chapter 7.

The 3T3 fibroblast used are commonly used for cell culture optimisation, due to their robust nature [278]. However, in the case of these scaffolds this may have resulted in negative results. PDEGMA has been observed to have a relatively lower hydrophilicity than other thermo-responsive materials [272]. Previous 3T3s fibroblast detachment

studies were performed with the more hydrophilic polymer PNIPAM (LCST of 32°C), resulting in greater difference of WCA and therefore, resulting in a more prominent thermo-responsive response. The PDEGMA thermo-responsive behaviour may be not strong enough for the robust fibroblast used. As these scaffolds are aimed for the cell culture of human corneal stromal cells (hCSCs), an initial study of cell detachment with the more sensitive cells (hCSCs) was performed. A significant increase in detachment was observed of approx. 100% compared to the 25% for 3T3s (see Figure 4.10D).

Thermo-responsive substrates are an increasing area of interest to overcome the disadvantages of enzymatic digestion detachment. Multiple different studies have confirmed successful detachment of cell sheets from thermo-responsive materials [154, 157–159, 163, 183, 271]. Only one study in our research group has reported the use of PDEGMA for successful cell sheet detachment from blend electrospun scaffolds [269]. However, on the PLA/PDEGMA manufactured scaffold only appr. 25% detachment of small clusters of cells were observed, instead of a cell sheet. This was likely due to the patches morphology of cells on the electrospun scaffolds. These cell patches could be due to the absence of polar functional groups in the PLA electrospun scaffolds resulting in a hydrophobic surface. This hydrophobicity affects the adsorption of proteins from the cell culture media via hydrophobic interaction, resulting in an unfolded or altered conformation of the protein structures to expose the hydrophobic domains which become tightly adherent to the hydrophobic surface, which subsequently affects the cellular response [276, 279, 280]. This could explain the clusters of cells observed when grown on scaffolds without PDEGMA and uneven coverage of cells on the PDEGMA containing scaffolds.

No significant difference in detachment percentage was observed when increasing time or temperature of the passage method. Also a physical difference in fibre diameters was observed to have no positive effect on the detachment. However, when comparing the blended polymer scaffolds with PLA scaffolds with PDEGMA coated scaffold surface and TCPS PDEGMA coated control, significantly more detachment was observed for the PDEGMA coated PLA scaffolds (50%) and PDEGMA coated TCPS (90%) compared to the electrospun scaffolds (25%, see Figure 4.9C). This finding in-

dicates possible hindrance of the PDEGMA thermo-responsive brushes to rehydrate within the fibres resulting in insufficient thermo-responsive behaviour on the scaffolds surface. However, when seeding and proliferating the more sensitive hCSCs on to the scaffold significantly more detachment was observed (approx. 100%). This finding concluded that these scaffolds may not result in sufficient detachment of robust cell lines, while resulting in sufficient detachment of more sensitive cells. Therefore, these scaffolds were taken forward for the investigation of the attachment, proliferation and thermo-responsive passaging of the hCSCs.

## 4.5 Conclusion

Thermo-responsive materials have been identified as suitable for enzymatic-free cell passaging. In this study, PLA/ PDEGMA thermo-responsive blend electrospun scaffolds were fabricated and 3T3s cells' adherence, proliferation and thermo-responsive detachment were investigated. Even distribution of the PDEGMA was confirmed by the fluorescent labeled PBI-PDEGMA polymer. This was concentration dependent and PDEGMA wt% to PLA below 10 wt% resulted in insufficient distribution. Thermo-responsive behaviour of the PDEGMA polymer and blend electrospun scaffolds was confirmed by cloud point and WCA measurements. 3T3 fibroblasts were observed to attach and proliferate well on the PDEGMA containing scaffolds, due to their lower hydrophobicity compared to PLA scaffolds. However, no significant detachment was observed when cells were cultured for up to 7 days. Only approximately 30% 3T3 fibroblast detachment was confirmed at day 7 of cell culture. No difference in detachment was observed from scaffolds containing more then 10 wt% PDEGMA. Therefore, 10 wt% PDEGMA containing scaffolds were concluded as most suitable for optimisation. Longer detachment times and increased fibre diameters did not result in an increase of percentage detached and the highest detachment was observed when the scaffolds were cooled for 30 mins at 8°C . Significantly more detachment was observed for PDEGMA coated PLA fibres and 2D coated TCPS. This indicates insufficient exposure of the PDEGMA thermo-responsive brushes on the fibres. Optimisation is needed to

improve the exposure of the PDEGMA on the surface of the fibres. Although the manufactured scaffolds were observed unsuitable for the robust fibroblast, significantly increased detachment was observed for the more sensitive intended cell line (hCSCs). For this reason, the optimised scaffolds were considered suitable for further investigation for the attachment, proliferation and detachment of hCSCs.

# Chapter 5

# human Corneal stromal cell (hCSCs) behaviour on the thermo-responsive fibrous electrospun scaffolds.

## 5.1 Introduction

The cornea is a key component of the eye. It is located in front of the iris therefore is required to be transparent and have a certain refractive index to direct light onto the retina (1.376 Rays) [281]. The cornea is composed of 6 layers, each of which contribute to its overall function (see Figure 5.1). The first and most outer layer, consisting of fast-growing regenerative epithelium cells, protects the eye from foreign materials such as dust, bacteria and water, while absorbs oxygen and soluble nutrients from fluids. The second most outer layer, the bowman's membrane, is composed mainly of collagen and forms a thin transparent film. Little is known about the contribution of this layer towards corneal physiology, however recently it has been postulated that the bowman's membrane may act as a physical barrier that prevents direct traumatic contact with the corneal stroma, and protects the sub-epithelial nerve plexus hastening epithelial innervation and sensory recovery. The third layer, the stroma, is by far

the thickest and the most complex layer making up around 90% of the total corneal thickness. This layer is composed of regularly arranged collagen fibres with sparsely distributed keratocytes or human cornea stromal cells (hCSCs, 3% of stroma volume) [282]. There are approximately 200 laminar layers (1.5-2.5 μm) of mostly type I collagen fibres, and are organised in ordered structure of remarkable uniformity in terms of fibril diameter. The unique shape, arrangement and spacing play a key role in the cornea's light-conducting transparency [283]. The scattered light interferes constructively singularly in a forward direction allowing light through to the retina. In 2013 , Dua et al. [284] detected the presence of an additional layer between the cornea stroma and Descent's membrane and has a thickness of 15 μm. This Dua layer is impermeable to air and very strong withstanding up to 2 bars of pressure [285–287]. The fifth layer, the Descent's membrane is composed ocollagen IV fibres and has higher flexibility when compared to collagen I [288]. The thickness of the membrane is dependent upon age, adults having thicker membranes (8-10 μm) as compared to children (3 μm) [289]. The sixth and final layer, the corneal endothelium is a single layer of cells on the inner surface of the cornea. This layer regulates the fluid movement into the cornea. Fluids from inside the stroma diffuse into the eye. Without this excess fluid being pumped away by the endothelium, the stroma would swell and lose its transparency thus its ability to function.

This study is focusing on keratocytes within the stroma layer of the cornea as a therapeutically relevant mammalian cell type. There is particular interest in the keratocyte expansion with the aim of producing tissue engineered corneal replacements. This will be discussed later in detail. In corneal homeostasis, quiescent cells control the transparency of the cornea by synthesis of collagen and tissue-specific keratan sulfate proteoglycans [282, 290]. They also play a role in degradation of stromal matrix by the secretion of collagenase and additional hydrolytic enzymes [291–293]. Moreover, it is suggested that they contribute to the structural stability of the interlamellar organisation of the collagen fibres, which provides the transparency of the cornea [294]. Keratocyte cells have been observed to express high levels of the water-soluble protein ALDH1 in rabbit studies [295]. Jester et al. [295] suggested that high expression of ALDH1 plays a vital role in the transparency of the cornea and optical properties.

When damage occurs in the stroma these quiescent keratocytes are activated and differentiate into corneal fibroblast (their repair phenotype) [296–298]. These corneal fibroblasts migrate to the area of damage and produces a substituted stromal matrix. To aid tissue repair, local populations of corneal fibroblasts differentiate into myofibroblasts as they have the ability to contract and close the wound area. These myofibroblast can be identified by the expression of α-smooth musle actin (α-SMA) [22].

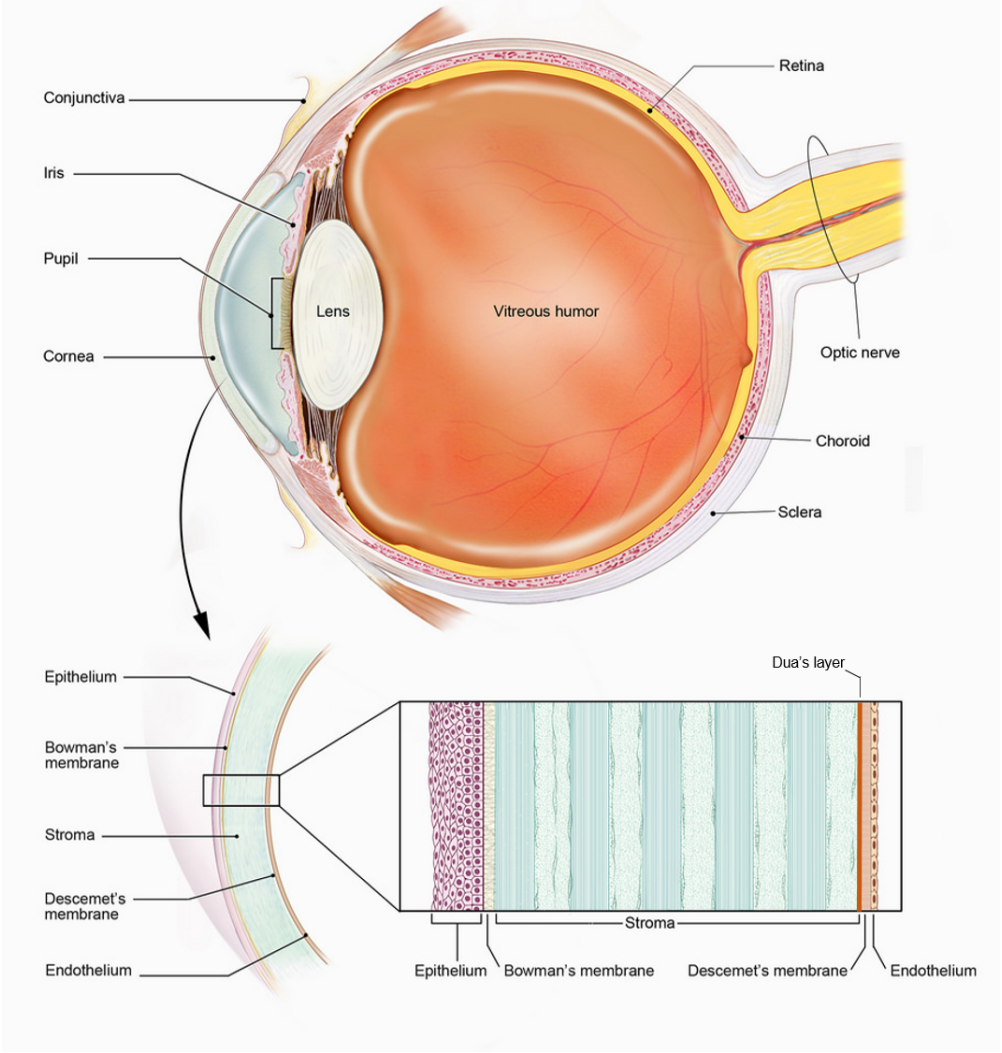



**Figure 5.1:** Schematic of the structures of the eye and corneas six different layers. Modified from [299].

However, this wound healing can lead to scar formation resulting in loss of corneal transparency leading to blindness, where upon transplantation is the only option. Scarring in response to wound healing is the fourth leading cause of blindness and affects more then 10 million people worldwide [300]. Common causes of corneal blindness include trachoma (bacterial infection) [301], keratitis (inflammation) [302], cataract (clouding of the eye) [303], glaucoma (optic nerve damage) [304] and age-related degeneration [305]. Currently the successful treatment is the replacement of the damaged cornea by transplantation, however this treatment is limited due to donor shortage, immune rejection and tissue quality issues. Stem cell therapies in development offer new possibilities of treatments [282]. Keratocytes extracted from the limbus (found at the border of the cornea and the sclera, the white part of the eye) have been observed to express CD105 in *in vitro*, a mesenchymal stomal cell marker [306]. This observation gave reason to believe that the limbal keratocytes have MSC potency [307] and gives rise to possible applications of this stem cell type in regenerative cell therapies for the cornea. However, expanding keratocytes in 2D conventional mammalian cell culture to the numbers required for viable tissue engineered therapies is limited due to change in phenotype to the active myofibroblast also being observed [308, 309]. Many strategies have been researched to maintain the keratocyte phenotype including altering/developing new media composition [193, 310], co-cultures [311] and culture on three dimensional structures [61, 312–314]. Soluble biomolecules within cell culture media can direct or maintain phenotype of cells supported on scaffolds. Sidney et al. [193] investigated different combinations of cell culture media (DMEM10, M199, SCM, EGM, MethoCult, K-SFM and Stem Pro-34) and their influence on the hCSCs phenotypic response. SCM media composed of DMEM/F12 with knock out serum and growth factors (see details chapter 2, section 2.7.2) was observed to support a cell phenotype closest to the pluripotent cell and was deemed the most suitable option for clinical-grade medium for cell expansion for cell therapies. In this chpater the fabricated PLA/PDEGMA thermo-responsive three dimensional scaffolds were proposed as possible alternative to the 2D conventional cell culture expansion platform for the expansion of hCSCs. As an initial experiment of thermo-responsive enzymatic-free passage of hCSCs on these scaffolds was observed successful (see chapter 4, Figure 4.10D).

SCM media composition reported by [193] was considered most appropriate as cell culture media in this study. The behaviour of hCSCs and their ability to maintain their quiescent phenotype on these scaffolds were investigated.

Transmembrane phosphoglycoprotein CD34 has been identified as a hematopoietic and progenitor cell marker and is believed to not be expressed by multipotent mesenchymal stromal cells (MSC) [315]. However, recent studies suggest that many more cell types express CD34, including nonhematopoietic cells [316, 317], multipotent mesenchymal stromal cells (MSC) [318], interstitial dendritic cells [319], epithelial progenitors [320] and corneal keratocytes [321]. In case of corneal keratocytes the expression of CD34 reduces over multiple passages in 2D and ultimately disappears when become activated/adopt an activated phenotype [295, 321, 322]. Therefore, CD34 was identified as a marker to identify the quiescent hCSCs phenotype. As mentioned before keratocytes express ALDH to maintain the cornea structure and transparency. Therefore, within this study ALDH1A3 (an isoform found in mammals) was also identified as one of the markers to confirm keratocyte phenotype expression. To identify the change into a fibroblastic phenotype, expression of α-SMA was considered for identification.

## 5.2 Aims and Objectives

The aim of the study presented in this chapter was the investigation of human corneal stromal cell behaviour on the thermo-responsive electrospun scaffolds and their detachment from the scaffold following cooling. Cell adherence, proliferation and phenotype expression will be observed on different scaffold morphologies and chemical characteristics of the electrospun scaffolds.

This study's aim was achieved through the following objectives:

1. Observe the adherence and proliferation on thermo-responsive scaffolds with different morphologies (big beads, beads-on-strings and uniform fibres).

2. To observe the phenotype expression on the different scaffolds fibre morpholo-

gies.

3. To functionalise the thermo-responsive polymer (PDEGMA) with a free thiol groups (PDEGMA/PDEGSH) for peptide functionalisation of the scaffolds using photo -initiated thiol-ene chemistry to improve hCSCs attachment and phenotype support on the thermo-responsive fibrous scaffolds.

4. Investigate the adherence and proliferation on peptide functionalised scaffolds and compare them with the original scaffolds (PLA/ 10 wt% PDEGMA).

5. Investigate the phenotype expression (CD34, CD105, ALDH and α-SMA) and morphology using actin and vimentin staining on peptide functionalised scaffolds and compare them with the original scaffolds (PLA/ 10 wt% PDEGMA).

6. To culture hCSCs on peptide funtionalised scaffolds and passage them from the scaffolds with the use of the thermo-responsive co-polymer (PDEGMA/PDEGSH) in the fibres by lowering the culture temperature.

## 5.3 Experimental Methods

### 5.3.1 Polymer synthesis

The thermo-responsive polymer poly(di(ethylene glycol) methyl ether methacrylate (PDEGMA) and poly(di(ethylene-glycol) methyl ether methacrylate-co-poly(di(ethylene-glycol) thiol (PDEGMA/PDEGSH) were synthesised by RAFT polymerisation, see methods section 2.5.2 and 2.6.3. Polymer structures were determined by $H^1$-NMR, $C^{13}$-NMR and 2D-NMR (see method section 2.3.1). Molecular weights were measured using GPC (see method section 2.3.2) and lower critical solution temperature (LCST) points were estimated using UV-VIS cloudy point measurements (2 mg/mL, see method section 2.3.4).

### 5.3.2 Free thiol confirmation of PDEGMA/PDEGSH polymers

Free thiol presence and percentages in the PDEGMA/PDEGSH polymers were analysed using Ellman's assay and fluorescein-5-maleimide staining, see methods section 2.6.4 and 2.6.5.

### 5.3.3 Blend electrospun scaffolds fabrication

PLA polymer were blend electrospun with 10 wt% of PDEGMA or PDEGMA/PDEGSH to obtain a thermo-responsive fibrous scaffolds (see method section 2.2.2).

### 5.3.4 Blend electrospun scaffold characterisation

Scaffolds fibre morphology was analysed using SEM (see method section 2.4.1). Average FD and SD were calculated using ImageJ software (see method section 2.4.2). Thermo-responsive behaviour of the fibrous scaffolds were analysed by static WCA measurements (see method section 2.4.4).

### 5.3.5 Free thiol confirmation on blend electrospun scaffolds

Free thiol presence on the blend electrospun scaffolds fibres were analysed using fluorescein-5-maleimide staining and Tof-SIMS analysis, see methods section 2.6.5 and 2.4.5. See schematics of fluorescein-5-maleimide labeling in Figure 5.2A.

### 5.3.6 Peptide synthesis

GGG-YIGSR peptide sequence with a norbornene acid N-terminal functionalised group was synthesised and purified with the use of HPLC. The peptide structure was determined with the use of MS, see method section 2.6.6.

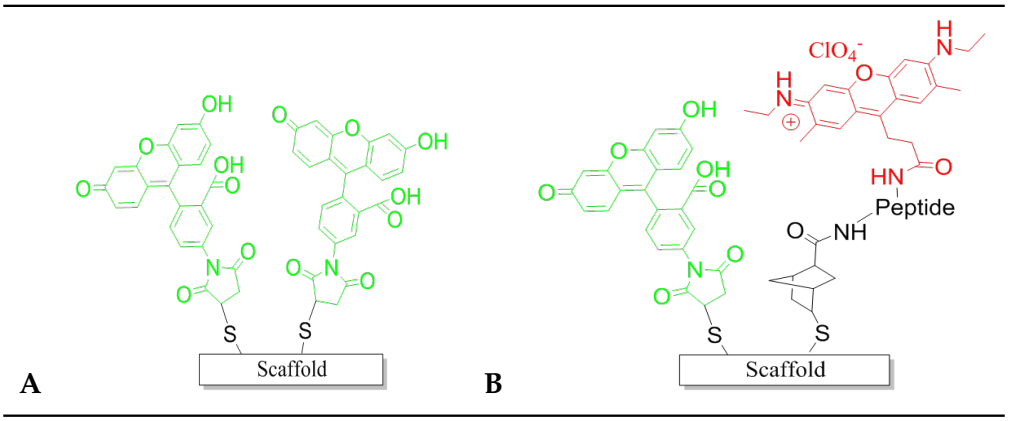



**Figure 5.2:** Schematics of photo-initiated and non photo-initiated peptide scaffold labeled with **fluorescein** and **ATTO**.

### 5.3.7 Photo-initiated thiol-ene chemistry confirmation

PDEGMA/PDEGSH polymer reactivity to photo-initiated thiol-ene chemistry of the free thiols to the alkene group of the norbornene acid of the Nor-GGG-YIGSR peptide was investigated using the method in section 2.6.7. Presence of the Nor-GGG-YIGSR peptide after photo-initiation on the scaffolds was investigated using NHS-ATTO fluorescence labeling (see method section 2.6.8) and ToF-SIMS analysis (see method section 2.4.5). Un-reacted free thiols after the thiol-ene reaction was investigated using fluorescein-5-maleimide fluorescence labeling (see method section 2.6.5). See schematics of ATTO labeling Figure 5.2B.

### 5.3.8 Cell proliferation, phenotypic and ECM expression studies

hCSCs were seeded onto the scaffolds at 60 000 cells/ml (n=9 scaffolds per different polymer containing scaffolds, see method section 2.7.6), proliferated for 9 days and cell numbers on different time point were calculated with the use of Alamar blue assays on 3 of the 9 scaffolds (see method section 2.7.6). 3 scaffolds of the 6 remaining scaffolds were used for immuno-staining studies at day 9. Cells were fixed onto the scaffolds, scaffolds were cut into 3 pieces and immuno-stained with two different

phenotypic marker combination (CD34/CD105 and ALDH/α-SMA) and morphology markers actin and vimentin (see method section 2.8). Remaining 3 scaffolds were used for ECM expression studies at day 9. Cells were fixed onto the scaffolds and immuno-stained with two ECM markers Collagen I and Lumican (see method section 2.8.2). See schematics of experimental timeline in Figure 5.3.

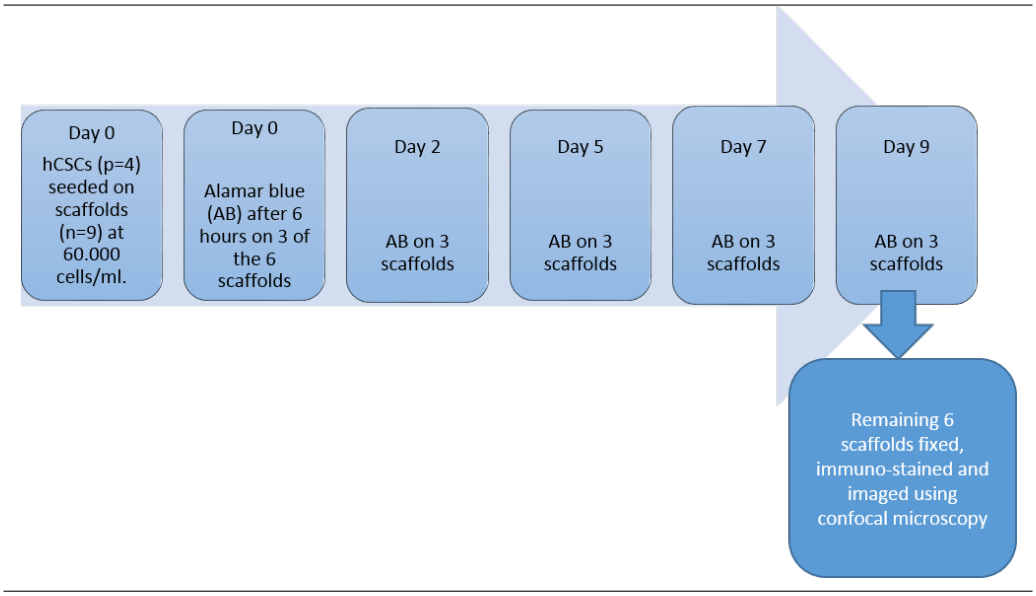



**Figure 5.3:** Schematic representing the Alamar blue (AB) and immunostaining experimental timeline for cultured hCSCs over 9 days on the different electrospun fibre morphology scaffolds (n=6 per different scaffold type).

### 5.3.9 Detachment studies

hCSCs were seeded onto the scaffolds at 60 000 cells/ml (n=6 scaffolds per different polymer containing scaffolds, see method section 2.7.6), proliferated for 9 days and cell numbers on different time point were calculated with the use of Alamar blue assays on 3 of the 6 scaffolds (see method section 2.7.6). Other 3 scaffolds were used for detachment studies at day 9. Cells were detached by different methods (see method section 2.9.2). Cells left attached on scaffold after the detachment step and cell detach numbers were calculated with the use of Alamar blue assay, see method section 2.7.6 and 2.9.1. See schematics of experimental timeline in Figure 5.4.

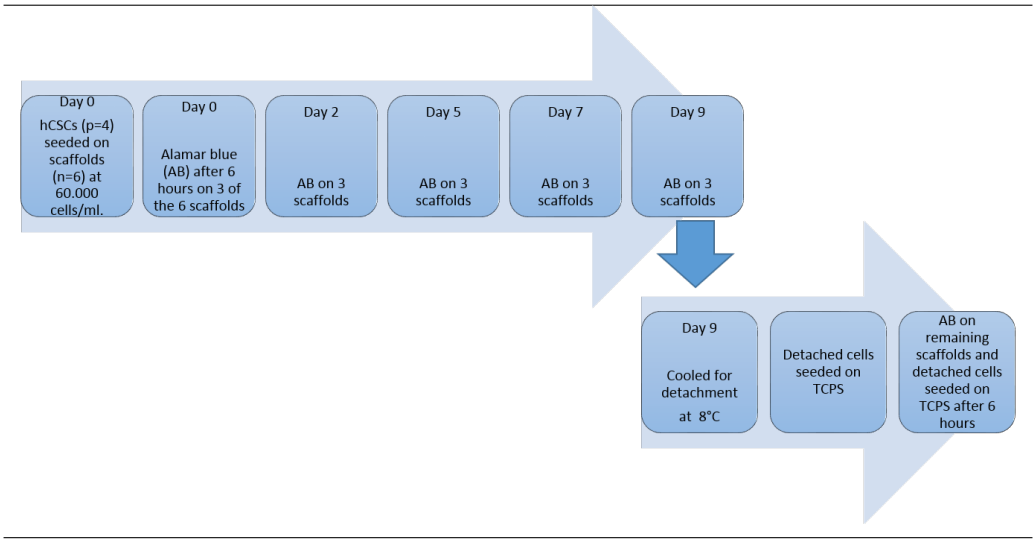



**Figure 5.4:** Schematic representing the Alamar blue (AB) and cell detachment experimental timeline for cultured hCSCs over 9 days on the different electrospun fibre morphology scaffolds (n=6 per different scaffold type).

### 5.3.10 Phenotype studies after detachment by FACS.

hCSCs detached from scaffolds were immuno-stained with CD34/CD105 and ALDH/α-SMA and analysed by FACS, see method section 2.10.2.

## 5.4 Results & Discussion

The quiescent phenotype of human corneal stromal cells (hCSCs) has been observed to be present when cells were grown on 3D structures. Wu et al. [323] investigated the gene expression of hCSCs cultured on poly(ester urethane) urea (PEUU) fibres. Their results showed differentiation of the corneal stromal stem cells to keratocytes on these structures. A more recent study showed similar results. Both ECM proteins and gene expression of keratocyte markers of hCSCs were observed up-regulated on 3D silk structures compared to 2D silk films (cultured for 9 weeks) [61]. For this reason the ability of 3D electrospun fibrous structures to support the phenotype of hCSCs was

investigated. The electrospinning process can result in different fibrous morphologies, as investigated in chapter 3. These three different morphologies were investigated further to observe the behaviour of hCSCs on these scaffolds with or without the thermo-responsive polymer, for trypsin free-passaging as investigated in Chapter 4 (PLA with 10 wt%, big beads, beads-on-strings, and PLA uniform as control). The hCSCs were observed to attach and proliferate on beads-on-strings (BoS) fibre morphologies and PLA uniform (PLA Uni) fibres. Significantly less proliferation was observed on the uniform (Uni) fibres with 10 wt% PDEGMA and big beads (BB) fibre morphology scaffolds, 1 x $10^4$ cells for Uni and BB compared to 3.5 x $10^4$ cells for the PLA Uni and BoS fibres (see Figure 5.5). Staining for actin and vimentin showed round clusters of cells on all scaffolds. This gives an indication of no real interaction of the cells onto the scaffolds fibrous surface, resulting in cells aggregating together.

Immuno-staining for the keratocyte marker CD34 was only observed on the uniform fibres with thermo-responsive PDEGMA. While, ALDH and CD 105 expression was observed when cells were cultured on all scaffold types. Concluding that, although, greater cell proliferation was observed on the beads-on-strings fibre scaffold and uniform PLA control, uniform fibres with thermo-responsive polymer were also able to support CD34 keratocyte expression. This could be due to the slightly lower hydrophobic characteristic of the scaffolds with PDEGMA compared to the PLA scaffolds (see Figure 4.3A). However, the fibroblastic marker α-SMA was expressed by cells cultured on all scaffold types with the strongest expression on the PLA uniform fibre control scaffolds (see Figure 5.6).

The cell aggregation observed could be due to the lack of serum in the cell culture media used. Previous work within our group on PLGA/PDEGMA scaffolds with hCSCs with the use of serum containing media DMEM10 resulted in cell being able to adhere to the scaffolds [269]. However, in this study the use of no serum containing cell culture media SCM resulting in no initial adsorption of essential attachment proteins onto the scaffold surface. Serum allows proliferation and rapid expansion of cells due to the combination of attachment and growth factors the serum provides. However, FBSs undefined biological combination and batch to batch variation makes serum unsuitable

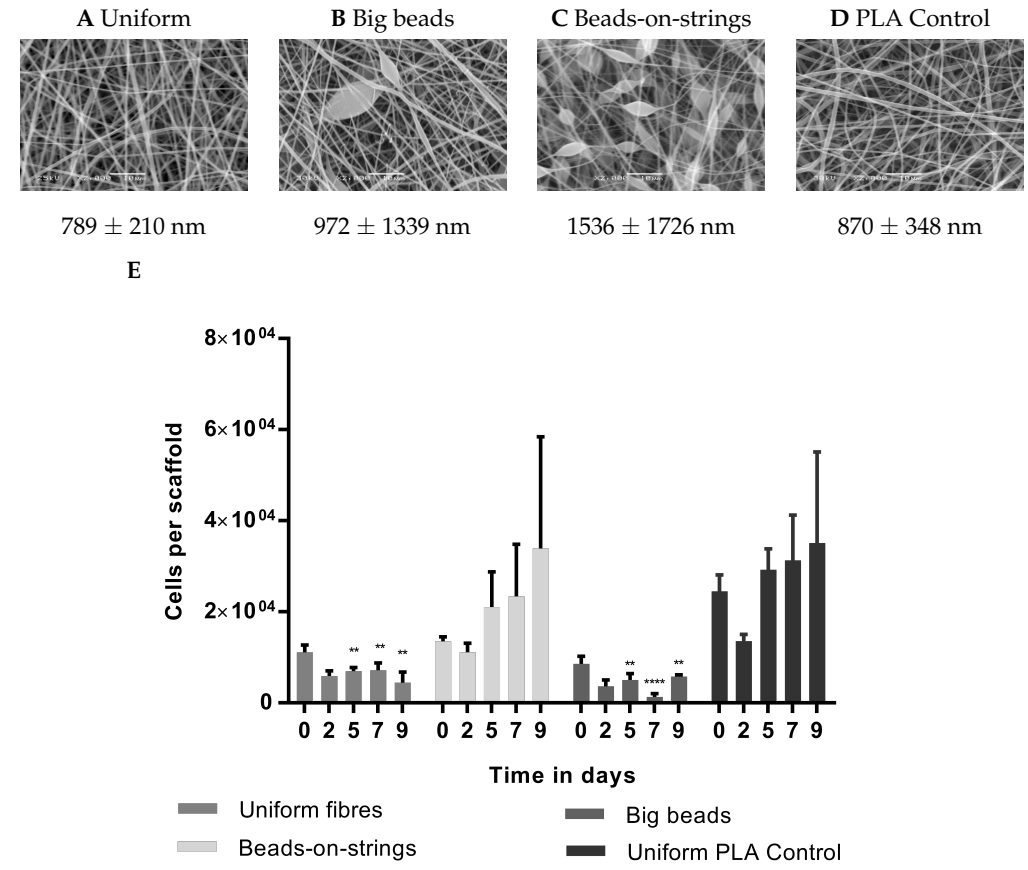



**Figure 5.5:** Representative SEM images of the different electrospun fibre morphologies with corresponding average fibre diameter. **A**) Uniform fibres of PLA/10 wt% PDEGMA, **B**) beads-on-strings fibre morphology of PLA/10 wt% PDEGMA,**C**) big beads fibre morphology of PLA/10 wt% PDEGMA and **D**) uniform fibres of PLA. hCSC were cultured on these scaffolds for 9 days in SCM and **E**) cell viability was measured. (n=3 scaffolds, two-way ANOVA, **=<0.01, ****=<0.0001, error bars=SD)

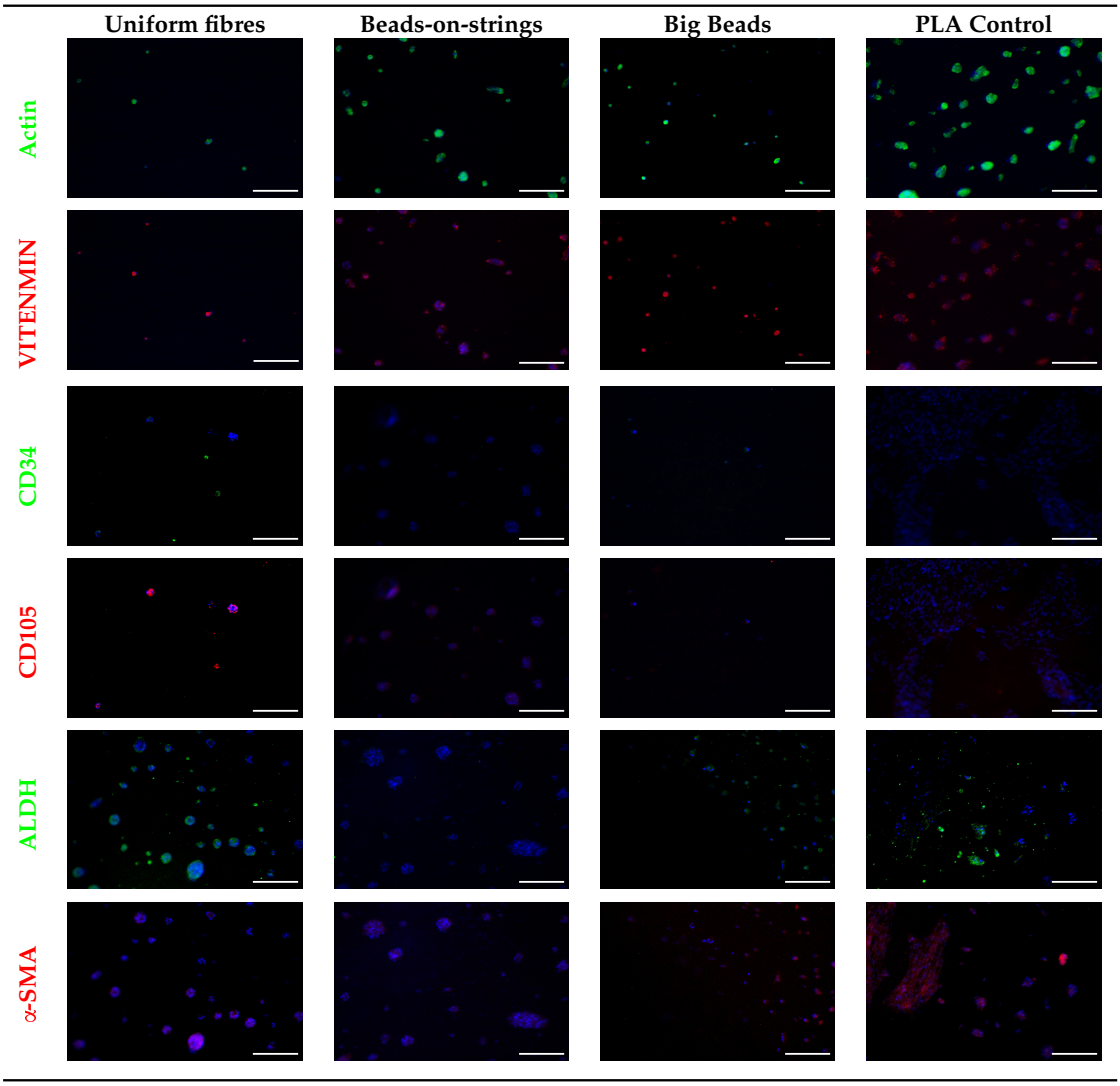



**Figure 5.6:** Representative confocal images of corneal stromal cells on the different electrospun fibre morphologies after 9 day culture. Cells were stained for keratocyte markers **CD34** and **ALDH**, as well as a mesenchymal stromal cell (MSC) marker **CD105** and myofibroblastic marker **α-SMA**. **Actin** and **VIMENTIN** were also stained to assess cell morphology on the scaffolds. All nuclei were stained with **DAPI**. Scale bar = 50 μm. (better contrast images can be found in the electronic version.)

for clinical grade research. Furthermore, FBS has been reported to trigger spontaneous differentiation of keratocytes to their fibroblastic or myofibroblastic phenotype [324–326]. Therefore, cell culture media composition without serum is desirable.

As none of the scaffolds supported quiescent hCSCs specific markers without the expression of the myofibroblastic marker α-SMA, and cell aggregates was observed on the fibrous scaffold. A new strategy was proposed with the use photo-initiated thiol-ene chemistry to functionalise the scaffolds with a peptide sequence to enhance the attachment and cell interaction and phenotype support of the uniform fibrous scaffold with 10 wt% PDEGMA. A thiol containing thermo-responsive polymer was obtained using RAFT polymerisation (see Figure 2.3). This brush like thiol containing polymer has two different side groups in different ratios; 1) poly(diethylene glycol) methyl methacrylate (PDEGMA) and 2) poly(diethylene glycol) ether thiol (PDEGSH). The diethylene glycol base for the thiol side groups was added to keep the thermo-responsive properties of the polymers as near to the original LCST of PDEGMA (see Figure 5.7A). This co-polymer was blended with PLA and electrospun to form fibrous scaffolds with free thiol groups available on the surface. Previous literature observed proliferation of hCSCs on tyrosine-isoleucine-glycine- serine-arginine (YIGSR) containing peptide nanofibre structures [327], as well as, has been reported to enhance cornea regeneration *in vivo* pigs when YIGSR containing collagen hydrogels were used [328]. This laminin peptide sequence was therefore considered suitable for this work. A spacer of three glycine groups was attached to increase the distance of the peptide from the surface creating access of the peptide from the fibrous scaffold surface. The peptide sequence was functionalised with a norbornene acid on the N-terminal group, resulting in the following full sequence norbornene-glycine-glycine-glycine-tyrosine-isoleucine-glycine- serine-arginine (Nor-GGG-YIGSR). The alkene group of the norbornene acid reacts with the free thiols presence on the surface when exposed with UV light. This photo-initiated thiol-ene chemistry reacts rapidly and is therefore commonly used for self-assembling bioconjugates [329–331] (see schematics Figure 5.7).

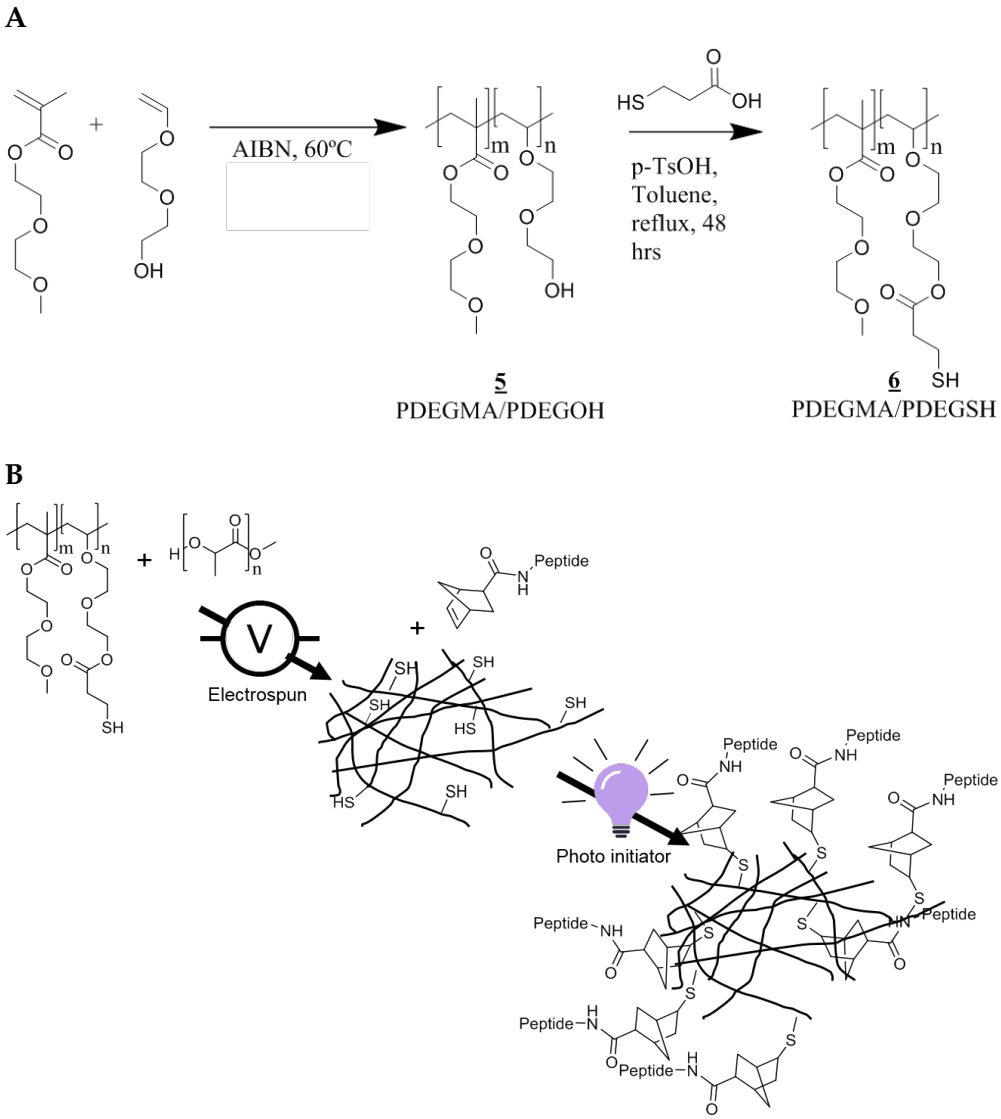



**Figure 5.7:** Schematics of **A)** PDEGMA/PDEGSH synthesis and **B)** the formation of polymer-peptide derivatives electrospun scaffolds.

### 5.4.1 Polymer and peptide synthesis

#### PDEGMA/PDEGOH

Free radical polymerisation of different ratios of the monomers di(ethylene glycol) methyl ether methacrylate (DEGMA) and di(ethylene glycol) vinyl ether (DEGOH; 100:0, 95:5, 90:10, 80:20, and 70:30) were performed, resulting in the polymer product poly(di(ethylene glycol) methyl ether methacrylate-co-poly(di(ethylene glycol) vinyl ether (PDEGMA/PDEGOH). $^{1}$H-NMR samples were taken at different time points during the reaction (60, 120, 280 and 240 mins) to observe the conversion rate of the RAFT polymerisation (see supplementary data Eq. 9.0.1). From 120 mins, a plateau was observed with a final conversion of 80% (see supplementary data Figure S38). Due to delays in commercial availability of di(ethylene glycol) vinyl methacrylate the monomer di(ethylene glycol) vinyl ether was used. This monomer is analogous to the oligo (ethylene glycol) methacrylate monomers but exhibits a less stable radical formation upon initiation and therefore earlier termination of the polymerisation chain with lower PDEGOH ratio than initially added monomer ratios. This was confirmed by $^{1}$H-NMR integration of the singlet -O-C$\underline{H_3}$ of PDEGMA to the triplet of the -C$\underline{H_2}$-OH of the PDEGOH (see Figure S9). In case of the di(ethylene glycol) methyl ether methacrylate the C=O stabilises the radical resulting in head-to-tail addition. However, di(ethylene glycol) vinyl ether has no groups around to stabilise the radicals resulting in possible head-to-head addition [332]. This was confirmed by $^{1}$H-NMR data showing a peak at 1.4 ppm for the CH of the C(PDEGMAchain)-CH(O-DEGOH) group. The real percentage co-monomer ratios after RAFT polymerisation were identified as 0, 2, 3, 4 and 10 mole % PDEGOH to PDEGMA (see supplementary data Table S6).

Molecular weights of the purified PDEGMA/PDEGOH polymers were measured in THF GPC-derived molecular weights (Mw) of 40 to 80 kDa with a Đ (polydispersity (PD)) of around 2 to 3 (see Table 5.1). DEGMA/DEGOH of 70:30 ratio showed a slightly lower molecular weight. As previously explained, this is due to the less stable diethylene glycol vinyl ether radicals resulting in earlier termination of the polymerisation and shorter polymer chain lengths. Increasing DEGOH within the reaction mixture re-

sulted in an increase of reactive unstable radicals and therefore earlier termination of the polymer chain.

**Table 5.1:** GPC data of PDEGMA/PDEGOH polymers in THF.

| % of -OH | Mn [kDa] | Mp [kDa] | Mw [kDa] | PD [Đ] |
|---|---|---|---|---|
| 0 | 31 | 43 | 59 | 2.1 |
| 2 | 35 | 56 | 79 | 2.2 |
| 3 | 34 | 59 | 86 | 2.5 |
| 4 | 30 | 51 | 75 | 2.5 |
| 10 | 16 | 33 | 43 | 2.7 |

**PDEGMA/PDEGSH**

The PDEGMA/PDEGOH polymers were functionalised with a free thiol end group by a condensation reaction with 3-mercaptopropanoic acid (see method section 2.6.3). The condensation product (PDEGMA/PDEGSH) was successfully obtained after precipitation and was confirmed using 2D-NMR interpretation; by the disappearance of the -$CH_2$OH peak (j at 3.7 ppm $^1$H-NMR) and the appearance of the $CH_2$ peaks of the $CH_2CH_2$SH group (k and l at 2.6 and 2.9 ppm $^1$H-NMR, see 2D-NMR spectra Figure 5.8).

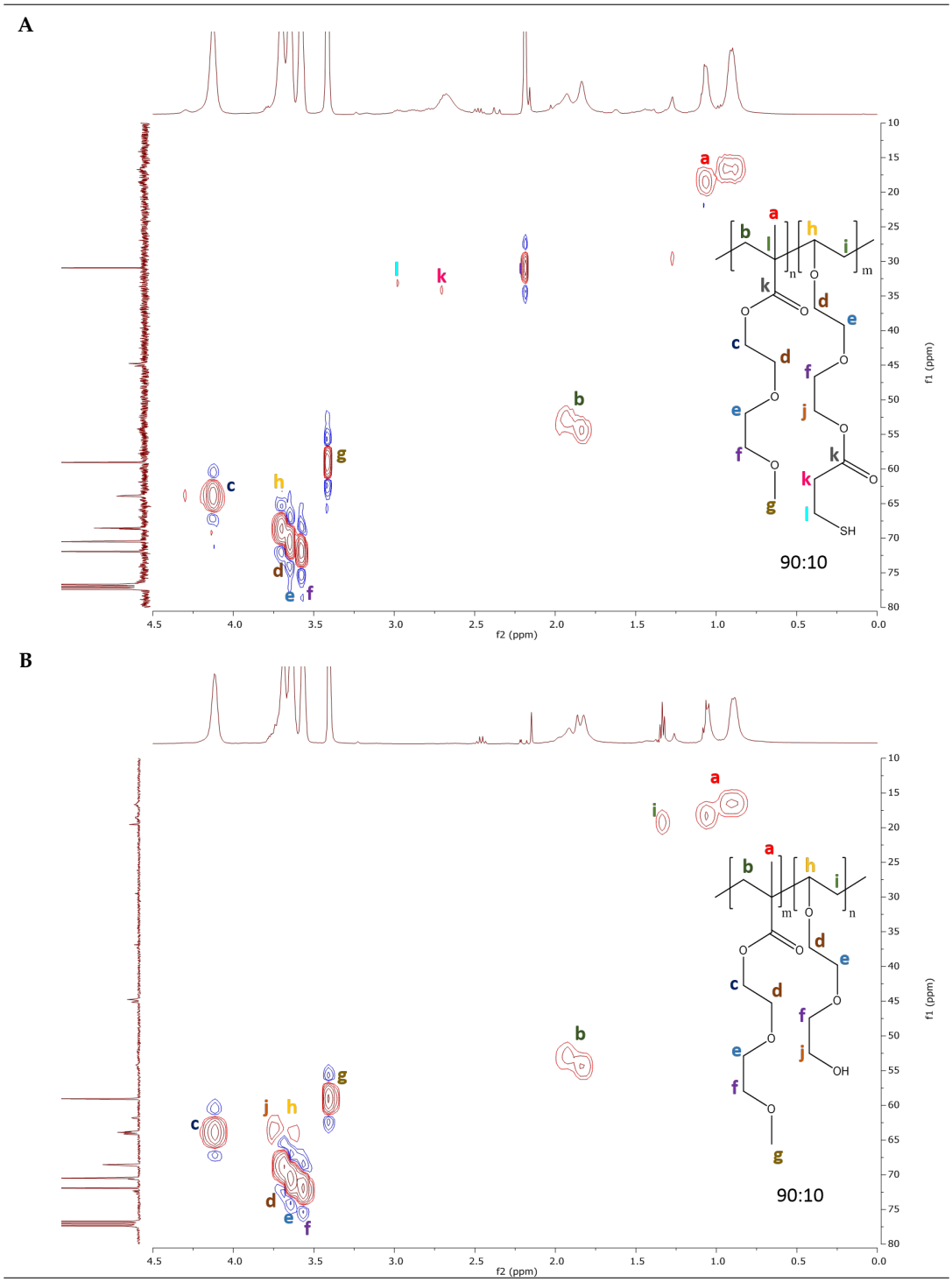



**Figure 5.8:** 2D-NMR spectra of **A)** PDEGMA/PDEGSH (90:10) and its starting product **B)** PDEGMA/PDEGOH (90:10) from RAFT polymerisation 70:30 monomer ratio. The success of the condensation reaction was confirmed by the disappearance of the $CH_2OH$ peak at 3.7 ppm (j) and the appearance of the thio-alkyl ester $CH_2$ peaks at 2.7 and 2.9 ppm (k and l).

Free thiol presence on all polymers was confirmed by Ellman's assay (see Table 5.2). A standard curve of known concentrations of thiols (cysteine solution, see Figure S26) was used to calculated the percentage of thiols. An increase in percentage of free thiols was observed when a higher percentage ratio of PDEGOH monomer was used in the PDEGMA/PDEGOH synthesis. However, the expected percentage thiol was slightly lower than the known percentage of PDEGOH. This could be due to the reaction of free thiols with themselves under aqueous conditions resulting in disulfide bond formation [333], which are not reactive with the Ellman's reagent. Ellman's assay is performed in aqueous conditions and an incubation time is required to obtain the fluorescent signal. This incubation time could be too long resulting in free thiols interacting with each other to form disulfides bonds. Although, this formation can occur, reduction agents can be used to reduce the disulfide bonds back to free thiols. However, most common thiol reducing agents (dithiothreitol (DTT) and b-mercaptoethanol (BME)) results in a free thiol containing by-product which will interfere with the Ellman's assay measurement. Tris(2-carboxyethyl) phosphine hydrochloride (TCEP) does not result in interfering by-products, which could be used to avoid disulphide bond formation during the Ellman's assay [334]. A second possible reason for the lower percentage of thiols then expected could be due to the similar boiling point of the 3-mercaptopropanoic to the toluene (110-111°C and 110.6°C respectively) resulting in evaporation of 3-mercaptopropanoic acid during the condensation reaction. A condensation reaction's solvent could be changed into a solvent with a lower evaporation rate such as chloroform; in which the water will be removed by a reverse Dean stark trap.

**Table 5.2:** Free thiol presence percentage in the PDEGMA/PDEGSH co-polymer as confirmed by Ellman's assay.

| % of -SH | Polymer concentration [mmol/mL] | Absorbance [412 nm] | Standard Curve/1000 [mmol/mL] | Thiol% |
|---|---|---|---|---|
| 2 | $70 * 10^{-4}$ | 0.0877 | $1.2 * 10^{-4}$ | 1.7 |
| 3 | $70 * 10^{-4}$ | 0.1249 | $1.5 * 10^{-4}$ | 2.2 |
| 4 | $70 * 10^{-4}$ | 0.2483 | $2.6 * 10^{-4}$ | 3.7 |
| 10 | $70 * 10^{-4}$ | 0.7328 | $6.8 * 10^{-4}$ | 9.7 |

To confirm the presence of free thiols in the purified polymers, the polymer was coated onto glass slides and labeled with maleimide-fluorescein. The maleimide alkene double bond reacts with the free thiols by a Michael-type addition reaction; if thiols are present a fluorescence signal of the attached fluorescein will be observed when imaged with confocal microscopy at 488 nm wavelength. A fluorescence signal was observed for all thiol containing co-polymer. An increase in signal was observed when the ratio of PDEGMA/PDEGSH increased; 10% PDEGSH resulted in the strongest fluorescence observed.

Cloud point hysteresis measurements were performed to investigate the thermo- responsive properties of the functionalised PDEGMA, PDEGMA/ PDEGOH and PDEGMA/PDEGSH polymers. Figure 5.10 and Table 5.3 shows the cloud point hysteresis patterns and corresponding LCST of the polymer in solution when heated or cooled. Unmodified PDEGMA has a LCST of 27°C when heated. However, a shift was observed when cooled to a LCST of 20°C. This is due to the nature of the polymer when hydrophobic as the PDEGMA branched polymer is folded and aggregated. This leads to a slower rate of unfolding during the cooling process and a change in polymer conformation as the chains rehydrate (as previously described in chapter 4) [181]. For all different concentrations of PDEGMA/PDEGOH a shift was observed from 27 to 29°C when heated, while an earlier cloud point changes was observed when cooled compared to the 100% PDEGMA polymer. This is due to the more hydrophilic nature

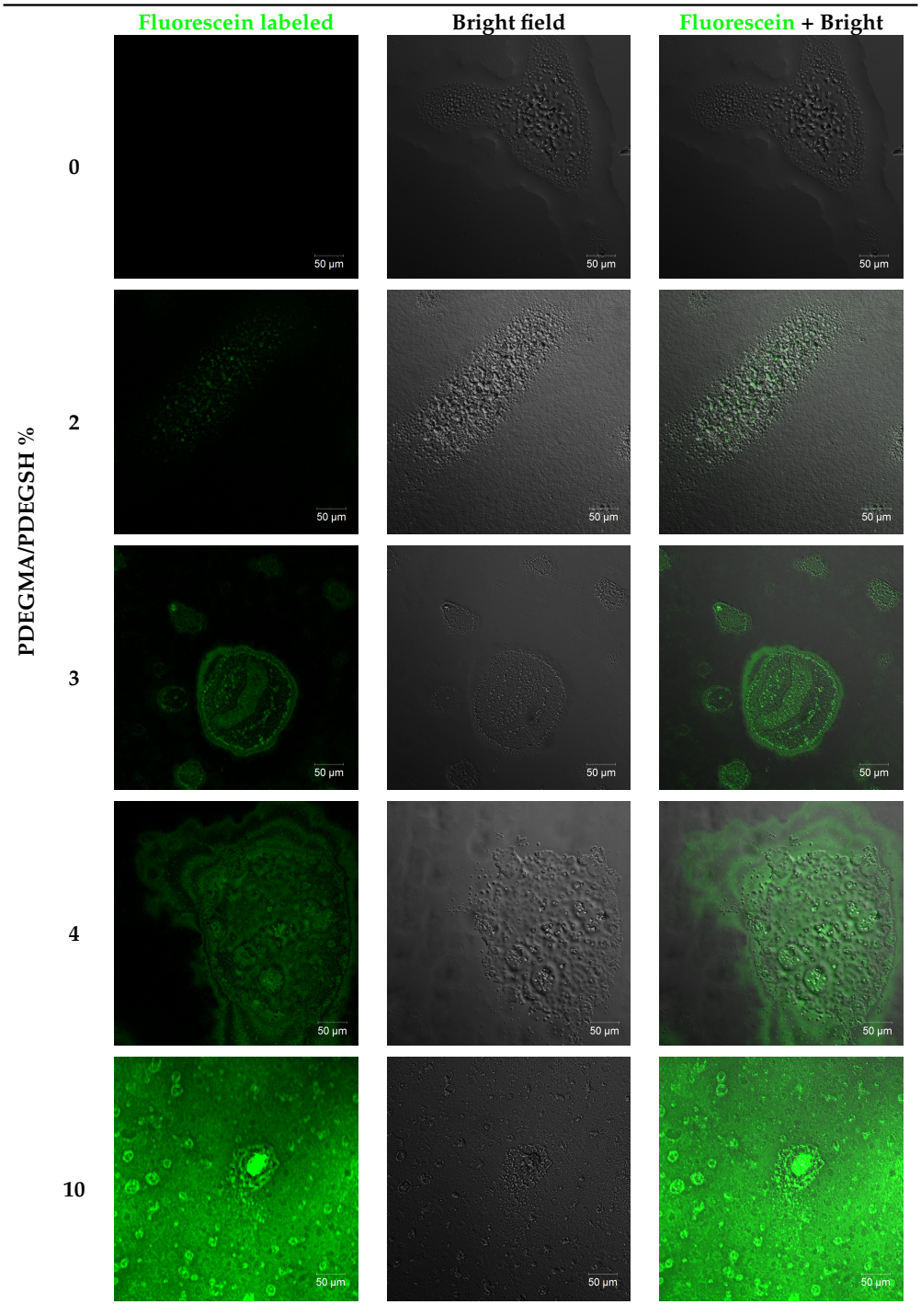



**Figure 5.9:** Fluorescein staining of free thiols presence on dried PDEGMA/PDEGSH polymer films on glass slides containing different ratios of -MA to -SH. Scale bar = 50 µm. (better contrast images can be found in the electronic version.)

of the polymer branches. The co-polymer PDEGOH alcoholic end group results in a slower transition to hydrophobic characteristics when heated and a faster transition to the hydrophilic state when cooled. The PDEGMA/PDEGSH with a thiol end group produced a different cloud point pattern then observed for the other polymers. The hydrophobic aggregation changes when heated occurred earlier, at 18, 22, 25, 18°C for 2, 3, 4, 10 PDEGSH respectively. As well as the change back, to the hydrophilic properties was observed to occur earlier (11, 18, 19, 13°C for 2, 3, 4, 10 mole % PDEGSH respectively, see Table 5.3). This is due to the increase in the hydrophobic nature of the co-polymer side group from PDEGOH to PDEG-C(=O)O($CH_2$)$_2$ SH. A decreasing slope was observed for concentration of SH group higher than 2% when cooled. This may be due to cross-reactivity with other thiol groups. Free thiols can oxidise to a disulfide bond in water and temperature can increase this reaction. However, a more in depth investigation into the kinetics is required to confirm this assumption.

**Table 5.3:** Cloud-points of all different PDEGMA, PDEGMA/PDEGOH and PDEGMA/PDEGSH polymers ratios when heated and cooled.

| | ratio % -OH or -SH | Heated | Cooled |
|---|---|---|---|
| **PDEGMA** | 0 | 28 | 22 |
| **PDEGMA/PDEGOH** | 2 | 27 | 23 |
| | 3 | 25 | 24 |
| | 4 | 27 | 26 |
| | 10 | 28 | 25 |
| **PDEGMA/PDEGSH** | 2 | 18 | 11 |
| | 3 | 22 | 18 |
| | 4 | 25 | 19 |
| | 10 | 18 | 13 |
| **PDEGMA/PDEGS-Nor-GGG-YIGSR** | 4 | 25 | 19 |

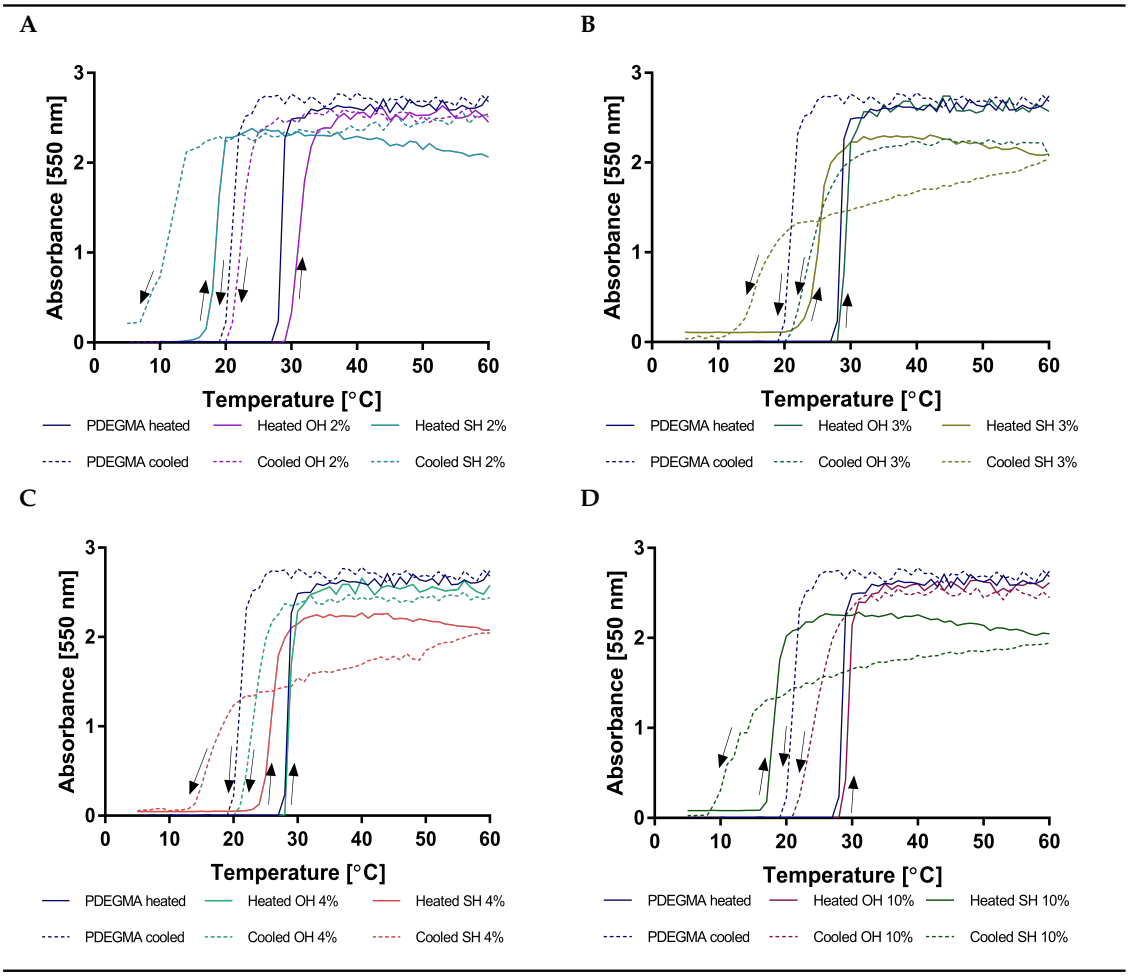



**Figure 5.10:** Cloud point hysteresis of PDEGMA, different ratios of PDEGMA/PDEGOH and PDEGMA/PDEGSH in water (2 mg/ml). **A**) 2, **B**) 3, **C**) 4 and **D**) 10% PDEGOH to PDEGMA. LCST shift down when polymer is cooled down. This is due to the aggregation of the polymer which takes time to break up. PDEGOH LCST is slightly higher in temperature due to the additional hydrophilic group OH. PDEGSH polymer shows an earlier LCST change than the PDEGMA and PDEGOH polymers as well as a slow steady slope when cooled.

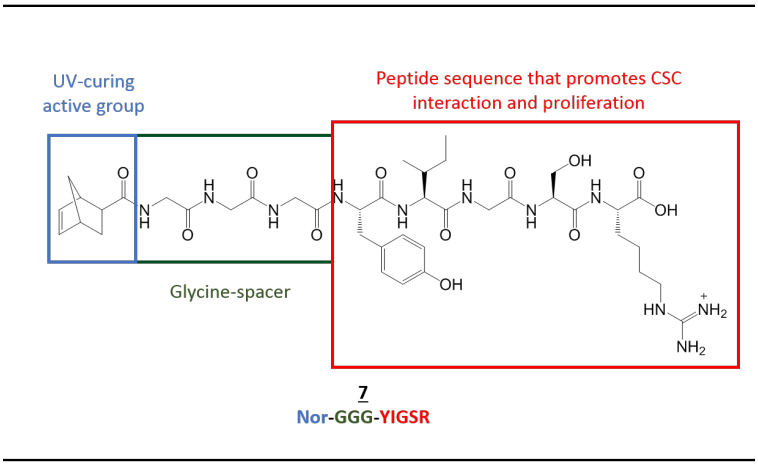



**Figure 5.11:** Chemical structure of the synthesised Nor-GGG-YIGSR peptide sequence. Nor (blue block) is the norbornene acid photo-initiative active group, GGG (green block) is used as a spacer and YIGSR (red block) sequence previously identified to promote hCSCs proliferation [327].

Nor-GGG-YIGSR peptide sequences (see Figure 5.11) with a norbornene acid terminal end group were synthesised successfully by solid-phase peptide synthesis on rink amide resin and purified by HPLC and identified by HPLC-MS spectra interpretation (see supplementary data Figure S28). The standard method cycle of Fmoc-deprotection, 4x washing and double couplings resulted in many by-products (see Figure S27A). Therefore, an extra two washes were added after the double coupling, which successfully reduced the amount of by-product contaminating the peptide product (see Figure S27B).

An initial study was performed to confirm the photo-initiated thiol-ene reaction between the PDEGMA/PDEGSH and crude Nor-GGG-YIGSR (before HPLC purification, see Figure S27B). Crude Nor-GGG-YIGSR and PDEGMA/PDEGSH (96:4) at 1:1 ratio were dissolved in PBS and exposed to UV-light for 15 mins at 365 nm, 6 W/cm$^2$ on ice (see method section 2.6.7). To measure the conversion, aliquots were taken at 0, 5, 10 and 15 mins. Polymers were successfully purified by precipitation. A decrease in percentage of free thiols was observed by Ellman's assay, confirming that the Nor-GGG-YIGSR had reacted with the thiols. The percentage of free thiols of 1.3% were

observed at 15 mins, indicating an conversion of 65% after 15 mins. However, crude Nor-GGG-YIGSR was used which could be the cause of the incomplete conversion observed. Beside a decrease of free thiols observed, FT-IR showed the disappearance of the double bond and the appearance of the amino-groups of the peptide in the case of the reacted peptide-thiol polymer (see Figure 5.12A). Therefore, the reaction between the free thiols to the double bond of the norbornene acid group was judged to be successful.

**Table 5.4:** Decrease of free thiol present of PDEGMA/PDEGSH (96:4) was observed when exposed to UV for a longer time with Nor-GGG-YIGSR.

| **Time UV exposed [min]** | **Polymer concentration [mmol/mL]** | **Absorbance [412 nm]** | **Standard Curve/1000 [mmol/mL]** | **Thiol %** | **Conversion %** |
|---|---|---|---|---|---|
| 0 | $70 * 10^{-4}$ | 0.2483 | $2.6 * 10^{-4}$ | 3.7 | 0 |
| 5 | $19 * 10^{-4}$ | 0.0300 | $6.8 * 10^{-4}$ | 2.0 | 46 |
| 10 | $19 * 10^{-4}$ | 0.0295 | $6.8 * 10^{-4}$ | 2.0 | 46 |
| 15 | $70 * 10^{-4}$ | 0.0537 | $0.9 * 10^{-4}$ | 1.3 | 65 |

Cloud point hysteresis of the PDEGMA/PDEGS-Nor-GGG-YIGSR derivatised polymer showed a similar cloud point transition of 22°C when heated and 12°C when cooled as PDEGMA/PDEGSH (see Figure 5.12B). However, the previous decreasing slope observed of PDEGMA/ PDEGSH when cooled did not occur in case of the derivatised PDEGMA/ PDEGS-Nor-GGG-YIGSR. This observation assumes that the decreasing slope was caused by the presence of free thiols in the polymer.

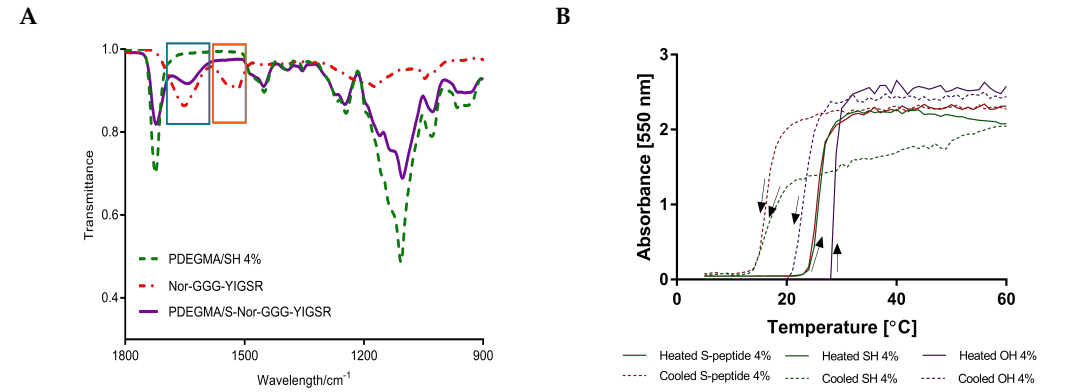



**Figure 5.12: A)** FT-IR spectra from pure Nor-GGG-YIGSR (red), PDEGMA/PDEGSH (green) and peptide functionalised PDEGMA/S-Nor-GGG-YIGSR by photo-initiated thiol-ene chemistry (purple). The double bond from the norbornene acid disappeared and the amino groups of the peptide appeared on the FT-IR of the functionalised polymer-peptide. **B)** Cloud point analysis showed a similar pattern for the peptide functionalised polymer to the PDEGMA/PDEGSH. However, the slow steady decrease of cooling down was not present after photo-initiated thiol-ene chemistry.

In summary the PDEGMA/PDEGOH and PDEGMA/PDEGSH were successfully synthesised and identified. Cloud point hysterises confirmed the thermo-responsive properties of the polymers. Free thiol presence in the PDEGMA/PDEGSH polymer was confirmed by Ellman's assay and fluorescein-5-maleimide labeling. The reactivity of the free thiol containing PDEGMA/PDEGSH to the alkene group of the norbornene acid functionalised peptide when UV exposed was confirmed in the initial experiment. Ellman's assay analysis showed decrease in free thiols on the polymer and FT-IR confirmed the presence of the peptide after the photo-initiated thiol-ene reaction.

### 5.4.2 PDEGMA/PDEGSH electrospun scaffolds

The synthesised PDEGMA/PDEGSH polymers were successfully blend electrospun with PLA in uniform fibres (19 kV, 17.5 cm, 0.5 hr/ml and 25 w/v% PLA and 10 wt% PDEGMA /PDEGSH polymers) with an average fibre diameter range of 800-1200 nm (see SEM images Figure 5.13 and fibre diameters Table 5.5). Aggregates of the PDEGMA/PDEGSH polymer (90:10) was observed when mixed with the PLA in Ac/DMF (1:1) solution. This was likely due to formation of disulfide bonds which can occur $10^3$ times faster in polar aprotic solvents (such as the DMF used in this study) than in polar protic solvents [333, 335]. Water contact angle (WCA) measurement were performed. Electrospun scaffolds with 10 wt% of 4 and 10 mole % PDEGMA/ PDEGSH showed an increasing WCA angle of 135° compared to approximately 110° for the other PDEGMA/PDEGSH containing scaffolds or control of PLA/PDEGMA (see supplementary data Figure S39). This could be due to the increase of hydrophobic nature of the co-polymer when the PDEGSH branch percentages increase.

**Table 5.5:** Representative range, average and standard deviation (SD) of the different scaffolds fibre diameters.

| %-SH | Fibre diameter range in nm | Average Fibre diameter in nm | ± SD |
|---|---|---|---|
| **0** | 450-1000 | 789 | 219 |
| **2** | 550-2700 | 1150 | 492 |
| **3** | 470-1660 | 887 | 220 |
| **4** | 570-2230 | 994 | 267 |
| **10** | 650-3100 | 1187 | 324 |

The PDEGMA/PDEGSH containing PLA electrospun scaffolds were labeled with fluor escein-5-maleimide (as described before 5.4.1) to confirm the presence of free thiols on the surface (Figure 5.13) . A second study was performed to confirm the presence of the peptide on the surface after photo-initiated thiol-ene chemistry. An ATTO NHS ester fluorescence label, which reacts with the amide group of the peptides arginine present in the peptide sequence, was added after photo-initiated thiol-ene reaction. When the peptide sequence is present a red fluorescence signal will be observed during imaging

(see Figure 5.13A). An additional fluorescein-5-maleimide staining was performed onto the derivatised scaffold surfaces to identify if any free un-reacted thiols were present after the photo-initiated thiol-ene chemistry step. Microscopy imaging showed fluorescein signals for all PDEGMA/PDEGSH containing scaffolds, confirming the presence of free thiols on the surface (see Figure 5.13) . A slight increase in intensity was observed when the percentage of thiols was higher. No fluorescein signals were present after photo- initiated thiol-ene chemistry on the derivatised scaffolds with the peptide, while ATTO fluorescent signals were observed. This confirms that the photo-initiated thiol-ene reaction was successful and no free thiols were present after the reaction. However, the expected fibrous pattern of thiols on the scaffold fibres was not observed for the fluorescein labeled thiols. This indicates an possible uneven distribution of the thiols on the fibres surface.

To investigate the distribution of the free thiols and presence of the peptides on the peptide derivatised fibrous surface in more detail Time-of-Flight Secondary Ion Mass Spectrometry (ToF-SIMS) analysis was performed. ToF-SIMS is a highly sensitive analysis method; detecting absorption of proteins on polymeric substrates as low as 10 $ng/cm^2$ [336] and was therefore considered for the chemical analysis of our scaffolds. Mass spectra peaks of the ion fragments were identified for PLA and was confirmed through literature (see supplementary data Table S7) [337–340]. The ion fragment peak $CH_3O^-$ was observed and attributed to the PDEGMA. A decrease in peak intensity of $CH_3O^-$ was observed for all the scaffolds containing PDEGMA/PDEGSH co-polymer. However, no significant correlation between the increase in intensity of the $SH^-$ and $S^-$ and increase percentage of PDEGSH present in the co-polymer was observed (see Figure 5.14). This may be due to the small difference in percentage of thiols between the scaffolds with 2-10% thiols. However, as ToF-SIMS only provides qualitative data, quantitative data (such as XPS) is needed to confirm the actual percentage of the thiols on the surface. Obtained ToF-SIMS distribution images show a fibrous pattern for the $SH^-$, while no significant fibrous structure was observed for the $CH_3O^-$ signals (see Figure 5.16, 2 and 4% thiols). This confirms an even distribution of the free thiols on the surface of the fibres, while the thermo-responsive $-OCH_3$ end group is likely

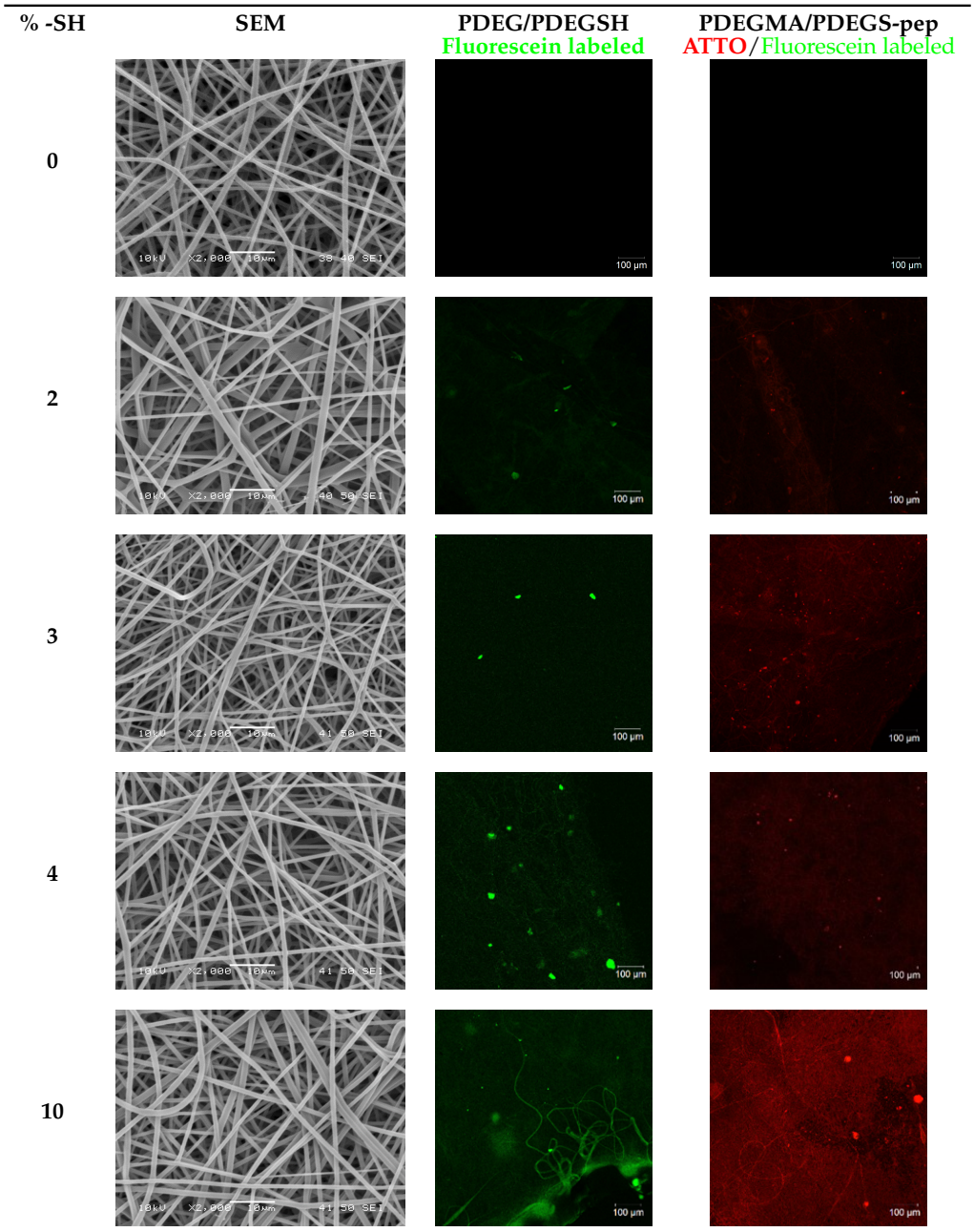



**Figure 5.13:** SEM images and fibre diameter measurement show fibres in the same diameter range for all different PDEGMA/PDEGSH ratios. Scale bar = 10 µm. Fluorescein and ATTO stained PDEGMA/PDEGSH and derivatised PDEGMA/PDEGS-Nor-GGG-YIGSR electrospun scaffolds confocal images. Thiol presence was observed by **fluorescein** staining on the PDEGMA/PDEGSH scaffolds and peptide presence after the thiol-ene reaction was observed by **ATTO** staining with subsequent **fluorescein** staining to confirm full conversion. Scale bar = 100 µm.

to be buried within the surface of the fibres and beyond the detection limit of the ion beam. The sampling depth in ToF-SIMS for Bismuth trimers is considered to be approx. 3 nm under the conditions used in these experiments. A decreases in $S^-$ was observed for photo-initiated thiol-ene derivated scaffolds (see Figure 5.15). However, the $SH^-$ 33 m/z peak was observed to increase in intensity due to the overlapping of the $PH_2$ peak from traces of PBS salts on the surface (see Figure S42), intensity are therefore not reported. This assumption was confirmed when looking at the distribution images, showing no fibrous structures for the 33 m/z peak. Instead large crystal like structures were observed (see Figure S40). This problem of overlapping peaks can be solved by more advanced ToF-SIMS orbitrap systems and improvement in the reflectron unit of the ToF-SIMS. The CNO- peak of the amino-groups of the peptide were observed for all scaffolds (included 0SH-P). Significantly higher intensity was observed for the scaffold 3S-P. While a decrease in CNO- intensity was observed for 4 and 10 S-P. Nor-GGG-YIGSR peptide fragment signals in positive spectra were identified and were corroborated to literature [341, 342]. See fragments structures of identified signals in Figure S41. Peptide fragment signals were observed for all scaffolds, including the PLA/PDEGMA scaffolds with thiol groups present. This observation of peptide on scaffolds without thiols present is due to the occurrence of non specific electrostatic binding with the surface of the scaffolds. When looking at the distribution images of the signal, an even distribution of peptide fragment peaks was observed on the 0% thiol scaffold without a defined fibre morphology. However, in case of the peptide derivatised scaffolds more defined fibre morphologies were observed (see Figure 5.17). This observation gives an indication that more specific binding onto the fibres surface occurs when free thiols are available, while some, albeit low-level, non-specific electrostatic interaction between the scaffolds surface and peptide was observed in case of scaffolds with no thiols present.

In summary, blend electrospun scaffolds of PLA with 10 wt% PDEGMA/PDEGSH (of different ratios MA:SH) polymers were fabricated. The presence of free thiol was confirmed by fluorescein-5-maleimide staining and ToF-SIMS analysis. Scaffolds were functionalised by photo-initiated thiol-ene chemistry between the free thiols and norbornene acid functionalised peptide sequence (Nor-GGG-YIGSR). Functionalisation

was confirmed by NMS-ATTO labeling and ToF-SIMS analysis.

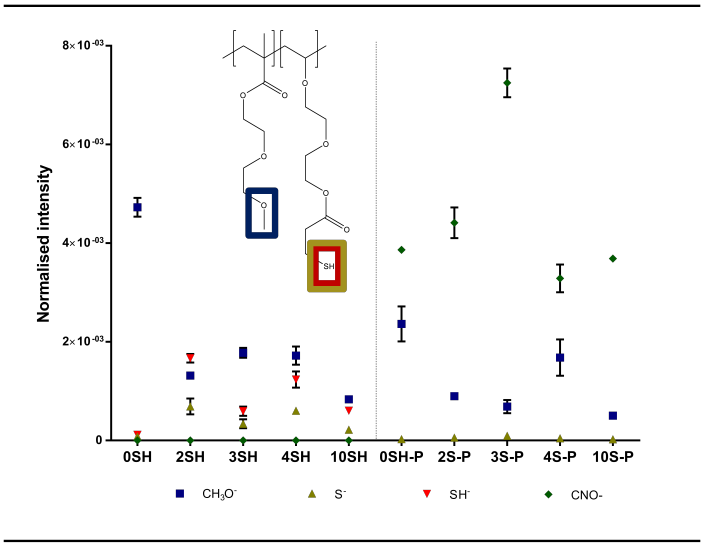



**Figure 5.14:** Total intensity of the ToF-SIMS peaks $CH_3O^-$ (31 m/z), $SH^-$ (33 m/z) and $S^-$ (32 m/z) from the free thiol containing scaffolds (n=3 measurement areas on one scaffold each, data normalised against total count, error bars = SD).

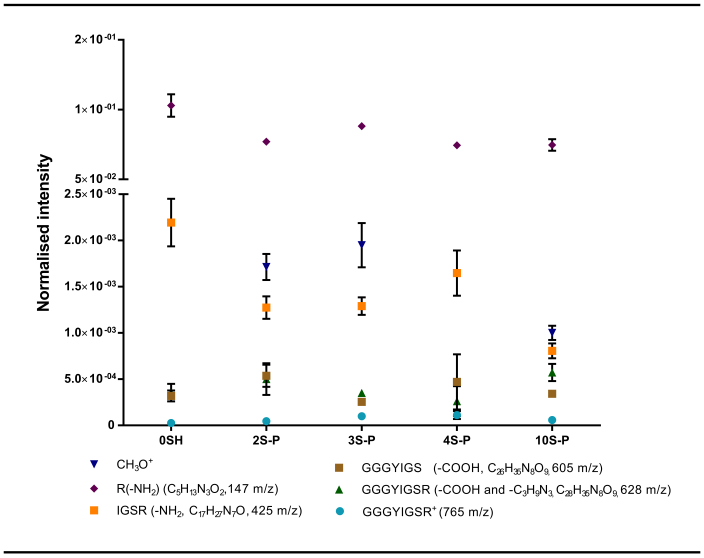



**Figure 5.15: B)** Total intensity of the ToF-SIMS peaks of different sequences of the Nor-GGGYIGSR peptide presences on the scaffold surfaces, (R(-$NH_2$, 147 m/z), GSR(-COOH, 326 m/z), IGSR (-$NH_2$, 425 m/z), GGGYIGS (-COOH, 605 m/z), GGGYIGSR (-COOH, 628 m/z) and GGGYIGSR (765 m/z) (n=3 measurement areas on one scaffold each, data normalised against total count, error bars=SD)

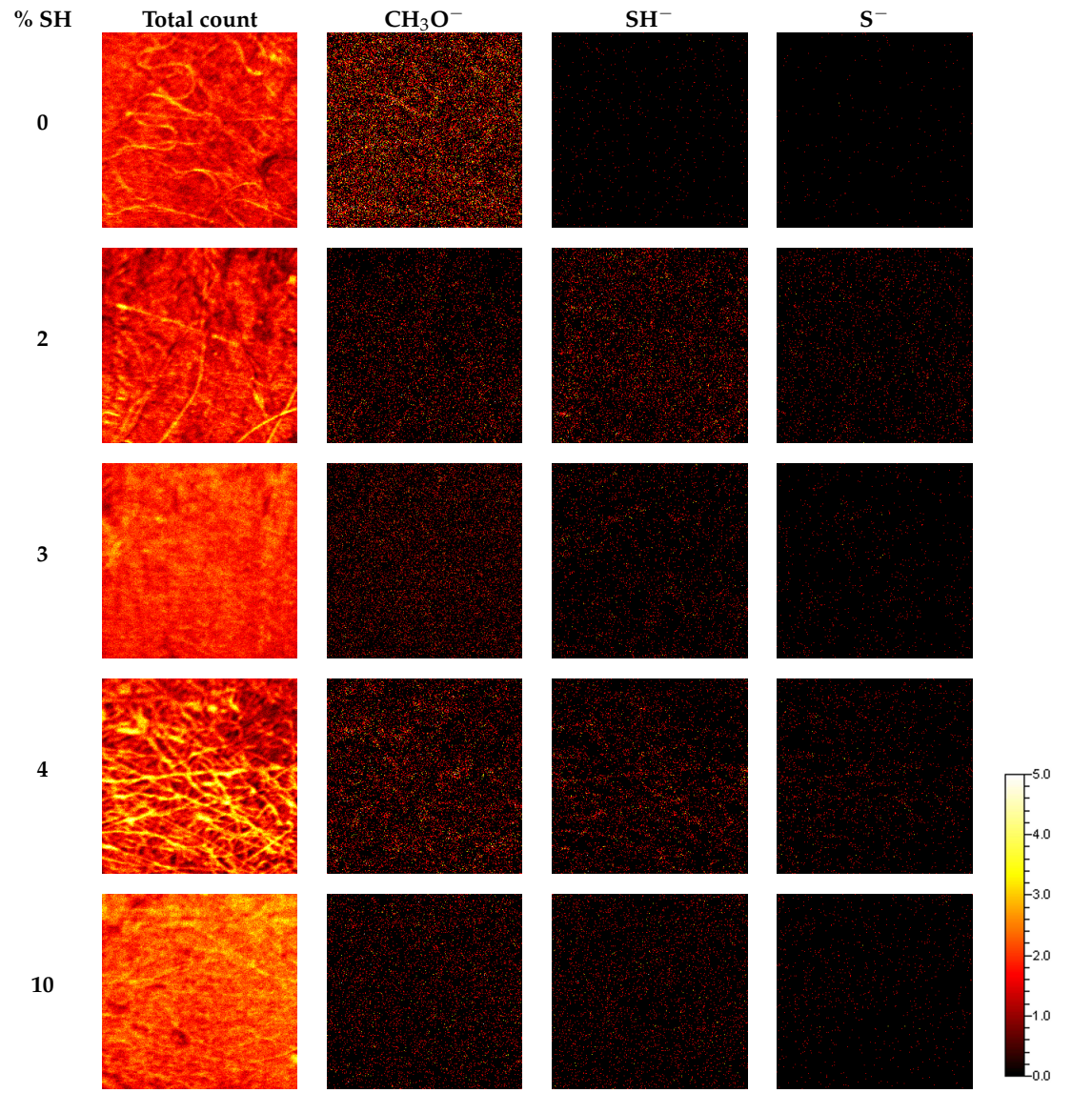



**Figure 5.16:** ToF-SIMS measurement of the free thiol containing scaffolds. **A)** Total count images, **B)** $CH_3O^-$ group of the PDEGMA thermo-responsive part of the co-polymer PDEGMA/PDEGSH, **C)** $SH^-$ group of the PDEGSH and **D)** $S^-$ group of the PDEGSH (image surface area is 500 x 500 nm, normalized to MC of 200 for total count and MC of 3 for all other signals).

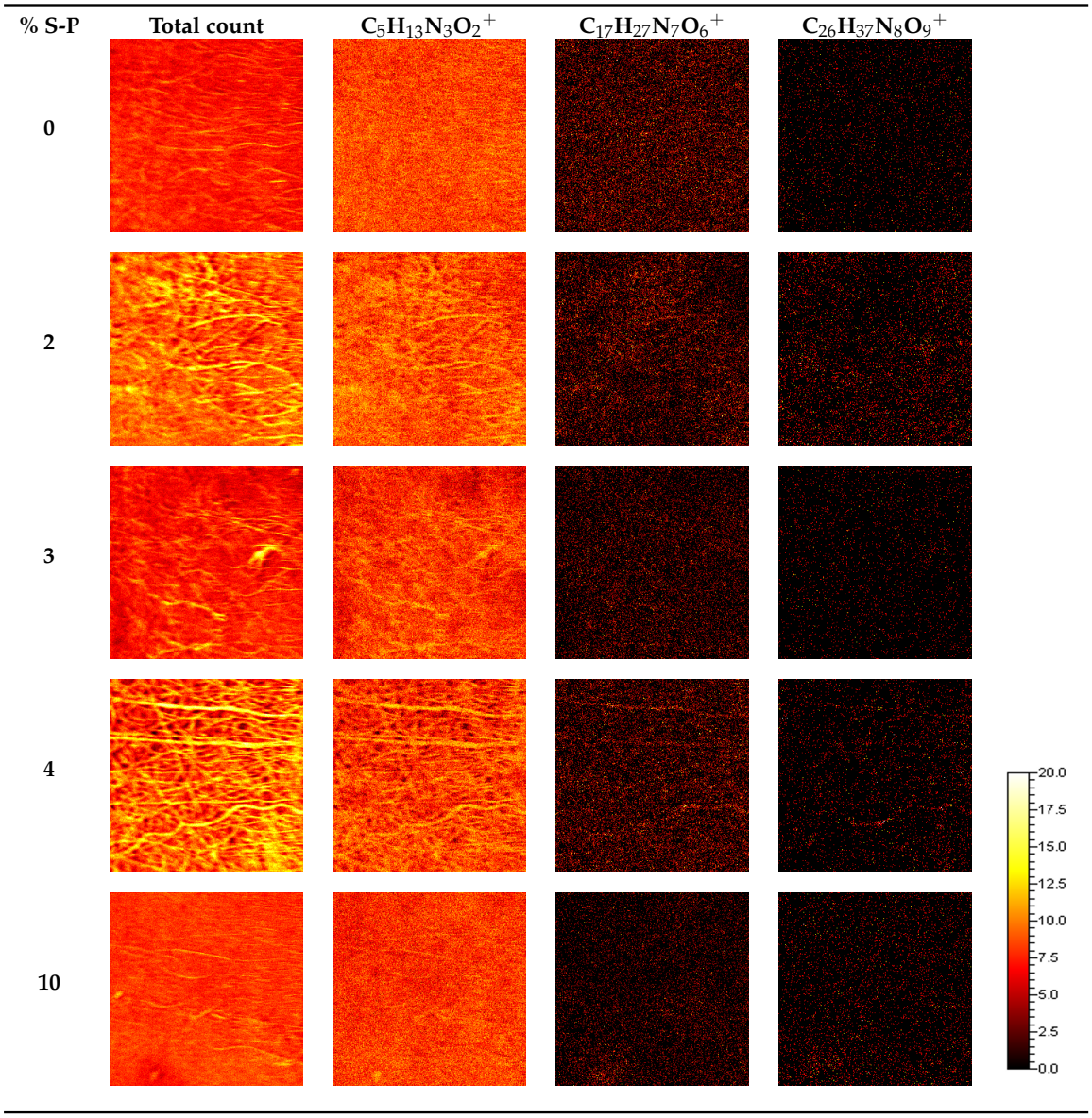



**Figure 5.17:** ToF-SIMS measurement of the derivatised scaffolds. **A)** Total count images, **B)** $C_5H_{13}N_3O_2^+$ lysine (R) part of the Nor-GGG-YIGSR sequence, **C)** $C_{17}H_{27}N_7O_6^+$ IGSR part of the Nor-GGG-YIGSR sequence and **D)** $C_{26}H_{36}N_8O_9^+$ GGGYIGS part of the Nor-GGG-YIGSR sequence (image surface area is 500 x 500 nm, normalized to MC of 200 for total count and MC of 3 for all other signals).

### 5.4.3 hCSCs behaviour studies on the photo-initiated thiol-ene peptide derivatised electrospun scaffolds.

hCSCs attachment, proliferation and phenotype expression were investigated on the different electrospun scaffolds of different surface chemistries. For this experiment the following scaffolds were used: PLA with 10 wt% PDEGMA (see Figure 5.18B), PLA with 10 wt% PDEGMA /PDEGSH (90:10) (see Figure 5.18C), PLA with 10 wt% PDEGMA/PDEGS-Nor-GGG-YIGSR (90:10) (see Figure 5.18D), PLA as negative control (see Figure 5.18A), and 0.1% gelatin coated 2D TCPS as a positive control. Significantly higher proliferation was observed on the scaffolds with free thiols and Nor-GGG-YIGSR compared to the PLA/PDEGMA scaffolds and was comparable to the positive control (see Figure 5.18E). No significant difference in cell proliferation were observed between the free thiols and Nor-GGG-YIGSR containing scaffolds. Morphology staining (actin and vimentin) studies showed clusters of cells on PLA and PLA with 10 wt% PDEGMA (as observed previously in Figure 5.6), elongated morphology on PLA with 10 wt% PDEGMA/PDEGSH (90:10), while showing spread out morphology of the cells on the peptide derivatised PLA scaffolds with 10 wt% PDEGMA/PDEGS-Nor-GGG-YIGSR (90:10). The round morphology of the cells on the PLA and PLA with 10 wt% PDEGMA scaffolds is the result of no interaction between the cells and the fibrous scaffold and can therefore be concluded unsuitable for cell attachment and support. The elongated morphology observed on the free thiol containing scaffolds is most probably due to the effect of the free thiols present. The strong nucleophilic thiolated functional group (-SH), which is also present in the cysteine groups of natural proteins, play a key role in the cross-linking of proteins. Consequently, thiolated surface can result in improved protein adsorption and subsequently better cell attachment and proliferation [343]. Esmaeilzadeh et al. [344] observed significantly more cell attachment of human keratinocyte cells (HaCaT) on thiolated polysaccharides multilayers (105 cells/mm) compared to natural polysaccharides multilayers (10 cells/mm). Jans et al. [345] also found a difference in cell morphologies of neurons cultured on thiol self-assembled monolayers with minor chemical composition differences. They concluded this was due to the protein adsorption influenced by the chemical composition.

Therefore, it can be concluded that the free thiols on the scaffolds support increased cell attachment [346]. A spread out morphology was observed when laminin mimetic sequence YIGSR peptide was present on the peptide derivatised fibres surfaces (see Figure 5.20). Uzunalli et al. [327] observed a similar spread out morphology of hCSCs when cultured on YIGSR containing nanofibres compared to fibronectin-mimetic peptide nanofibres, as well as, increased proliferation, supporting the findings reported here.

Immuno-staining of the hCSCs showed the keratocyte phenotype markers CD34 and ALDH, and mesenchymal stem cell (MSC) expression of CD105 on all the different surfaces (see Figure 5.19). However, the undesired myofibroblast phenotype expression of α-SMA was observed on the PLA, PLA with 10 wt% PDEGMA and 2D TCPS control. As well as, a very low expression of α-SMA was observed on the PLA with 10 wt% PDEGMA/ PDEGSH (90:10). While no α-SMA expression was observed on the derivatised PLA with 10 wt% PDEGMA/PDEGS-Nor-GGG-YIGSR (90:10) scaffolds. This confirms that the peptide supports keratocyte phenotype expression and suppresses de-differentiation of the keratocytes to their myofibroblast phenotype. The PLA with 10 wt% PDEGMA/PDEGSH (90:10) and derivatised PLA with 10 wt% PDEGMA/PDEGS-Nor-GGG-YIGSR (90:10) scaffolds shows increased phenotype support and cell attachment compared to the PLA and PLA with 10 wt% PDGEMA. However, the presence of α-SMA and and elongated morphology of the cells on the scaffolds with 10 wt% PDEGMA/PDEGSH (90:10) indicates a slight change to fibroblastic characteristics. While, the derivatised PLA with 10 wt% PDEGMA/PDEGS-Nor-GGG-YIGSR (90:10) scaffolds showed increased support of the keratocyte phenotype, showing only the keratocyte antibody expression and morphology. Therefore, the presence of the YIGSR peptide sequence can be concluded to support the desired keratocyte phenotype compared to all other scaffolds and the 2D TCPS control.

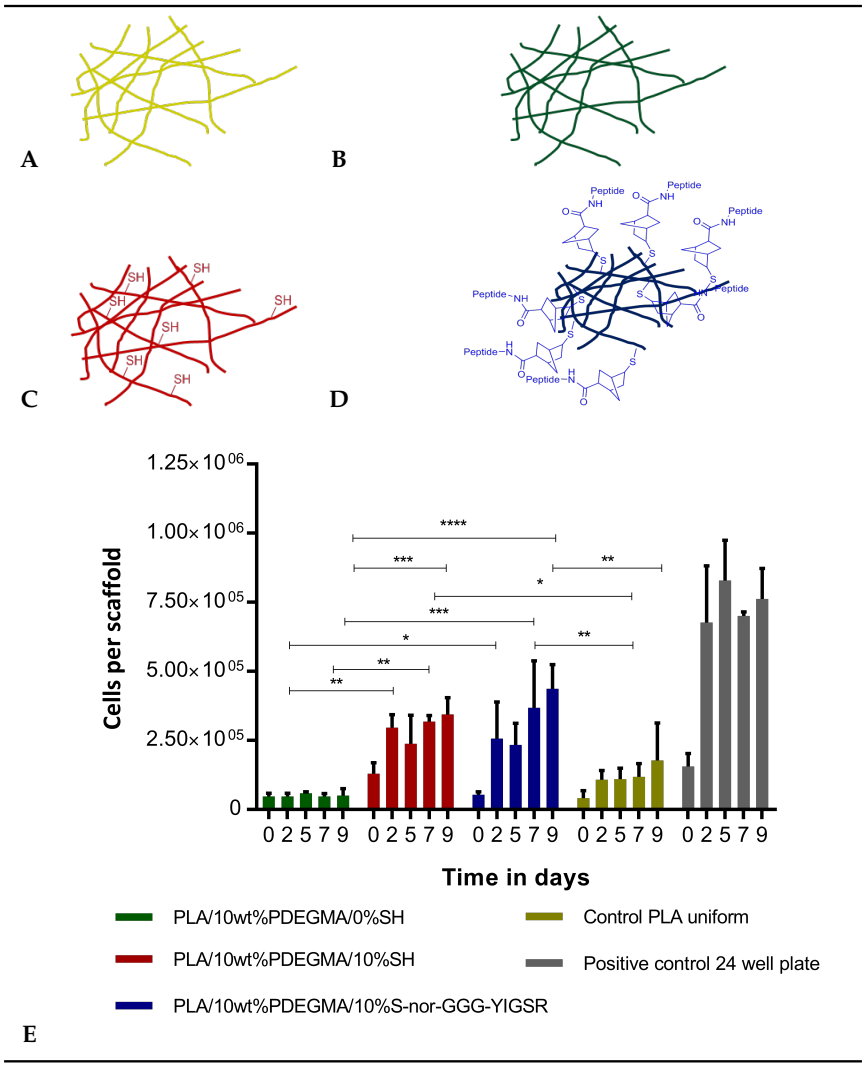



**Figure 5.18:** hCSCs cultured on PLA fibrous scaffolds with different surface chemistry as compared with 2D control. **A)** PLA, **B)** PLA with PDEGMA, **C)** PLA with PDEGMA/PDEGSH and **D)** derivatised PLA with PDEGMA-DPEGS-Nor-GGG-YIGSR. **E)** Number of cells per scaffold were identified using Alamar blue assay. Increased proliferation was observed on thiol and peptide functionalised scaffold. (n=3 scaffolds, hCSCs of one donor. two-way ANOVA, *=<0.05, **=<0.01, ***=<0.001, ****=<0.0001, error bars=SD)

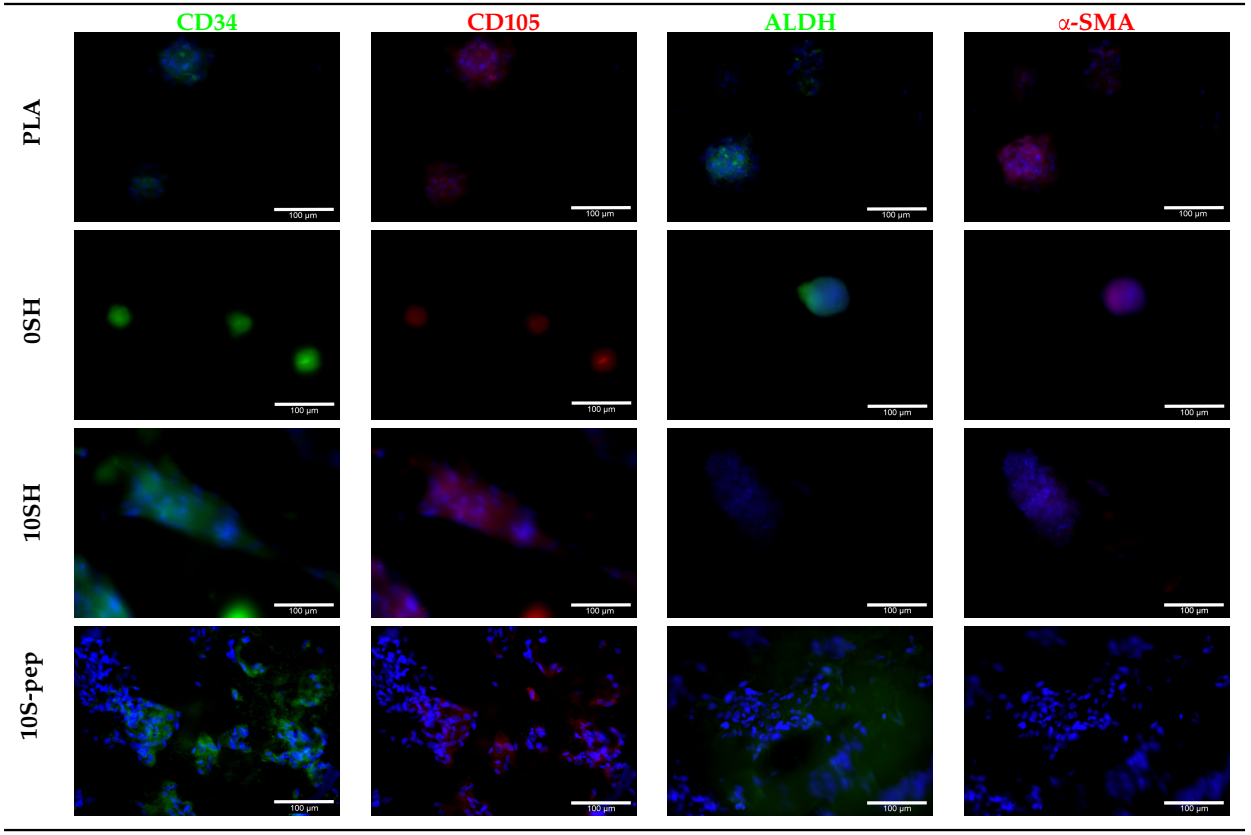



**Figure 5.19:** Representative confocal images of hCSCs cultured on PLA fibrous scaffolds with different surface chemistry and their corresponding phenotype expression. Cell immuno-stained with keratocytes markers CD34 and ALDH, MSC marker CD105 and fibroblast marker α-SMA. The nuclei was stained with DAPI. Scale bar = 100 µm.

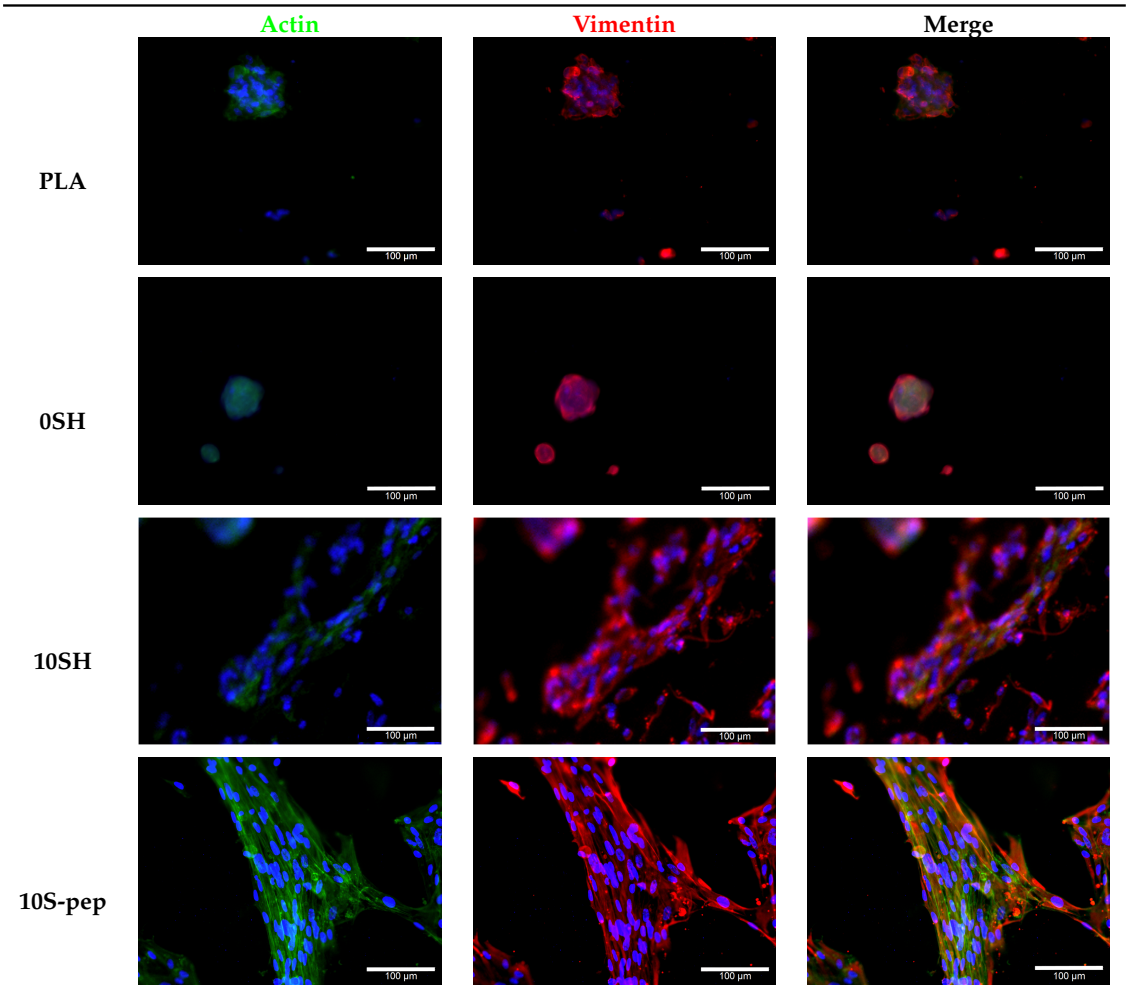



**Figure 5.20:** Representative confocal images of hCSCs cultured on PLA fibrous scaffolds with different surface chemistry and their corresponding morphology. Cells immuno-stained with Actin, Vimentin and the nuclei with DAPI. Scale bar = 100 µm.

ECM expression after 9 days cell culture on thiol containing and peptide derivatised scaffolds was investigated to confirm the hypotheses that the free thiol group containing scaffold supports ECM expression and adsorption and hence cell adhesion and proliferation as observed in Figure 5.18 and Figure 5.20. Cells were fixed and stained with collagen I and lumican to observe their ECM expression. Collagen I expression was observed for all scaffolds (see Figure 5.21). The collagen I expression is increasingly higher and more evenly distributed on the peptide containing scaffolds. Stromal keratocytes in normal unwounded cornea express the keratan proteoglycan (KSPG) lu-

mican. Lumican is a key regulator of collagen fibrilogenesis, responsible for the unique corneal transparency [347, 348]. For keratocytes to express lumican, collagen I needs to be present as well. Lumican expression is therefore identified as a marker of the quiescent phenotype of hCSCs in a later stage of ECM expression. Lumican was observed on the scaffold with peptide present, including the 0SH scaffold wiht non-specific bound peptide. This shows that the non-specific bounded Nor-GGG-YIGSR on the surface observed during ToF-SIMS analysis does support ECM expression. However, clusters of cells were still observed. This observation shows that non specifically bound peptide does not support cell interaction with the scaffold. Only when the peptide is bound to the fibres surface cells are able to spread out on the scaffolds' surface. Increased amount of Lumican was observed for the peptide bound scaffold with 3, 4 and 10% PDEGSH presence confirming this statement.

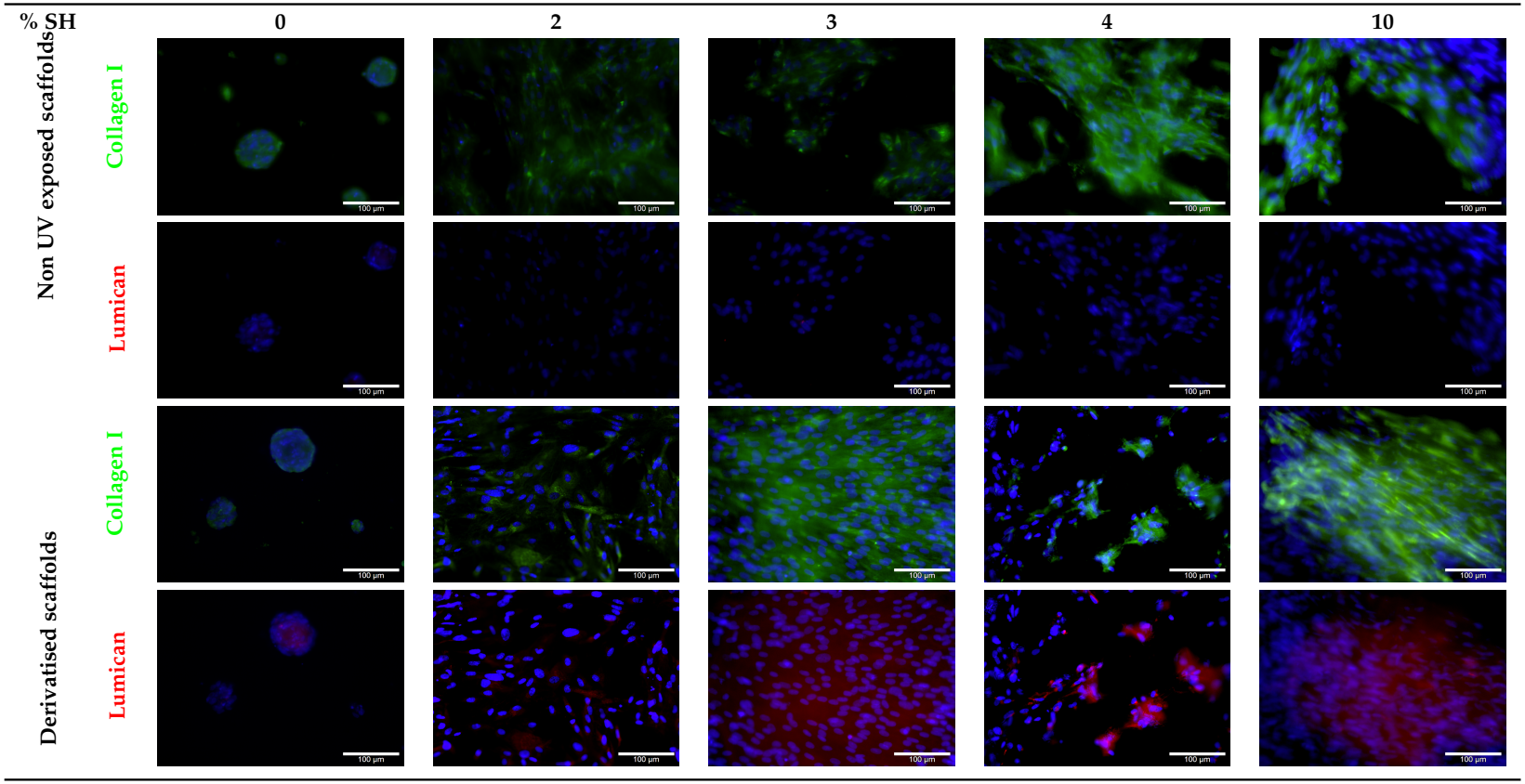



**Figure 5.21:** Representative confocal images of ECM deposition onto free thiol containing scaffolds and derivatised peptide containing scaffolds following culture of hCSCs. Cell immuno-stained with Collagen I, Lumican and the nuclei with DAPI. Scale bar = 100 µm.

As the derivatised scaffolds with the Nor-GGG-YIGSR peptide was observed to promote the desired phenotype and ECM expression, the proliferation and response of hCSCs on a range of different concentrations of PDEGMA/PDES-Nor-GGG-YIGSR scaffolds were investigated. After 9 days cell culture, significantly higher proliferation was observed for 3 and 10% peptide derivatised scaffolds(see Figure 5.22A). The keratocyte phenotype CD34 and ALDH markers were observed for all different concentrations of peptide. A significantly increased expression of ALDH was observed for the 3% peptide scaffold (see Figure 5.23). As ALDH expression plays an important role in the maintenance of the cornea's transparency, this expression is desired to be maintained in cell culture. CD105 MSC marker expression was observed on all scaffolds. This change to a more stem cell like phenotype suggests a loss of the differentiated quiescent phenotype [194]. The myofibroblastic α-SMA expression was observed for 2% peptide and 0% control. These observations give an indication that there is a threshold of peptide percentage needed to be present to avoid myofibroblast activation. Peptide concentrations of 2% was too low to support the quiescent phenotype and resulted in myofibroblastic change, while scaffolds containing 3% peptide and above resulted in no α-SMA expression. The previously rounded and cluster cell morphology was observed on the scaffolds containing 0 and 2% peptide concentrations, while a more spread out morphology was observed for concentration above 2% (see Figure 5.24). Therefore, this threshold peptide percentage on the scaffold above 2% resulted in a higher interaction of the cells with the scaffolds' surface. It can therefore be concluded that a percentage above 2% of Nor-GGG-YIGSR bound to the scaffolds fibres surface significantly improves the cell attachment, proliferation and support a quiescent cell phenotype.

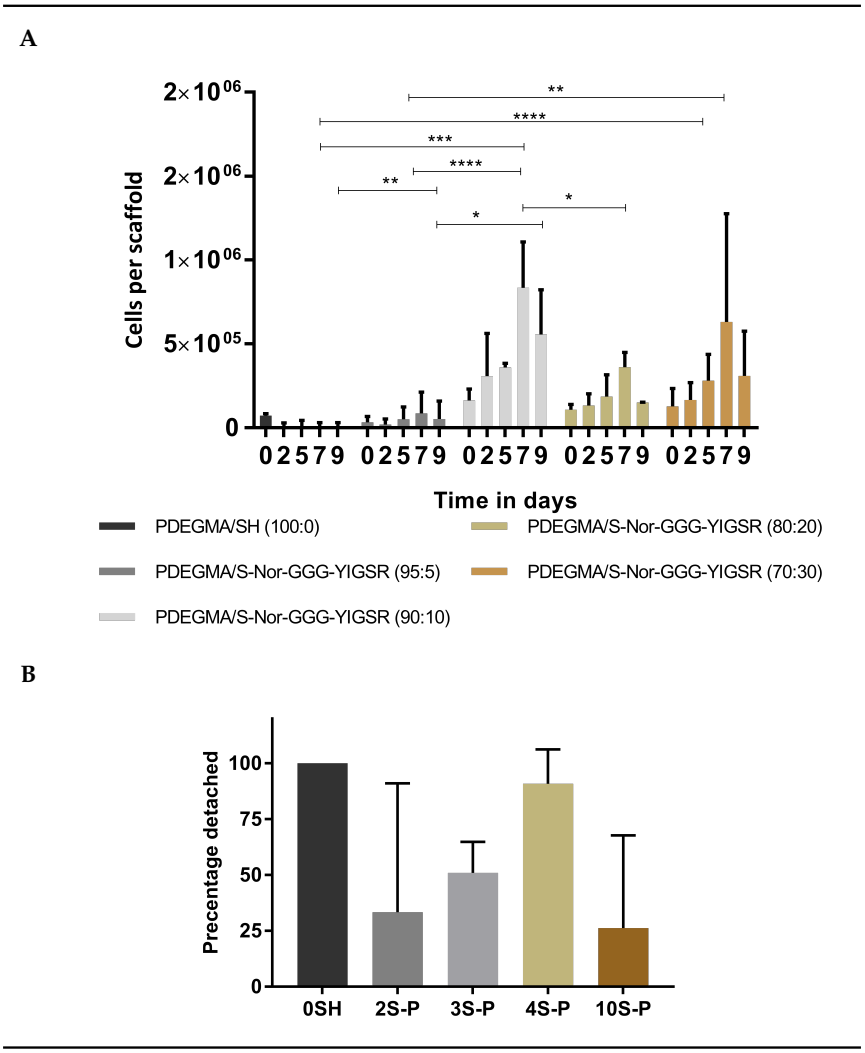



**Figure 5.22:** hCSCs cell culture over 9 days in serum free media on different % peptide derivatised onto the fibrous surface. **A)** Number of cells per scaffold were identified by Alamar blue assay. Increased proliferation was observed on thiol and peptide functionalised scaffold. **B)** Cell number per scaffolds before thermo-responsive passaging after 9 days cell culture at 37°C and after thermo-responsive passaging at 8°C for 30 mins (n=3 scaffolds, two-way ANOVA, *=<0.05, **=<0.01, ***=<0.001, ****=<0.0001, error bars=SD)

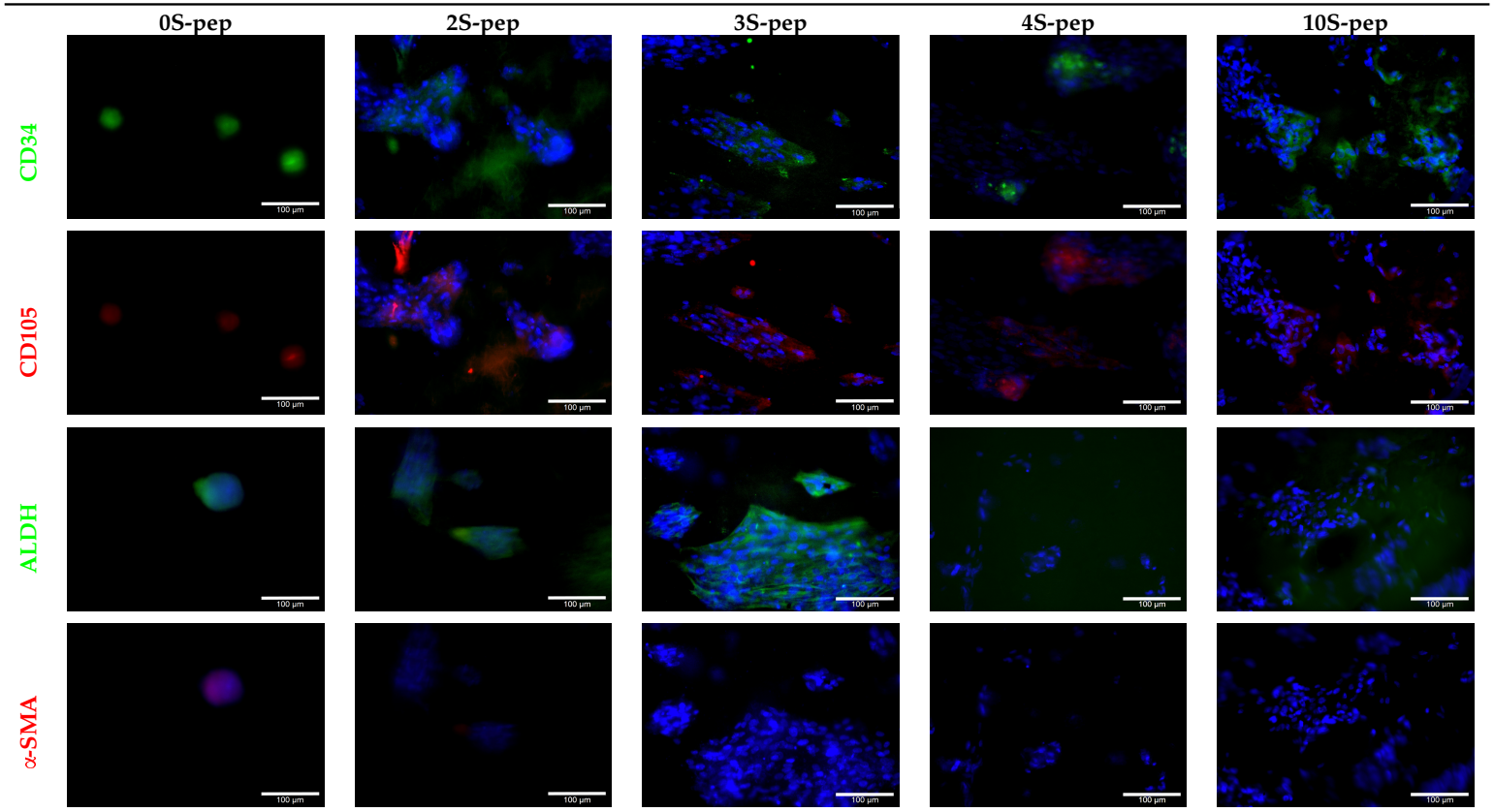



**Figure 5.23:** Representative confocal images of hCSCs on scaffolds containing different percentages of bound Nor-GGG-YIGSR peptide and their corresponding phenotype expression. Cell immuno-stained with keratocytes markers CD34 and ALDH, MSC marker CD105 and fibroblast marker α-SMA. The nuclei was stained with DAPI. Scale bar = 100 µm.

### 5.4.4 Thermo-responsive passaging

The thermo-responsive PDEGMA/PDEGS-Nor-GGG-YIGSR polymer PLA scaffolds were not only designed to improve the cell attachment and phenotype support, but also to prevent cell damage observed through enzymatic passaging. Many studies to date have investigated the potential of the thermo-responsive polymer PNIPAM for corneal cell type detachment [157, 159, 173, 174]. Teichmann et al. [157] successfully detached human corneal endothelial cells (HCEC) from 2D coated PNIPAM/poly(vinyl methyl ether)-based composites. Positive function-associated marker and extracellular matrix proteins expression before and after cell detachment transfer has been observed. Nara et al. [159] also investigated the use of PNIPAM for the detachment of keratocytes from silk-PNIPAM and gelatin-PNIPAM patterned surfaces. They observed cell sheet detachment of keratocytes within 10 mins of temperature change (37°C to 20°C). However, no studies to day have reported the use of thermo-responsive polymer PDEGMA used in this study. In this section a preliminary experiment illustrating the ability to culture and detach cells from PDEGMA and PDEGMA/PDEGS-Nor-GGG-YIGSR containing scaffolds and subsequent quantitative assessment of the cells phenotype by flow cytometry analysis (FACS). hCSCs grown on peptide derivatised fibrous scaffolds containing different concentrations of PDEGMA/PDEGS-Nor-GGG-YIGSR were passaged after 9 days of cell culture at 37°C by placing the scaffolds in the fridge for 30 mins at 8°C. Cell numbers on scaffolds were calculated by Alamar blue assay before and after thermo-responsive passaging (see standard curve used Figure S29B) and percentage detached was calculated. Cell detachment was observed for all scaffolds with no significant difference in percentage of population detached. However, large standard deviations were observed for the scaffolds containing 2 and 10% PDEGMA/PDEGS-Nor-GGG-YIGSR (see Figure 5.22B). This was due to no detachment observed for two of the three samples and one of the three samples containing 2 and 10% PDEGMA/PDEGS-Nor-GGG-YIGSR respectively. This may be due to hindrance of the thermo-responsive brushes by the peptide sequence attached to the same polymer. Nonetheless, more consistent detachment cell numbers were observed for the scaffold containing 3 and 4% PDEGMA/PDEGS-Nor-GGG-YIGSR. The thermo-

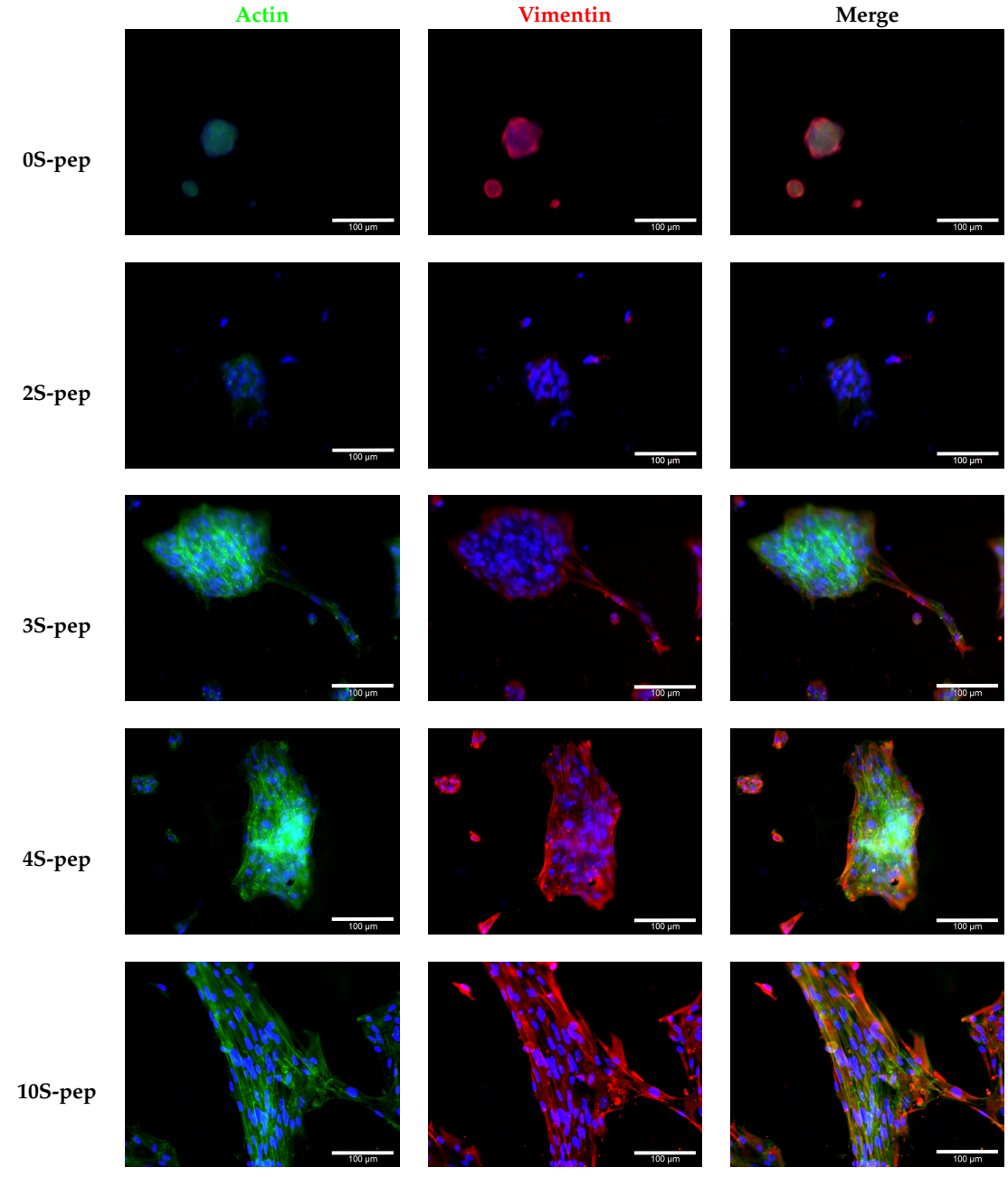



**Figure 5.24:** Representative confocal images of hCSCs on scaffolds containing different percentages of bound Nor-GGG-YIGSR peptide. Cell immuno-stained with Actin, Vimentin and the nuclei with DAPI. Scale bar = 100 µm.

responsive behaviour of the scaffold was therefore considered inconsistent and further work is required.

Flow cytometry was conducted for the cells detached from the scaffolds to support immuno-staining findings. Cells grown on gelatin coated 2D TCPS and passaged by TripLE were used as control. Cell number obtained after staining and washes ranged from 1000 to 2000 cells per scaffold. This is significantly lower than the number of cells seeded of 60.000 cells per scaffold. This difference may be due to loss of cells during the washing steps of the staining protocol. Cells cultured on 3% peptide scaffolds were observed to have an increased cell sub-population of 15.98% of only expressing the $CD34^{+}/CD105^{-}$ keratocyte marker (see Table 5.6) compared to all other scaffolds. However, $CD34^{-}/CD105^{+}$ and $CD34^{+}/CD105^{+}$ sub-populations combined comprised of half of the total cell population (53%, see Table S10 and Table S11). While $CD34^{+}/CD105^{+}$ and $CD34^{+}/CD105^{-}$ comprised 45% of the total cell population. Therefore, a significant percentage of the population show MSC characteristics beside the desired keratocyte CD34 marker.

**Table 5.6:** Flow cytometry % of cell population of keratocyte phenotype expression. Two groups of combination staining were performed (CD34/CD105 and ALDH/α-SMA). -/- is population of cells with no staining observed. -/+ is population of cells with the undesired activated phenotype expression. +/- is population of cells with the desired quiescent phenotype expression and +/+ is population of cells with the both desired and undesired activated phenotype expression. (n=3 scaffolds per staining group)

| | % of cell population | | | | | | | |
|---|---|---|---|---|---|---|---|---|
| | CD34/CD105 | | | | ALDH/α-SMA | | | |
| | -/- | -/+ | +/- | +/+ | -/- | -/+ | +/- | +/+ |
| **0S-P** | 68.11 | 9.3 | 5.76 | 16.83 | 22.11 | 10.89 | 34.49 | 32.51 |
| **2S-P** | 37.38 | 31.07 | 7.22 | 24.33 | 46.30 | 10.49 | 29.63 | 13.58 |
| **3S-P** | 31.45 | 23.98 | 15.96 | 28.62 | 38.91 | 3.04 | 32.83 | 25.23 |
| **4S-P** | 45.40 | 16.25 | 3.58 | 34.78 | 37.71 | 4.97 | 44.24 | 13.61 |
| **10S-P** | 28.81 | 21.15 | 3.52 | 46.51 | 38.94 | 16.13 | 28.80 | 16.13 |
| **2D-Gelatin** | 9.07 | 21.44 | 4.48 | 65.01 | 0.75 | 0.13 | 6.54 | 92.58 |

A similar sub-population percentage of $CD34^-/CD105^+$ and $CD34^+/CD105^+$ of 51% was observed for the scaffolds with 4% peptide on the surface, nevertheless an increase of total cell population expressed the CD34 marker (38% of total cell population). Significantly less $CD34^+/CD105^+$ was observed for all scaffolds compared to the 2D TCPS control when comparing the Y-mean (see means and ANOVA values Table S8 and Table S9). This observation shows that the 3D structure significantly reduces the expression of MSC marker CD105. While, no significant difference could be observed for the different percentage peptides. This may be due to the small scaffold size and small sample size (n=3 scaffolds), as well as, the largest population percentage of cells expressing no markers (-/-). This high percentage -/- could be due to insufficient staining and therefore the experiment needs to be repeated. Equally an increased expression of $ALDH^+/\alpha\text{-SMA}^-$ was observed for 3 and 4% peptide scaffolds. Only 24, 28, 19 and 32% of the total cell population ($ALDH^+/\alpha\text{-SMA}^-$ and $ALDH^+/\alpha\text{-SMA}^-$ combined, see Table S10 and Table S11) for 2, 3, 4 and 10% peptide respectively were observed to express the α-SMA activated myofibroblastic marker. This was significantly less than the 93% observed for the 2D control. Hence the 3D structure of the scaffolds containing specifically bound peptide on the surface reduces the differentiation to the undesired activated myofibroblastic phenotype expression compared to the 2D control. Although no significant difference could be observed between the scaffolds for the CD34/CD105 expression. A significant decrease of $ALDH^+/\alpha\text{-SMA}^-$ was observed for the scaffolds with 3 and 4% peptide compared to 2D and non-specific bound peptide 0% scaffold when comparing the X-mean (see means and ANOVA values Table S8 and Table S9). This gives an indication that the specific bounded peptide does reduce the change to the active myofibroblast phenotype and supports increased ALDH expression.

3D fibrous scaffolds for cell culture and tissue engineering has been an increasing area of interest within the research community [71, 276, 349–351]. The nanofibrous structure is designed to mimic ECM properties, resulting in an increased in desired cell response. However, these synthetic polymers are non native to the cells which could result to no cell detachment, inflammation or undesired cell differentiation due to their mechanical or chemical properties (such as stiffness and hydrophobicity). Peptide or protein incorporation or functionalisation has been investigated to overcome this hur-

dle [276, 327, 352–354]. For example, Rodina et al. [276] investigated migration and proliferation of mesenchymal stromal stem cells (MSSCs) on collagen protein modified PLA fibrous scaffolds. They observed more uniform distribution and cell penetration into these modified scaffolds. Beside proteins more specific peptide sequences can be used. Arg-Gly-Asp (RGD) collagen peptide sequence is the most commonly used peptide incorporated in biomaterials to increase their cell adherence properties. For instance Hogrebe and Gooch [355] incorporated a RGD to improve cell binding in self-assembling fibrous peptide hydrogel systems for hMSCs cell culture. Similarly, Shin et al. [356] observed significant improvement in the physical interaction of cells on RGD incorporated alginate particles. Besides, incorporation of known cell attachment peptide sequences (such as RGD), more cell specific peptide sequence can be incorporated to improve specific cell type behaviour or differentiation on the materials. For example, Li et al. [354] incorporated the specific bone morphogenetic protein-2-related peptide P24 and $rhBMP_2$ into PLGA/CS micro-spheres to the improvement of the repair of rat cranial bone defects. They observed significantly improved bone repair for PLGA/CS micro-spheres containing P24 and $rhBMR_2$ compared to the blank PLGA/CS spheres.

This study showed a similar approach by functionalising thermo-responsive fibrous scaffolds with a laminin-1 peptide conjugate YIGSR to promote hCSCs interaction and to support quiescent keratocyte to the designed thermo- responsive PLA/PDEGMA scaffolds. Previous studies have demonstrated that laminin improves growth, organisation and differentiation of many cell types [327, 357–360]. Nonetheless, laminin has many disadvantages such as degradation, tumorigenesis and immuno responses, which make the full sequence unsuitable for clinical application [361]. This risk can be minimised by selecting small peptide sequences within the laminin sequence which have the ability to improve adhesion and cell migration. One of these sequences is YIGSR which has been observed to improve cell adhesion and migration [362–364]. For example, Nam et al. [364] observed promotion of wound healing of the salivary gland tissue by laminin 1 peptide-conjugated (YIGSR-A99) containing fibrin hydrogels. While, Zhu et al. [73] observed axonal regeneration and functional recovery on non-covalent bounded RGD/YIGSR poly($\epsilon$-caprolactone) (PCL) electrospun conduits. Neuronal and salivary cells exhibited similar cell adhesion and proliferation

as observed for cells from the cornea. Nibourg et al. [365] investigated the use of two laminin-derived peptides (IKVAV and YIGSR) in different ratios when incorporated in nanogels to moderate the common compilation capsular opacification (CO) seen after cataract surgery. This decline in transparency is due to lens epithelial cell (LECs) proliferation, migration and trans-differentiation, also referred to as epithelial-to-mesenchymal transformation (EMT). They observed no LEC transformation in the form of cellular spreading when peptides-nanogels were implanted in the lens after the surgery. While in a previous study [366] severe cellular spreading was observed in case of nanogels not containing peptides. Uzunalli et al. [327] investigated the response of hCSCs on bioactive self-assembled peptides nanofibres. They investigated two peptide sequences 1) YIGSR (laminin derived) and 2) RGD (fibronectin derived). hCSCs were observed to maintain their characteristic morphology, and their proliferation was enhanced when YIGSR was present. Significantly less proliferation was observed for the RGD fibres as well as less cell adhesion was observed. This concludes that the use of YIGSR sequence has a direct impact on cell adherence, proliferation and migration on 3D structures. These observations are in line with the increase in proliferation observed of the hCSCs on our scaffolds with increasing ratio of GGG-YIGSR covalently bound on the surface. Many studies have reported improved adherence and proliferation of human cornea epithelial cells [75, 328, 367–369]. However, only one paper reports the response of hCSCs on YIGSR incorporated scaffolds [327], and no phenotypic support study has been performed to our knowledge. The immuno-staining and FACS data reported here concluded that not only does YIGSR support adherence and proliferation on the fibrous scaffold, but also supports a higher percentage of population of cells expressing the desired phenotype. Down-regulation of the undesired myofibroblastic marker α-SMA was observed, while up-regulation of keratocyte markers CD34 and ALDH were also observed. hCSCs have a low limit of passages (5 passages max.) before dedifferentiation into activated myofibroblasts. Phenotype characteristics were observed to stay constant when passaged by the thermo-responsive enzymatic free passaging capabilities of the scaffolds. This gives an indication that the designed scaffold can support the desired phenotype during cell culture and passaging and give rise to possible uses of these scaffolds as hCSCs cell culture platforms. However, only

one passage was performed in a small scale. More research is needed to confirm if the desired phenotype stays present when cultured for multiple passage cycles.

## 5.5 Conclusion

The aim of this chapter was to use the thermo-responsive electrospun scaffolds for human cornea stromal cells (hCSCs) proliferation, phenotype support and enzymatic digestion-free passaging. The initially proposed scaffolds (PLA with 10 wt% PDEGMA) did not support hCSCs adhesion and proliferation. Therefore, a peptide functionalised scaffold was produced to improve the hCSCs attachment on the scaffold and support the quiescent phenotype. PDEGMA/PDEGSH polymers were successfully synthesised. Thermo-responsive properties and free thiols of the polymers were confirmed present. The polymers were successfully blend-electrospun with PLA into fibrous scaffolds. Free thiol presence on the scaffolds' surfaces was confirmed by fluorescein-5-maleimide labeling and ToF-SIMS analysis. The peptide sequence Nor-GGG-YIGSR derivatised on the surface of these fibres was successfully performed and confirmed by ATTO labeling and ToF-SIMS analysis. Non-specific binding (electrostatic binding) was observed on the thermo-responsive fibrous scaffold with no thiols present. However, morphology studies showed aggregated cells on these scaffolds, while elongated and spread cell morphologies were observed on thiol containing scaffold. Therefore, specifically bounded peptide on the fibres only results in increasing hCSCs interaction with the scaffold. The undesired myofibroblastic phenotype was observed to decrease with increased percentage of Nor-GGG-YIGSR bound to the scaffolds surface. However, a high conc. of peptide resulted in a decrease in keratocyte specific markers ALDH and CD34. However, a concentration of between 3 and 4% Nor-GGG-YIGSR resulted to the highest expression of keratocyte markers, while suppressing the active myofibroblastic phenotype. Cells were observed to detach from the scaffolds in cell population percentages of 80-100%. However, some scaffolds resulted in no full detachment. Despite inconsistent detachment of the cells from the scaffolds, cells were able to retain their cell phenotype after thermo-passaging. Hence it can be concluded

that the design thermo-responsive peptide conjugate fibrous scaffolds are suitable for the adherence, proliferation and quiescent keratocyte phenotype support and thermo-passaging of hCSCs. Making them a possible alternative for the expansion of hCSCs for tissue engineering and clinical applications.

# Chapter 6

# Conclusion

This PhD study aimed to fabricate an enzymatic digestion free thermo-responsive 3D cell culture platform for the expansion of cells, which can be tailored to the cell type of choice. 3D PLA scaffolds were fabricated with the use of electrospinning. Process parameter interactions were investigated and optimised with the use of a Design of Experiment approach. The interaction of the flow rate and polymer concentration was observed to have a significant impact on the resultant electrospun fibre diameter, while fibre morphology and the extent of beading was mainly controlled by the polymer concentration. The obtained prediction model was tested experimentally and the prediction of the fibre diameter and morphology was observed successful. Cell culture on the obtained different fibrous scaffolds (uniform, beads-on-strings and big beads) showed no significant difference in the proliferation of 3T3 fibroblast on uniform and beads-on-string morphologies. In conclusion, the presence of fibre defects (such as beading) has no significant impact on the cell behaviour. The optimised electrospun method was taken forward for the fabrication of PDEGMA containing PLA scaffolds. Even distribution of the thermo-responsive polymer in the fibrous scaffolds was confirmed by fluorescent labeled PBI-PDEGMA. Scaffolds with a 10 wt% PDGEMA ratio to PLA were observed to show the higher levels of 3T3 cell detachment by thermo-responsive behaviour when cooled for 30 mins at 8 °C. However, only a maximum of 25% of the 3T3 cells detached was observed. Increasing fibre diameter and different

cooling methods did not result in higher levels of cell detachment. While, PDEGMA coated PLA fibres and PDEGMA coated TCPS showed a significantly higher detachment percentage. This finding concludes an insufficient thermo-responsive behaviour of the scaffolds for the detachment of 3T3 fibroblasts. However, detachment of hCSCs observed to be significantly higher from these same scaffolds.

The optimised scaffolds were functionalised with Nor-GGG-YIGSR with the use of photo-initiated thiol-ene chemistry to improve the hCSCs behaviour and phenotypic expression on the PDEGMA/PLA scaffolds. The co-polymer PDEGMA/PDEGSH was successfully synthesised and blend electrospun with PLA into fibrous scaffolds. Fluorescent labeling and ToF-SIMS analysis confirmed the presence of free thiol and peptide groups when functionalised by thiol-ene chemistry on the surface of the fibres in an even distribution. However, electrostatic interaction of peptide to the PDEGMA/PLA control was observed. Nonetheless, no improved cell interaction of the hCSCs on the control was observed. This concluded that non-specific bound peptides did not improve the cellular behaviour on the scaffolds. In contrast, specifically bound peptide (achieved by photo-initiated thiol-ene conjugation) was observed to improve the cellular attachment to the scaffolds, as well as, supporting the desired quiescent phenotype of the hCSCs. hCSCs were successfully detached from the scaffolds after proliferation and flow cytometry analysis showed an increase in the cell population of the desired quiescent hCSCs phenotype. These findings demonstrate the potential of the optimised thermo-responsive YIGSR derived PLA scaffolds for the adherence, proliferation and recovery of quiescent hCSCs as a cell expansion technique for cellular therapies and tissue engineering applications. Additionally, these scaffolds can be tailored with different peptides for adherence, proliferation and detachment of the cell type of choice.

# Chapter 7

# Future work

## 7.1 Electrospinning optimisation and scaffold characterisation.

The discussed DoE model in this study could be expanded with many more input factors to improve electrospinning process parameter understanding. This could include different solvents, different polymers or polymer blends and subsequently will increase the accuracy of the model.

The measurement of the random electrospun scaffolds Young's modulus was challenging, due to AFM tip disconnection. Although many studies have investigated one fibre tensile testing, no real method has been establish for the measurement of bulk fibres in a random formation. Future possibilities are to change the pointed conventional AFM tip with a beaded AFM colloid probe with a size greater than the porosity of the fibrous scaffolds (diameter size similar to cell size), which reduces the possible disconnection of the tip to the fibrous surface when measured (see Figure 7.1). This will give a more accurate representation of the Young's modulus experienced by the cells when in contact with the fibrous surface.

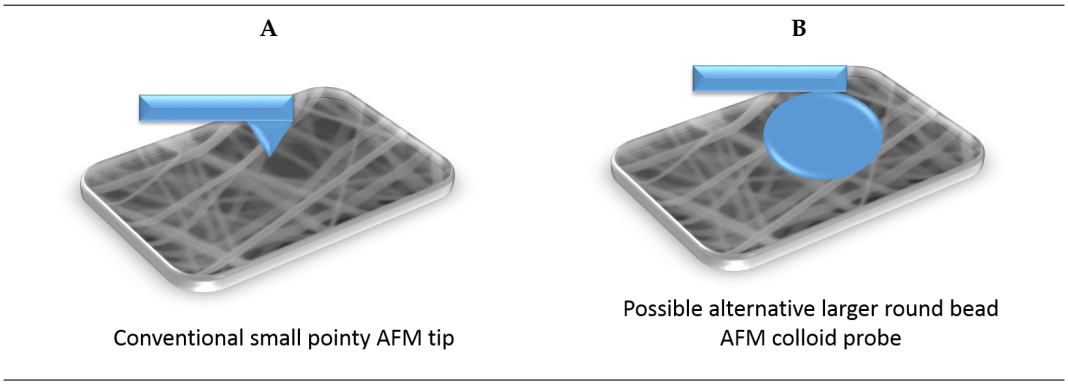



**Figure 7.1:** Schematic example of possible alternative AFM method to measure a more accurate Young's modulus of randomised fibrous scaffolds. **A)** Conventional AFM tip and **B)** colloid probe.

## 7.2 Thermo-responsive electrospun scaffolds fibrous design.

Although the obtained blend electrospun PDEGMA/PLA scaffolds resulted in sufficient detachment of the hCSCs, no significant detachment of the more robust 3T3 fibroblast was not observed. A thermo-responsive electrospun scaffold platform which has a universal cell application is preferred. Therefore, the use of these scaffolds for multiple cell lines should be investigated. As no more than 25% of detached 3T3 fibroblast cells was collected from the supernatant following detachment, a different electrospinning approach could be investigated to improve the contact of the thermo-responsive polymer to the cells attached. This can be done with the use of a co-axial electrospinning approach [370, 371] which has the PDEGMA as a sheet while having a supporting polymer as the fibrous core (see Figure 7.2).

Beside the improvement of the thermo-responsive behaviour of the fibrous scaffolds by co-axial electrospinning, a different thermo-responsive material could be used. A polymer with an upper critical solution temperature (UPLC) could be implemented instead of a polymer with a LCST as used in this study. For example, Xue et al. [258] observed successful cell detachment from poly(N-acryloyl glycinamide)-*stat*-poly(N-phenylacrylamide) (PNAGAm–PNPhAm) grafted TCPS surface when heated to 37°C. While no detachment was observed at temperature below 37°C.

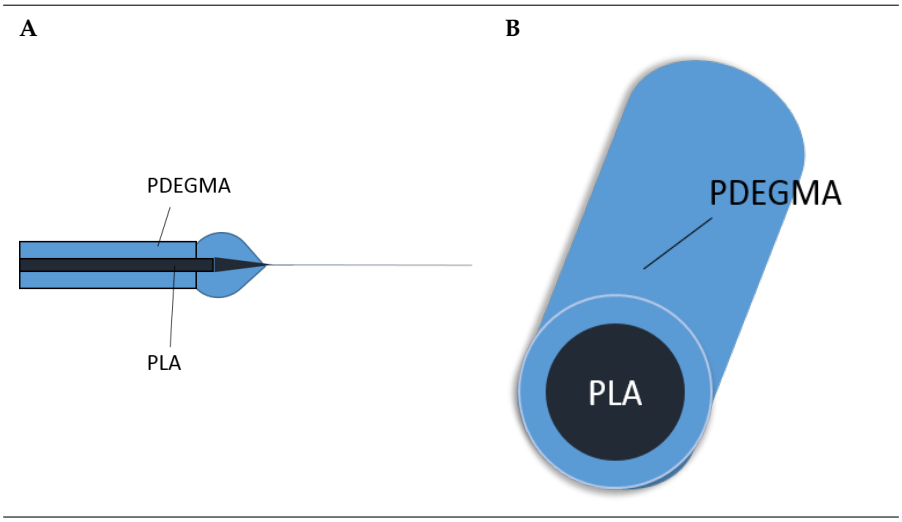



**Figure 7.2:** Schematic explanation of the co-axial electrospun fibre formation. **A)** The co-axial needle has a sheet and core needle, the thermo-responsive material will be drawn out as a sheet, while the supporting polymer PLA will be drawn out as the core of the fibre. **B)** shows the obtained co-axial fibre build up.

## 7.3 hCSCs detachment studies on the fabricated scaffolds.

Although initial results are promising more research is needed. This study conducted experiment with hCSCs cells from one donor, however experiments using cells from different donors should be conducted to increase the reproducibility of this study. In addition, the size of the experiment should be increased to obtain a higher number of cells for more reproducible flow cytometry data.

## 7.4 Cell specific peptide functionalisation on the fabricated scaffolds.

In this study the peptide sequence GGG-YIGSR was used to increase hCSCs response. However, this platform can be implemented for many different cell types, in which the peptide sequence can be altered. Any peptide sequence can be conjugated to the fabricated scaffolds with the use of a N-terminal functionalised norbornene acid group,

which will conjugate with the free thiols on the fibres surface. These could be adherence peptides (including RGD and IKVAV) [73], peptides that induce a desired cell response (such as KIPKASSVPTELSAISTLYL; which triggers osteogenic differentiation of pMSCs) [372] or enzyme responsive peptides (such as Fmoc-propargyl-GAARGD which can be cleaved to ARGD by the enzyme elastase expressed by porcine pancreas) [373, 374].

## 7.5 Scale-up of the fabricated scaffolds.

Scale-up experiments can be investigated in the future to make these scaffolds a cell culture platform for large scale expansion platforms.

# Chapter 8

# References


[1] M. Yamato, M. Utsumi, A. Kushida, C. Konno, A. Kikuchi, and T. Okano. Thermo-responsive culture dishes allow the intact harvest of multilayered keratinocyte sheets without dispase by reducing temperature. Tissue Engineering, 7(4):473–480, 2001.

[2] K.M. Kim and G.R.D. Evans. Topics in Tissue Engineering. N. Ashammakhi & R.L.Reis, 2006.

[3] C. Mason and P. Dunnil. A brief definition of regenerative medicine. Regenerative Medicine, 3(1):1–5, 2008.

[4] L. R. Kaiser. The future of multihospital systems. Top Health Care Financing, 18(4):32–45, 1992.

[5] G.M. Fahy. Dr. william haseltine on regenerative medicine, aging and human immortality. Life Extension, 8:58, 2002.

[6] G. Sampogna, S. Y. Guraya, and A. Forgione. Regenerative medicine: Historical roots and potential strategies in modern medicine. Journal of Microscopy and Ultrastructure, 3(3):101–107, 2015.

[7] V. Bisceglie. Über die antineoplastische immunität; heterologe einpflanzung von tumoren in hühner-embryonen. Ztschr Krebsforsch, 40:122–140, 1933.

[8] W. L. Chick, A. A. Like, and V. Lauris. Beta cell-culture on synthetic capillaries - artificial endocrine pancreas. Science, 187(4179):847–849, 1975.

[9] Y.C. Fung. Cellular growth in soft tissues affected by the stress level in service. In: Tissue Engineering. Alan Liss, 1988.

[10] S. Cohen. Design of synthetic polymeric structures for cell transplantation and tissue engineering. Clinical materials, 13(1-4):3–10, 1993.

[11] A. Vats, N. S. Tolley, J. M. Polak, and L. D. K. Buttery. Stem cells: sources and applications. Clinical Otolaryngology, 27(4):227–232, 2002.

[12] J.M. Polak and A.E. Bishop. Stem cells and tissue engineering: past, present, and future. Annals of the New York Academy of Sciences, 1068(1):352–366, 2006.

[13] J.W. Haycock. 3D cell culture: a review of current approaches and techniques, in 3D Cell Culture. Springer, 2011.

[14] A. Rodriguez, C. Cao, Y.L. Ibarra, S. Pap, M. Vacanti, R.D. Eavey, and C.A. Vacanti. Characteristics of cartilage engineered from human pediatric auricular cartilage. Plastic and Reconstructive Surgery, 103(4):1111–1119, 1999.

[15] V. Karantalis, I. H. Schulman, W. Balkan, and J. M. Hare. Allogeneic cell therapy: A new paradigm in therapeutics. Circulation Research, 116(1):12–5, 2015.

[16] D.L. Eizirik, M. Sammeth, T. Bouckenooghe, G. Bottu, G. Sisino, M. Igoillo-Esteve, F. Ortis, I. Santin, M. L. Colli, J. Barthson, L. Bouwens, L. Hughes, L. Gregory, G. Lunter, L. Marselli, P. Marchetti, M. I. McCarthy, and M. Cnop. The human pancreatic islet transcriptome: Expression of candidate genes for type 1 diabetes and the impact of pro-inflammatory cytokines. PLOS Genetics, 8(3):1–17, 2012.

[17] M. B. Drake, S. Iacobelli, A. van Biezen, C. Morris, J. F. Apperley, D. Niederwieser, B. Björkstrand, and G. Gahrton. Primary plasma cell leukemia and autologous stem cell transplantation. Haematologica, 95(5):804–809, 2010.

[18] P. O'Connell. Pancreatic islet xenotransplantation. Xenotransplantation, 9(6):367–371, 2002.

[19] C. G. Groth, O. Korsgren, A. Tibell, J. Tollemar, E. Moller, J. Bolinder, J. Ostman, F. P. Reinholt, C. Hellerstrom, and A. Andersson. Transplantation of porcine fetal pancreas to diabetic patients. The Lancet, 344(8934):1402–1404, 1994.

[20] A. S. Edge, M. E. Gosse, and J. Dinsmore. Xenogeneic cell therapy: current progress and future developments in porcine cell transplantation. Cell Transplantation, 7(6):525–539, 1998.

[21] A.J. Freemont and J. Hoyland. Lineage plasticity and cell biology of fibrocartilage and hyaline cartilage: its significance in cartilage repair and replacement. European journal of radiology, 57(1):32–36, 2006.

[22] J. V. Jester, W. M. Petroll, and H. D. Cavanagh. Corneal stromal wound healing in refractive surgery: the role of myofibroblasts. Progress in retinal and eye research, 18(3): 311–356, 1999.

[23] C. Nombela-Arrieta, J. Ritz, and L. E. Silberstein. The elusive nature and function of mesenchymal stem cells. Nature Reviews Molecular Cell Biology, 12(2):126–131, 2011.

[24] S. J. Shieh and J. P. Vacanti. State-of-the-art tissue engineering: from tissue engineering to organ building. Surgery, 137(1):1–7, 2005.

[25] J. F. Burke, I. V. Yannas, W. C. Quinby, C. C. Bondoc, and W. K. Jung. Successful use of a physiologically acceptable artificial skin in the treatment of extensive burn injury. Annals of Surgery, 194(4):413–428, 1981.

[26] M. Schindler, A. Nur-E-Kamal, I. Ahmed, J. Kamal, H. Y. Liu, N. Amor, A. S. Ponery, D. P. Crockett, T. H. Grafe, H. Y. Chung, T. Weik, E. Jones, and S. Meiners. Living in three dimensions - 3d nanostructured environments for cell culture and regenerative medicine. Cell Biochemistry and Biophysics, 45(2):215–227, 2006.

[27] T. Dvir, B. P. Timko, D. S. Kohane, and R. Langer. Nanotechnological strategies for engineering complex tissues. Nature Nanotechnology, 6(1):13–22, 2011.

[28] R.I. Freshney. Aseptic Technique, in Culture of Animal Cells. John Wiley & Sons, 2010.

[29] R. Edmondson, J. J. Broglie, A. F. Adcock, and L. Yang. Three-dimensional cell culture systems and their applications in drug discovery and cell-based biosensors. Assay and Drug Development Technologies, 12(4):207–218, 2014.

[30] K. Duval, H. Grover, L. H. Han, Y. Mou, A. F. Pegoraro, J. Fredberg, and Z. Chen. Modeling physiological events in 2d vs. 3d cell culture. Physiology (Bethesda), 32(4):266–277, 2017.

[31] O. W. Petersen, L. Rønnov-Jessen, A. R. Howlett, and M. J. Bissell. Interaction with basement membrane serves to rapidly distinguish growth and differentiation pattern of normal and malignant human breast epithelial cells. Proceedings of the National Academy of Sciences, 89(19):9064–9068, 1992.

[32] K.A. Moore and I.R. Lemischka. Stem cells and their niches. Science, 311(5769):1880–1885, 2006.

[33] R. D. Xu, M. B. Taskin, M. Rubert, D. Seliktar, F. Besenbacher, and M. L. Chen. hips-mscs differentiation towards fibroblasts on a 3d ecm mimicking scaffold. Scientific Reports, 5: 8480, 2015.

[34] A. Radhakrishnan, G. M. Jose, and M. Kurup. Peg-penetrated chitosan-alginate co-polysaccharide-based partially and fully cross-linked hydrogels as ecm mimic for tissue engineering applications. Progress in Biomaterials, 4(2-4):101–112, 2015.

[35] J. Barthes, N. E. Vrana, H. Ozcelik, R. Gahoual, Y. N. Francois, J. Bacharouche, G. Francius, J. Hemmerle, M. H. Metz-Boutigue, P. Schaaf, and P. Lavalle. Priming cells for their final destination: microenvironment controlled cell culture by a modular ecm-mimicking feeder film. Biomaterials Science, 3(9):1302–1311, 2015.

[36] P. Beauchamp, W. Moritz, J. M. Kelm, N. D. Ullrich, I. Agarkova, B. D. Anson, T. M. Suter, and C. Zuppinger. Development and characterization of a scaffold-free 3d spheroid model of induced pluripotent stem cell-derived human cardiomyocytes. Tissue Engineering Part C Methods, 21(8):852–861, 2015.

[37] K. Chitcholtan, P. H. Sykes, and J. J. Evans. The resistance of intracellular mediators to doxorubicin and cisplatin are distinct in 3d and 2d endometrial cancer. Journal of Translational Medicine, 10:38, 2012.

[38] O. M. Maria, O. Maria, Y. Liu, S. V. Komarova, and S. D. Tran. Matrigel improves functional properties of human submandibular salivary gland cell line. International Journal of Biochemistry & Cell Biology, 43(4):622–31, 2011.

[39] C. Petti, B. Herner, and A. Walker. Monolithic 3D integrated circuits. Spinger, 2008.

[40] Anna C. Luca, Sabrina Mersch, René Deenen, Stephan Schmidt, Isabelle Messner, Karl-Ludwig Schäfer, Stephan E. Baldus, Wolfgang Huckenbeck, Roland P. Piekorz, Wolfram T. Knoefel, Andreas Krieg, and Nikolas H. Stoecklein. Impact of the 3d microenvironment on phenotype, gene expression, and egfr inhibition of colorectal cancer cell lines. PLOS ONE, 8(3):1–11, 2013.

[41] X. Wang, L. Sun, M. V. Maffini, A. Soto, C. Sonnenschein, and D. L. Kaplan. A complex 3d human tissue culture system based on mammary stromal cells and silk scaffolds for modeling breast morphogenesis and function. Biomaterials, 31(14):3920–3929, 2010.

[42] V. Hongisto, S. Jernstrom, V. Fey, J. P. Mpindi, K. Kleivi Sahlberg, O. Kallioniemi, and M. Perala. High-throughput 3d screening reveals differences in drug sensitivities between culture models of jimt1 breast cancer cells. PLoS One, 8(10):e77232, 2013.

[43] F. J. O'Brien. Biomaterials & scaffolds for tissue engineering. Materials Today, 14(3): 88–95, 2011.

[44] D.L. Kiss, L.C.E. Windus, and V.M. Avery. Chemokine receptor expression on integrin-mediated stellate projections of prostate cancer cells in 3d culture. Cytokine, 64(1):122 – 130, 2013.

[45] E. T. Pineda, R. M. Nerem, and T. Ahsan. Differentiation patterns of embryonic stem cells in two- versus three-dimensional culture. Cells Tissues Organs, 197(5):399–410, 2013.

[46] K. M. Mabry, S. Z. Payne, and K. S. Anseth. Microarray analyses to quantify advantages of 2d and 3d hydrogel culture systems in maintaining the native valvular interstitial cell phenotype. Biomaterials, 74:31–41, 2016.

[47] S. J. Hollister. Porous scaffold design for tissue engineering. Nature Materials, 4(7):518–524, 2005.

[48] F. S. L. Bobbert and A. A. Zadpoor. Effects of bone substitute architecture and surface properties on cell response, angiogenesis, and structure of new bone. Journal of Materials Chemistry B, 5(31):6175–6192, 2017.

[49] A. J. Berger, K. M. Linsmeier, P. K. Kreeger, and K. S. Masters. Decoupling the effects of stiffness and fiber density on cellular behaviors via an interpenetrating network of gelatin-methacrylate and collagen. Biomaterials, 141:125–135, 2017.

[50] A. J. Engler, C. Carag-Krieger, C. P. Johnson, M. Raab, H. Y. Tang, D. W. Speicher, J. W. Sanger, J. M. Sanger, and D. E. Discher. Embryonic cardiomyocytes beat best on a matrix with heart-like elasticity: scar-like rigidity inhibits beating. Journal of Cell Science, 121 (22):3794–802, 2008.

[51] K. Saha, A. J. Keung, E. F. Irwin, Y. Li, L. Little, D. V. Schaffer, and K. E. Healy. Substrate modulus directs neural stem cell behavior. Biophysical Journal, 95(9):4426–38, 2008.

[52] K. E. Kadler, D. F. Holmes, J. A. Trotter, and J. A. Chapman. Collagen fibril formation. Biochemical Journal, 316(Pt 1):1–11, 1996.

[53] E. L. Monzack, J. Rodriguez, K, C. M. McCoy, X. Gu, and K. S. Masters. Natural Materials in Tissue Engineering Applications, pages 209–241. Springer Vienna, 2011.

[54] F. Li, M. Griffith, Z. Li, S. Tanodekaew, H. Sheardown, M. Hakim, and D. J. Carlsson. Recruitment of multiple cell lines by collagen-synthetic copolymer matrices in corneal regeneration. Biomaterials, 26(16):3093–3104, 2005.

[55] C. R. Weinstein-Oppenheimer, D. I. Brown, R. Coloma, P. Morales, M. Reyna-Jeldes, M. J. Diaz, E. Sanchez, and C. A. Acevedo. Design of a hybrid biomaterial for tissue engineering: Biopolymer-scaffold integrated with an autologous hydrogel carrying mesenchymal stem-cells. Materials Science & Engineering C-Materials for Biological Applications, 79: 821–830, 2017.

[56] X. Zhao, K. Long, Y. Liu, W. C. Li, S. Liu, L. Wang, and L. Ren. To prepare the collagen-based artificial cornea with improved mechanical and biological property by ultraviolet-a/riboflavin crosslinking. Journal of Applied Polymer Science, 134(38), 2017.

[57] Y. C. Kuo, H. F. Ku, and R. Rajesh. Chitosan/gamma-poly(glutamic acid) scaffolds with surface-modified albumin, elastin and poly-l-lysine for cartilage tissue engineering. Materials Science & Engineering C-Materials for Biological Applications, 78:265–277, 2017.

[58] C. H. Yao, C. Y. Lee, C. H. Huang, Y. S. Chen, and K. Y. Chen. Novel bilayer wound dressing based on electrospun gelatin/keratin nanofibrous mats for skin wound repair. Materials Science & Engineering C-Materials for Biological Applications, 79:533–540, 2017.

[59] K.S. Rho, L. Jeong, G. Lee, B. Seo, Y.J. Park, S. Hong, S. Roh, J.J. Cho, W.H. Park, and B Min. Electrospinning of collagen nanofibers: Effects on the behavior of normal human keratinocytes and early-stage wound healing. Biomaterials, 27(8):1452 – 1461, 2006.

[60] N. Greer, N. Foman, J. Dorrian, P. Fitzgerals, I. Rutks, and T.J. Wilt. Advanced wound care therapies for nonhealing diabetic, venous, and arterial ulcers: A systematic review. Annals of Internal Medicine, 159(8):532–542, 2013.

[61] C. E. Ghezzi, B. Marelli, F. G. Omenetto, J. L. Funderburgh, and D. L. Kaplan. 3d functional corneal stromal tissue equivalent based on corneal stromal stem cells and multi-layered silk film architecture. Plos One, 12(1), 2017.

[62] T. Re'em, O. Tsur-Gang, and S. Cohen. The effect of immobilized rgd peptide in macroporous alginate scaffolds on tgf beta 1-induced chondrogenesis of human mesenchymal stem cells. Biomaterials, 31(26):6746–6755, 2010.

[63] B. D. Ratner and S. J. Bryant. Biomaterials: where we have been and where we are going. Annual Review of Biomedical Engineering, 6:41–75, 2004.

[64] Z. W. Ma, M. Kotaki, T. Yong, W. He, and S. Ramakrishna. Surface engineering of electrospun polyethylene terephthalate (pet) nanofibers towards development of a new material for blood vessel engineering. Biomaterials, 26(15):2527–2536, 2005.

[65] L. Cont, D. Grant, C. Scotchford, M. Todea, and C. Popa. Composite pla scaffolds reinforced with pdo fibers for tissue engineering. Journal of Biomaterials Applications, 27(6): 707–716, 2013.

[66] M. Khakestani, S. H. Jafari, P. Zahedi, R. Bagheri, and R. Hajiaghaee. Physical, morphological, and biological studies on pla/nha composite nanofibrous webs containing equisetum arvense herbal extract for bone tissue engineering. Journal of Applied Polymer Science, 134(39), 2017.

[67] S. Toosi, H. Naderi-Meshkin, F. Kalalinia, M. T. Peivandi, H. HosseinKhani, A. R. Bahrami, A. Heirani-Tabasi, M. Mirahmadi, and J. Behravan. Pga-incorporated collagen: Toward a biodegradable composite scaffold for bone-tissue engineering. Journal of Biomedical Materials Research Part A, 104(8):2020–2028, 2016.

[68] F. Zamani, M. Latifi, M. Amani-Tehran, and M. A. Shokrgozar. Effects of plga nanofibrous scaffolds structure on nerve cell directional proliferation and morphology. Fibers and Polymers, 14(5):698–702, 2013.

[69] B. Komur, F. Bayrak, N. Ekren, M. S. Eroglu, F. N. Oktar, Z. A. Sinirlioglu, S. Yucel, O. Guler, and O. Gunduz. Starch/pcl composite nanofibers by co-axial electrospinning technique for biomedical applications. Biomedical Engineering Online, 16:40–53, 2017.

[70] O. Evrova, V. Hosseini, V. Milleret, G. Palazzolo, M. Zenobi-Wong, T. Sulser, J. Buschmann, and D. Eberli. Hybrid randomly electrospun poly(lactic-co-glycolic acid):poly(ethylene oxide) (plga:peo) fibrous scaffolds enhancing myoblast differentiation and alignment. ACS Applied Materials & Interfaces, 8(46):31574–31586, 2016.

[71] J. M. Lee, T. Chae, F. A. Sheikh, H. W. Ju, B. M. Moon, H. J. Park, Y. R. Park, and C. H.

Park. Three dimensional poly(ε-caprolactone) and silk fibroin nanocomposite fibrous matrix for artificial dermis. Materials Science and Engineering: C, 68:758–767, 2016.

[72] C. Chollet, C. Labrugere, and M. C. Durrieu. Impact of rgd peptide density grafted onto poly(ethylene terephthalate) on mc3t3 cell attachment. Conference proceedings : ...Annual International Conference of the IEEE Engineering in Medicine and Biology Society.IEEE Engineering in Medicine and Biology Society.Conference, 2007:5123–5126, 2007.

[73] L. Zhu, K. Wang, T. Ma, L. L. Huang, B. Xia, S. Zhu, Y. F. Yang, Z. Y. Liu, X. Quan, K. Luo, D. L. Kong, J. H. Huang, and Z. J. Luo. Noncovalent bonding of rgd and yigsr to an electrospun poly(epsilon-caprolactone) conduit through peptide self-assembly to synergistically promote sciatic nerve regeneration in rats. Advanced Healthcare Materials, 6 (8):1600860, 2017.

[74] S. J. Hollister. Scaffold engineering: a bridge to where? Biofabrication, 1(1):012001, 2009.

[75] X. Duan and H. Sheardown. Incorporation of cell-adhesion peptides into collagen scaffolds promotes corneal epithelial stratification. Journal of Biomaterials Science Polymer Edition, 18(6):701–711, 2007.

[76] J. W. Nichol, S. T. Koshy, H. Bae, C. M. Hwang, S. Yamanlar, and A. Khademhosseini. Cell-laden microengineered gelatin methacrylate hydrogels. Biomaterials, 31(21):5536–5544, 2010.

[77] E. M. Ahmed, F. S. Aggor, A. M. Awad, and A. T. El-Aref. An innovative method for preparation of nanometal hydroxide superabsorbent hydrogel. Carbohydrate Polymers, 91(2):693–698, 2013.

[78] E. M. Ahmed. Hydrogel: Preparation, characterization, and applications: A review. Journal of Advanced Research, 6(2):105–121, 2015.

[79] T. Xu, J. Jin, C. Gregory, J. J. Hickman, and T. Boland. Inkjet printing of viable mammalian cells. Biomaterials, 26(1):93–99, 2005.

[80] T. Xu, W. Zhao, J. M. Zhu, M. Z. Albanna, J. J. Yoo, and A. Atala. Complex heterogeneous tissue constructs containing multiple cell types prepared by inkjet printing technology. Biomaterials, 34(1):130–139, 2013.

[81] J. Visser, B. Peters, T. J. Burger, J. Boomstra, W. J. Dhert, F. P. Melchels, and J. Malda. Biofabrication of multi-material anatomically shaped tissue constructs. Biofabrication, 5 (3):035007, 2013.

[82] J. A. Barron, B. R. Ringeisen, H. Kim, B. J. Spargo, and D. B. Chrisey. Application of laser printing to mammalian cells. Thin Solid Films, 453:383 – 387, 2004.

[83] R. Chang, J. Nam, and W. Sun. Effects of dispensing pressure and nozzle diameter on cell survival from solid freeform fabrication-based direct cell writing. Tissue Engineering Part A, 14(1):41–48, 2008.

[84] M. Costantini, S. Testa, P. Mozetic, A. Barbetta, C. Fuoco, E. Fornetti, F. Tamiro, S. Bernardini, J. Jaroszewicz, W. Swieszkowski, M. Trombetta, L. Castagnoli, D. Seliktar, P. Garstecki, G. Cesareni, S. Cannata, A. Rainer, and C. Gargioli. Microfluidic-enhanced 3d bioprinting of aligned myoblast-laden hydrogels leads to functionally organized myofibers in vitro and in vivo. Biomaterials, 131:98–110, 2017.

[85] T. J. Sill and H. A. von Recum. Electro spinning: Applications in drug delivery and tissue engineering. Biomaterials, 29(13):1989–2006, 2008.

[86] W. Gilbert. De Magnete, Magneticisque Corporibus, et de Magno Magnete Tellure (On the Magnet and Magnetic Bodies, and on That Great Magnet the Earth). Peter Short, 1628.

[87] C V Boys. On the production, properties, and some suggested uses of the finest threads. Proceedings of the Physical Society of London, 9(1):8, 1887.

[88] J.F. Cooley. Apparatus for electrically dispersing fluids, 1902. US692631 A.

[89] W.J. Morton. Method of dispersing fluids, 1902. US705691 A.

[90] F. Anton. Process and apparatus for preparing artificial threads, 1934. US1975504 A.

[91] F. Anton. Method and apparatus for spinning, 1944. US2349950 A.

[92] J. Lannutti, D. Reneker, T. Ma, D. Tomasko, and D. Farson. Electrospinning for tissue engineering scaffolds. Materials Science and Engineering: C, 27(3):504–509, 2007.

[93] S. Ramakrishna, K. Fujihara, W. Teo, T. Lim, and Z. Ma. An Introduction to Electrospinning and Nanofibers. World Scientific Publishing Co. Pte. Ltd., 2005.

[94] A. K. A. S. Brun-Graeppi, C. Richard, M. Bessodes, D. Scherman, and O. Merten. Thermoresponsive surfaces for cell culture and enzyme-free cell detachment. Progress in Polymer Science, 35(11):1311–1324, 2010.

[95] W. Liu, S. Thomopoulos, and Y. Xia. Electrospun nanofibers for regenerative medicine. Advanced Healthcare Materials, 1(1):10–25, 2012.

[96] N. Bhardwaj and S. C. Kundu. Electrospinning: A fascinating fiber fabrication technique. Biotechnology Advances, 28(3):325–347, 2010.

[97] G. Fortunato, A. G. Guex, A. M. Popa, R. M. Rossi, and R. Hufenus. Molecular weight driven structure formation of peg based e-spun polymer blend fibres. Polymer, 55(14): 3139–3148, 2014.

[98] J. Tao and S. Shivkumar. Molecular weight dependent structural regimes during the electrospinning of pva. Materials Letters, 61:2325–2328, 2007.

[99] A. Koski, K. Yim, and S. Shivkumar. Effect of molecular weight on fibrous pva produced by electrospinning. Materials Letters, 58(3-4):493–497, 2004.

[100] Z. Jun, H. Hou, A. Schaper, J. H. Wendroff, and A. Greiner. Poly-l-lactide nanofibers by electrospinning - influence of solution viscosity and eletrical conductivity on fiber diameter and morphology. e-Polymers, 3(1):102–110, 2003.

[101] R. Casasola, N. L. Thomas, A. Trybala, and S. Georgiadou. Electrospun poly lactic acid (pla) fibres: Effect of different solvent systems on fibre morphology and diameter. Polymer, 55(18):4728–4737, 2014.

[102] R. M. Nezarati, M. B. Eifert, and E. Cosgriff-Hernandez. Effects of humidity and solution viscosity on electrospun fiber morphology. Tissue Engineering Part C-Methods, 19(10): 810–819, 2013.

[103] L. Diaz-Gomez, F. M. Ballarin, G. A. Abraham, A. Concheiro, and C. Alvarez-Lorenzo. Random and aligned plla : Prgf electrospun scaffolds for regenerative medicine. Journal of Applied Polymer Science, 132(5):41372, 2015.

[104] J. Zhang, D. Yang, F. Xu, Z. Zhang, R. Yin, and J. Nie. Electrospun core-shell structure nanofibers from homogeneous solution of poly(ethylene oxide)/chitosan. Macromolecules, 42(14):5278–5284, 2009.

[105] M. Wei, J. Lee, B. Kang, and J. Mead. Preparation of core-sheath nanofibers from conducting polymer blends. Macromolecular Rapid Communications, 26(14):1127–1132, 2005.

[106] M. G. McKee, G. L. Wilkes, R. H. Colby, and T. E. Long. Correlations of solution rheology with electrospun fiber formation of linear and branched polyesters. Macromolecules, 37 (5):1760–1767, 2004.

[107] S. Basu, N. Gogoi, S. Sharma, M. Jassal, and A. K. Agrawal. Role of elasticity in control of diameter of electrospun pan nanofibers. Fibers and Polymers, 14(6):950–956, 2013.

[108] I. Greenfeld and E. Zussman. Polymer entanglement loss in extensional flow: Evidence from electrospun short nanofibers. Journal of Polymer Science Part B-Polymer Physics, 51(18):1377–1391, 2013.

[109] J. H. Yu, S. V. Fridrikh, and G. C. Rutledge. The role of elasticity in the formation of electrospun fibers. Polymer, 47(13):4789–4797, 2006.

[110] C. Mit-uppatham, M. Nithitanakul, and P. Supaphol. Ultratine electrospun polyamide-6 fibers: Effect of solution conditions on morphology and average fiber diameter. Macromolecular Chemistry and Physics, 205(17):2327–2338, 2004.

[111] L. A. Bosworth and S. Downes. Acetone, a sustainable solvent for electrospinning poly(epsilon-caprolactone) fibres: Effect of varying parameters and solution concentrations on fibre diameter. Journal of Polymers and the Environment, 20(3):879–886, 2012.

[112] C. J. Angammana and S. H. Jayaram. Analysis of the effects of solution conductivity on electrospinning process and fiber morphology. IEEE Transactions on Industry Applications, 47(3):1109–1117, 2011.

[113] J. S. Choi, S. W. Lee, L. Jeong, S. H. Bae, B. C. Min, J. H. Youk, and W. H. Park. Fiect of organosoluble salts on the nanofibrous structure of electrospun poly(3-hydroxybutyrate-co-3-hydroxyvalerate). International journal of biological macromolecules, 34(4):249–256, 2004.

[114] Z. Z. Zhao, J. Q. Li, X. Y. Yuan, X. Li, Y. Y. Zhang, and J. Sheng. Preparation and properties of electrospun poly(vinylidene fluoride) membranes. Journal of Applied Polymer Science, 97(2):466–474, 2005.

[115] D. Fallahi, M. Rafizadeh, N. Mohammadi, and B. Vahidi. Effect of applied voltage on jet electric current and flow rate in electrospinning of polyacrylonitrile solutions. Polymer International, 57(12):1363–1368, 2008.

[116] R. Samatham and K. J. Kim. Electric current as a control variable in the electrospinning process. Polymer Engineering & Science, 46(7):954–959, 2006.

[117] B. Kim, H. Park, S. H. Lee, and W. M. Sigmund. Poly(acrylic acid) nanofibers by electrospinning. Materials Letters, 59(7):829–832, 2005.

[118] S. Zargham, S. Bazgir, A. Tavakoli, A. S. Rashidi, and R. Damerchely. The effect of flow rate on morphology and deposition area of electrospun nylon 6 nanofiber. Journal of Engineered Fibers and Fabrics, 7(4):42–49, 2012.

[119] X. Tang, N. Si, L. Xu, and H. Liu. Effect of flow rate on diameter of electrospun nanoporous fibers. Thermal Science, 18(5):1447–1449, 2014.

[120] V. Pillay, C. Dott, Y. E. Choonara, C. Tyagi, L. Tomar, P. Kumar, L. C. du Toit, and V. M. K. Ndesendo. A review of the effect of processing variables on the fabrication of electrospun nanofibers for drug delivery applications. Journal of Nanomaterials, page 789289, 2013.

[121] A. H. Hekmati, A. Rashidi, R. Ghazisaeidi, and J. Drean. Effect of needle length, electrospinning distance, and solution concentration on morphological properties of polyamide-6 electrospun nanowebs. Textile Research Journal, 83(14):1452–1466, 2013.

[122] S. Megelski, J. S. Stephens, D. B. Chase, and J. F. Rabolt. Micro- and nanostructured surface morphology on electrospun polymer fibers. Macromolecules, 35(22):8456–8466, 2002.

[123] S. De Vrieze, T. Van Camp, A. Nelvig, B. Hagstrom, P. Westbroek, and K. De Clerck. The effect of temperature and humidity on electrospinning. Journal of Materials Science, 44 (5):1357–1362, 2009.

[124] M. Chen, M. Dong, R. Havelund, V. R. Regina, R. L. Meyer, F. Besenbacher, and P. Kingshott. Thermo-responsive core-sheath electrospun nanofibers from poly (n-isopropylacrylamide)/polycaprolactone blends. Chemistry of Materials, 22(14):4214–4221, 2010.

[125] O. Hardick, B. Stevens, and D. G. Bracewell. Nanofibre fabrication in a temperature and humidity controlled environment for improved fibre consistency. Journal of Materials Science, 46(11):3890–3898, 2011.

[126] D. H. Reneker and I. Chun. Nanometre diameter fibres of polymer, produced by electrospinning. Nanotechnology, 7(3):216–223, 1996.

[127] Y. Cai and M. Gevelber. The effect of relative humidity and evaporation rate on electrospinning: fiber diameter and measurement for control implications. Journal of Materials Science, 48(22):7812–7826, 2013.

[128] C. L. Casper, J. S. Stephens, N. G. Tassi, D. B. Chase, and J. F. Rabolt. Controlling surface morphology of electrospun polystyrene fibers: Effect of humidity and molecular weight in the electrospinning process. Macromolecules, 37(2):573–578, 2004.

[129] D. H. Reneker, A. L. Yarin, H. Fong, and S. Koombhongse. Bending instability of electrically charged liquid jets of polymer solutions in electrospinning. Journal of Applied Physics, 87(9):4531–4547, 2000.

[130] W. Li, , C. T. Laurencin, E. J. Caterson, R. S. Tuan, and F. K. Ko. Electrospun nanofibrous structure: A novel scaffold for tissue engineering. Journal of biomedical materials research, 60(4):613–621, 2002.

[131] D. Annis, A. Bornat, R.O. Edwards, A. Higham, B. Loveday, and J. Wilson. An elastometric vascular prosthesis. Transaction - American Society for Artificial Internal Organs, 24: 209 – 214, 1978.

[132] Q. H. Zhou, J. Xie, M. Bao, H. H. Yuan, Z. Y. Ye, X. X. Lou, and Y. Z. Zhang. Engineering aligned electrospun plla microfibers with nano-porous surface nanotopography for modulating the responses of vascular smooth muscle cells. Journal of Materials Chemistry B, 3(21):4439–4450, 2015.

[133] H. Wang, Y. Feng, B. An, W. Zhang, M. Sun, Z. Fang, W. Yuan, and M. Khan. Fabrication of pu/pegma crosslinked hybrid scaffolds by in situ uv photopolymerization favoring human endothelial cells growth for vascular tissue engineering. Journal of Materials Science. Materials in Medicine, 23(6):1499–1510, 2012.

[134] W. He, T. Yong, Z. W. Ma, R. Inai, W. E. Teo, and S. Ramakrishna. Biodegradable polymer nanofiber mesh to maintain functions of endothelial cells. Tissue Engineering, 12(9):2457–2466, 2006.

[135] H. Kenar, G. T. Kose, and V. Hasirci. Design of a 3d aligned myocardial tissue construct from biodegradable polyesters. Journal of Materials Science: Materials in Medicine, 21 (3):989–997, 2010.

[136] P. H. Kim and J. Y. Cho. Myocardial tissue engineering using electrospun nanofiber composites. BMB Reports, 49(1):26–36, 2016.

[137] H. B. Wang, M. E. Mullins, J. M. Cregg, C. W. McCarthy, and R. J. Gilbert. Varying the diameter of aligned electrospun fibers alters neurite outgrowth and schwann cell migration. Acta Biomaterialia, 6(8):2970–2978, 2010.

[138] J. G. Zhang, K. X. Qiu, B. B. Sun, J. Fang, K. H. Zhang, H. Ei-Hamshary, S. S. Al-Deyab, and X. M. Mo. The aligned core-sheath nanofibers with electrical conductivity for neural tissue engineering. Journal of Materials Chemistry B, 2(45):7945–7954, 2014.

[139] D. Phu, L. S. Wray, R. V. Warren, R. C. Haskell, and E. J. Orwin. Effect of substrate composition and alignment on corneal cell phenotype. Tissue Engingeering Part A, 17 (5-6):799–807, 2011.

[140] B. Kong, W. Sun, G. Chen, S. Tang, M. Li, Z. Shao, and S. Mi. Tissue-engineered cornea constructed with compressed collagen and laser-perforated electrospun mat. Scientific Reports, 7(970), 2017.

[141] M. Shin, H. Yoshimoto, and J. P. Vacanti. In vivo bone tissue engineering using mesenchymal stem cells on a novel electrospun nanofibrous scaffold. Tissue Engineering, 10 (1-2):33–41, 2004.

[142] S. Chew, Y. Wen, Y. Dzenis, and K. Leong. The role of electrospinning in the emerging field of nanomedicine. Current Pharmaceutical Design, 12(36):4751–4770, 2006.

[143] M. A. Derakhshan, G. Pourmand, J. Ai, H. Ghanbari, R. Dinarvand, M. Naji, and R. Faridi-Majidi. Electrospun plla nanofiber scaffolds for bladder smooth muscle reconstruction. International Urology Nephrology, 48(7):1097–1104, 2016.

[144] C. Feng and Y. Xu. Tissue Regeneration - From Basic Biology to Clinical Application. InTech, 2012.

[145] X. Wu, Y. Wang, C. Zhu, X. Tong, M. Yang, L. Yang, Z. Liu, W. Huang, F. Wu, H. Zong, H. Li, and H. He. Preclinical animal study and human clinical trial data of co-electrospun poly(l-lactide-co-caprolactone) and fibrinogen mesh for anterior pelvic floor reconstruction. International Journal of Nanomedicine, 11:389–397, 2016.

[146] J. Lv, L. Chen, Y. Zhu, L. Hou, and Y. Liu. Promoting epithelium regeneration for esophageal tissue engineering through basement membrane reconstitution. ACS Applied Materials & Interfaces, 6(7):4954–4964, 2014.

[147] R. Ricardo and K. Phelan. Trypsinizing and subculturing mammalian cells. Journal of Visualized Experiments, 16:755, 2008.

[148] P. Danhier, T. Copetti, G. De Preter, P. Leveque, O. Feron, B. F. Jordan, P. Sonveaux, and B. Gallez. Influence of cell detachment on the respiration rate of tumor and endothelial cells. PloS One, 8(1):e53324, 2013.

[149] S. Vedicherla and C.T. Buckley. Rapid chondrocyte isolation for tissue engineering applications: The effect of enzyme concentration and temporal exposure on the matrix forming capacity of nasal derived chondrocytes. BioMed Research International, page 12, 2017.

[150] H. Huang, H. Hsing, T. Lai, Y. Chen, T. Lee, H. Chan, P. Lyu, C. Wu, Y. Lu, S. Lin, C. Lin, C. Lai, H. Chang, H. Chou, and H. Chan. Trypsin-induced proteome alteration during cell subculture in mammalian cells. Journal of Biomedical Science, 17:36, 2010.

[151] U. Batista, M. Garvas, M. Nemec, M. Schara, P. Veranic, and T. Koklic. Effects of different detachment procedures on viability, nitroxide reduction kinetics and plasma membrane heterogeneity of v-79 cells. Cell biology international, 34(6):663–668, 2010.

[152] D. Cunliffe, C. D. Alarcon, V. Peters, J. R. Smith, and C. Alexander. Thermoresponsive surface-grafted poly(n-isopropylacrylamide) copolymers: Effect of phase transitions on protein and bacterial attachment. Langmuir, 19(7):2888–2899, 2003.

[153] J. Edahiro, K. Sumaru, Y. Tada, K. Ohi, T. Takagi, M. Kameda, T. Shinbo, T. Kanamori, and Y. Yoshimi. In situ control of cell adhesion using photoresponsive culture surface. Biomacromolecules, 6(2):970–974, 2005.

[154] B. Chen, F. J. Xu, N. Fang, K. G. Neoh, E. T. Kang, W. N. Chen, and V. Chan. Engineering cell de-adhesion dynamics on thermoresponsive poly(n-isopropylacrylamide). Acta Biomaterialia, 4(2):218–229, 2008.

[155] N. G. Patel and G. Zhang. Responsive systems for cell sheet detachment. Organogenesis, 9(2):93–100, 2013.

[156] X.Dou, X. Yang, P. Li, Z. Zhang, H. Schoenherr, D. Zhang, and C. Feng. Novel ph responsive hydrogels for controlled cell adhesion and triggered surface detachment. Soft Matter, 8(37):9539–9544, 2012.

[157] J. Teichmann, M. Nitschke, D. Pette, M. Valtink, S. Gramm, F. V. Hartel, T. Noll, R. H. W. Funk, K. Engelmann, and C. Werner. Thermo-responsive cell culture carriers based on poly(vinyl methyl ether)-the effect of biomolecular ligands to balance cell adhesion and stimulated detachment. Science and Technology of Advanced Materials, 16(4):045003, 2015.

[158] F. Gambinossi, L. S. Sefcik, E. Wischerhoff, A. Laschewsky, and J. K. Ferri. Engineering adhesion to thermoresponsive substrates: Effect of polymer composition on liquid-liquid-solid wetting. ACS Applied Materials & Interfaces, 7(4):2518–2528, 2015.

[159] S. Nara, S. Chameettachal, S. Midha, H. Singh, R. Tandon, S. Mohanty, and S. Ghosh. Strategies for faster detachment of corneal cell sheet using micropatterned thermoresponsive matrices. Journal of Materials Chemistry B, 3(20):4155–4169, 2015.

[160] M. Nakayama, Y. Kimura, H. Kanazawa, M. Yamato, and T. Okano. 2014 International Symposium on Micro-Nanomechatronics and Human Science(MHS). Nagoya, 2014.

[161] H. Tsai, K. Vats, M. Z. Yates, and D. S. W. Benoit. Two-dimensional patterns of poly(n-isopropylacrylamide) microgels to spatially control fibroblast adhesion and temperature-responsive detachment. Langmuir, 29(39):12183–12193, 2013.

[162] L. S. Sefcik, A. Kaminski, K. Ling, A. Laschewsky, J. Lutz, and E. Wischerhoff. Effects of peg-based thermoresponsive polymer brushes on fibroblast spreading and gene expression. Cellular and Molecular Bioengineering, 6(3):287–298, 2013.

[163] S. Dey, B. Kellam, M. R. Alexander, C. Alexander, and F. R. A. J. Rose. Enzyme-passage free culture of mouse embryonic stem cells on thermo-responsive polymer surfaces. Journal of Materials Chemistry, 21(19):6883–6890, 2011.

[164] K. Fukumori, Y. Akiyama, Y. Kumashiro, J. Kobayashi, M. Yamato, K. Sakai, and T. Okano. Characterization of ultra-thin temperature-responsive polymer layer and its polymer thickness dependency on cell attachment/detachment properties. Macromolecular Bioscience, 10(10):1117–1129, 2010.

[165] K. G. Neoh and E. T. Kang. Responsive surfaces for biomedical applications. Mrs Bulletin, 35(9):673–681, 2010.

[166] J. Yang, M. Yamato, C. Kohno, A. Nishimoto, H. Sekine, F. Fukai, and T. Okano. Cell sheet engineering: recreating tissues without biodegradable scaffolds. Biomaterials, 26 (33):6415–6422, 2005.

[167] K. Achiha, R. Ojima, Y. Kasuya, K. Fujimoto, and H. Kawaguchi. Interactions between themperature-sentitive hydrogel microspheres and granulocytes. Polymers for Advanced Technologies, 6(7):534–540, 1995.

[168] A. Kushida, M. Yamato, C. Konno, A. Kikuchi, Y. Sakurai, and T. Okano. Decrease in culture temperature releases monolayer endothelial cell sheets together with deposited fibronectin matrix from temperature-responsive culture surfaces. Journal of Biomedical Materials Research, 45(4):355–362, 1999.

[169] Motohiro Hirose, Oh Hyeong Kwon, Masayuki Yamato, Akihiko Kikuchi, and Teruo Okano. Creation of designed shape cell sheets that are noninvasively harvested and moved onto another surface. Biomacromolecules, 1(3):377–381, 2000.

[170] K. Ohashi, T. Yokoyama, M. Yamato, H. Kuge, H. Kanehiro, M. Tsutsumi, T. Amanuma, H. Iwata, J. Yang, T. Okano, and Y. Nakajima. Engineering functional two- and three-dimensional liver systems in vivo using hepatic tissue sheets. Nature Medicine, 13(7): 880–885, 2007.

[171] Y. Miyahara, N. Nagaya, M. Kataoka, B. Yanagawa, K. Tanaka, H. Hao, K. Ishino, H. Ishida, T. Shimizu, K. Kangawa, S. Sano, T. Okano, S. Kitamura, and H. Mori. Monolayered mesenchymal stem cells repair scarred myocardium after myocardial infarction. Nature Medicine, 12(4):459–465, 2006.

[172] V. Malheiro, Y. Elbs-Glatz, M. Obarzanek-Fojt, K. Maniura-Weber, and A. Bruinink. Harvesting pre-polarized macrophages using thermo-responsive substrates. Scientific Reports, 7:42495, 2017.

[173] K. Nishida, T. Okano, and M. Yamato. Cell sheets for ectocornea formation, method of producing the same and method of using the same, 2005. EP1602383 A1.

[174] T. Sumide, K. Nishida, M. Yamato, T. Ide, Y. Hayashida, K. Watanabe, J. Yang, C. Kohno, A. Kikuchi, N. Maeda, H. Watanabe, T. Okano, and Y. Tano. Functional human corneal endothelial cell sheets harvested from temperature-responsive culture surfaces. FASEB Journal: Official publication of the Federation of American Societies of Experimental Biology, 20(2):392–394, 2006.

[175] T. Shimizu, M. Yamato, A. Kikuchi, and T. Okano. Cell sheet engineering for myocardial tissue reconstruction. Biomaterials, 24(13):2309–2316, 2003.

[176] M. Yamato and T. Okano. Cell sheet engineering. Materials Today, 7(5):42–47, 2004.

[177] Y. Haraguchi, T. Shimizu, M. Yamato, A. Kikuchi, and T. Okano. Electrical coupling of cardiomyocyte sheets occurs rapidly via functional gap junction formation. Biomaterials, 27(27):4765 – 4774, 2006.

[178] S. Masuda, T. Shimizu, M. Yamato, and T. Okano. Cell sheet engineering for heart tissue repair. Advanced Drug Delivery Reviews, 60(2):277–285, 2008.

[179] T. Iwata, M. Yamato, H. Tsuchioka, R. Takagi, S. Mukobata, K. Washio, T. Okano, and I. Ishikawa. Periodontal regeneration with multi-layered periodontal ligament-derived cell sheets in a canine model. Biomaterials, 30(14):2716–2723, 2009.

[180] T. Shimizu, H. Sekine, Y. Isoi, M. Yamato, A. Kikuchi, and T. Okano. Long-term survival and growth of pulsatile myocardial tissue grafts engineered by the layering of cardiomyocyte sheets. Tissue Engineering, 12(3):499–507, 2006.

[181] X. Wang, X. Qiu, and C. Wu. Comparison of the coil-to-globule and the globule-to-coil transitions of a single poly(n-isopropylacrylamide) homopolymer chain in water. Macromolecules, 31(9):2972–2976, 1998.

[182] P. Kujawa, F. Segui, S. Shaban, Charbel Diab, Y. Okada, F. Tanaka, and F. M. Winnik. Impact of end-group association and main-chain hydration on the thermosensitive properties of hydrophobically modified telechelic poly(n-isopropylacrylamides) in water. Macromolecules, 39(1):341–348, 2006.

[183] M. A. Cooperstein, P. A. H. Nguyen, and H. E. Canavan. Poly(n-isopropyl acrylamide)-coated surfaces: Investigation of the mechanism of cell detachment. Biointerphases, 12 (2), 2017.

[184] J. Lutz. Polymerization of oligo(ethylene glycol) (meth)acrylates: Toward new generations of smart biocompatible materials. Journal of Polymer Science Part A: Polymer Chemistry, 46(11):3459–3470, 2008.

[185] Z. Hu, T. Cai, and C. Chi. Thermoresponsive oligo(ethylene glycol)-methacrylate- based polymers and microgels. Soft Matter, 6:2115–2123, 2010.

[186] E. Wischerhoff, K. Uhlig, A. Lankenau, H.G. Börner, A. Laschewsky, C. Duschl, and J. Lutz. Controlled cell adhesion on peg-based switchable surfaces. Angewandte Chemie International Edition, 47(30):5666–5668, 2008.

[187] C. L. Rossouw, A. Chetty, F. S. Moolman, L. M. Birkholtz, H. Hoppe, and D. T. Mancama. Thermo-responsive non-woven scaffolds for "smart" 3d cell culture. Biotechnology and Bioengineering, 109(8):2147–2158, 2012.

[188] W. Wang, H. Liang, R. Cheikh Al Ghanami, L. Hamilton, M. Fraylich, K. M. Shakesheff, Br. Saunders, and C. Alexander. Biodegradable thermoresponsive microparticle dispersions for injectable cell delivery prepared using a single-step process. Advanced Materials, 21(18):1809–1813, 2009.

[189] H. Yang, Q. Zhang, B. P. Lin, G. D. Fu, X. Q. Zhang, and L. X. Guo. Thermo-sensitive electrospun fibers prepared by a sequential thiol-ene click chemistry approach. Journal of Polymer Science Part A-Polymer Chemistry, 50(20):4182–4190, 2012.

[190] H. Okuzaki, K. Kobayashi, F. Hishiki, S. J. Su, and H. Yan. Thermo-responsive nanofiber mats fabricated by electrospinning of poly(n-isopropylacrylamide-co-stearyl acrylate). Journal of Nanoscience and Nanotechnology, 11(6):5193–5198, 2011.

[191] A. M. Aladdad, L. J. White, C. Alexander, and F. R. Rose. Creating thermo-responsive co-electrospun fibres for 3d cell growth. Tissue Engineering Part A, 21:S304–S304, 2015.

[192] Food and drug administration department. Ethylene oxide, ethylene chlorohydrin, and ethylene glycol. pages 27474–27483, 1978.

[193] L. E. Sidney, M. J. Branch, H. S. Dua, and A. Hopkinson. Effect of culture medium on propagation and phenotype of corneal stroma-derived stem cells. Cytotherapy, 17(12): 1706–1722, 2015.

[194] K. Hashmani, M. J. Branch, L. E. Sidney, P. S. Dhillon, M. Verma, O. D. McIntosh, A. Hopkinson, and H. S. Dua. Characterization of corneal stromal stem cells with the potential for epithelial transdifferentiation. Stem Cell Research & Therapy, 4:226–226, 2013.

[195] R. J. Wade, E. J. Bassin, C. B. Rodell, and J. A. Burdick. Protease-degradable electrospun fibrous hydrogels. Nature Communications, 6:6639, 2015.

[196] D. Grafahrend, K. Heffels, M. V. Beer, P. Gasteier, M. Möller, G. Boehm, P. D. Dalton, and J. Groll. Degradable polyester scaffolds with controlled surface chemistry combining minimal protein adsorption with specific bioactivation. Nature Materials, 10(1):67–73, 2011.

[197] N. L. Nerurkar, Brendon M. Baker, S. Sen, E. E. Wible, D. M. Elliott, and R. L. Mauck. Nanofibrous biologic laminates replicate the form and function of the annulus fibrosus. Nature Materials, 8(12):986–992, 2009.

[198] C. M. Rogers, G. E. Morris, T. W. A. Gould, R. Bail, S. Toumpaniari, H. Harrington, J. E. Dixon, K. M. Shakesheff, J. Segal, and Fraj Rose. A novel technique for the production of electrospun scaffolds with tailored three-dimensional micro-patterns employing additive manufacturing. Biofabrication, 6(3):035003, 2014.

[199] G. E. Morris, J. C. Bridge, O. M. I. Eltboli, M. P. Lewis, A. J. Knox, J. W. Aylott, C. E. Brightling, A. M. Ghaemmaghami, and F. R. Rose. Human airway smooth muscle maintain in situ cell orientation and phenotype when cultured on aligned electrospun scaffolds. American Journal of Physiology-Lung Cellular and Molecular Physiology, 307(1): L38–L47, 2015.

[200] G. Taylor. Disintegration of water drops in an electric field. Proceedings of the Royal Society of London A: Mathematical, Physical and Engineering Sciences, 280(1382):383–397, 1964.

[201] S. O. Gonen, M. E. Taygun, and S. Kucukbayrak. Effects of electrospinning parameters on gelatin/poly(epsilon-caprolactone) nanofiber diameter. Chemical Engineering & Technology, 38(5):844–850, 2015.

[202] Q. P. Pham, U. Sharma, and A. G. Mikos. Electrospinning of polymeric nanofibers for tissue engineering applications: A review. Tissue Engineering, 12(5):1197–1211, 2006.

[203] M. El Fray and H. D. Wagner. Influence of peg molecular masses on electrospinning of new multiblock terpoly(ester-ether-ester)s. Designed Monomers and Polymers, 15(6): 547–559, 2012.

[204] R. Rosic, J. Pelipenko, P. Kocbek, S. Baumgartner, M. Bester-Rogac, and J. Kristl. The role of rheology of polymer solutions in predicting nanofiber formation by electrospinning. European Polymer Journal, 48(8):1374–1384, 2012.

[205] S. Basu, M. Jassal, and A. K. Agrawal. Concept of minimum electrospinning voltage (mev) in electrospinning of pan-dmf system: effect of distance. Journal of the Textile Institute, 104(2):158–163, 2013.

[206] C. X. Zhang, X. Y. Yuan, L. L. Wu, Y. Han, and J. Sheng. Study on morphology of electrospun poly(vinyl alcohol) mats. European Polymer Journal, 41(3):423–432, 2005.

[207] Y. Yang, Z. Jia, J. Liu, L. Wang, and Z. Guan. The effects of flow rate and the distance between the nozzle and the target on the operating conditions of electrospinning. Journal of Polymer Engineering, 28(1-2):67–86, 2008.

[208] R. A. Fisher. The Arrangement of Field Experiments, chapter 8, pages 82–91. Springer Series in Statistics. Springer New York, 1992.

[209] R. Seyedmahmoud, A. Rainer, P. Mozetic, S. M. Giannitelli, M. Trombetta, E. Traversa, S. Licoccia, and A. Rinaldi. A primer of statistical methods for correlating parameters and

properties of electrospun poly(l-lactide) scaffolds for tissue engineering-part 1: Design of experiments. Journal of Biomedical Materials Research Part A, 103(1):91–102, 2015.

[210] Y. S. Castillo. Design of experimentation to systematically determine the interaction between electrospinning variables and to optimize the fiber diameter of electrospun poly (d,l-lactide-co-glycolide) scaffolds for tissue engineered constructs. BME MS Thesis, California Polytechnic State University, San Luis Obispo, United States of America, 2012.

[211] G. Ico, A. Showalter, W. Bosze, S. C. Gott, B. S. Kim, M. P. Rao, N. V. Myung, and J. Nam. Size-dependent piezoelectric and mechanical properties of electrospun p(vdf-trfe) nanofibers for enhanced energy harvesting. Journal of Materials Chemistry A, 4(6): 2293–2304, 2016.

[212] M. A. Badawi and L. K. El-Khordagui. A quality by design approach to optimization of emulsions for electrospinning using factorial and d-optimal designs. European Journal of Pharmaceutical Sciences, 58:44–54, 2014.

[213] M. Yanilmaz, F. Kalaoglu, and H. Karakas. Investigation on the effect of process variables on polyurethane nanofibre diameter using a factorial design. Fibres and Textiles in Eastern Europe, 21(2):19–21, 2013.

[214] H. M. Khanlou, B. C. Ang, S. Talebian, A. M. Afifi, and A. Andriyana. Electrospinning of polymethyl methacrylate nanofibers: optimization of processing parameters using the taguchi design of experiments. Textile Research Journal, 85(4):356–368, 2015.

[215] S. C. S. Marques, P. I. P. Soares, C. Echeverria, M. H. Godinho, and J. P. Borges. Confinement of thermoresponsive microgels into fibres via colloidal electrospinning: experimental and statistical analysis. RSC Advances, 6(80):76370–76380, 2016.

[216] A. Nazir, N. Khenoussi, L. Schacher, T. Hussain, D. Adolphe, and A. H. Hekmati. Using the taguchi method to investigate the effect of different parameters on mean diameter and variation in pa-6 nanofibres produced by needleless electrospinning. RSC Advances, 5 (94):76892–76897, 2015.

[217] K. Desai and K. Sung. Doe optimization and phase morphology of electrospun nanofibers of pani/pmma blends. NSTI-Nanotech, 3:429–432, 2004.

[218] W. Cui, X. Li, S. Zhou, and J. Weng. Investigation on process parameters of electrospinning system through orthogonal experimental design. Journal of Applied Polymer Science, 103(5):3105–3112, 2007.

[219] D. E. Heath, J. J. Lannutti, and S. L. Cooper. Electrospun scaffold topography affects endothelial cell proliferation, metabolic activity, and morphology. Journal of Biomedical Materials Research Part A, 94A(4):1195–1204, 2010.

[220] S. Gnavi, B. E. Fomasari, C. Tonda-Turo, G. Ciardelli, M. Zanetti, S. Geuna, and I. Perroteau. The influence of electrospun fibre size on schwann cell behaviour and axonal outgrowth. Materials Science & Engineering C-Materials for Biological Applications, 48: 620–631, 2015.

[221] R. Seyedmahmoud, P. Mozetic, A. Rainer, S. M. Giannitelli, F. Basoli, M. Trombetta, E. Traversa, S. Licoccia, and A. Rinaldi. A primer of statistical methods for correlating parameters and properties of electrospun poly(l-lactide) scaffolds for tissue engineering-part 2: Regression. Journal of Biomedical Materials Research Part A, 103(1):103–114, 2015. Seyedmahmoud, Rasoul Mozetic, Pamela Rainer, Alberto Giannitelli, Sara Maria Basoli, Francesco Trombetta, Marcella Traversa, Enrico Licoccia, Silvia Rinaldi, Antonio.

[222] J. Ko, N. K. Mohtaram, F. Ahmed, A. Montgomery, M. Carlson, P. C. D. Lee, S. M. Willerth, and M. B. G. Jun. Fabrication of poly (epsilon-caprolactone) microfiber scaffolds with varying topography and mechanical properties for stem cell-based tissue engineering applications. Journal of Biomaterials Science-Polymer Edition, 25(1):1–17, 2014.

[223] J. Pelipenko, P. Kocbek, B. Govedarica, R. Rosic, S. Baumgartner, and J. Kristl. The topography of electrospun nanofibers and its impact on the growth and mobility of keratinocytes. European Journal of Pharmaceutics and Biopharmaceutics, 84(2):401–411, 2013.

[224] J. Ballester-Beltran, M. Lebourg, H. Capella, A. D. Lantada, and M. Salmeron-Sanchez. Robust fabrication of electrospun-like polymer mats to direct cell behaviour. Biofabrication, 6(3), 2014.

[225] W. Liu, Y. Su, J. Fang, C. Wu, and X. Mo. Effect of topological structure of electrospun substrates on cell proliferation and morphology. Journal of Controlled Release, 172(1): E141, 2013.

[226] L. Xiao, B. Wang, G. Yang, and M. Gauthier. Poly(lactic acid)-based biomaterials: Synthesis, modification and applications. Biomedical Science, Engineering and Technology, pages 247–282, 2011.

[227] B. Gupta, N. Revagade, and J. Hilborn. Poly(lactic acid) fiber: An overview. Progress in Polymer Science, 32(4):455–482, 2007.

[228] K. Hamad, M. Kaseem, H. W. Yang, F. Deri, and Y. G. Ko. Properties and medical applications of polylactic acid: A review. Express Polymer Letters, 9(5):435–455, 2015.

[229] E. Bormashenko. Progress in understanding wetting transitions on rough surfaces. Advances in Colloid and Interface Science, 222:92–103, 2015.

[230] J. Seyfi, I. Hejazi, S. H. Jafari, H. A. Khonakdar, G. M. M. Sadeghi, A. Calvimontes, and F. Simon. On the combined use of nanoparticles and a proper solvent/non-solvent system in preparation of superhydrophobic polymer coatings. Polymer, 56:358–367, 2015.

[231] A. Marmur. Superhydrophobic and superhygrophobic surfaces: from understanding non-wettability to design considerations. Soft Matter, 9(33):7900–7904, 2013.

[232] A. Nakajima. Design of hydrophobic surfaces for liquid droplet control. NPG Asia Mater, 3:49–56, 2011.

[233] M. Nosonovsky and B. Bhushan. Biologically inspired surfaces: Broadening the scope of roughness**. Advanced Functional Materials, 18(6):843–855, 2008.

[234] A. B. D. Cassie and S. Baxter. Wettability of porous surfaces. Transactions of the Faraday Society, 40:546–551, 1944.

[235] R. N. Wenzel. Resistance of solid surfaces to wetting by water. Industrial & Engineering Chemistry, 28(8):988–994, 1936.

[236] C. W. Extrand. Uncertainty in contact angle measurements from the tangent method. Journal of Adhesion Science and Technology, 30(15):1597–1601, 2016.

[237] C. Dorrer and J. Ruhe. Wetting of silicon nanograss: From superhydrophilic to superhydrophobic surfaces. Advanced Materials, 20(1):159–163, 2008.

[238] W. Choi, A. Tuteja, J. M. Mabry, R. E. Cohen, and G. H. McKinley. A modified cassie–baxter relationship to explain contact angle hysteresis and anisotropy on non-wetting textured surfaces. Journal of Colloid and Interface Science, 339(1):208–216, 2009.

[239] S. R. Baker, S. Banerjee, K. Bonin, and M. Guthold. Determining the mechanical properties of electrospun poly-ε-caprolactone (pcl) nanofibers using afm and a novel fiber anchoring technique. Materials Science and Engineering: C, 59:203–212, 2016.

[240] F. Croisier, A. S. Duwez, C. Jérôme, A. F. Léonard, K. O. van der Werf, P. J. Dijkstra, and M. L. Bennink. Mechanical testing of electrospun pcl fibers. Acta Biomaterialia, 8(1): 218–224, 2012.

[241] H. Liang, G. Zeng, Y. Li, S. Zhang, H. Zhao, L. Guo, B. Liu, and M. Dong. Exploring the complex mechanical properties of xanthan scaffolds by afm-based force spectroscopy. Beilstein Journal of Nanotechnology, 5:365–73, 2014.

[242] S. N. Patra, A. J. Easteal, and D. Bhattacharyya. Parametric study of manufacturing poly(lactic) acid nanofibrous mat by electrospinning. Journal of Materials Science, 44 (2):647–654, 2009.

[243] S. R. Coles, D. K. Jacobs, J. O. Meredith, G. Barker, A. J. Clark, K. Kirwan, J. Stanger, and N. Tucker. A design of experiments (doe) approach to material properties optimization of electrospun nanofibers. Journal of Applied Polymer Science, 117(4):2251–2257, 2010.

[244] H. Tong and M. Wang. An investigation into the influence of electrospinning parameters on the diameter and alignment of poly(hydroxybutyrate-co-hydroxyvalerate) fibers. Journal of Applied Polymer Science, 120(3):1694–1706, 2011.

[245] Y. P. Neo, S. Ray, A. J. Easteal, M. G. Nikolaidis, and S. Y. Quek. Influence of solution and processing parameters towards the fabrication of electrospun zein fibers with sub-micron diameter. Journal of Food Engineering, 109(4):645–651, 2012.

[246] S. V. Guerra Nista, L. Peres, M. A. D'Avila, F. L. Schmidt, and L. H. Innocentini Mei. Nanostructured membranes based on cellulose acetate obtained by electrospinning, part 1: Study of the best solvents and conditions by design of experiments. Journal of Applied Polymer Science, 126:E70–E78, 2012.

[247] S. Y. Gu, J. Ren, and G. J. Vancso. Process optimization and empirical modeling for electrospun polyacrylonitrile (pan) nanofiber precursor of carbon nanofibers. European Polymer Journal, 41(11):2559–2568, 2005.

[248] S. Y. Gu and J. Ren. Process optimization and empirical modeling for electrospun poly(d,l-lactide) fibers using response surface methodology. Macromolecular Materials and Engineering, 290(11):1097–1105, 2005.

[249] T. Senthil, G. George, and S. Anandhan. Chemical-resistant ultrafine poly(styrene-co-acrylonitrile) fibers by electrospinning: Process optimization by design of experiment. Polymer-Plastics Technology and Engineering, 52(4):407–421, 2013.

[250] T. Senthil and S. Anandhan. Fabrication of styrene-acrylonitrile random copolymer nanofiber membranes from n,n-dimethyl formamide by electrospinning. Journal of Elastomers & Plastics, 47(4):327–346, 2015.

[251] P. Gupta, C. Elkins, T. E. Long, and G. L. Wilkes. Electrospinning of linear homopolymers of poly(methyl methacrylate): exploring relationships between fiber formation, viscosity, molecular weight and concentration in a good solvent. Polymer, 46(13):4799–4810, 2005.

[252] K. Nakajima, S. Honda, Y. Nakamura, F. López-Redondo, S. Kohsaka, M. Yamato, A. Kikuchi, and T. Okano. Intact microglia are cultured and non-invasively harvested without pathological activation using a novel cultured cell recovery method. Biomaterials, 22(11):1213 – 1223, 2001.

[253] A. Bundscherer, M. Malsy, R. Lange, P. Hofmann, T. Metterlein, B. M. Graf, and M. Gruber. Cell harvesting method influences results of apoptosis analysis by annexin v staining. Anticancer Research, 33(8):3201–3204, 2013.

[254] D. Ren, G. D. Pipes, D. Liu, L. Y. Shih, A. C. Nichols, M. J. Treuheit, D. N. Brems, and P. V. Bondarenko. An improved trypsin digestion method minimizes digestion-induced modifications on proteins. Analytical Biochemistry, 392(1):12–21, 2009.

[255] S. Marino, J. G. Logan, D. Mellis, and M. Capulli. Generation and culture of osteoclasts. Bonekey Reports, 3:570, 2014.

[256] Y. Voss, E. Wassel, S. Y. Jiang, Q. M. Song, S. I. Druzhinin, and H. Schonherr. Thin poly(di(ethylene glycol) methyl ether methacrylate) homopolymer brushes allow controlled adsorption and desorption of patu 8988t cells. Macromolecular Bioscience, 17(4), 2017.

[257] E. Wassel, S. Y. Jiang, Q. M. Song, S. Vogt, G. Noll, S. I. Druzhinin, and H. Schonherr. Thickness dependence of bovine serum albumin adsorption on thin thermoresponsive poly(diethylene glycol) methyl ether methacrylate brushes by surface plasmon resonance measurements. Langmuir, 32(36):9360–9370, 2016.

[258] X. Xue, L. Thiagarajan, S. Braim, B. R. Saunders, K. M. Shakesheff, and C. Alexander. Upper critical solution temperature thermo-responsive polymer brushes and a mechanism for controlled cell attachment. Journal of Materials Chemistry B, pages 4926–4933, 2017.

[259] J. Heyda and J. Dzubiella. Thermodynamic description of hofmeister effects on the lcst of thermosensitive polymers. The Journal of Physical Chemistry B, 118(37):10979–10988, 2014.

[260] Y. Kim and Y. T. Matsunaga. Thermo-responsive polymers and their application as smart biomaterials. Journal of Material Chemistry B, 5:4307–4321, 2017.

[261] Giuseppe Graziano. On the temperature-induced coil to globule transition of poly-n-isopropylacrylamide in dilute aqueous solutions. International Journal of Biological Macromolecules, 27(1):89 – 97, 2000.

[262] M. J. Taylor, P. Tomlins, and T. S. Sahota. Thermoresponsive gels. Gels, 3(1):3010004, 2017.

[263] H. E. Canavan, X. Cheng, D. J. Graham, B. D. Ratner, and D. G. Castner. Cell sheet detachment affects the extracellular matrix: A surface science study comparing thermal liftoff, enzymatic, and mechanical methods. Journal of Biomedical Materials Research Part A, 75A(1):1–13, 2005.

[264] M. A. Cooperstein and H. E. Canavan. Assessment of cytotoxicity of (n-isopropyl acrylamide) and poly(n-isopropyl acrylamide)-coated surfaces. Biointerphases, 8(1):19–31, 2013.

[265] M. Ebara, M. Yamato, T. Aoyagi, A. Kikuchi, K. Sakai, and T. Okano. The effect of extensible peg tethers on shielding between grafted thermo-responsive polymer chains and integrin-rgd binding. Biomaterials, 29(27):3650–3655, 2008.

[266] E. Wassel, D. Wesner, and H. Schonherr. Colloidal force probe study of poly(di(ethylene glycol)methylether methacrylate) homopolymer brush layers in aqueous media at different temperatures. European Polymer Journal, 89:440–448, 2017.

[267] H. Y. Li, G. R. Williams, J. Z. Wu, Y. Lv, X. Z. Sun, H. L. Wu, and L. M. Zhu. Thermosensitive nanofibers loaded with ciprofloxacin as antibacterial wound dressing materials. International Journal of Pharmaceutics, 517(1-2):135–147, 2017.

[268] G. Liu, Y. Li, L. Yang, Y. Wei, X. Wang, Z. Wang, and L. Tao. Cytotoxicity study of polyethylene glycol derivatives. RSC Advances, 7:18252–18259, 2017.

[269] A.M. Aladdad. Dynamic Patterned Electrospun Fibres for 3D Cell Culture. PhD thesis, University of Nottingham, 2016. Ph.D. Thesis, United Kingdom.

[270] H. Tai, W. Wang, T. Vermonden, F. Heath, W. E. Hennink, C. Alexander, K. M. Shakesheff, and S. M. Howdle. Thermoresponsive and photocrosslinkable pegmema-ppgma-egdma copolymers from a one-step atrp synthesis. Biomacromolecules, 10(4):822–828, 2009.

[271] H. H. Oh, Y. Ko, H. Uyama, W. H. Park, D. Cho, and O. H. Kwon. Fabrication and characterization of thermoresponsive polystyrene nanofibrous mats for cultured cell recovery. BioMed Research International, page 480694, 2014.

[272] L.D. Blackman, M.I. Gibson, and R.K. O'Reilly. Probing the causes of thermal hysteresis using tunable $n_{agg}$ micelles with linear and brush-like thermoresponsive coronas. Polymer Chemistry, 8:233–244, 2017.

[273] C. M. Schilli, A. H. E. Müller, E. Rizzardo, S. H. Thang, and Y. K. Chong. Advances in Controlled/Living Radical Polymerization. American Chemical Society, 2003.

[274] K. Van Durme, G. Van Assche, and B. Van Mele. Kinetics of demixing and remixing in poly(n-isopropylacrylamide)/water studied by modulated temperature dsc. Macromolecules, 37(25):9596–9605, 2004.

[275] L. Wang, L. Xu, K. G. Neoh, and E. Kang. Water-soluble highly fluorescent poly[poly(ethylene glycol) methyl ether methacrylate] for cell labeling. Journal of Materials Chemistry, 21(18):6502–6505, 2011.

[276] A. V. Rodina, T. K. Tenchurin, V. P. Saprykin, A. D. Shepelev, V. G. Mamagulashvili, T. E. Grigor'ev, K. I. Lukanina, A. S. Orekhov, E. Y. Moskaleva, and S. N. Chvalun. Migration and proliferative activity of mesenchymal stem cells in 3d polylactide scaffolds depends on cell seeding technique and collagen modification. Bulletin of Experimental Biology and Medicine, 162(1):120–126, 2016.

[277] C. M. Gabbott, Z. X. Zhou, G. X. Han, and T. Sun. A novel scale-down cell culture and imaging design for the mechanistic insight of cell colonisation within porous substrate. Journal of Microscopy, 267(2):150–159, 2017.

[278] L. D. Roberts, S. Virtue, A. Vidal-Puig, A. W. Nicholls, and J. L. Griffin. Metabolic phenotyping of a model of adipocyte differentiation. Physiol Genomics, 39(2):109–119, 2009.

[279] G. Harvers and D.W. Grainger. An introduction to biomaterials. CRC Press, 2006.

[280] P. Thevenot, W. Hu, and L. Tang. Surface chemistry influence implant biocompatibility. Current Topics in Medicinal Chemistry, 8(4):270–280, 2008.

[281] J Krachmer, M. Mannis, and E. Holland. Cornea. Mosby, 3 edition, 2010.

[282] N. Pinnamaneni and J. L. Funderburgh. Concise review: Stem cells in the corneal stroma. Stem cells, 30(6):1059–1063, 2012.

[283] H. Y. Zhou, Y. Cao, J. Wu, and W. S. Zhang. Role of corneal collagen fibrils in corneal disorders and related pathological conditions. International Journal of Ophthalmology, 10(5):803–811, 2017.

[284] Ha. S. Dua, L. A. Faraj, D. G. Said, T. Gray, and J. Lowe. Human corneal anatomy redefined. Ophthalmology, 120(9):1778–1785, 2013.

[285] H. S. Dua, L. A. Faraj, and D. G. Said. Dua's layer: discovery, characteristics, clinical applications, controversy and potential relevance to glaucoma. Expert Review of Ophthalmology, 10(6):531–547, 2015.

[286] C. Costet and D. Touboul. Viscodissection of dua's layer after partial big bubble. Journal Francais D Ophtalmologie, 39(4):404–404, 2016.

[287] H. S. Dua and D. G. Said. Clinical evidence of the pre-descemets layer (dua's layer) in corneal pathology. Eye, 30(8):1144–1145, 2016.

[288] H. Lodish, A. Berk, S.L. Zipursky, P Matsudaira, D. Baltimore, and J Darnell. Molecular Cell Biology. New York: W. H. Freeman, 4th edition edition, 2000.

[289] D. H. Johnson, W. M. Bourne, and R. J. Campbell. The ultrastructure of descemet's membrane. i. changes with age in normal corneas. Archives of Ophthalmology, 100(12):1942–1947, 1982.

[290] G. J. Parfitt, C. Pinali, R. D. Young, A. J. Quantock, and C. Knupp. Three-dimensional reconstruction of collagen-proteoglycan interactions in the mouse corneal stroma by electron tomography. Journal of Structural Biology, 170(2):392–397, 2010.

[291] J.E. Scott and A.M. Thomlinson. The structure of interfibrillar proteoglycan bridges (shape modules') in extracellular matrix of fibrous connective tissues and their stability in various chemical environments. Journal of Anatomy, 192(3):391–405, 1998.

[292] Y.M. Michelacci. Collagens and proteoglycans of the corneal extracellular matrix. Brazilian Journal of Medical and Biological Research, 36(8):1037–1046, 2003.

[293] K.M. Meek and C. Boote. The organization of collagen in the corneal stroma. Experimental Eye Research, 78(3):503–512, 2004.

[294] M. C. Snyder, J. Bergmanson, and M. J. Doughty. Keratocytes: no more the quiet cells. Journal of the American Optometric Association, 69(3):180–187, 2003.

[295] J.V. Jester, T. Moller-Pedersen, J. Huang, C.M. Sax, W.T. Kays, H.D. Cavangh, W.M. Petroll, and J. Piatigorsky. The cellular basis of corneal transparency: evidence for 'corneal crystallins'. Journal of Cell Science, 112(5):613–622, 1999.

[296] H. Matsuda and G.K. Smelser. Electron microscopy of corneal wound healing. Experimental eye research, 16(6):427–442, 1973.

[297] D. J. Armstrong, P. Hiscott, M. Batterbury, and S. Kaye. Corneal stromal cells (keratocytes) express thrombospondins 2 and 3 in wound repair phenotype. The International Journal of Biochemistry & Cell Biology, 34:558–593, 2002.

[298] J. L. Funderburgh, M. M. Mann, and M. L. Funderburgh. Keratocyte phenotype mediates proteoglycan structure: a role for fibroblasts in corneal fibrosis. Journal of Biological Chemistry, 278(46):45629–45637, 2003.

[299] The National Eye Institute (NEI). Facts about the cornea and corneal disease, 2017. URL `https://nei.nih.gov/health/cornealdisease`.

[300] J. P. Whitcher, M. Srinivasan, and M. P. Upadhyay. Corneal blindness: a global perspective. Bull World Health Organ, 79(3):104–117, 2001.

[301] B. Munoz and S. West. Trachoma: The forgotten cause of blindness. Epidemiologic Reviews, 19(2):205–217, 1997.

[302] A. Al-Mujaini, N. Al-Kharusi, A. Thakral, and U. K. Wali. Bacterial keratitis: Perspective on epidemiology, clinico-pathogenesis, diagnosis and treatment. Sultan Qaboos University Medical Journal, 9(2):184–95, 2009.

[303] H. Limburg, F.B. von Bischhoffshausen, F. Gomez, J.C. Silva, and S. Foster. Review of recent surveys on blindness and visual impairment in latin america. British Journal of Opthalmology, 92(3):315–319, 2008.

[304] L. Rossetti, M. Digiuni, M. Giovanni, M. Centofanti, A. M. Fea, M. Iester, P. Frezzotti, M. Figus, A. Ferreras, F. Oddone, L. Tanga, T. Rolle, V. Battaglino, C. Posarelli, I. Motolese, P. Mittica, S. A. Bagaglia, C. Menicacci, S. De Cilla', A. Autelitano, and P. Fogagnolo. Blindness and glaucoma: A multicenter data review from 7 academic eye clinics. PLOS ONE, 10(8):1–12, 2015.

[305] M. J. Burton. Corneal blindness: Prevention, treatment and rehabilitation. Community Eye Health, 22(71):33–35, 2009.

[306] N. Polisetty, A. Fatima, S. L. Madhira, V. S. Sangwan, and G. K. Vemuganti. Mesenchymal cells from limbal stroma of human eye. Molecular Vision, 14(46-53):431–442, 2008.

[307] G. G. Li, Y. T. Zhu, H. T. Xie, S. Y. Chen, and S. C. G. Tseng. Mesenchymal stem cells derived from human limbal niche cells. Investigative Ophthalmology & Visual Science, 53(9):5686–5697, 2012.

[308] J. Wu, Y. Du, M.M. Mann, Funderburgh J.L., and W.R. Wagner. Corneal stromal stem cells versus corneal fibroblasts in generating structurally appropriate corneal stromal tissue. Experimental Eye Research, 120:71–81, 2014.

[309] S. L. Wilson, Y. Yang, and A. J. El Haj. Corneal stromal cell plasticity: In vitro regulation of cell phenotype through cell-cell interactions in a three-dimensional model. Tissue Engineering Part A, 20(1-2):225–238, 2014.

[310] T. Kawakita, E. M. Espana, H. He, R. Smiddy, J. M. Parel, C. Y. Liu, and S. C. G. Tseng. Preservation and expansion of the primate keratocyte phenotype by downregulating tgf-beta signaling in a low-calcium, serum-free medium. Investigative Ophthalmology & Visual Science, 47(5):1918–1927, 2006.

[311] A. A. Chan, A. J. Hertsenberg, M. L. Funderburgh, M. M. Mann, Y. Q. Du, K. A. Davoli, J. D. Mich-Basso, L. Yang, and J. L. Funderburgh. Differentiation of human embryonic stem cells into cells with corneal keratocyte phenotype. Plos One, 8(2), 2013.

[312] I. Ortega, A. J. Ryan, P. Deshpande, S. MacNeil, and F. Claeyssens. Combined microfabrication and electrospinning to produce 3-d architectures for corneal repair. Acta Biomaterialia, 9(3):5511–5520, 2013.

[313] J. Diao, X. Pang, Y. Qiu, Y. Miao, M. Yu, and T. Fan. Construction of a human corneal stromal equivalent with non-transfected human corneal stromal cells and acellular porcine corneal stromata. Experimental eye research, 132:216–224, 2015.

[314] S. Salehi, M. Fathi, S. H. Javanmard, T. Bahners, J. S. Gutmann, S. Erguen, K. P. Steuhl, and T. A. Fuchsluger. Generation of pgs/pcl blend nanofibrous scaffolds mimicking corneal stroma structure. Macromolecular Materials and Engineering, 299(4):455–469, 2014.

[315] G. Lin, E. Finger, and J. C. Gutierrez-Ramos. Expression of cd34 in endothelial cells, hematopoietic progenitors and nervous cells in fetal and adult mouse tissues. European Journal of Immunology, 25(6):1508–1516, 1995.

[316] L. Fina, H. V. Molgaard, D. Robertson, N. J. Bradley, P. Monaghan, D. Delia, D. R. Sutherland, M. A. Baker, and M. F. Greaves. Expression of the cd34 gene in vascular endothelial cells. Blood, 75(12):2417–2426, 1990.

[317] J. Brown, M. F. Greaves, and H. V. Molgaard. The gene encoding the stem cell antigen, cd34, is conserved in mouse and expressed in haemopoietic progenitor cell lines, brain, and embryonic fibroblasts. International Immunology, 3(2):175–184, 1991.

[318] C. S. Lin, H. Ning, G. Lin, and T. F. Lue. Is cd34 truly a negative marker for mesenchymal stem cells? Cytotherapy, 14(10):1159–1163, 2012.

[319] J. S. Nielsen and K. M. McNagny. Novel functions of the cd34 family. Journal of Cell Science, 121(22):3683–3692, 2008.

[320] C. Blanpain, W. E. Lowry, A. Geoghegan, L. Polak, and E. Fuchs. Self-renewal, multipotency, and the existence of two cell populations within an epithelial stem cell niche. Cell, 118(5):635–648, 2004.

[321] L. E. Sidney, M. J. Branch, S. E. Dunphy, H. S. Dua, and A. Hopkinson. Concise review: Evidence for cd34 as a common marker for diverse progenitors. Stem Cells, 32(6):1380–9, 2014.

[322] G. Perrella, P. Brusini, R. Spelat, P. Hossain, A. Hopkinson, and H. S. Dua. Expression of haematopoietic stem cell markers, cd133 and cd34 on human corneal keratocytes. British Journal of Ophthalmology, 91(1):94–99, 2007.

[323] J. Wu, Y. Du, S. C. Watkins, J. L. Funderburgh, and W. R. Wagner. The engineering of organized human corneal tissue through the spatial guidance of corneal stromal stem cells. Biomaterials, 33(5):1343–1352, 2012.

[324] J. Wu, Y. Du, M. M. Mann, E. Yang, J. L. Funderburgh, and W. R. Wagner. Bioengineering organized, multilamellar human corneal stromal tissue by growth factor supplementation on highly aligned synthetic substrates. Tissue Engineering Part A, 19(17-18):2063–2075, 2013.

[325] J. V. Jester, P. A. Barry-Lane, H. D. Cavanagh, and W. M. Petroll. Induction of alpha-smooth muscle actin expression and myofibroblast transformation in cultured corneal keratocytes. Cornea, 15(5):505–516, 1996.

[326] S. H. Park, K. W. Kim, Y. S. Chun, and J. C. Kim. Human mesenchymal stem cells differentiate into keratocyte-like cells in keratocyte-conditioned medium. Experimental Eye Research, 101:16–26, 2012.

[327] G. Uzunalli, Z. Soran, T. S. Erkal, Y. S. Dagdas, E. Dinc, A. M. Hondur, K. Bilgihan, B. Aydin, M. O. Guler, and A. B. Tekinay. Bioactive self-assembled peptide nanofibers for corneal stroma regeneration. Acta Biomaterialia, 10(3):1156–1166, 2014.

[328] F. Li, D. Carlsson, C. Lohmann, E. Suuronen, S. Vascotto, K. Kobuch, H. Sheardown, R. Munger, M. Nakamura, and M. Griffith. Cellular and nerve regeneration within a biosynthetic extracellular matrix for corneal transplantation. Proceedings of the National Academy of Sciences, 100(26):15346–15351, 2003.

[329] A. D. Baldwin and K. L. Kiick. Reversible maleimide-thiol adducts yield glutathione-sensitive poly(ethylene glycol)-heparin hydrogels. Polymer Chemistry, 4(1):133–143, 2013.

[330] C. L. McGann, R. E. Dumm, A. K. Jurusik, I. Sidhu, and K. L. Kiick. Thiol-ene photocrosslinking of cytocompatible resilin-like polypeptide-peg hydrogels. Macromolecular Bioscience, 16(1):129–138, 2016.

[331] Y. Liu, W. Hou, H. Sun, C. Cui, L. Zhang, Y. Jiang, Y. Wu, Y. Wang, J. Li, B. S. Sumerlin, Q. Liu, and W. Tan. Thiol-ene click chemistry: a biocompatible way for orthogonal bioconjugation of colloidal nanoparticles. Chemical Science, pages 6182–6187, 2017.

[332] P.H. Bruice. Organic Chemistry. Pearson, 5 edition, 2007.

[333] Singh R. and Whitesides G.M. Supplement S: The chemistry of sulphur-containing functional groups. Thiol-disulfide interchange, chapter Chapter 13. Mosby, 3 edition, 1993.

[334] D. Rabuka, J. S. Rush, G. W. deHart, P. Wu, and C. R. Bertozzi. Site-specific chemical protein conjugation using genetically encoded aldehyde tags. Nature Protocols, 7(6): 1052–67, 2012.

[335] R. Singh and G. M. Whitesides. Degenerate intermolecular thiolate-disulfide interchange involving cyclic five-membered disulfides is faster by -1o$^3$ than that involving six- or seven-membered disulfides. Journal of American Chemistry Society, 112:6304–6309, 1990.

[336] M. S. Wagner, S. L. McArthur, M. Shen, T. A. Horbett, and D. G. Castner. Limits of detection for time of flight secondary ion mass spectrometry (tof-sims) and x-ray photoelectron spectroscopy (xps): detection of low amounts of adsorbed protein. Journal of Biomaterials Science. Polymer Edition, 13(4):407–428, 2002.

[337] P. Kingshott, S. McArthur, H. Thissen, D. G. Castner, and H. J. Griesser. Ultrasensitive probing of the protein resistance of peg surfaces by secondary ion mass spectrometry. Biomaterials, 23(24):4775–85, 2002.

[338] C. M. Mahoney, S. V. Roberson, and G. Gillen. Depth profiling of 4-acetamindophenol-doped poly(lactic acid) films using cluster secondary ion mass spectrometry. Analytical Chemistry, 76(11):3199–207, 2004.

[339] D. Cossement, R. Gouttebaron, V. Cornet, P. Viville, M. Hecq, and R. Lazzaroni. Pla-pmma blends: A study by xps and tof-sims. Applied Surface Science, 252(19):6636 – 6639, 2006.

[340] H. K. Shon, M. Son, K. M. Park, C. K. Rhee, N. W. Song, H. M. Park, D. W. Moon, and T. G. Lee. Tof-sims imaging and spectroscopic analyses of peg-conjugated aunps. Surface and Interface Analysis, 43(1-2), 2011.

[341] Y. Yokoyama, S. Aoyagi, M. Fujii, J. Matsuo, J. S. Fletcher, N. P. Lockyer, J. C. Vickerman, M. K. Passarelli, R. Havelund, and M. P. Seah. Peptide fragmentation and surface structural analysis by means of tof-sims using large cluster ion sources. Analytical Chemistry, 88(7):3592–3597, 2016.

[342] M. Körsgen, A. Pelster, K. Dreisewerd, and H. F. Arlinghaus. 3d tof-sims analysis of peptide incorporation into maldi matrix crystals with sub-micrometer resolution. Journal of The American Society for Mass Spectrometry, 27(2):277–284, 2016.

[343] S. Y. Lee, C. Y. Ahn, J. Lee, J. H. Lee, and J. H. Chang. Rapid and selective separation for mixed proteins with thiol functionalized magnetic nanoparticles. Nanoscale Research Letters, 7(1):279–285, 2012.

[344] P. Esmaeilzadeh, A. Kowitsch, F. Heyroth, G. Schmidt, S. Fischer, K. Richter, and T. Groth. Synthesis of thiolated polysaccharides for formation of polyelectrolyte multilayers with improved cellular adhesion. Carbohydrate Polymers, 157:1205–1214, 2017.

[345] K. Jans, B. Van Meerbergen, G. Reekmans, K. Bonroy, W. Annaert, G. Maes, Y. Engelborghs, G. Borghs, and C. Bartic. Chemical and biological characterization of thiol sams for neuronal cell attachment. Langmuir, 25(8):4564–70, 2009.

[346] A. Blau. Cell adhesion promotion strategies for signal transduction enhancement in microelectrode array in vitro electrophysiology: An introductory overview and critical discussion. Current Opinion in Colloid & Interface Science, 18(5):481–492, 2013.

[347] S. Ying, A. Shiraishi, C. W. Kao, R. L. Converse, J. L. Funderburgh, J. Swiergiel, M. R. Roth, G. W. Conrad, and W. W. Kao. Characterization and expression of the mouse lumican gene. Journal of Biological Chemistry, 272(48):30306–30313, 1997.

[348] S. Saika, A. Shiraishi, S. Saika, C.-Y Liu, J.L. Funderburgh, C.W.C Kao, R.L. Converse, and W.W. Kao. Role of lumican in the corneal epithelium during wound healing. Journal of Biological Chemistry, 275:2607–2612, 2000.

[349] J. M. Holzwarth and P. X. Ma. 3d nanofibrous scaffolds for tissue engineering. Journal of Materials Chemistry, 21(28):10243–10251, 2011.

[350] N. Masoumi, D. Copper, P. Chen, A. Cubberley, K. Guo, R. Z. Lin, B. Ahmed, D. Martin, E. Aikawa, J. Melero-Martin, and J. Mayer. Elastomeric fibrous hybrid scaffold supports in vitro and in vivo tissue formation. Advanced Functional Materials, 27(27):1606614, 2017.

[351] T.D. Stocco, B.V.M. Rodrigues, F.R. Marciano, and A.O. Lobo. Design of a novel electrospinning setup for the fabrication of biomimetic scaffolds for meniscus tissue engineering applications. Materials Letters, 196:221–224, 2017.

[352] D. N. Woolfson and Z. N. Mahmoud. More than just bare scaffolds: towards multicomponent and decorated fibrous biomaterials. Chemical Society Reviews, 39(9):3464–3479, 2010.

[353] J. E. Gough, A. Saiani, and A. F. Miller. Peptide hydrogels: mimicking the extracellular matrix. Bioinspired Biomimetic and Nanobiomaterials, 1(1):4–12, 2012.

[354] J. F. Li, L. Jin, M. B. Wang, S. B. Zhu, and S. Y. Xu. Repair of rat cranial bone defect by using bone morphogenetic protein-2-related peptide combined with microspheres composed of polylactic acid/polyglycolic acid copolymer and chitosan. Biomedical Materials, 10(4), 2015.

[355] N. J. Hogrebe and K. J. Gooch. Direct influence of culture dimensionality on human mesenchymal stem cell differentiation at various matrix stiffnesses using a fibrous self-assembling peptide hydrogel. Journal of Biomedical Materials Research Part A, 104(9): 2356–2368, 2016.

[356] Y. M. Shin, T. G. Kim, J. S. Park, H. J. Gwon, S. I. Jeong, H. Shin, K. S. Kim, D. Kim, M. H. Yoon, and Y. M. Lim. Engineered ecm-like microenvironment with fibrous particles for

guiding 3d-encapsulated hmsc behaviours. Journal of Materials Chemistry B, 3(13):2732–2741, 2015.

[357] A. M. Baur, T. I. Gamberger, H. G. Weerda, M. Gjuric, and E. R. Tamm. Laminin promotes differentiation, adhesion and proliferation of cell cultures derived from human acoustic nerve schwannoma. Acta Otolaryngol, 115(4):517–521, 1995.

[358] K. Stamati, J. V. Priestley, V. Mudera, and U. Cheema. Laminin promotes vascular network formation in 3d in vitro collagen scaffolds by regulating vegf uptake. Experimental Cell Research, 327(1):68–77, 2014.

[359] C. L. Maruyama, N. J. Leigh, J. W. Nelson, A. D. McCall, R. E. Mellas, P. Lei, S. T. Andreadis, and O. J. Baker. Stem cell-soluble signals enhance multilumen formation in smg cell clusters. Journal of Dental Research, 94(11):1610–7, 2015.

[360] C. V. Leiton, A. Aranmolate, C. Eyermann, M. J. Menezes, L. F. Escobar-Hoyos, S. Husain, S. J. Winder, and H. Colognato. Laminin promotes metalloproteinase-mediated dystroglycan processing to regulate oligodendrocyte progenitor cell proliferation. Journal of Neurochemistry, 135(3):522–538, 2015.

[361] P. Topley, D.C. Jenkins, E.A. Jessup, and J.N. Stables. Effect of reconstituted basement membrane components on the growth of a panel of human tumour cell lines in nude mice. British Journal of Cancer, 67(5):953–958, 1993.

[362] Y. Hosokawa, Y. Takahashi, Y. Kadoya, M Yamashina, S. Nomizu, Y Yamada, and H. Nogawa. Significant role of laminin-1 in branching morphogenesis of mouse salivary epithelium cultured in basement membrane matrix. Development, Growth & Differentiation, 41(2):207–216, 1999.

[363] Y. Yamada, K. Hozumi, F. Katagiri, Y. Kikkawa, and M. Nomizu. Laminin-111-derived peptide-hyaluronate hydrogels as a synthetic basement membrane. Biomaterials, 34(28): 6539–6547, 2013.

[364] K. Nam, C. S. Wang, C. L. M. Maruyama, P. Lei, S. T. Andreadis, and O. J. Baker. L1 peptide-conjugated fibrin hydrogels promote salivary gland regeneration. Journal of Dental Research, 96(7):798–806, 2017.

[365] L. M. Nibourg, E. Gelens, S. A. F. Nibourg, M. R. de Jong, R. Kuijer, T. G. van Kooten, and S. A. Koopmans. Effects of peptide ratios in nanofibre-based hydrogels for the prevention of capsular opacification. Acta Ophthalmologica, 94(7):721–729, 2016.

[366] L. M. Nibourg, E. Gelens, M. R. de Jong, R. Kuijer, T. G. van Kooten, and S. A. Koopmans. Nanofiber-based hydrogels with extracellular matrix-based synthetic peptides for the prevention of capsular opacification. Experimental Eye Research, 143:60–67, 2016.

[367] K. Merrett, C. M. Griffith, Y. Deslandes, G. Pleizier, and H. Sheardown. Adhesion of corneal epithelial cells to cell adhesion peptide modified phema surfaces. Journal of Biomaterials Science-Polymer Edition, 12(6):647–671, 2001.

[368] L. Aucoin, C. M. Griffith, G. Pleizier, Y. Deslandes, and H. Sheardown. Interactions of corneal epithelial cells and surfaces modified with cell adhesion peptide combinations. Journal of Biomaterials Science-Polymer Edition, 13(4):447–462, 2002.

[369] X. D. Duan, C. McLaughlin, M. Griffith, and H. Sheardown. Biofunctionalization of collagen for improved biological response: Scaffolds for corneal tissue engineering. Biomaterials, 28(1):78–88, 2007.

[370] H. B. Zhang, M. Zhu, and R. Q. You. Modified biopolymer scaffolds by co-axial electrospinning, volume 160-162 of Advanced Materials Research, pages 1062–1066. Trans Tech Publications Ltd, 2011.

[371] I. C. Liao and K. W. Leong. Efficacy of engineered fviii-producing skeletal muscle enhanced by growth factor-releasing co-axial electrospun fibers. Biomaterials, 32(6):1669–1677, 2011.

[372] V. Lukasova, M. Buzgo, V. Sovkova, J. Dankova, M. Rampichova, and E. Amler. Osteogenic differentiation of 3d cultured mesenchymal stem cells induced by bioactive peptides. Cell Proliferation, 50(4), 2017.

[373] J. N. Roberts, J. K. Sahoo, L. E. McNamara, K. V. Burgess, J. Yang, E. V. Alakpa, H. J. Anderson, J. Hay, L. A. Turner, S. J. Yarwood, M. Zelzer, R. O. Oreffo, R. V. Ulijn, and M. J. Dalby. Dynamic surfaces for the study of mesenchymal stem cell growth through adhesion regulation. ACS Nano, 10(7):6667–79, 2016.

[374] J. K. Sahoo, N. M. S. Sirimuthu, A. Canning, M. Zelzer, D. Graham, and R. V. Ulijn. Analysis of enzyme-responsive peptide surfaces by raman spectroscopy. Chemical Communications, 52:4698–4701, 2016.

[375] G. R. Fulmer, A. J. M. Miller, N. H. Sherden, H. E. Gottlieb, A. Nudelman, B. M. Stoltz, J. E. Bercaw, and K. I. Goldberg. Nmr chemical shifts of trace impurities: Common labo-

ratory solvents, organics, and gases in deuterated solvents relevant to the organometallic chemist. Organometallics, 29(9):2176–2179, 2010.

# Chapter 9

# Supplementary data

### 9.0.1 Hydrogen Nuclear Magnetic Resonance spectroscopy ($^1$H-NMR)

Nuclear Magnetic Resonance spectroscopy is an analytical technique which gives information on the molecular structure and purity of the sample. This is done by using the magnetic properties of atomic nuclei in the sample. Nuclei are electrically charge and some can spin and act as a magnet. By applying an external magnetic field an energy transfer occurs from the base energy to a higher energy level. This energy transfer takes place at a wavelength corresponding to a radio frequency. When the spin returns to its base energy the energy emitted is the same frequency. The precise resonant frequency of the energy transition depends on the effective magnetic field of the nucleus. Electron shielding and chemical environment affect this field. Therefore, nucleus chemical environment can be observed from its resonant frequency. The higher resonant frequencies correspond to more electronegative nucleus. Other factors such as ring currents and bond strain affect the frequency shift. The exact chemical shift are slightly affected by isotopic substitution, such as solvent, temperature etc, known as isotope shift.

Besides the slight affect of the isotope shift nuclei are affected by there orientation in the molecular structure and there neighbouring nuclei. This phenomenon is known as spin-spin coupling, this causes the signal to split for each type of nucleus into two or

more lines. The coupling constant or J is the size of the splitting and is independent of the magnetic field and is measured as an absolute frequency (Hertz). The number of splitting gives information on the number of chemically bonded nuclei around the observed nucleus. When dealing with more then two spins, extra signals may appear, these are called second order coupling.

### 9.0.2 Gel permeation chromatography (GPC)

Gel permeation chromatography (GPC) is used to measure the molecular weight distribution of a sample and is a type of size exclusion chromatography (SEC). Separation is based on the size or hydrodynamic volume (radius of gyration) of the sample. A packed porous beads column is used to separate the samples different size molecules. Smaller molecules can easily enter these porous beads pores, as a result they spend more time in these pores, increasing their retention time. Larger molecules spend less time in the pores and eluted more quickly. Every column has there own range of molecular weight they can separate. Too small molecules will get stuck on the column ( resulting in pore blockage) while too large molecules will pass through directly. Therefore, its important to carefully review the correct column separation range before analysis.

### 9.0.3 Fourier transform infra-red (FT-IR)

Fourier transform infrared is the study of absorption of IR radiation. This radiation causes a vibrational transition in the molecules electrons. Functional group in molecular structures absorb characteristics frequencies of the IR radiation spectrum. This results in a specific peak value of this functional group. Only functional groups with dipole moment will result in IR absorption and vibration.

### 9.0.4 Time-of-Flight Secondary Ion Mass Spectrometry (ToF-SIMS)

ToF-SIMS is an analytic method to observe the chemical topography of the sample's surface. A pulsed particle beam (in this case a 10 keV $Argon_1455$ cluster ion source) is focused on to the surface and removes the chemical species on a materials surface. Dissociated ions (positive or negative) fly of from the surface and are measured by mass spectrometry. Smaller particles fly faster to the detector then the larger (secondary particles) with are mostly molecular compounds, resulting in a spectrum the correlates with the detected particles mass.



**Figure S1:** Examples of Tensile test samples. Blue role was wrapped on both sides of the sample for improved clamp grip. Samples were image after tensile testing. **A)** Uniform fibrous scaffold, **B)** bead-on-string samples and **C)** big beads morphology scaffold.

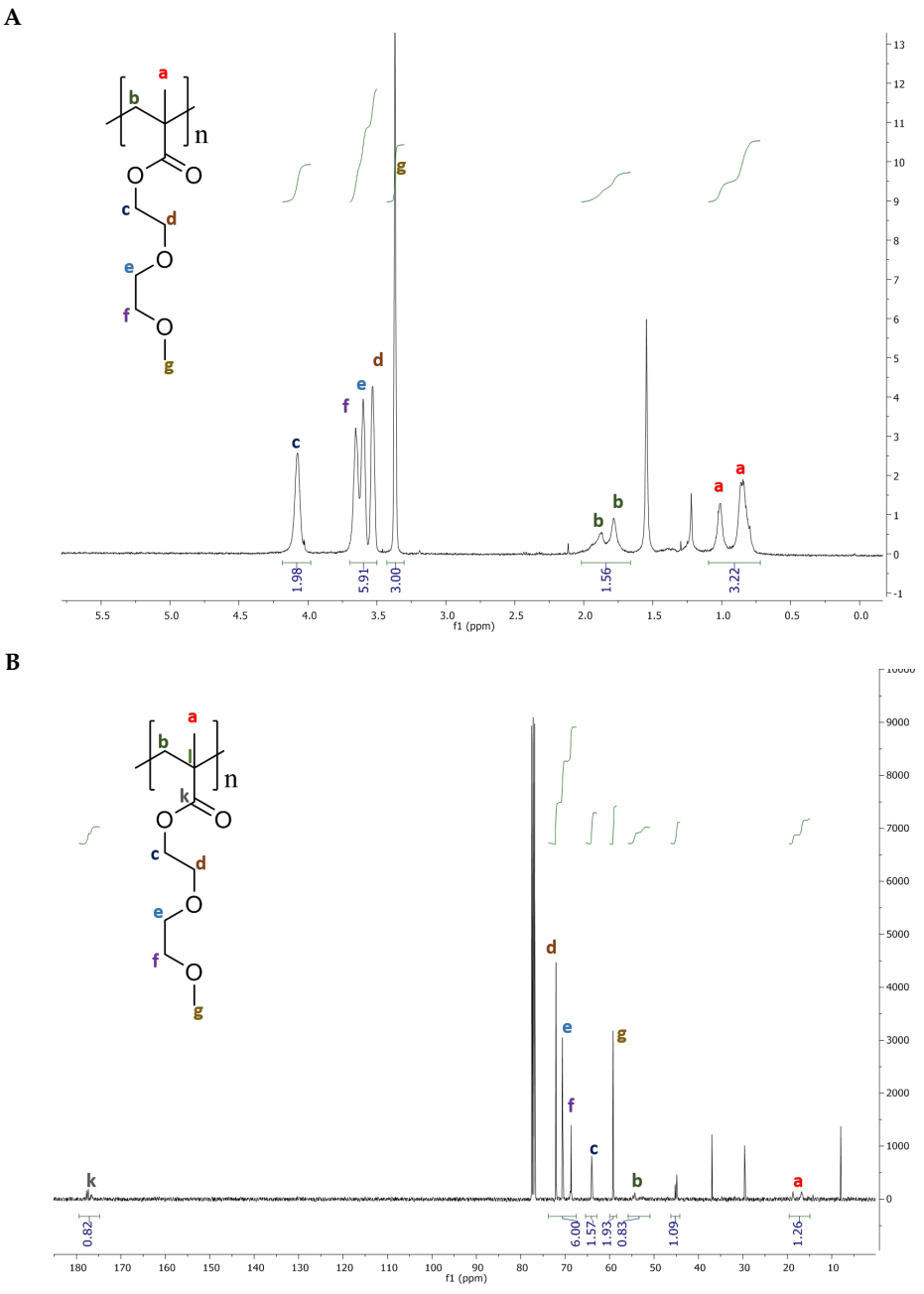



**Figure S2: A)** $^{1}$H-NMR and **B)** C$^{13}$-NMR of PDEGMA

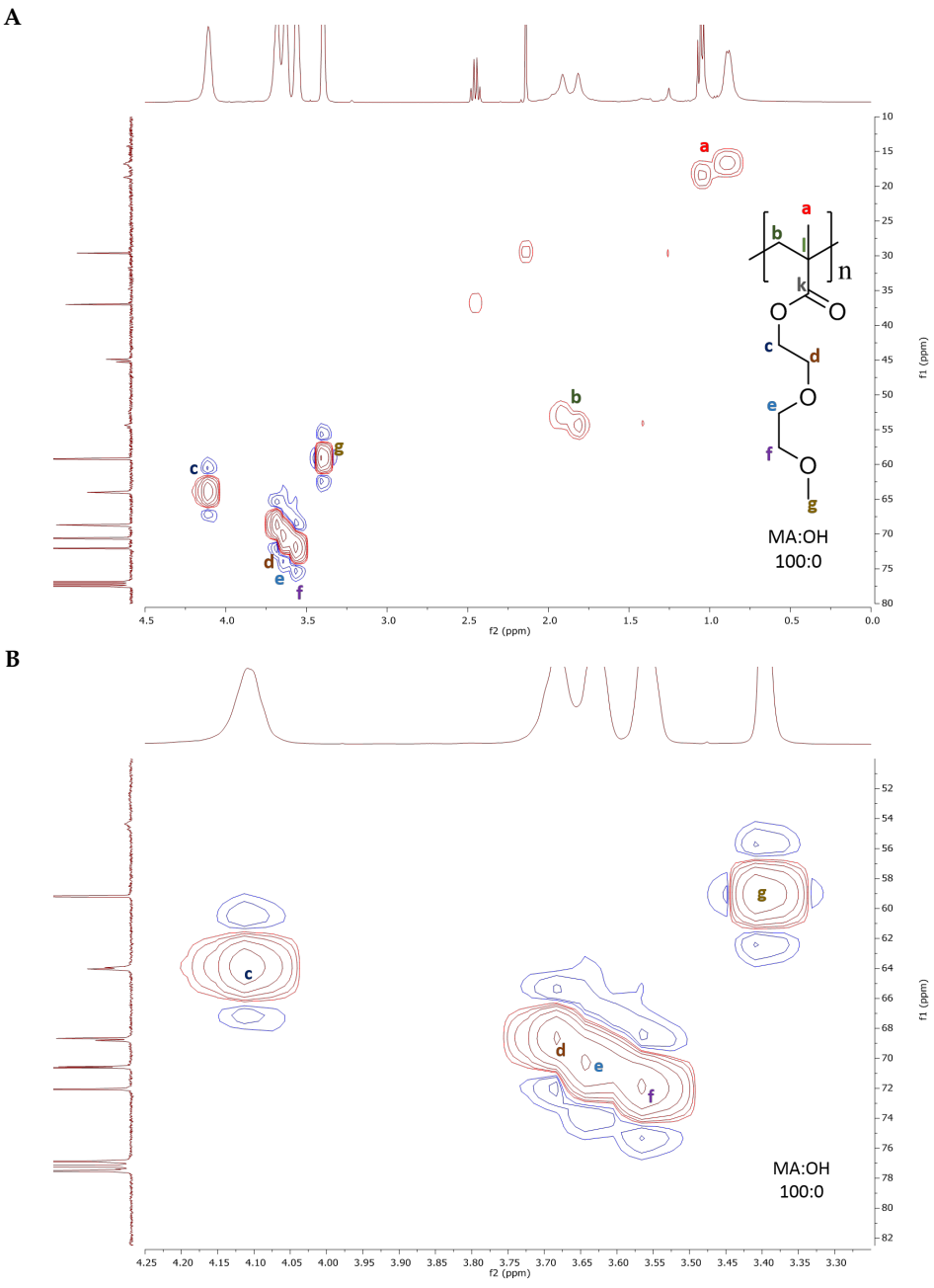



**Figure S3: A)** 2D-NMR and **B)** zoomed in 2D-NMR spectra of PDEGMA.

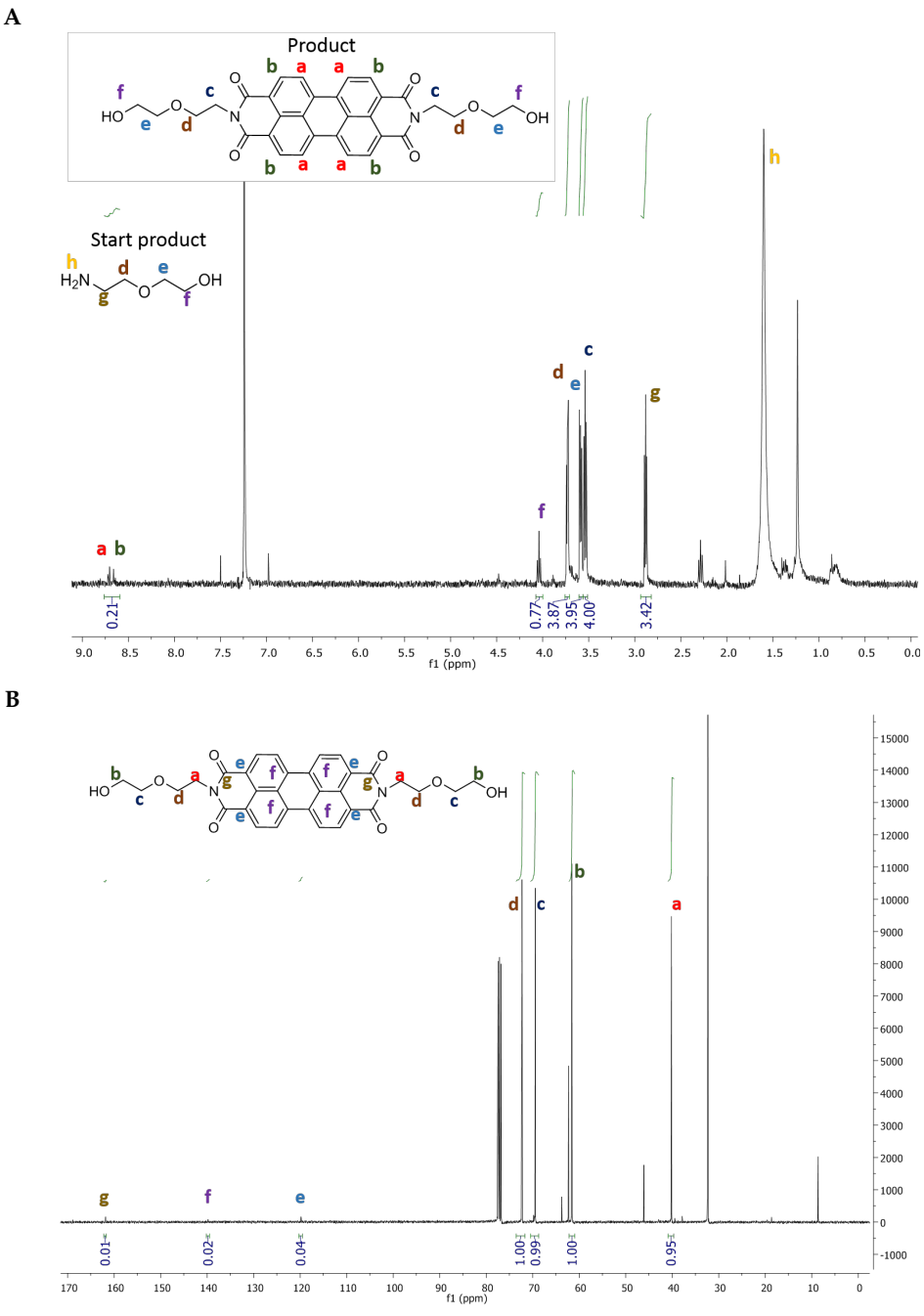



**Figure S4: A)** $^{1}$H-NMR and **B)** C$^{13}$-NMR of PBI-OH. **A)** PBI-OH with trashes of the starting product 2-(2-hydroxyethoxy)ethamine which was used in excess. Only a very low signal of the florescence molecule is visible on PBI-OH spectra, signal is lost in background for all other products. Trashes of starting product 2-(2-hydroxyethoxy)ethamine was observed.

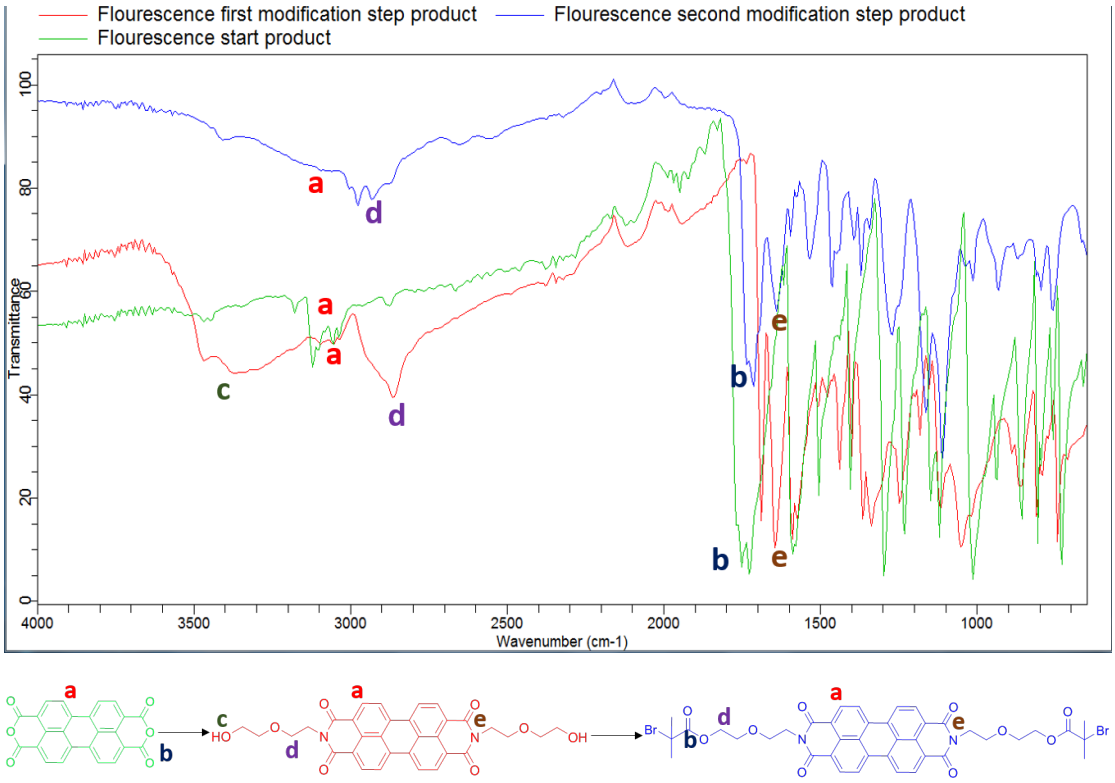



**Figure S5:** IR graph of PBI, PBI-OH and PBI-Br products.

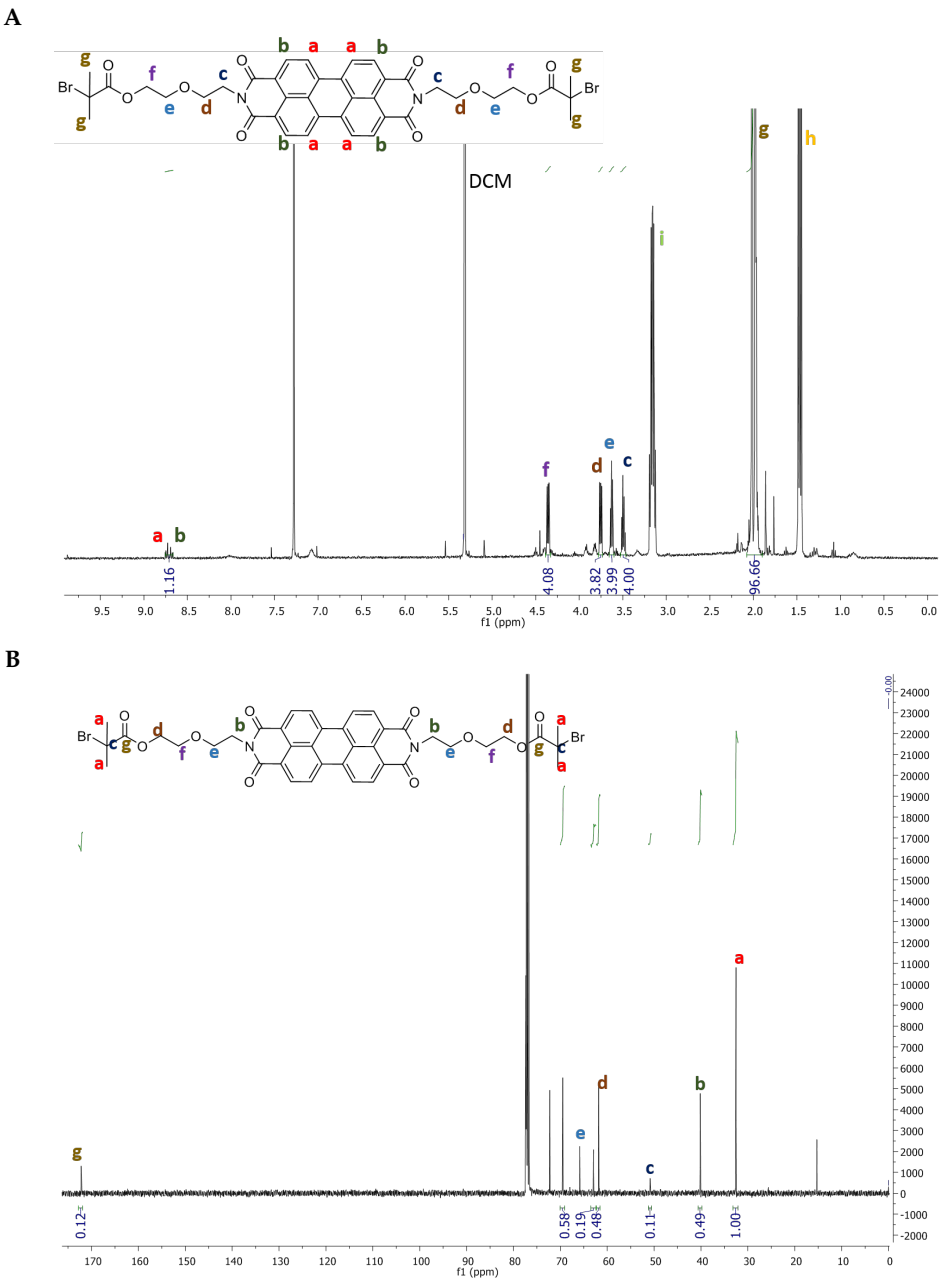



**Figure S6:** **A)** $^{1}$H-NMR and **B)** C$^{13}$-NMR of PBI-Br. **A)** PBI-Br, trashes of 2-(2-hydroxyethoxy)ethamine from previous step were removed during column purification of the PBI-Br product. Only a very low signal of the florescence molecule is visible on PBI-OH spectra, signal is lost in background for all other products. Trashes of starting product 2-(2-hydroxyethoxy)ethamine was observed.

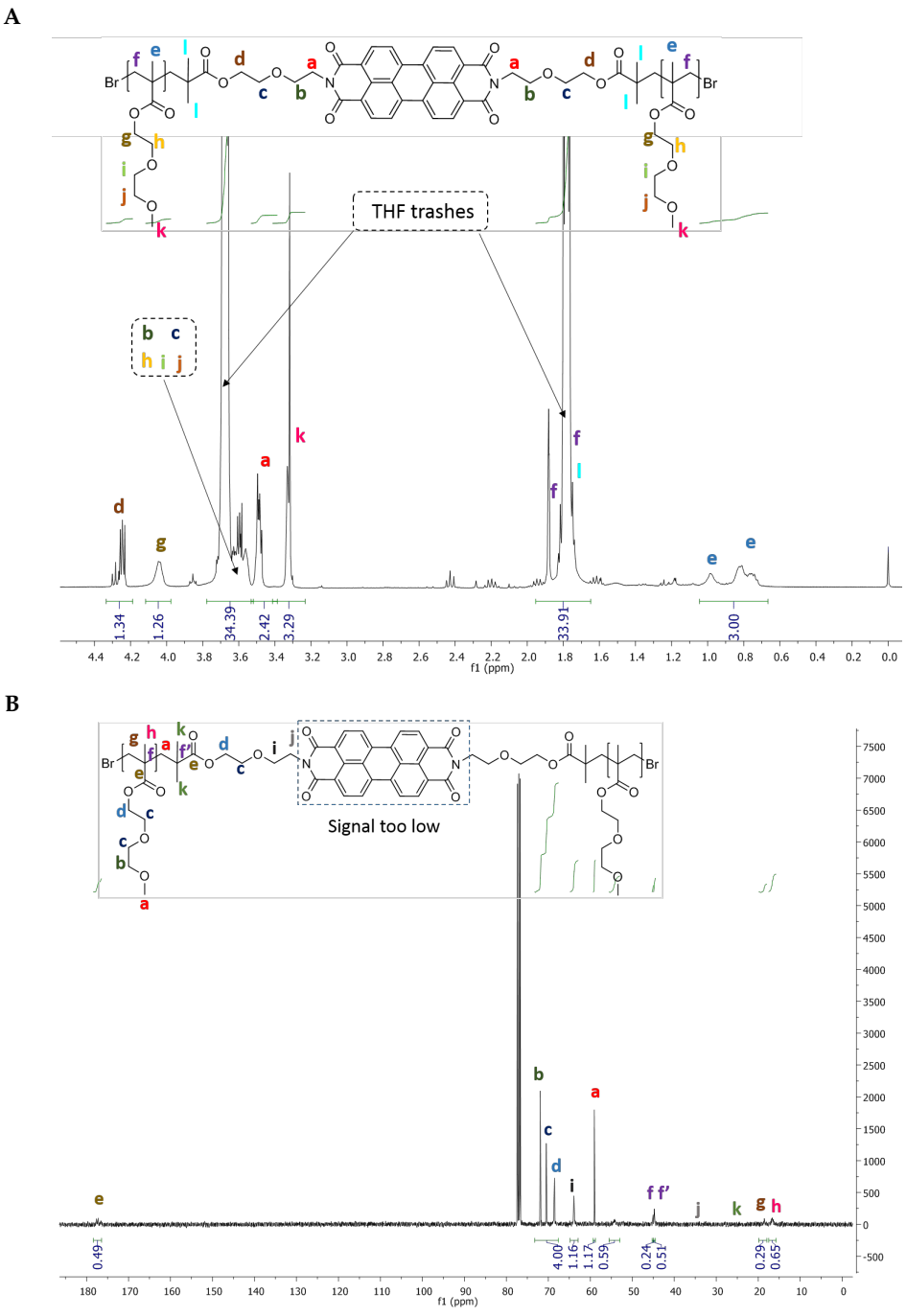



**Figure S7: A)** $^{1}$H-NMR and **B)** C$^{13}$-NMR of PBI-Br. **A)** PPBI-PDEGMA, trashes of THF[375] were observed and overlap with peak b, c, h, i, j, l and backbone peaks f.

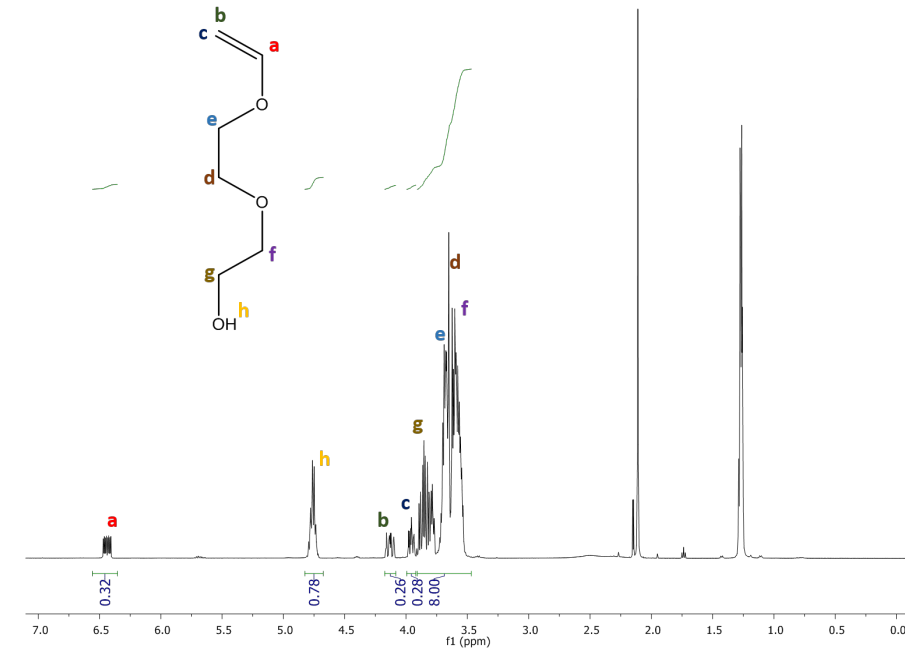



**Figure S8:** $^{1}$H-NMR of DEGOH impurities in starting product were observed.

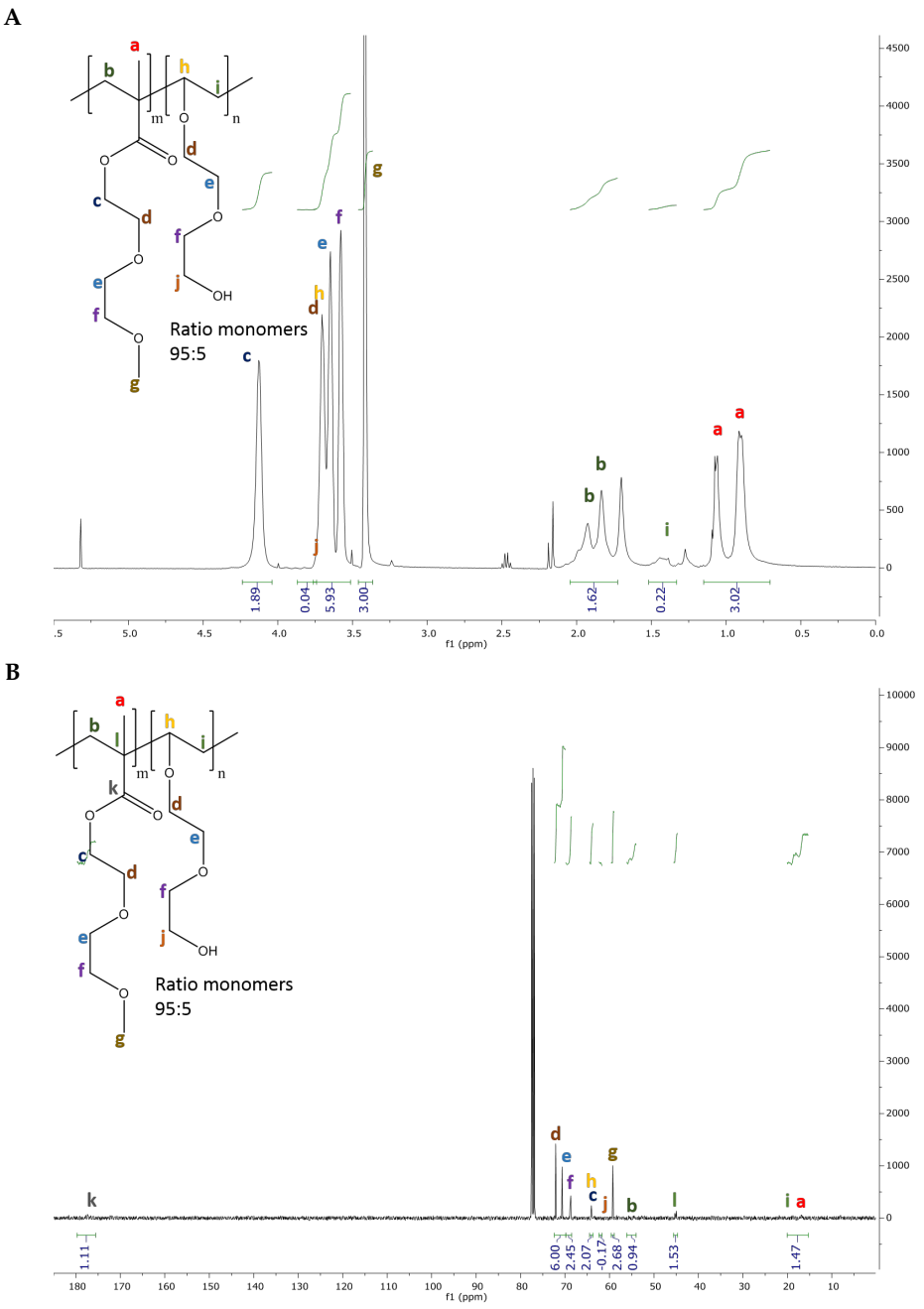



**Figure S9: A)** $^{1}$H-NMR and **B)** C$^{13}$-NMR of PDEGMA/PDEGOH 95:5 monomer ratio, trashes re-suspending solvent 2-butanone was observed present and overlap with the peak a.

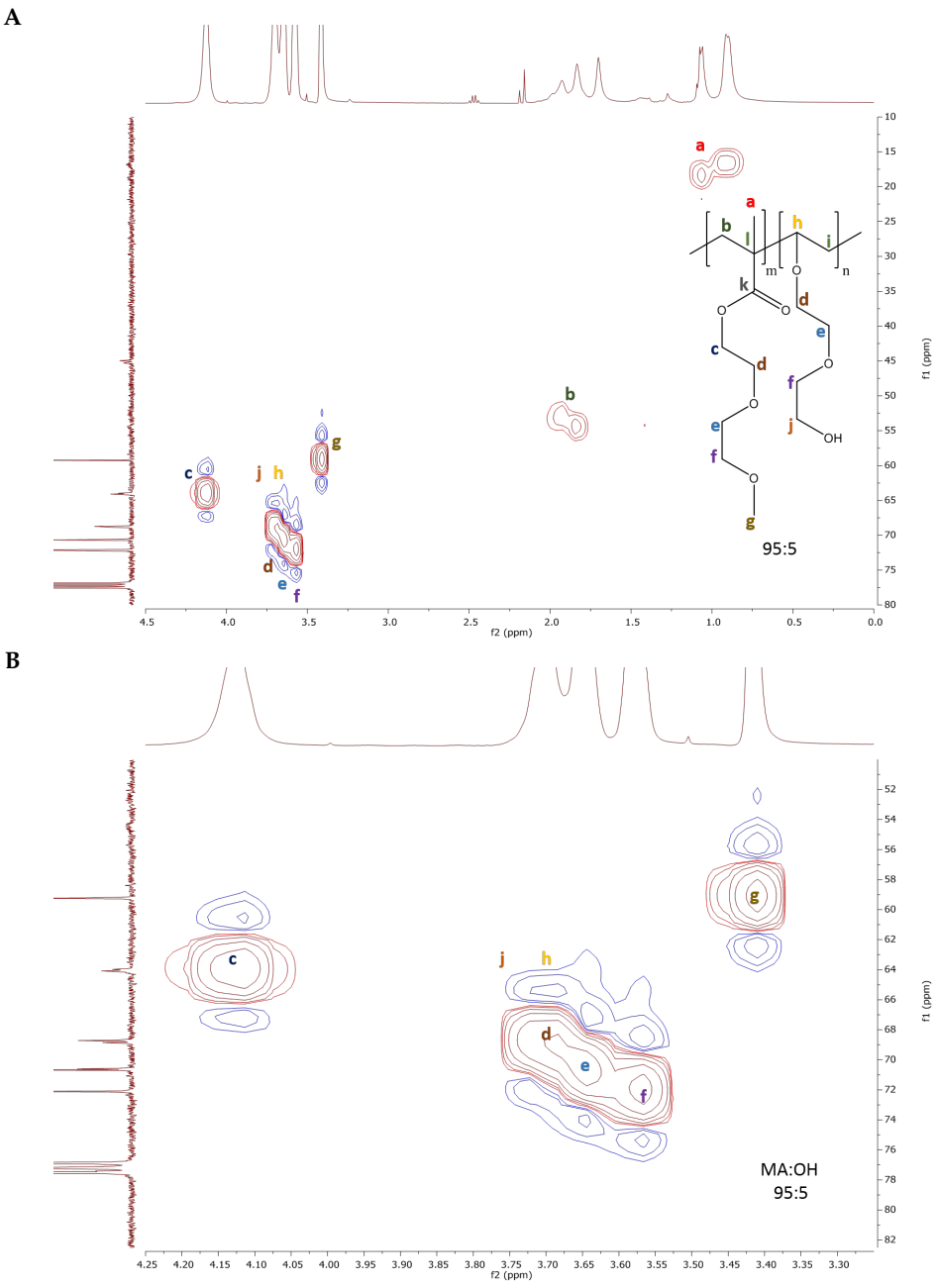



**Figure S10: A)** 2D-NMR and **B)** zoomed in 2D-NMR spectra of PDEGMA/PDEGOH 95:5 monomer ratio.

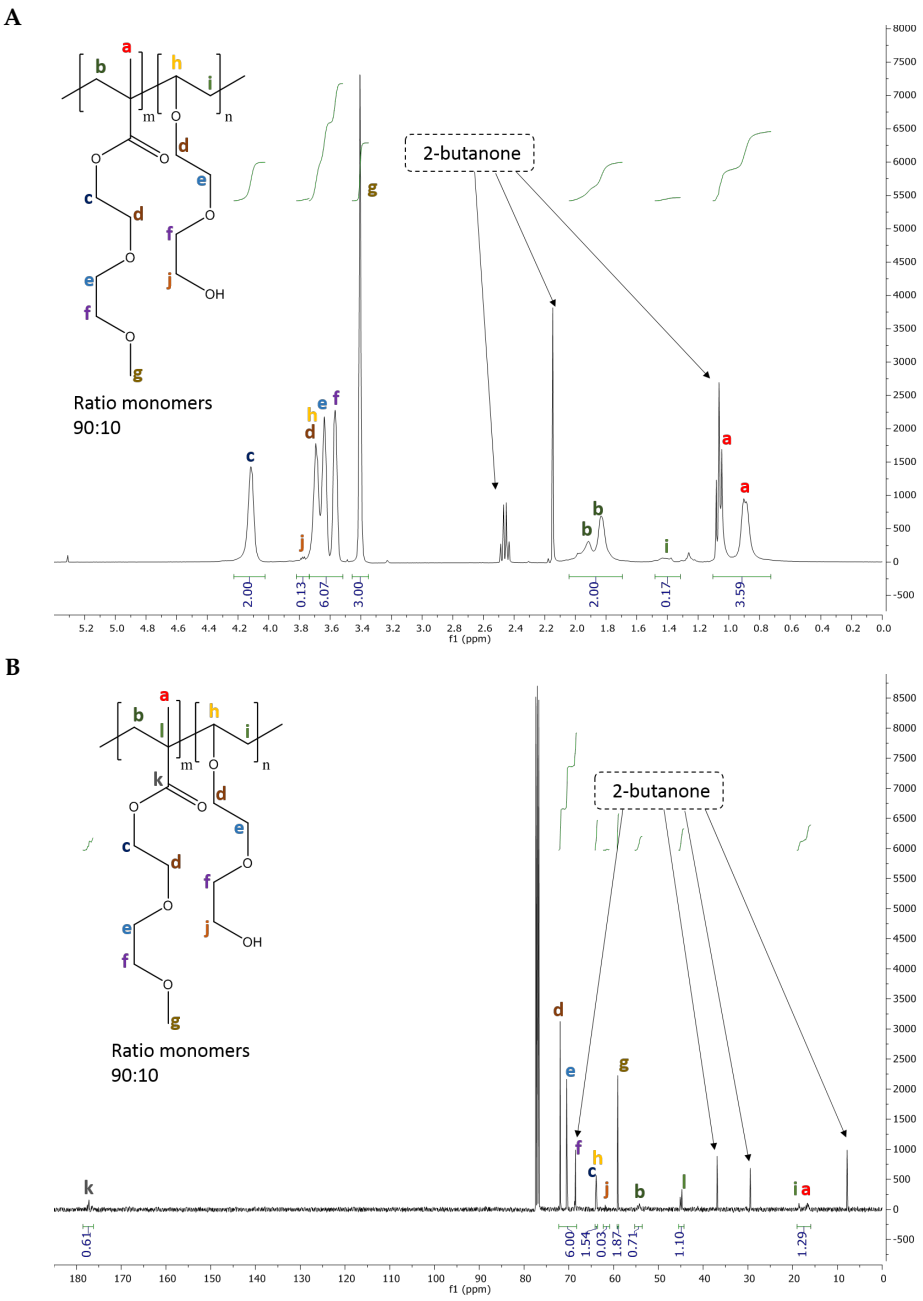



**Figure S11: A)** $^{1}$H-NMR and **B)** C$^{13}$-NMR of PDEGMA/PDEGOH 90:10 monomer ratio, trashes re-suspending solvent 2-butanone was observed present and overlap with the peak a.

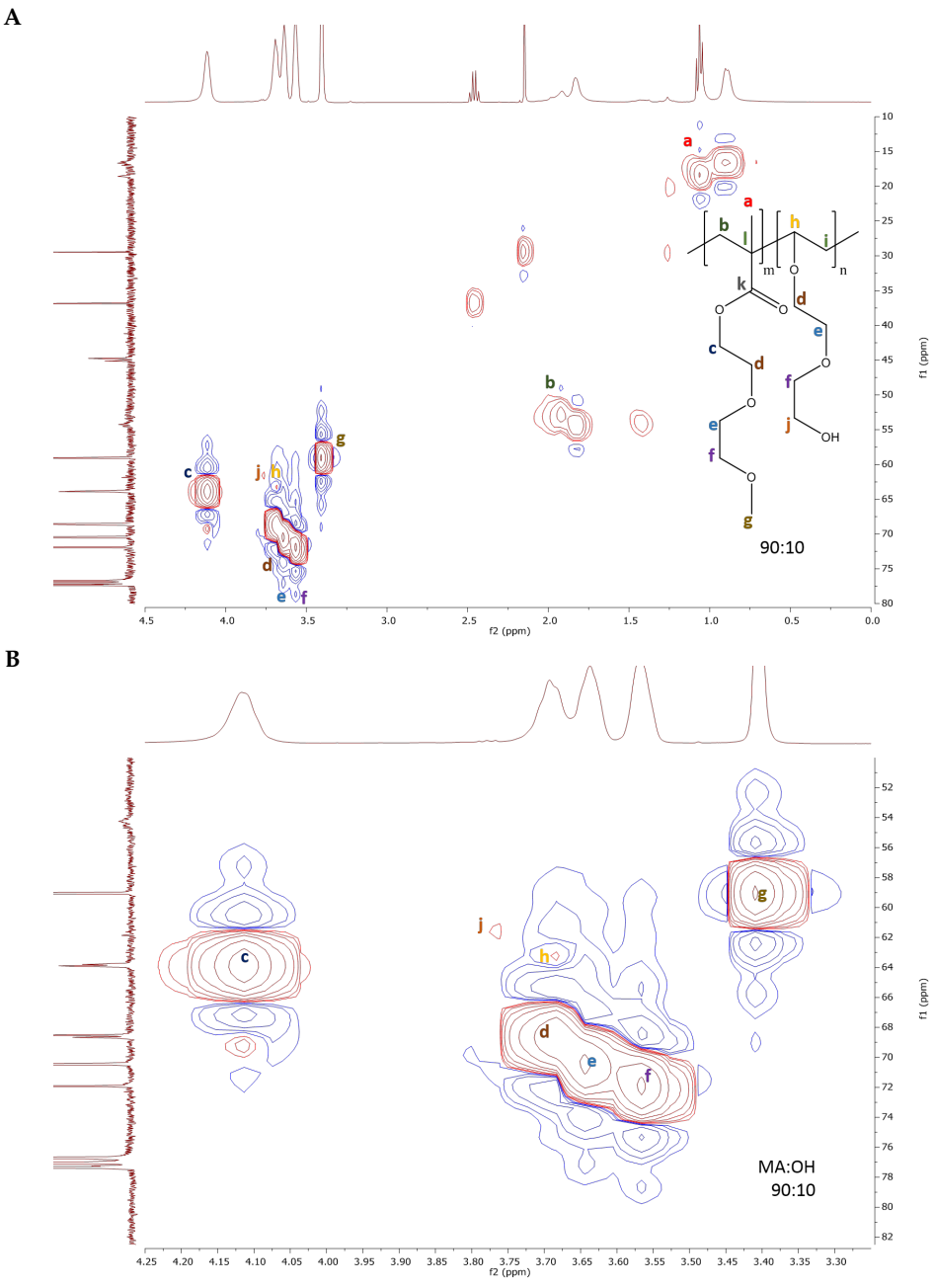



**Figure S12: A)** 2D-NMR and **B)** zoomed in 2D-NMR spectra of PDEGMA/PDEGOH 90:10 monomer ratio.

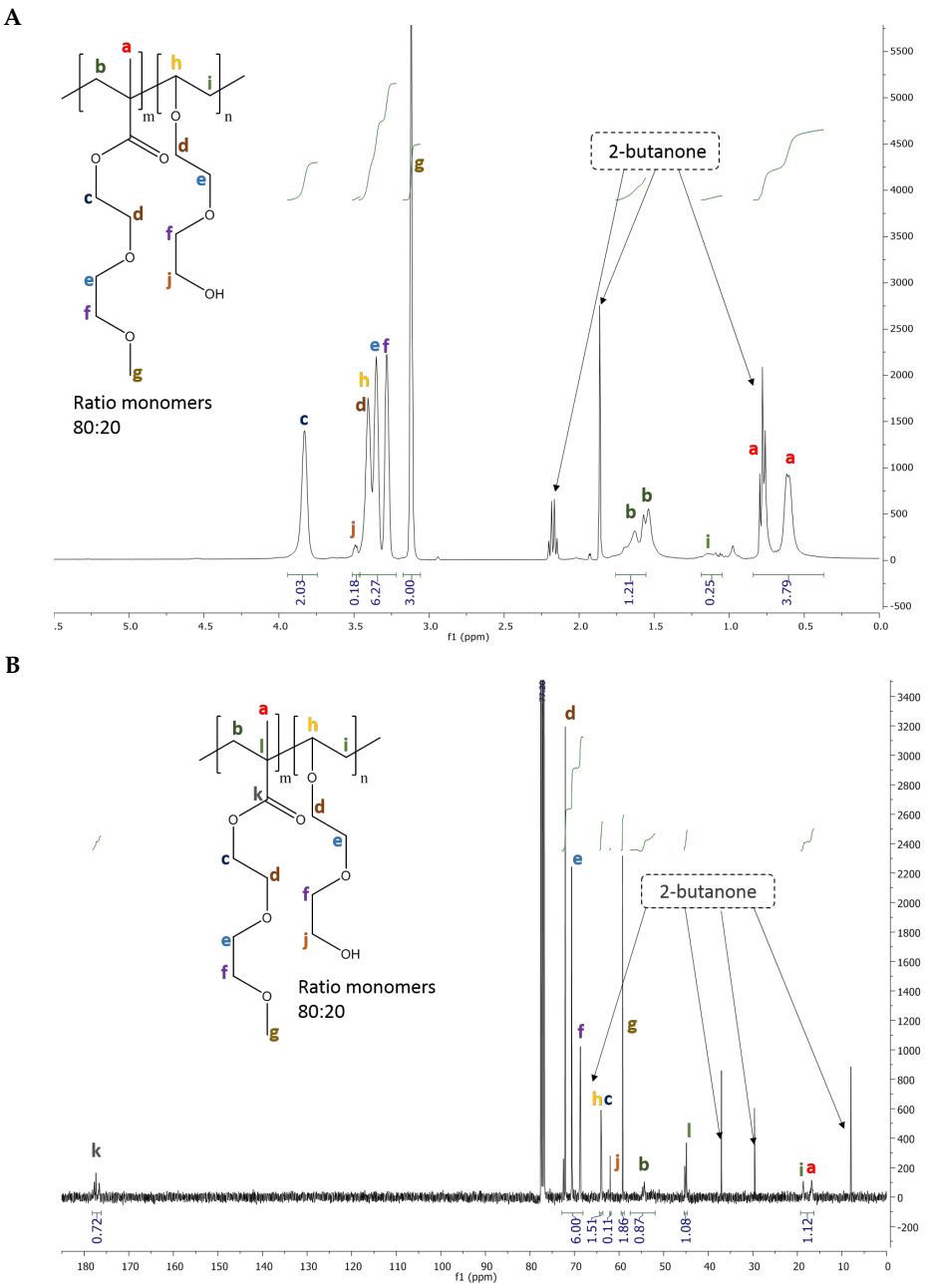



**Figure S13:** **A)** $^{1}$H-NMR and **B)** $C_{1}3$-NMR of PDEGMA/PDEGOH 80:20 monomer ratio, trashes re-suspending solvent 2-butanone was observed present and overlap with the peak a in **A**.

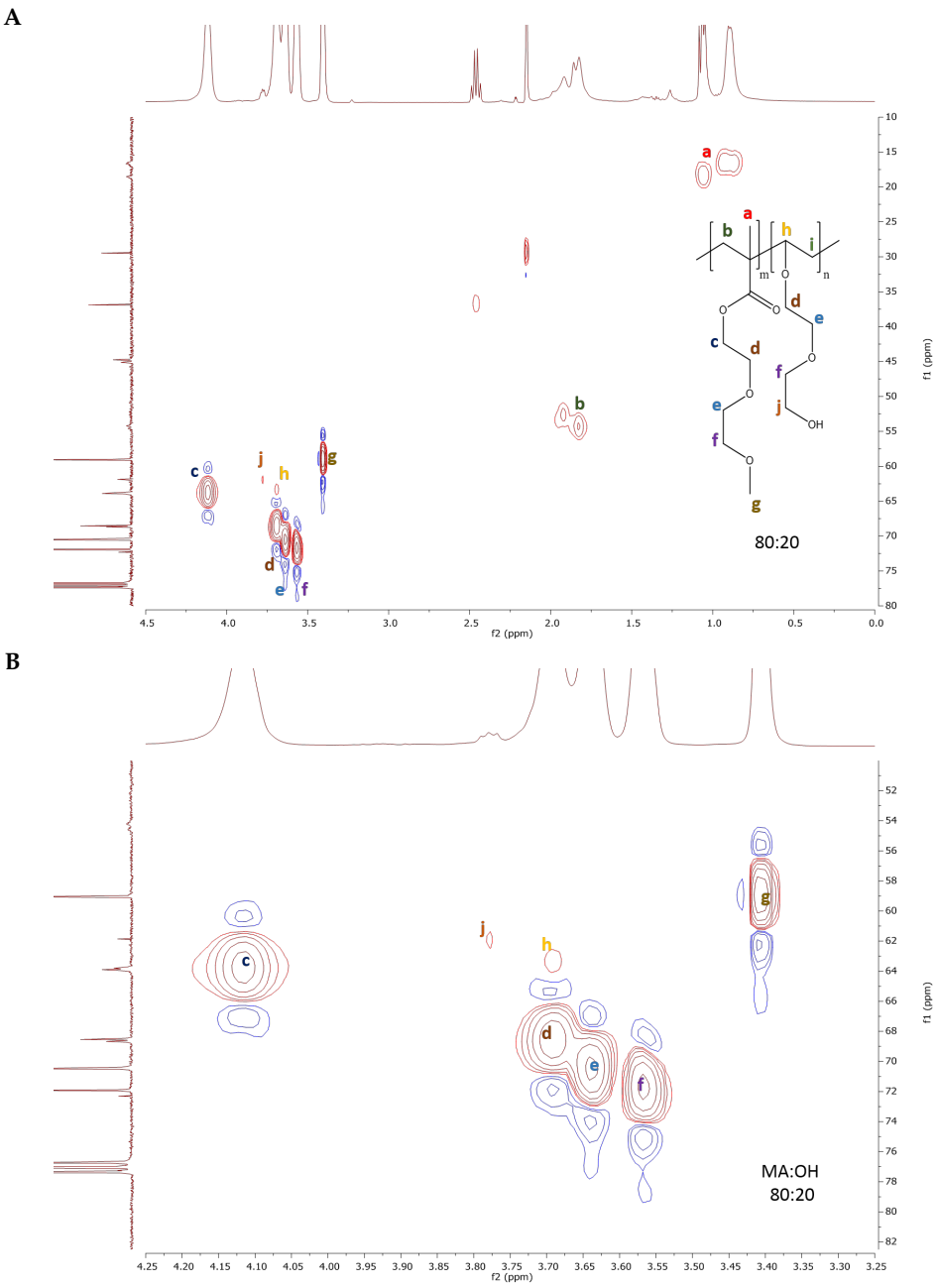



**Figure S14: A)** 2D-NMR and **B)** zoomed in 2D-NMR spectra of PDEGMA/PDEGOH 80:20 monomer ratio.

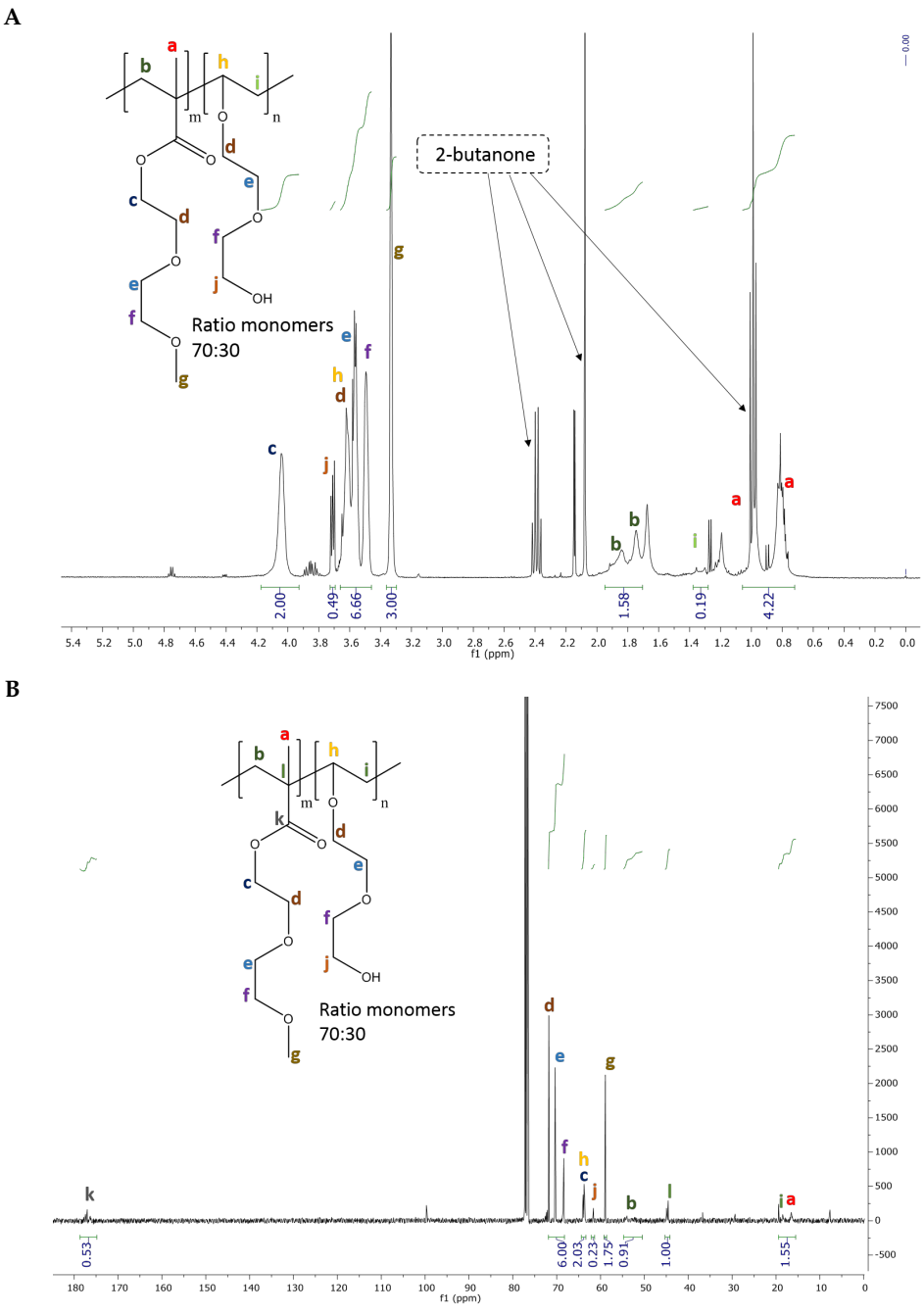



**Figure S15:** $^{1}$H-NMR and $C_{13}$-NMR of PDEGMA/PDEGOH 70:30 monomer ratio, trashes re-suspending solvent 2-butanone was observed present and overlap with the peak a.

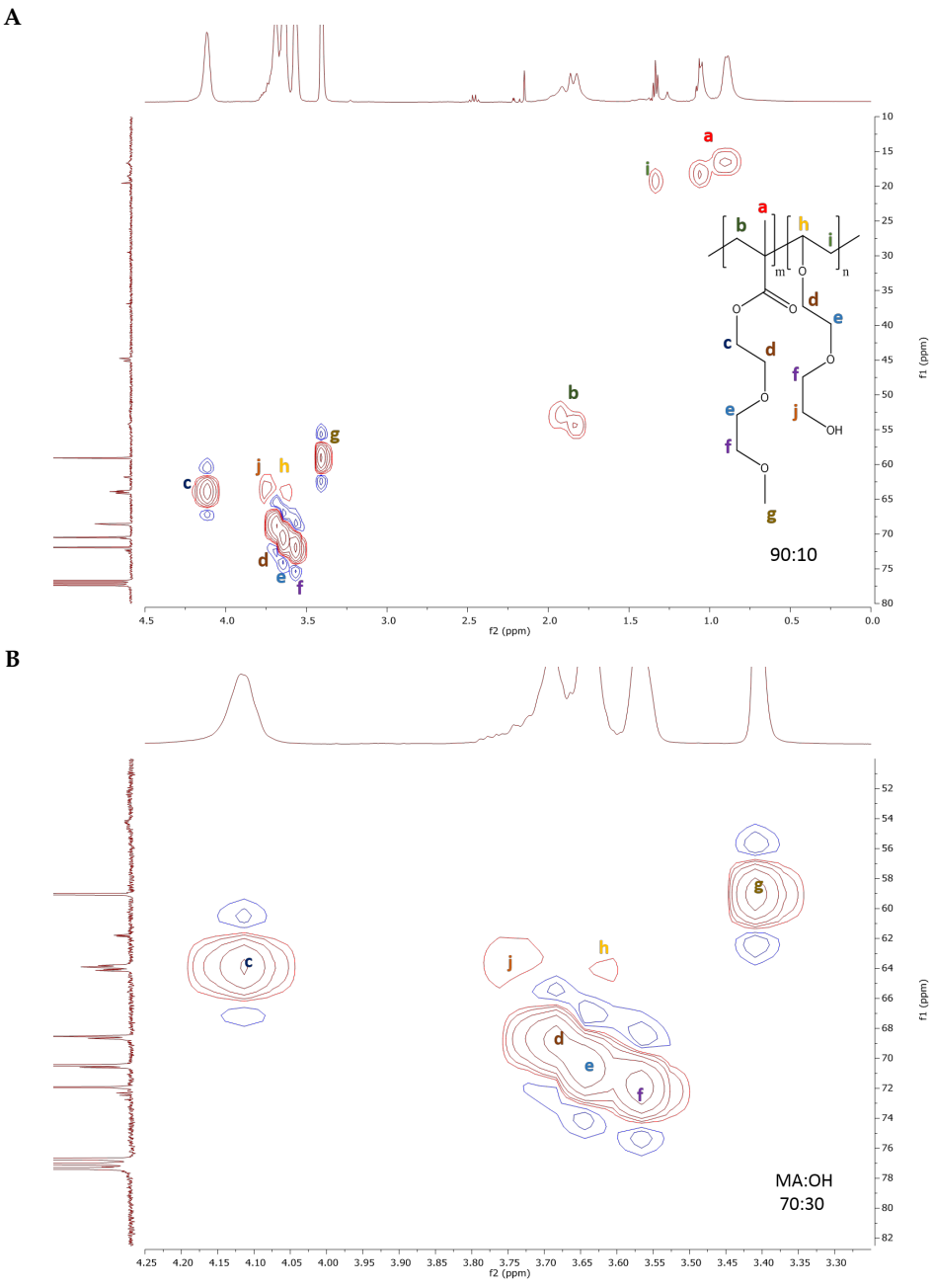



**Figure S16: A)** 2D-NMR and **B)** zoomed in 2D-NMR spectra of PDEGMA/PDEGOH 70:30 monomer ratio.

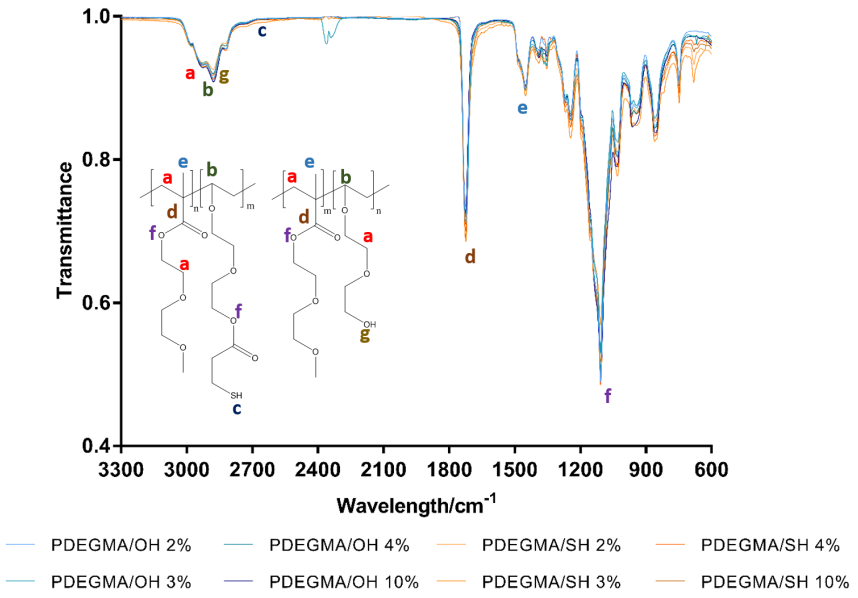



**Figure S17:** FT-IR of all PDEGMA/PDEGOH and PDEGMA/PDEGSH polymers. Peak -OH weak intermolecular bond stretching (g, 3200-2700 $cm^{-1}$) and -SH peak weak stretching (c, 2600-2550 $cm^{-1}$) are too weak too identify in the spectra.

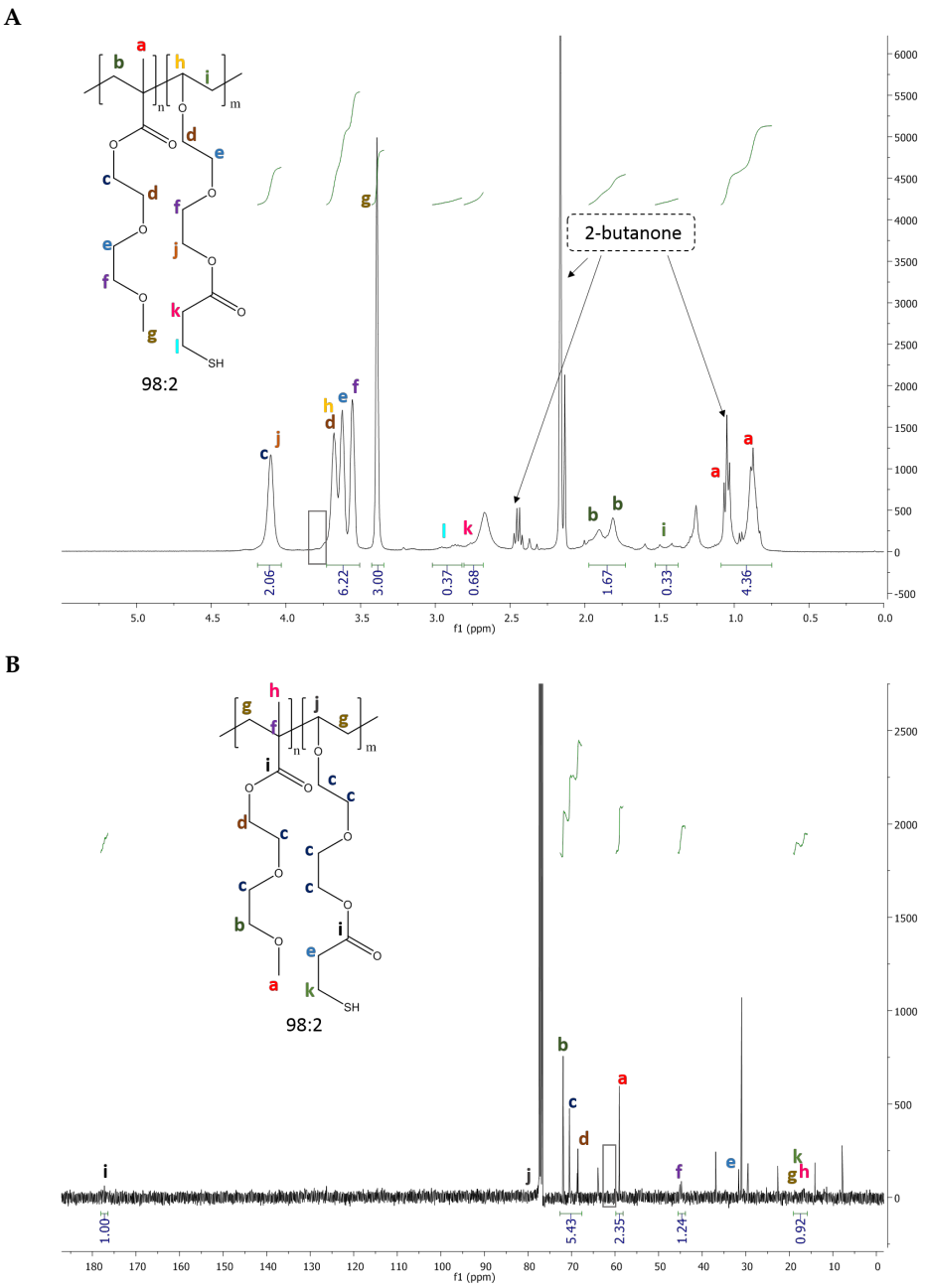



**Figure S18:** **A)** $^{1}$H-NMR and **B)** $C_{13}$-NMR of PDEGMA/PDEGSH 98:2 ratio, **A)** trashes re-suspending solvent 2-butanone was observed present and overlaps with the peak a. Water from the condensation reaction was observed in the spectra and overlaps with the peak b. **B)** Peak of $CH_2OH$ in block has disappeared.

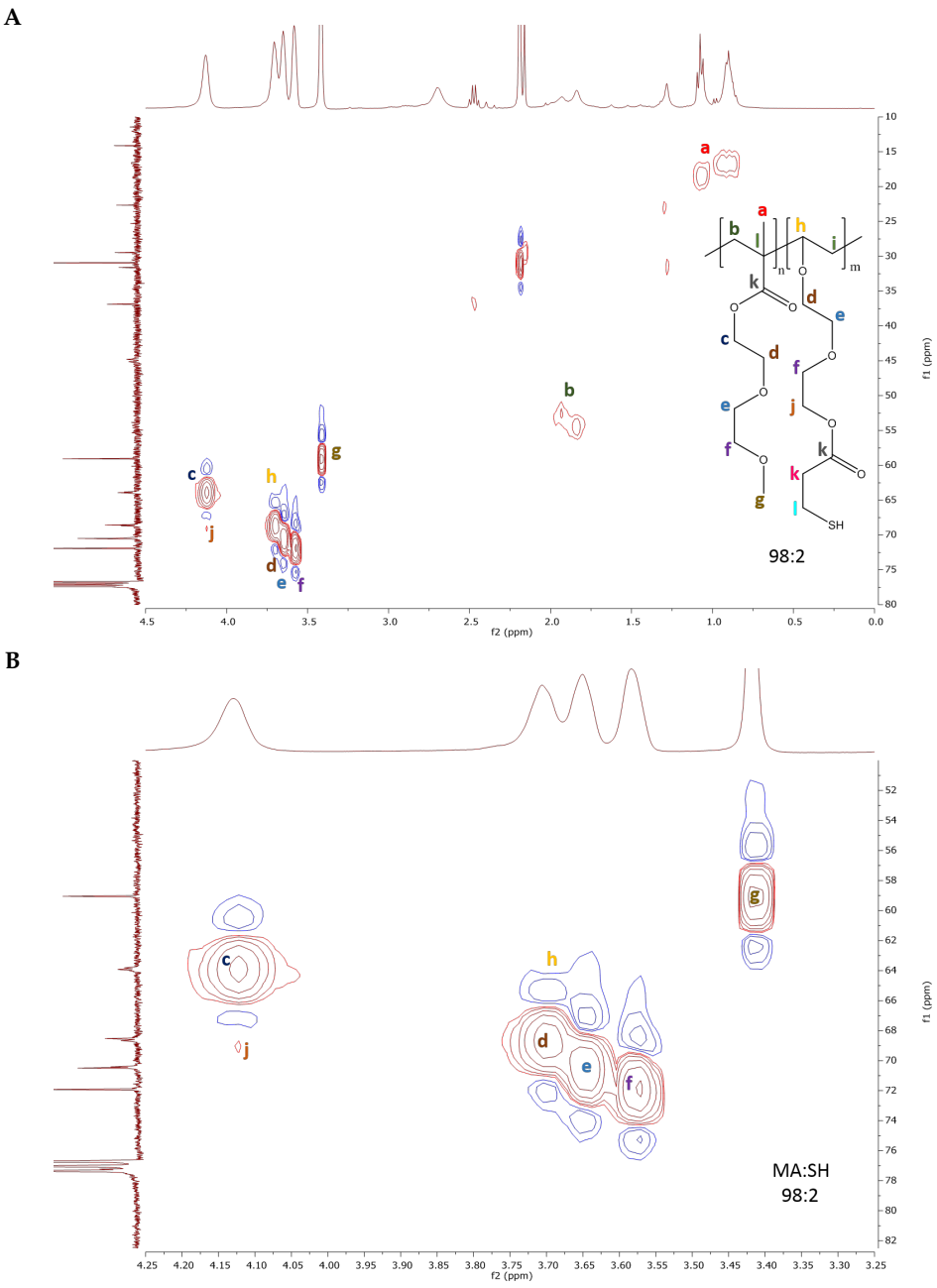



**Figure S19: A)** 2D-NMR and **B)** zoomed in 2D-NMR spectra of PDEGMA/PDEGSH 98:2 ratio.

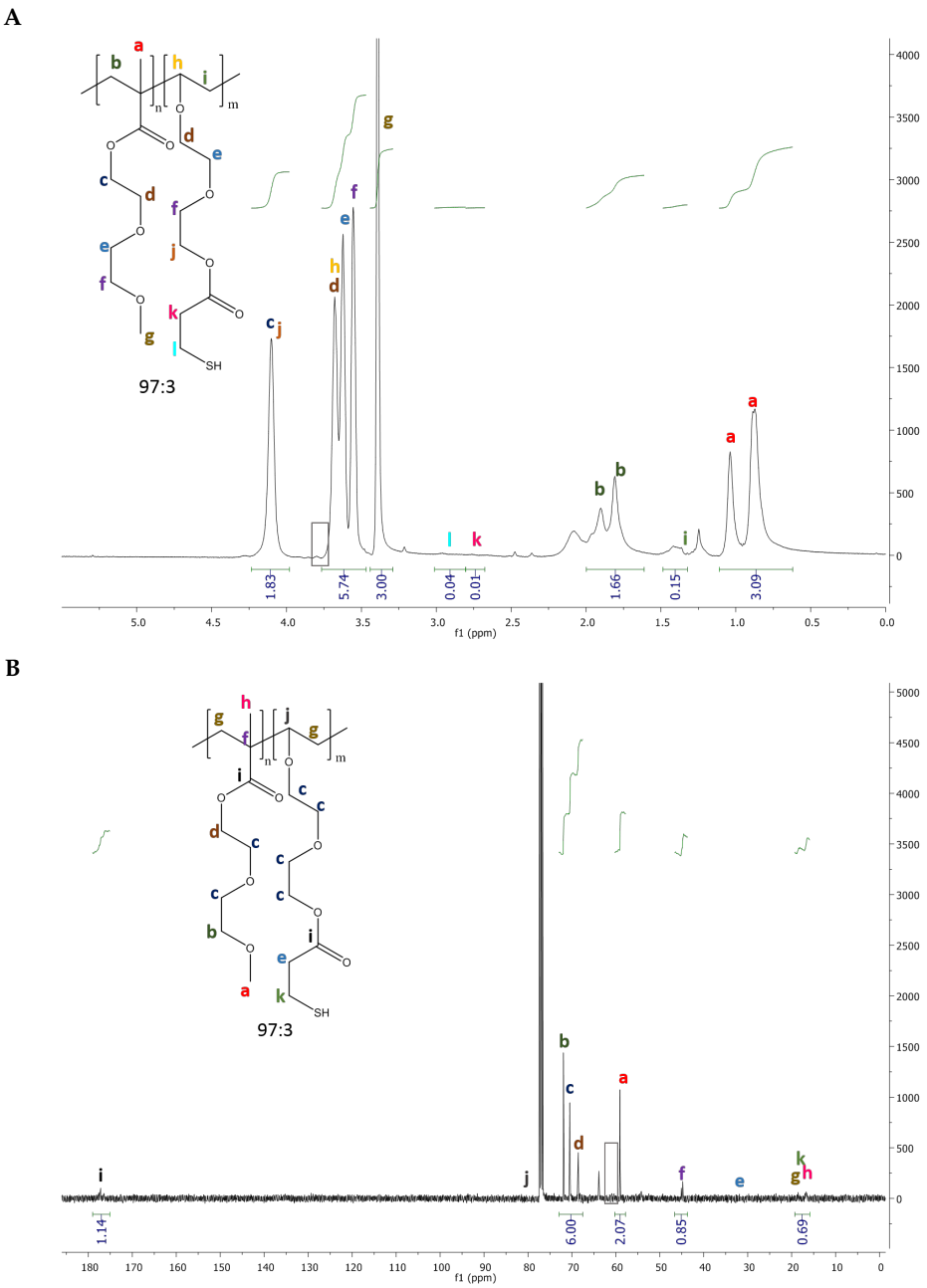



**Figure S20:** **A)** $^{1}$H-NMR and **B)** $C_{13}$-NMR of PDEGMA/PDEGSH 97:3 ratio, **A)** trashes re-suspending solvent 2-butanone was observed present and overlaps with the peak a. Water from the condensation reaction was observed in the spectra and overlaps with the peak b. **B)** Peak of $CH_2OH$ in block has disappeared.

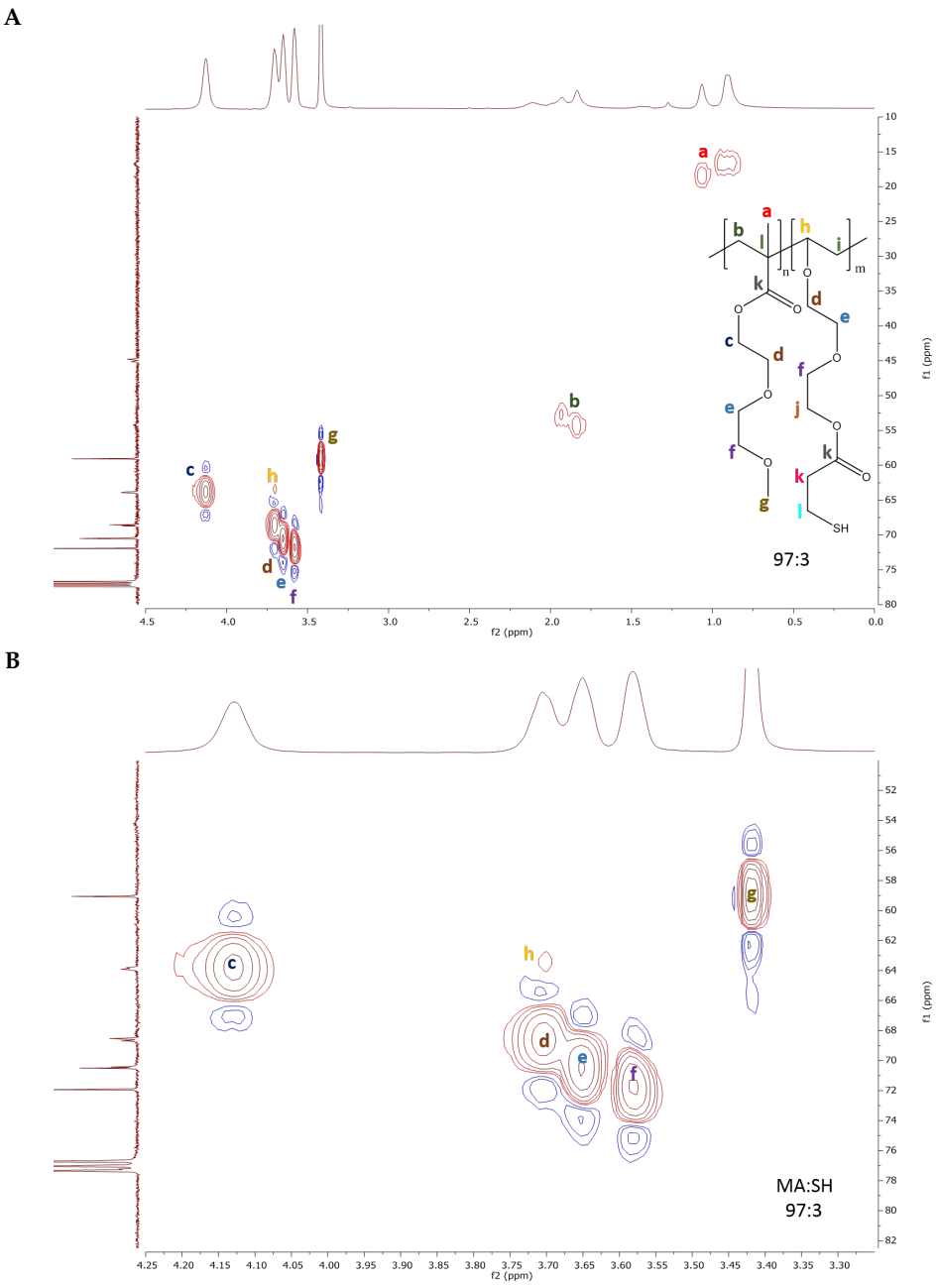



**Figure S21: A)** 2D-NMR and **B)** zoomed in 2D-NMR spectra of PDEGMA/PDEGSH 97:3 ratio.

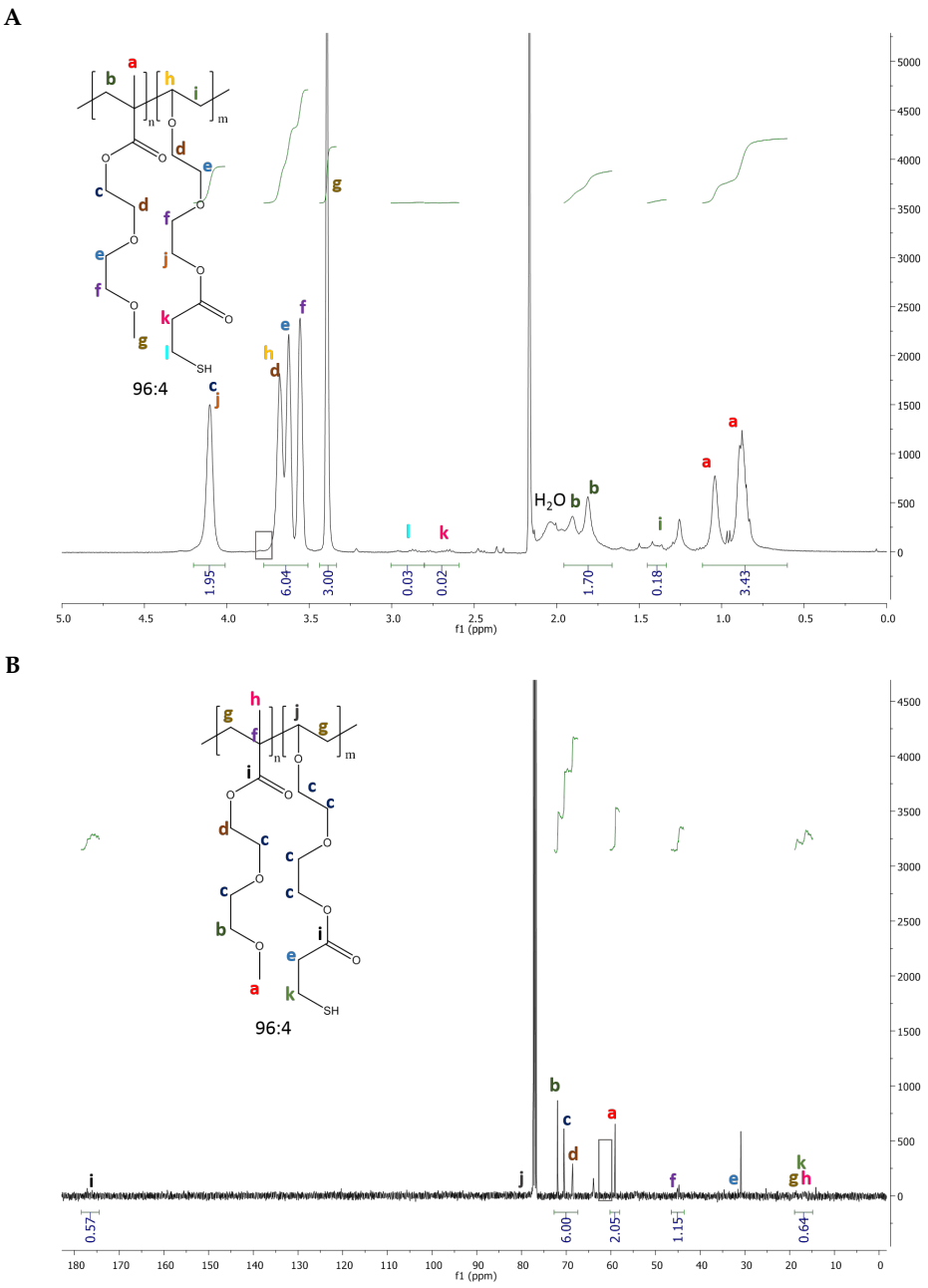



**Figure S22:** **A)** $^{1}$H-NMR and **B)** $C_{13}$-NMR of PDEGMA/PDEGSH 96:4 ratio, **A)** trashes re-suspending solvent 2-butanone was observed present and overlaps with the peak a. Water from the condensation reaction was observed in the spectra and overlaps with the peak b. **B)** Peak of $CH_2OH$ in block has disappeared.

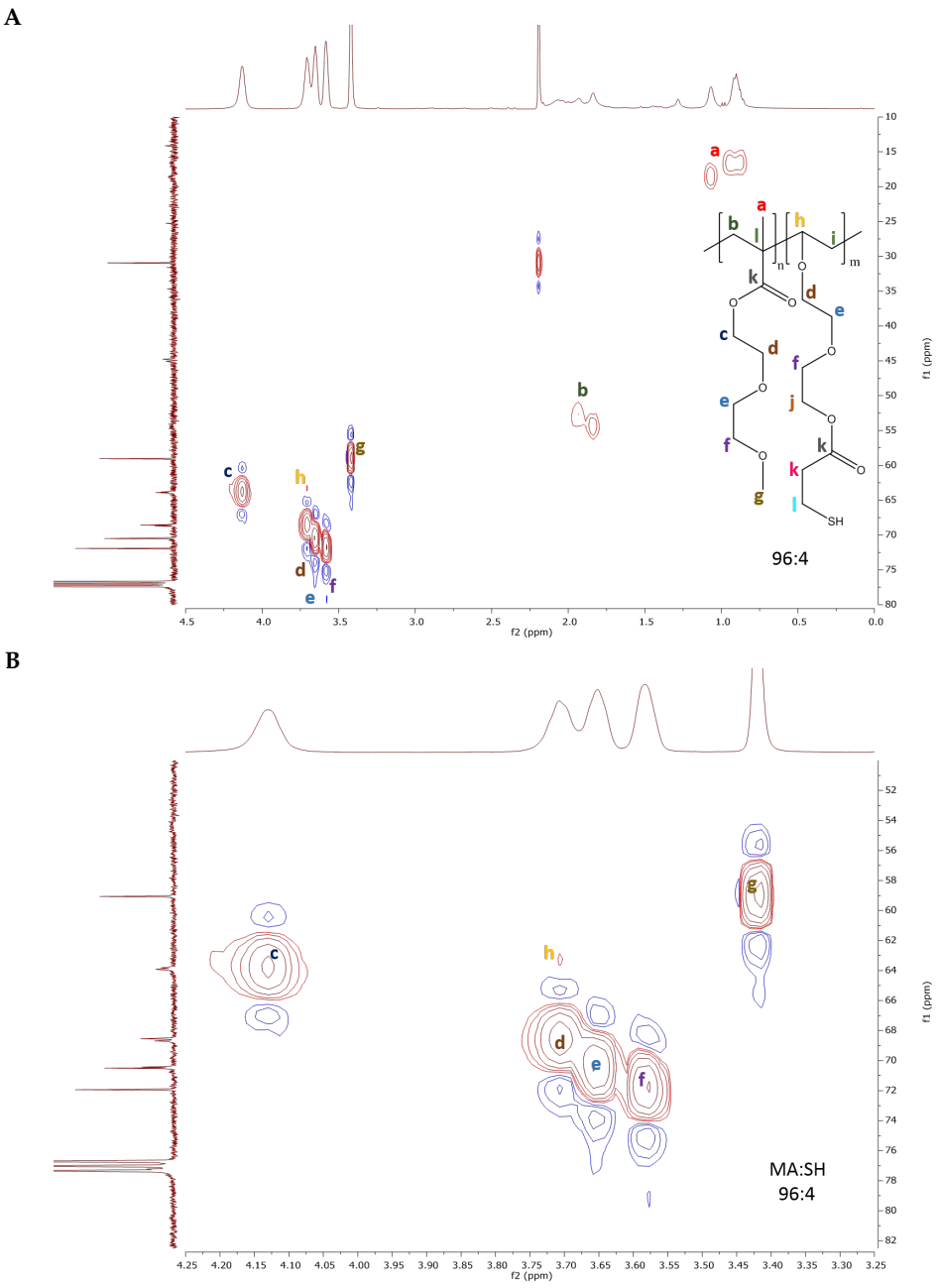



**Figure S23: A)** 2D-NMR and **B)** zoomed in 2D-NMR spectra of PDEGMA/PDEGSH 96:4 ratio.

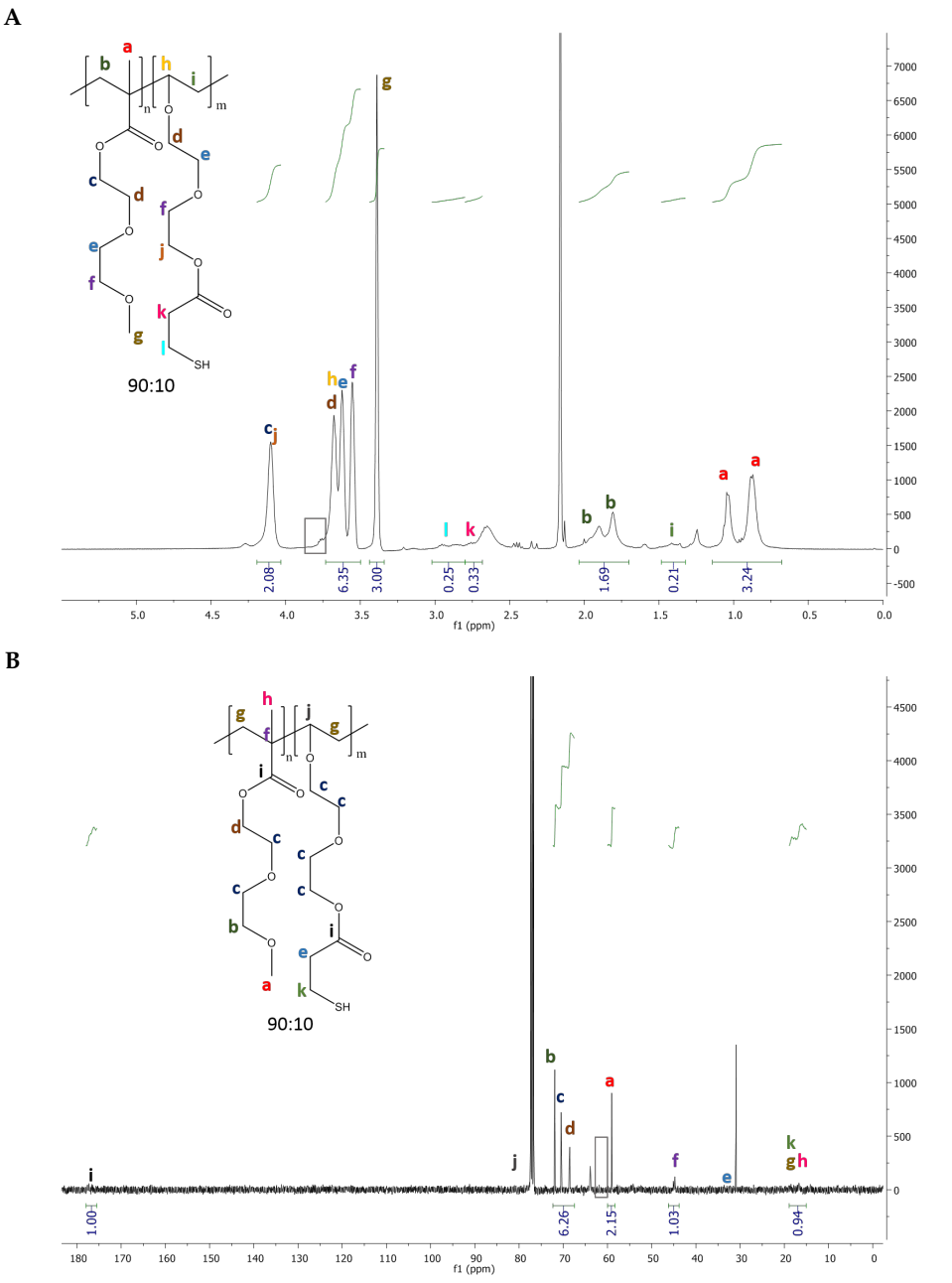



**Figure S24: A)** $^{1}$H-NMR and **B)** $C_{1}3$-NMR of PDEGMA/PDEGSH 90:10 ratio, **A)** trashes re-suspending solvent 2-butanone was observed present and overlaps with the peak a. Water from the condensation reaction was observed in the spectra and overlaps with the peak b. **B)** Peak of $CH_2OH$ in block has disappeared.

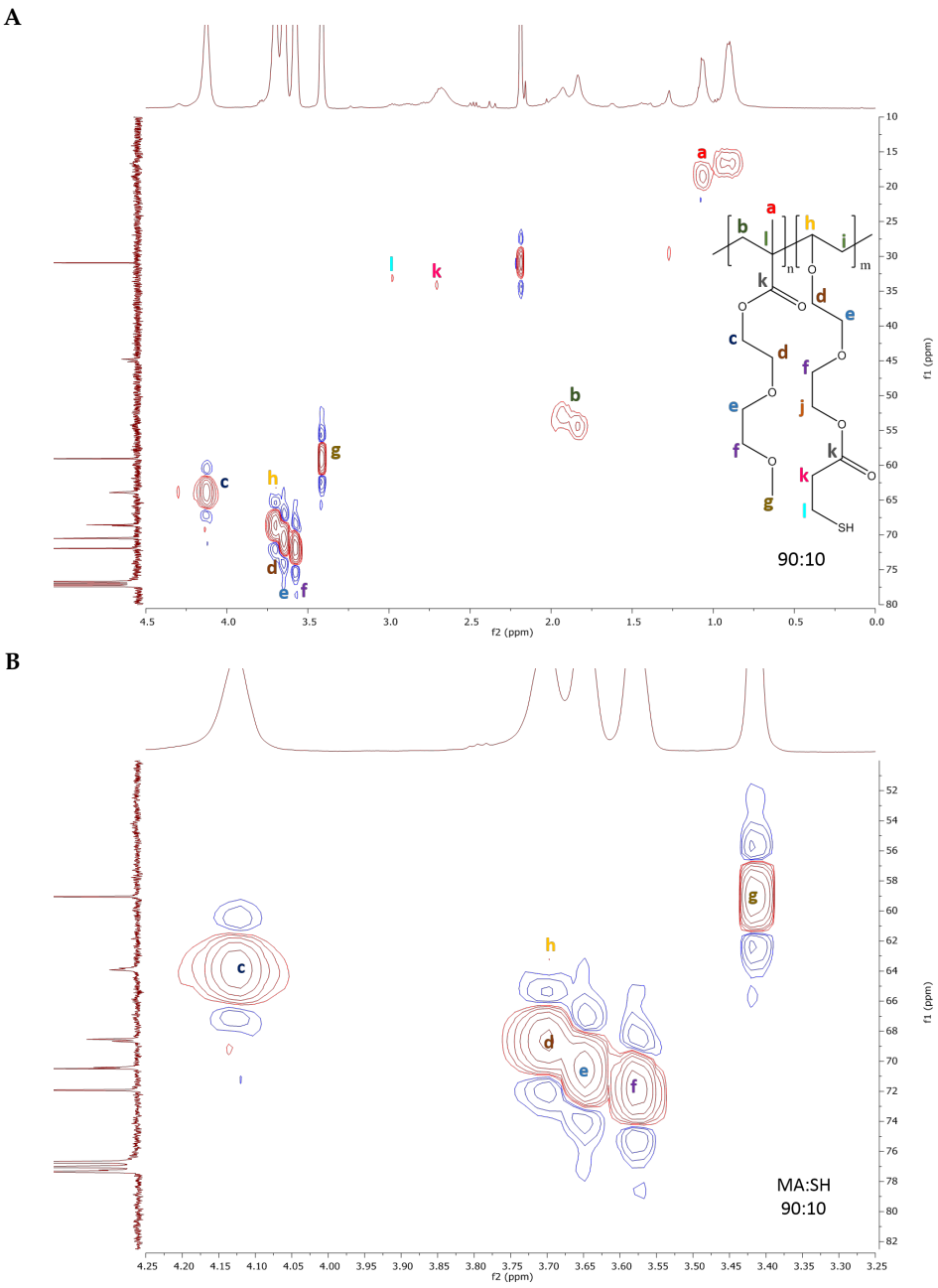



**Figure S25: A)** 2D-NMR and **B)** zoomed in 2D-NMR spectra of PDEGMA/PDEGSH 90:10 ratio.

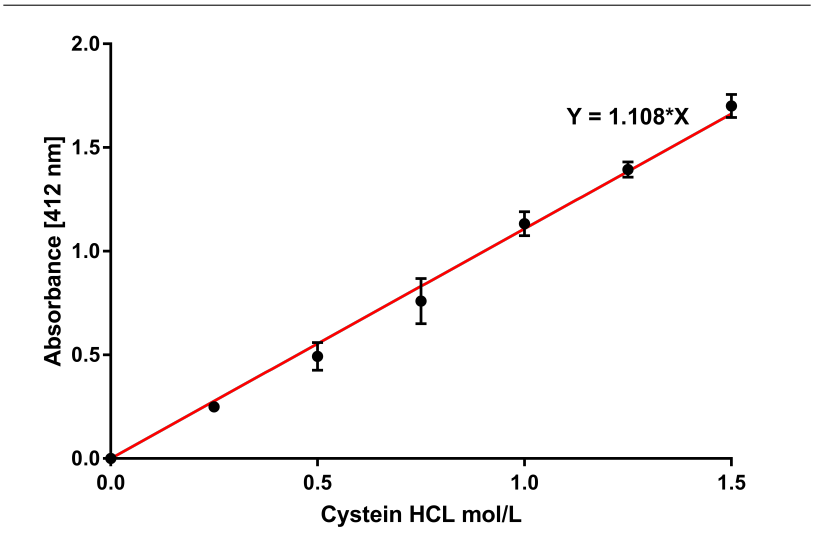



**Figure S26:** Ellman's assay standard curve amount of cysteine HCL mol/L. ($R^2$=0.9965, error bars=SD)

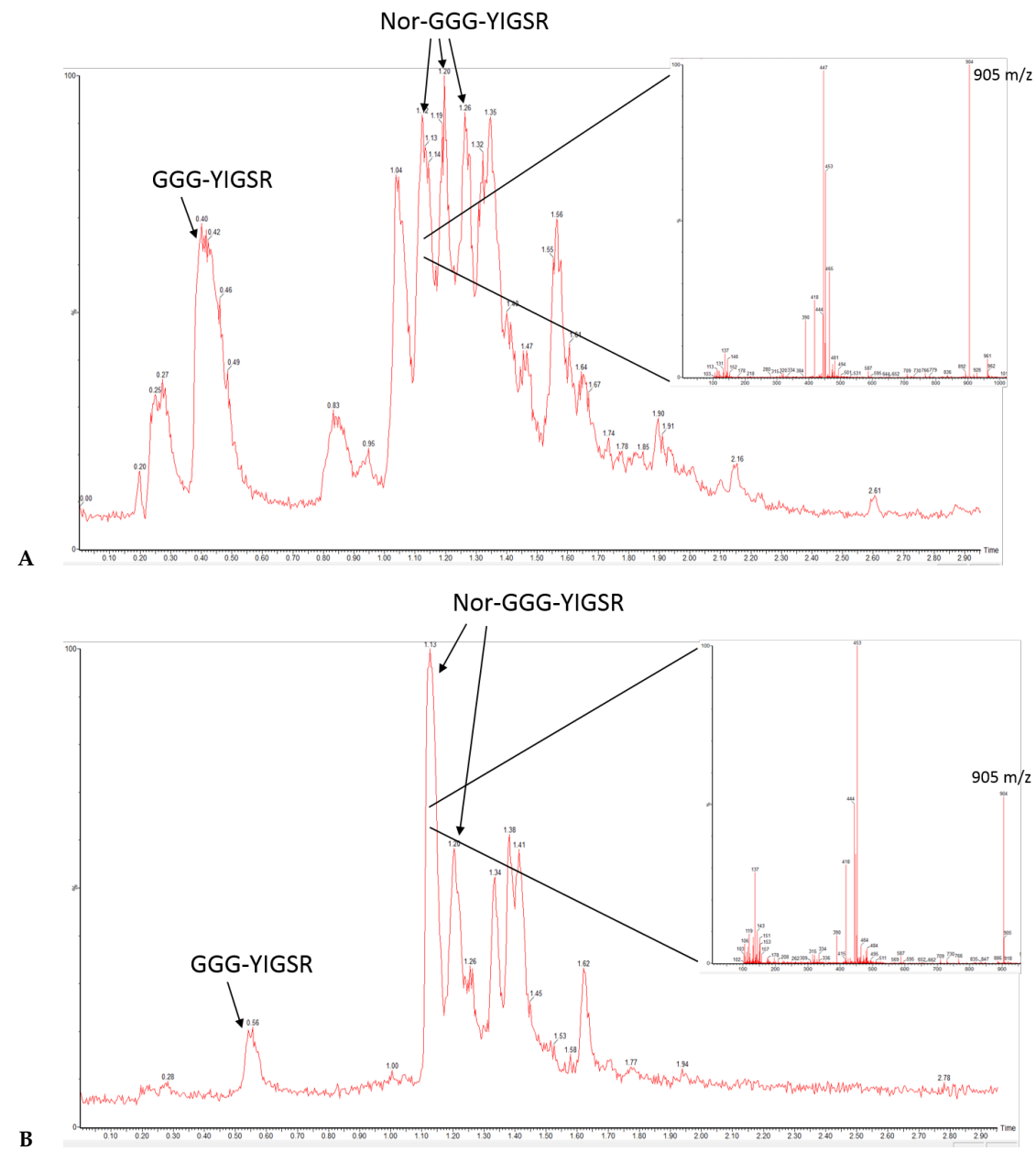



**Figure S27:** HPLC-MS data of A) crude-product synthesis cycle without extra washes and B) crude-product synthesis cycle with two extra washes.

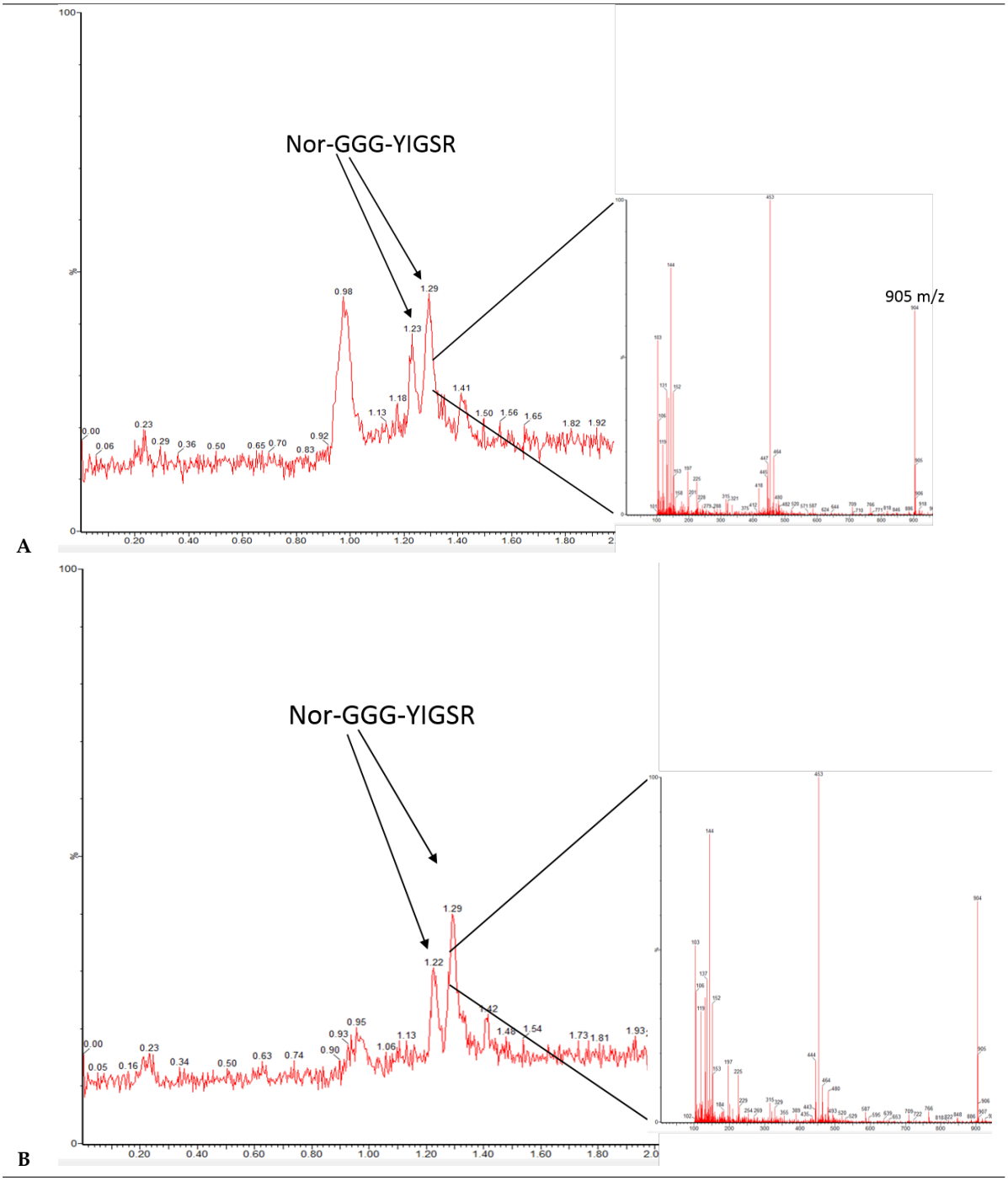



**Figure S28:** HPLC-MS data of A) purified Nor-GGG-YIGSR product peak and B) purified Nor-GGG-YIGSR shoulder of product peak.

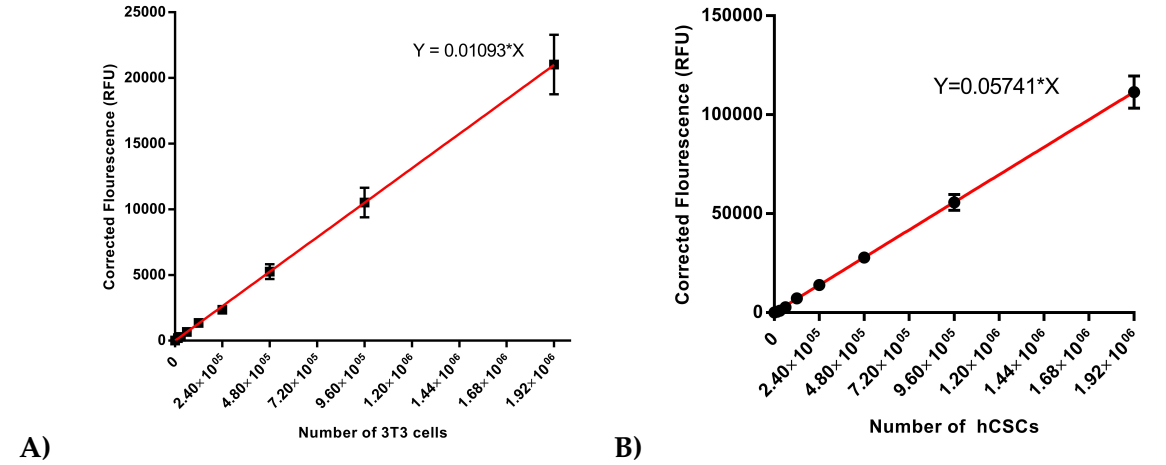



**Figure S29:** Representative standard curves used to determine cell number using the Alamar blue assay. **A)** Standard curve for 3T3 fibroblast cells and **B)** standard curve for human corneal stromal cells (hCSC). (n=6 scaffolds, **A)** $R^2$=0.9998, **B)** $R^2$=1, error bars=SD)

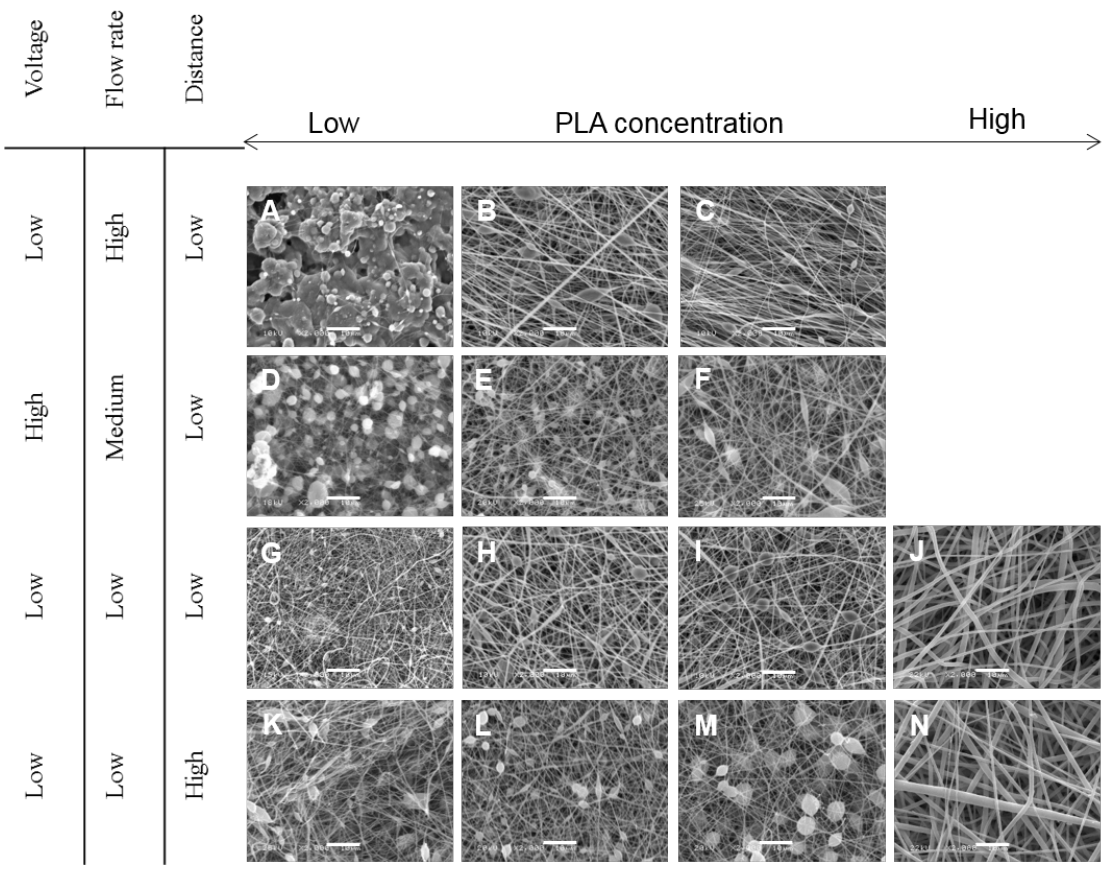



**Figure S30:** Preliminary study performed to identify the right limitations per parameter to include all fibre morphologies into the DoE model. **A**) 15 kV, 15 cm, 6 ml/hr, 10 w/v%; **B**) 15 kV, 15 cm, 6 ml/hr, 15 w/v%; **C**) 15 kV, 15 cm, 6 ml/hr, 20 w/v%; **D**) 25 kV, 15 cm, 3 ml/hr, 10 w/v%; **E**) 25 kV, 15 cm, 3 ml/hr, 15 w/v%; **F**) 25 kV, 15 cm, 3 ml/hr, 20 w/v%; **G**) 15 kV, 15 cm, 1 ml/hr, 10 w/v%; **H**) 15 kV, 15 cm, 1 ml/hr, 15 w/v%; **I**) 15 kV, 15 cm, 1 ml/hr, 20 w/v%; **J**) 15 kV, 15 cm, 1 ml/hr, 25 w/v%; **K**) 15 kV, 20 cm, 1 ml/hr, 10 w/v%; **L**) 15 kV, 20 cm, 1 ml/hr, 15 w/v%; **M**) 15 kV, 20 cm, 1 ml/hr, 20 w/v%; **N**) 15 kV, 20 cm, 1 ml/hr, 25 w/v%. Scale bar is 10 $\mu$m. (n=3, 3 scaffolds per combination.)

**Table S1:** DoE model parameter combinations with corresponding average of replicated (n=120, 3 scaffolds, 6 SEM images per scaffold, 20 fibre measurements per SEM images) mean fibre diameters (FD), standard deviations (Stdev) and number of beads per $\mu m^2$.

| Exp. Name | $X_1$ | $X_2$ | $X_3$ | $X_4$ | FD ($Y_1$) | Stdev ($Y_2$) | No. beads per $\mu m^2$ |
|---|---|---|---|---|---|---|---|
| **N1** | -1 | -1 | -1 | -1 | 866 | 1226 | 1.32 |
| **N2** | 1 | -1 | -1 | -1 | 831 | 1064 | 1.17 |
| **N3** | -1 | 1 | -1 | -1 | 1094 | 1439 | 0.43 |
| **N4** | 1 | 1 | -1 | -1 | 866 | 1070 | 2.37 |
| **N5** | -1 | -1 | 1 | -1 | 1154 | 1441 | 2.29 |
| **N6** | 1 | -1 | 1 | -1 | 830 | 942 | 2.34 |
| **N7** | -1 | 1 | 1 | -1 | 1100 | 1322 | 2.77 |
| **N8** | 1 | 1 | 1 | -1 | 875 | 1094 | 2.63 |
| **N9** | -1 | -1 | -1 | 1 | 992 | 351 | 0 |
| **N10** | 1 | -1 | -1 | 1 | 861 | 352 | 0 |
| **N11** | -1 | 1 | -1 | 1 | 1091 | 434 | 0 |
| **N12** | 1 | 1 | -1 | 1 | 744 | 261 | 0 |
| **N13** | -1 | -1 | 1 | 1 | 588 | 490 | 0.09 |
| **N14** | 1 | -1 | 1 | 1 | 625 | 414 | 0.02 |
| **N15** | -1 | 1 | 1 | 1 | 796 | 919 | 0.39 |
| **N16** | 1 | 1 | 1 | 1 | 760 | 878 | 0.26 |
| **N17** | -1 | 0 | 0 | 0 | 879 | 1031 | 0.50 |
| **N18** | 1 | 0 | 0 | 0 | 821 | 1054 | 0.11 |
| **N19** | 0 | -1 | 0 | 0 | 853 | 1146 | 0.23 |
| **N20** | 0 | 1 | 0 | 0 | 886 | 1256 | 0.27 |
| **N21** | 0 | 0 | -1 | 0 | 921 | 1068 | 0.61 |
| **N22** | 0 | 0 | 1 | 0 | 788 | 1007 | 0.99 |
| **N23** | 0 | 0 | 0 | -1 | 915 | 1239 | 1.45 |
| **N24** | 0 | 0 | 0 | 1 | 991 | 420 | 0 |
| **N25** | 0 | 0 | 0 | 0 | 826 | 1070 | 0.31 |

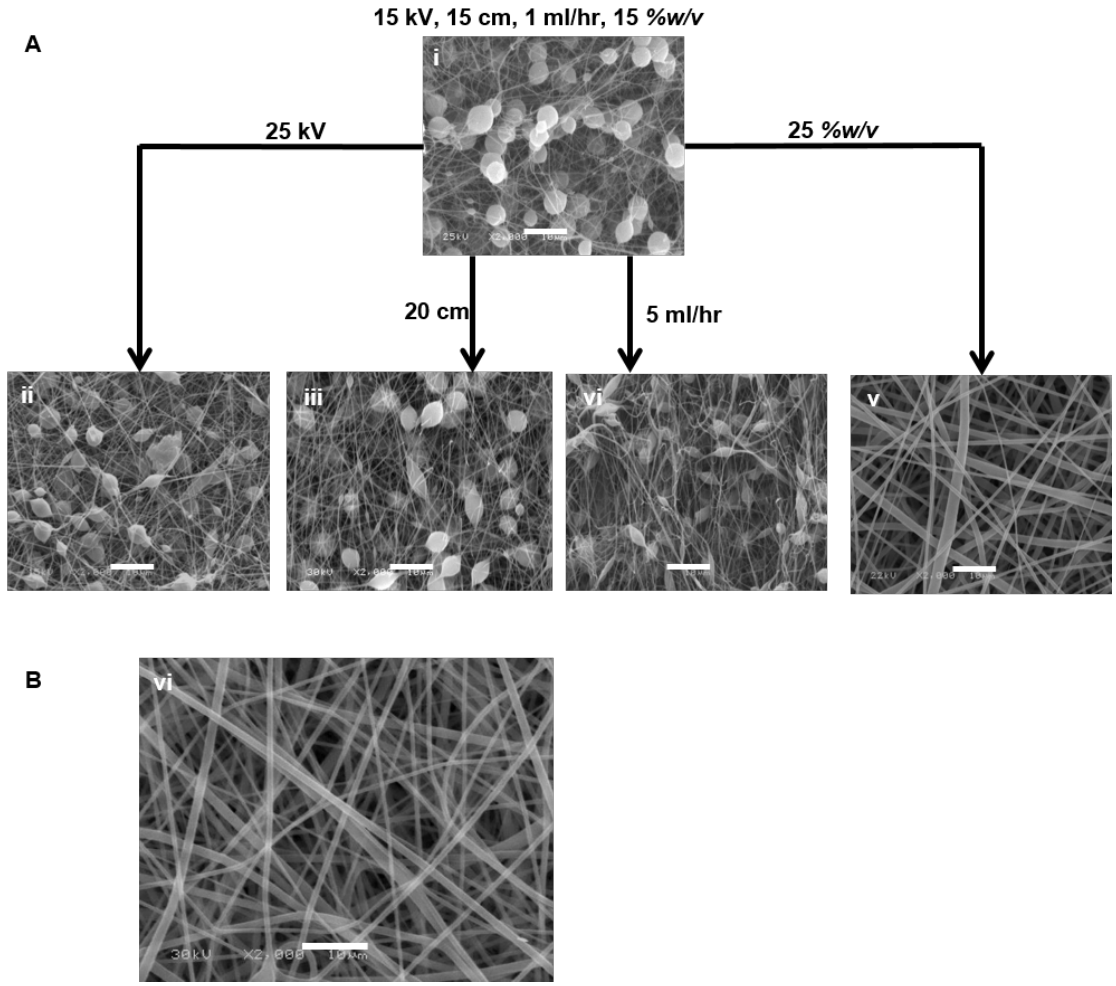



**Figure S31:** SEM images of different parameter combinations; applied voltage, distance needle to collector, flow rate and PLA polymer concentration. **A**) Example of a one fractional design model changing one factor at a time. Starting from **i**) changing higher voltage resulting in **ii**); when changing distance resulting in **iii**); when changing flow rate resulting in **iv**); and when changing concentration resulting in v) which showed fibre formation, but no uniform fibre diameter distribution. SEM images of different parameter combinations; applied voltage, distance needle to collector, flow rate and PLA polymer concentration.) By changing multiple parameters from starting v) resulted in more uniform fibre formation of vi). Scale bar is 10 $\mu$m.

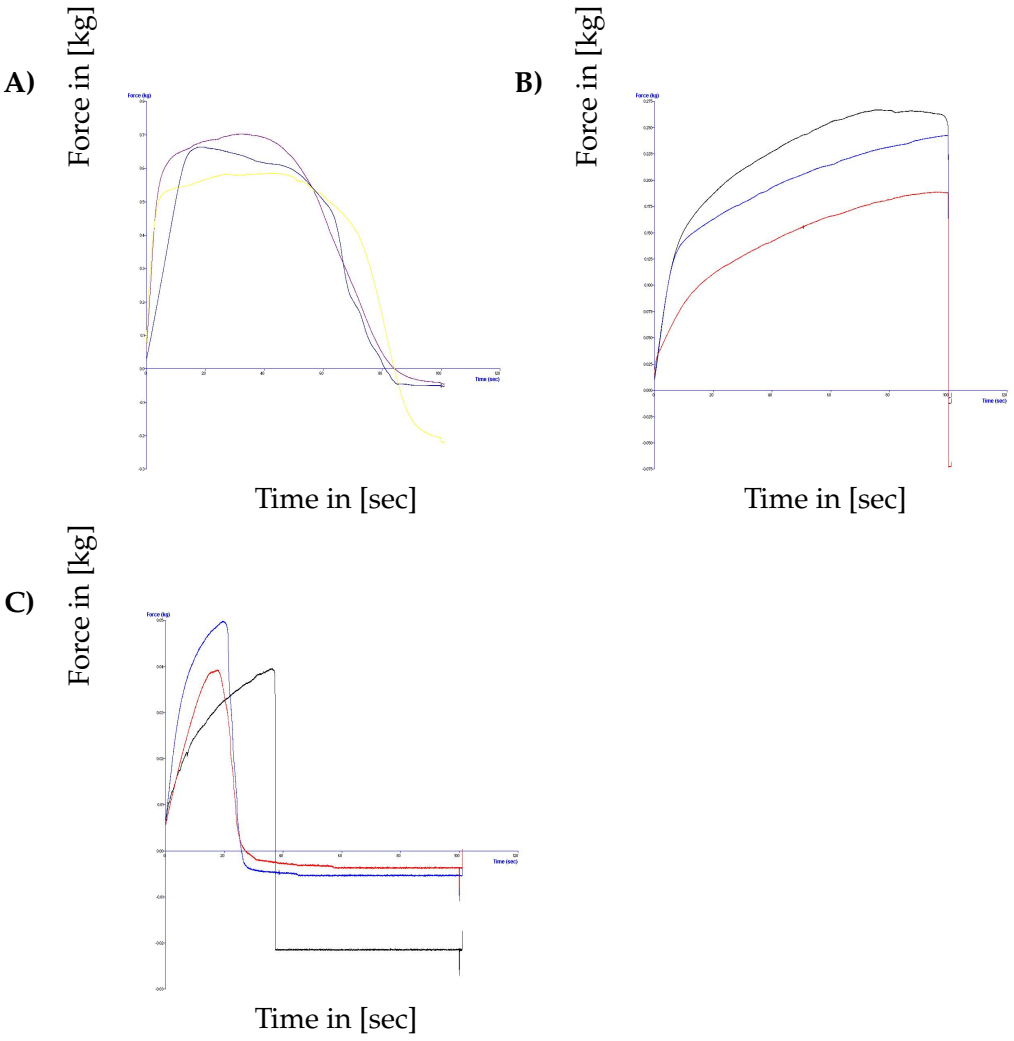



**Figure S32:** Representative tensile testing graphs of the scaffolds with uniform fibres **A**), beads-on-string morphology **B**), and big beaded morphology **C**).

**Table S2:** Optimum electrospinning parameters for different % PDEGMA with 25 w/v% PLA.

| wt% PDEGMA | Voltage [kV] | Distance [cm] | Flow rate [mL/hr] |
|---|---|---|---|
| **0** | 15 | 15 | 1 |
| **2.5** | 19 | 17.5 | 0.5 |
| **5** | 19 | 17.5 | 0.5 |
| **10** | 19 | 17.5 | 0.5 |
| **15** | 12 | 17.5 | 0.5 |
| **20** | 12 | 17.5 | 0.5 |
| ***wt%* PBI-PDEGMA** | **Voltage [kV]** | **Distance [cm]** | **Flow rate [ml/hr]** |
| **0** | 15 | 15 | 1 |
| **2.5** | 19 | 17.5 | 0.5 |
| **5** | 19 | 17.5 | 0.5 |
| **10** | 19 | 17.5 | 0.5 |
| **15** | 12 | 17.5 | 0.5 |
| **20** | 12 | 17.5 | 0.5 |

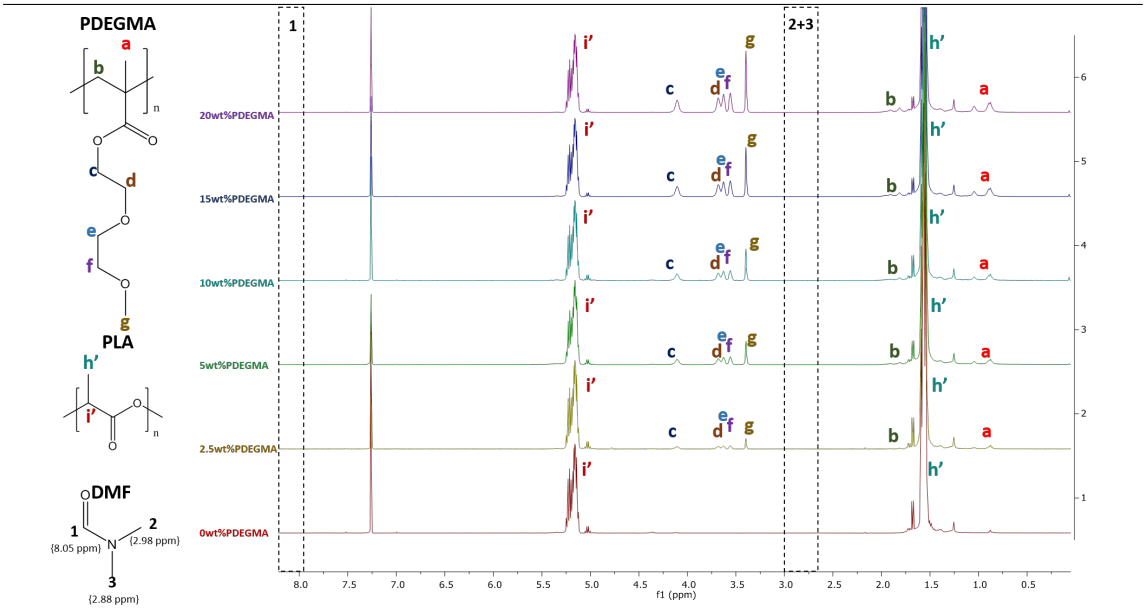



**Figure S33:** Representative $^{1}$H-NMR spectra of PLA/PDEGMA blend electrospun scaffolds at different wt% PDEGMA to PLA. No trashes of the toxic electrospinning solvent DMF was observed in the spectra.

**Table S3:** WCA hysteresis values of PLA with different wt% PDEGMA scaffolds. (n=3, ± SD)

| wt% PDEGMA | ACA | RCA | H | cos $\theta_a dv$ | cos $\theta_r ed$ | cos $\Delta\theta$ | $\Delta\theta$% |
|---|---|---|---|---|---|---|---|
| 0 | 135 ± 1.0 | 110 ± 1.3 | 26 | -0.71 | -0.33 | 0.38 | 19 |
| 2.5 | 146 ± 3.0 | 96 ± 0.4 | 49 | -0.83 | -0.10 | 0.72 | 36 |
| 5 | 139 ± 7.1 | 97 ± 0.2 | 42 | -0.76 | -0.12 | 0.64 | 32 |
| 10 | 134 ± 0.2 | 94 ± 1.2 | 40 | -0.70 | -0.07 | 0.63 | 31 |
| 15 | 145 ± 4.0 | 97 ± 1.8 | 48 | -0.82 | -0.12 | 0.71 | 35 |
| 20 | 147 ± 2.6 | 52 ± 6.6 | 95 | -0.84 | 0.61 | 1.45 | 73 |

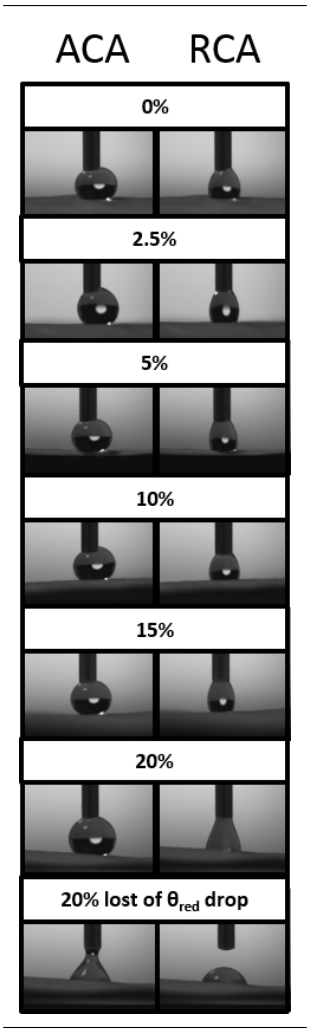



**Figure S34:** WCA images of hysteresis measurements. ACA is advanced contact angle and RCA is reduced contact angle. Lost of droplet was observed for 20wt% PDEGMA scaffolds.

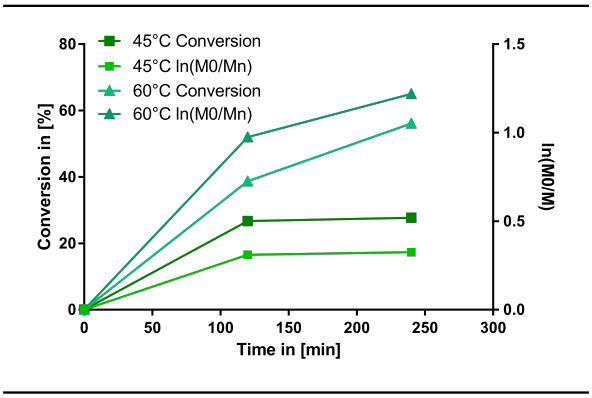



**Figure S35:** Conversion and ln($M_0$/M) for ATRP polymerisation of PBI-PDEGMA.

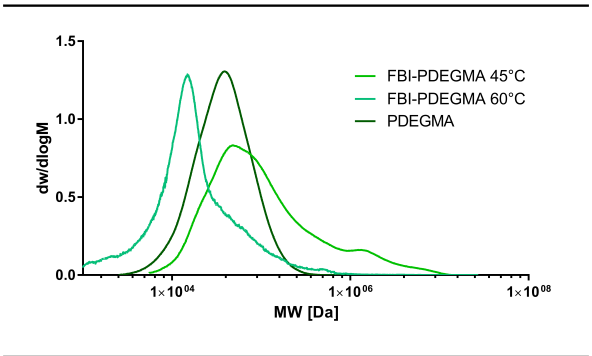



**Figure S36:** GPC peaks for PDEGMA, PBI-PDEGMA(45°C) and PBI-PDEGMA(60°C) in DMF.

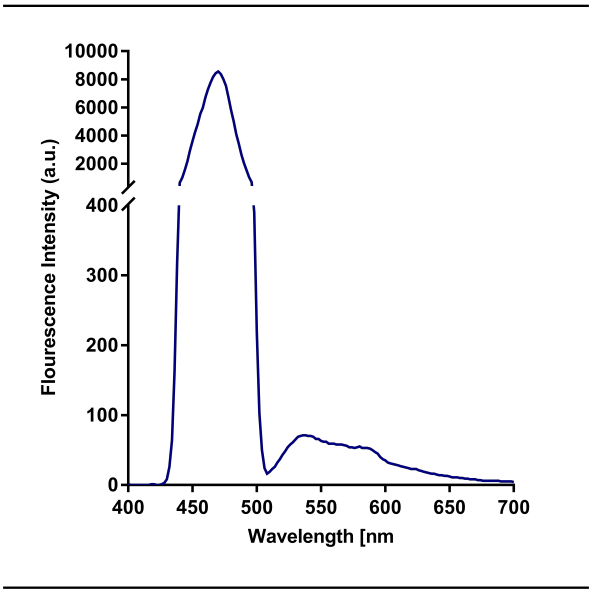



**Figure S37:** Fluorescence intensity of PBI-PDEGMA(60°C) in water at different wavelengths.

**Table S4:** Two-way ANOVA values for different %wt PDEGMA or PBI-PDEGMA proliferation studies. Tukey test of different cell numbers per day for PDEGMA or PBI-PDEGMA. (*=<0.05, **=<0.01, ***=<0.001 and ****=<0.0001)

| **A** | | PBI-PDEGMA | | | | | |
|---|---|---|---|---|---|---|---|
| | **Day 5** | **0%** | **2.5%wt** | **5%wt** | **10%wt** | **15%wt** | **20%wt** |
| PBI-PDEGMA | **0%wt** | - | ns | ns | *** | ns | ns |
| | **2.5%wt** | ns | - | ns | **** | *** | *** |
| | **5%wt** | ns | ns | - | * | ns | ns |
| | **10%wt** | *** | **** | * | - | ns | ns |
| | **15%wt** | ns | *** | ns | ns | - | ns |
| | **20%wt** | ns | *** | ns | ns | ns | - |

| **B** | | PDEGMA | | | | | |
|---|---|---|---|---|---|---|---|
| | **Day 7** | **0%** | **2.5%wt** | **5%wt** | **10%wt** | **15%wt** | **20%wt** |
| PDEGMA | **0%wt** | - | ns | ns | * | * | ns |
| | **2.5%wt** | ns | - | ns | ns | ns | ns |
| | **5%wt** | ns | ns | - | ns | ns | ns |
| | **10%wt** | * | ns | ns | - | ns | ns |
| | **15%wt** | * | ns | ns | ns | - | ns |
| | **20%wt** | ns | ns | ns | ns | ns | - |

**Table S5:** Two-way ANOVA values for different %wt PDEGMA or PBI-PDEGMA compared per day. Tukey test of different cell numbers per day for PDEGMA or PBI-PDEGMA. (*=<0.05, **=<0.01, ***=<0.001 and ****=<0.0001)

| **A** | | PBI-PDEGMA | | | | | |
|---|---|---|---|---|---|---|---|
| | **Day 5** | **0%** | **2.5%wt** | **5%wt** | **10%wt** | **15%wt** | **20%wt** |
| PDEGMA | **0%wt** | ns | ** | ns | ns | ns | ns |
| | **2.5%wt** | ns | ** | ns | ns | ns | ns |
| | **5%wt** | ns | *** | ns | ns | ns | ns |
| | **10%wt** | ns | **** | ns | ns | ns | ns |
| | **15%wt** | ns | **** | ns | ns | ns | ns |
| | **20%wt** | ns | **** | ns | ns | ns | - |

| **B** | | PBI-PDEGMA | | | | | |
|---|---|---|---|---|---|---|---|
| | **Day 7** | **0%** | **2.5%wt** | **5%wt** | **10%wt** | **15%wt** | **20%wt** |
| PDEGMA | **0%wt** | ns | ns | ns | ** | ns | ns |
| | **2.5%wt** | ns | ns | ns | ns | ns | ns |
| | **5%wt** | ns | ns | ns | ns | ns | ns |
| | **10%wt** | ns | ** | ns | ns | ns | ns |
| | **15%wt** | ns | ** | ns | ns | ns | ns |
| | **20%wt** | ns | ns | ns | ns | ns | - |

$$Conversion\% = \frac{C - C\ peakingration}{0.5} / 3 * 100 \tag{9.0.1}$$

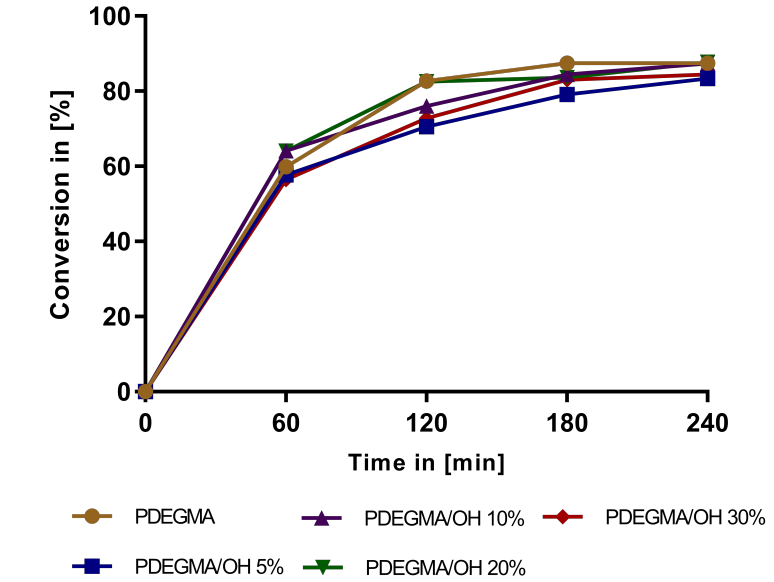



**Figure S38:** Conversion rate of the PDEGMA and PDEGMA/PDEGOH different ratios RAFT polymerisation.

**Table S6:** Calculated percentage of OH in co-polymer vs. observed percentage free thiol after condensation reaction.

| DEGMA:DEGOH | | Integration | Protons | % of -OH | Thiol [%] |
|---|---|---|---|---|---|
| **70:30** | $C\underline{H_2}O$ | 6.66-5.91=0.7 | 7 | 10 | 9.7 |
| | $C\underline{H_2}OH$ | 0.49 | 2 | 25 | |
| **80:20** | $C\underline{H_2}O$ | 6.20-5.91=0.29 | 7 | 4.1 | 3.7 |
| | $C\underline{H_2}OH$ | 0.11 | 2 | 5.5 | |
| **90:10** | $C\underline{H_2}O$ | 6-5.91=0.09 | 7 | 1.3 | 2.2 |
| | $C\underline{H_2}OH$ | 0.05 | 2 | 2.5 | |
| **95:5** | $C\underline{H_2}O$ | 6.16-5.91=0.25 | 7 | 3.6 | 1.7 |
| | $C\underline{H_2}OH$ | 0.34 | 2 | 17 | |
| **100:0** | $C\underline{H_2}O$ | 5.91-5.91=0 | 6 | 0 | 0 |
| | $C\underline{H_2}OH$ | 0 | 0 | 0 | |

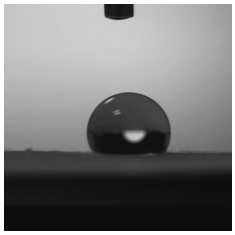
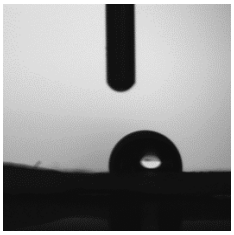
| 0% -SH | 2% -SH | 3% -SH |
|---|---|---|
|  |  |  |
| $115 \pm 7\,^{\circ}$ | $105 \pm 16\,^{\circ}$ | $114 \pm 13\,^{\circ}$ |
| **4% -SH** | **10% -SH** | |
|  |  | |
| $134 \pm 4\,^{\circ}$ | $134 \pm 1\,^{\circ}$ | |

**Figure S39:** Water contact angle on the different PDEGMA or PDEGMA/PDEGSH scaffolds. Increasing contact angle was observed when more thiols were present in the scaffolds. (n=3 scaffolds per scaffold type)

**Table S7:** Negative and Positive secondary ions reported from the electrospun scaffolds of different chemical composition.

| | | | Assignment deviation [ppm] | | | | | | | | | | |
|---|---|---|---|---|---|---|---|---|---|---|---|---|---|
| | **m/z** | **Structure** | **PLA** | **0SH** | **2SH** | **3SH** | **4SH** | **10SH** | **0S-P** | **2S-P** | **3S-P** | **4S-P** | **10S-P** |
| **PLA** | 55.022 | $C_3H_3O^-$ | -15.4 | 25 | -15.8 | -39.3 | 5.8 | -16.6 | -22.3 | -11.6 | -59.3 | -6.3 | -9.7 |
| | 56.028 | $C_3H_4O^-$ | 28.3 | 97.1 | 56.9 | 33.3 | 86.5 | 43 | 112.9 | 100.3 | 84.7 | 118.7 | 84.4 |
| **PDEGMA** | 31.026 | $CH_3O^+$ | - | -49.7 | -55.6 | 31 | 36.4 | -127.6 | 34.6 | 11.9 | 48.5 | 20.5 | -5.2 |
| | 31.026 | $C_2H_4O^+$ | - | 4 | -7.5 | -34.1 | 9.2 | -6.1 | -22.3 | -25.1 | -60.1 | -6.3 | -20.7 |
| **PDEGSH** | 31.969 | $S^-$ | - | -30.4 | -16.3 | -101.2 | -88.9 | -65.9 | -206.9 | -144.6 | -129.5 | -140.2 | -125 |
| | 32.984 | $SH^-$ | - | 311.9 | 122.6 | 112.2 | 104.5 | 152 | 330.1 | 161.1 | 173.3 | 242 | 196.6 |
| **Peptide** | 32.984 | $CNO^-$ | - | - | - | - | - | - | 141.3 | 130.7 | 102.9 | 136.6 | 132.7 |
| | 147.091 | $C_5H_{13}N_3O_2{}^+$ | - | - | - | - | - | - | -65.0 | -58.6 | -59.2 | -63.7 | -76.3 |
| | 425.258 | $C_17H_27N_7O^+$ | - | - | - | - | - | - | 128.5 | 138.7 | 167.3 | 167.1 | 166.9 |
| | 605.236 | $C_{26}H_{35}N_8O_9{}^+$ | - | - | - | - | - | - | -59.4 | -64.5 | -75.2 | -68.9 | -77.5 |
| | 627.206 | $C_{28}H_{35}N_8O_9{}^+$ | - | - | - | - | - | - | -72.7 | -86.9 | -88.9 | -93.3 | -93.4 |
| | 765.366 | $C_{32}H_{51}N_11O_11^+$ | - | - | - | - | - | - | -36.7 | 20.9 | -6 | 0.3 | 13.2 |

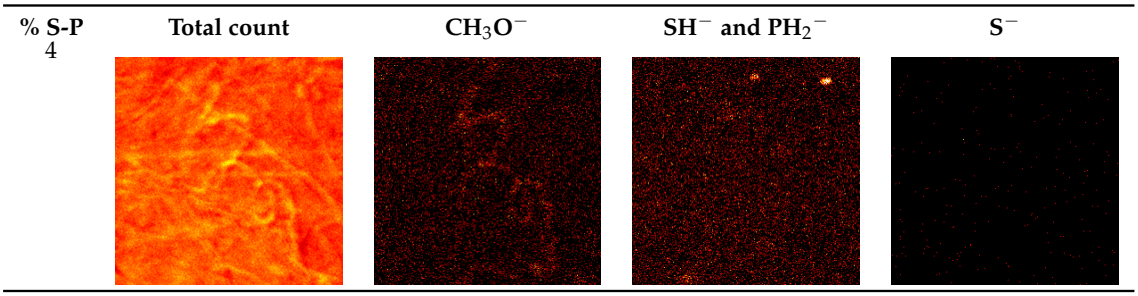



**Figure S40:** ToF-SIMS measurement of the non derivatised scaffolds. A) Total count images, B) $CH_3O^-$ group of the PDEGMA thermo-responsive part of the co-polymer PDEGMA/PDEGSH, C) $SH^-$ group of the PDEGSH or -$PH_2$ PBS salt and D) $S^-$ group of the PDEGSH (image surface area is 500 x 500 nm, normalized to MC of 200 for total count and MC of 3 for all other signals).

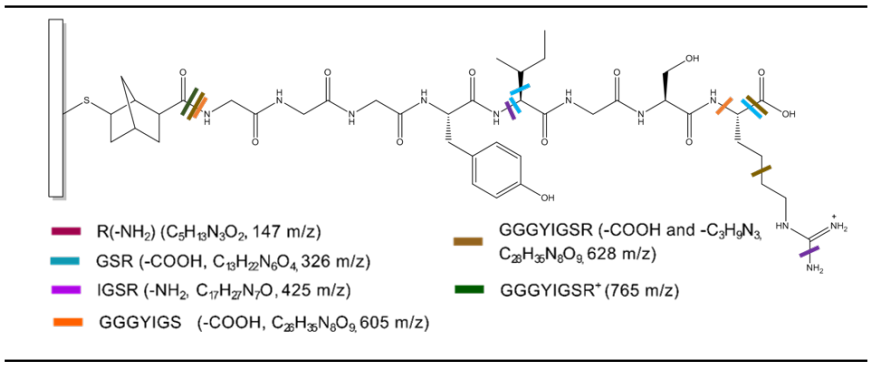



**Figure S41:** Schematics of possible fragments of Nor-GGG-YIGSR observed by ToF-SIMS.

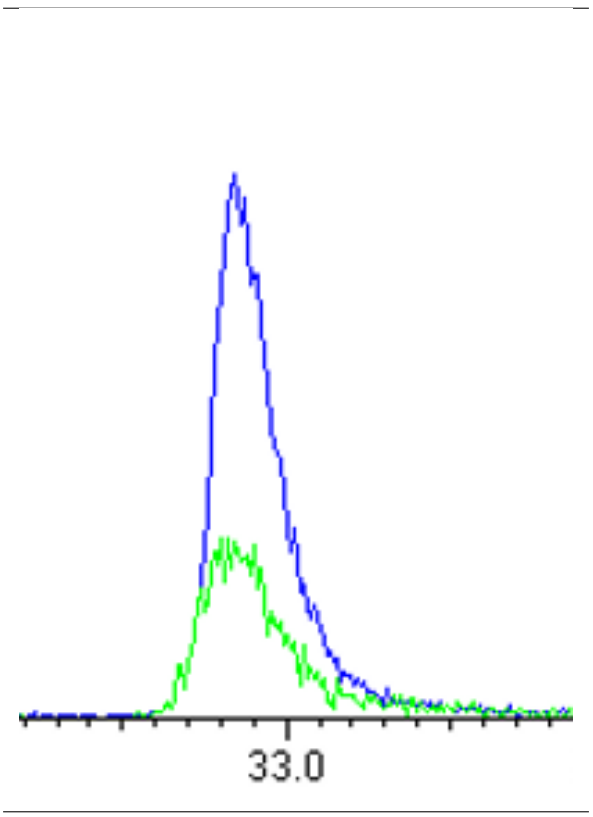



**Figure S42:** ToF-SIMS peak 32 m/z overlap of signal $SH^-$ (red) and $PH_2$ (green). Standard deviation of peak -$SH^-$ for non derivatised scaffold is -60 dev, while increase of the derivatised scaffolds signal peak this increased to 223 dev, however, when identified to $PH_2$ this reduced to -59.3 dev. Indicating that the peak represents a deposit of salt from the PBS used during UV-curing.

**Table S8:** Flow cytometry Y-mean and X-mean cell population of keratocyte phenotype expression of the two group of stains CD34/CD105 and ALDH/α-SMA. -/- is population of cells with no staining observed. -/+ is population of cells with the undesired activated phenotype expression. +/- is population of cells with the desired quiescent phenotype expression and +/+ is population of cells with the both desired and undesired activated phenotype expression.(n=3, scaffold per staining group)

| | **X-axis median** | | | | | | | |
|---|---|---|---|---|---|---|---|---|
| | **CD34/CD105** | | | | **ALDH/α-SMA** | | | |
| | **-/-** | **-/+** | **+/-** | **+/+** | **-/-** | **-/+** | **+/-** | **+/+** |
| **0S-P** | $4.84E^{+05}$ | $1.34E^{+06}$ | $5.08E^{+}06$ | $6.25E^{+}06$ | $8.36E^{+}05$ | $1.52E^{+}06$ | $6.48E^{+}06$ | $7.12E^{+}06$ |
| **2S-P** | $6.65E^{+05}$ | $1.94E^{+06}$ | $3.58E^{+06}$ | $4.02E^{+06}$ | $7.34E^{+05}$ | $7.51E^{+05}$ | $1.95E^{+07}$ | $3.61E^{+07}$ |
| **3S-P** | $7.61E^{+05}$ | $1.96E^{+06}$ | $3.08E^{+06}$ | $4.56E^{+06}$ | $9.67E^{+05}$ | $1.55E^{+06}$ | $6.76E^{+06}$ | $9.13E^{+07}$ |
| **4S-P** | $6.09E^{+05}$ | $1.69E^{+06}$ | $3.88E^{+06}$ | $4.98E^{+06}$ | $8.36E^{+05}$ | $1.23E^{+06}$ | 1.35E+07 | $9.18E^{+07}$ |
| **10S-P** | $6.79E^{+05}$ | $1.82E^{+06}$ | $3.56E^{+06}$ | $4.90E^{+06}$ | $7.26E^{+05}$ | $7.22E^{+05}$ | $8.61E^{+06}$ | $4.00E^{+07}$ |
| **2D-Gelatin** | $1.39E^{+06}$ | $1.72E^{+06}$ | $3.88E^{+06}$ | $5.60E^{+06}$ | $1.16E^{+06}$ | $1.04E^{+06}$ | $7.67E^{+07}$ | $1.30E^{+08}$ |
| | **Y-axis median** | | | | | | | |
| | **-/-** | **-/+** | **+/-** | **+/+** | **-/-** | **-/+** | **+/-** | **+/+** |
| **0S-P** | $5.19E^{+05}$ | $2.44E^{+07}$ | $1.52E^{+06}$ | $7.54E^{+07}$ | $4.61E^{+05}$ | $5.59E^{+06}$ | $3.76E^{+05}$ | $8.04E^{+06}$ |
| **2S-P** | $5.67E^{+05}$ | $3.47E^{+07}$ | $7.94E^{+05}$ | $6.00E^{+07}$ | $3.66E^{+05}$ | $1.56E^{+07}$ | $5.21E^{+05}$ | $5.84E^{+06}$ |
| **3S-P** | $7.13E^{+05}$ | $2.25E^{+07}$ | $5.71E^{+05}$ | $5.92E^{+07}$ | $3.83E^{+05}$ | $6.84E^{+06}$ | $7.38E^{+05}$ | $6.56E^{+06}$ |
| **4S-P** | $6.08E^{+05}$ | $1.96E^{+07}$ | $1.88E^{+06}$ | $6.88E^{+07}$ | $4.27E^{+05}$ | $5.25E^{+06}$ | $6.34E^{+05}$ | $6.54E^{+06}$ |
| **10S-P** | $6.38E^{+05}$ | $1.49E^{+07}$ | $1.82E^{+06}$ | $2.80E^{+07}$ | $5.18E^{+05}$ | $1.15E^{+07}$ | $5.80E^{+05}$ | $6.05E^{+06}$ |
| **2D-Gelatin** | $1.22E^{+05}$ | $1.14E^{+07}$ | $8.97E^{+04}$ | $1.67E^{+07}$ | $2.59E^{+05}$ | $8.61E^{+06}$ | $2.20E^{+06}$ | $4.22E^{+06}$ |

**Table S9:** [ANOVA value of Y-mean and X-mean of FACS.Two-way ANOVA analysis by Tukey test of the X-axis medains for $CD34^+/CD105^+$ and Y-axis medains of $ALDH^+/\alpha\text{-}SMA^+$. (*=<0.05, **=<0.01 and ***=<0.001)

| | **X-axis medians $ALDH^+/\alpha\text{-}SMA^+$** | | | | | |
|---|---|---|---|---|---|---|
| | **0S-P** | **2S-P** | **3S-P** | **4S-P** | **10S-P** | **2D Gel** |
| **0S-P** | - | ns | * | * | ns | *** |
| **2S-P** | ns | - | ns | ns | ns | ** |
| **3S-P** | * | ns | - | ns | ns | ns |
| **4S-P** | * | ns | ns | - | ns | ns |
| **10S-P** | ns | ns | ns | ns | - | * |
| **2D-Gelatin** | *** | ** | ns | ns | * | - |
| | **Y-axis medians $CD34^+/CD105^+$** | | | | | |
| | **0S-P** | **2S-P** | **3S-P** | **4S-P** | **10S-P** | **2D Gel** |
| **0S-P** | - | ns | ns | ns | ** | *** |
| **2S-P** | ns | - | ns | ns | ns | * |
| **3S-P** | ns | ns | - | ns | ns | * |
| **4S-P** | ns | ns | ns | - | ns | ** |
| **10S-P** | ** | ns | ns | ns | - | ns |
| **2D-Gelatin** *** | * | * | ** | ns | - | |

**Table S10:** Total % of cell population expression ($CD34^+/CD105^-$ + $CD34^+/CD105^+$), CD105 ($CD34^-/CD105^+$ + $CD34^+/CD105^+$), ALDH ($ALDH^+/\alpha\text{-}SMA^-$ + $ALDH^+/\alpha\text{-}SMA^+$) or α-SMA ($ALDH^-/\alpha\text{-}SMA^+$ + $ALDH^+/\alpha\text{-}SMA^+$) in which sub-populations were combined.

| | **% of cell population** | | | |
|---|---|---|---|---|
| | **CD34** | **CD105** | **ALDH** | **α-SMA** |
| **0S-P** | 22.59 | 26.13 | 67 | 43.4 |
| **2S-P** | 31.55 | 55.37 | 43.21 | 24.07 |
| **3S-P** | 44.58 | 52.58 | 58.06 | 28.27 |
| **4S-P** | 38.36 | 51.02 | 57.85 | 18.58 |
| **10S-P** | 50.03 | 67 | 44.93 | 32.26 |
| **2D-Gelatin** | 69.49 | 86.45 | 92.96 | 99.12 |

**Table S11:** Two-way ANOVA analysis by Tukey test of the total % of cell population expressing CD34 ($CD34^+/CD105^-$ + $CD34^+/CD105^+$), CD105 ($CD34^-/CD105^+$ + $CD34^+/CD105^+$), ALDH ($ALDH^+/\alpha\text{-}SMA^-$ + $ALDH^+/\alpha\text{-}SMA^+$) or α-SMA ($ALDH^-/\alpha\text{-}SMA^+$ + $ALDH^+/\alpha\text{-}SMA^+$). (*=<0.05 and **=<0.01

| | **% of cell population expressing CD34** | | | | | |
|---|---|---|---|---|---|---|
| | **0S-P** | **2S-P** | **3S-P** | **4S-P** | **10S-P** | **2D Gel** |
| **0S-P** | - | ns | ns | ns | ns | ns |
| **2S-P** | ns | - | ns | ns | ns | ns |
| **3S-P** | ns | ns | - | ns | ns | ns |
| **4S-P** | ns | ns | ns | - | ns | ns |
| **10S-P** | ns | ns | ns | ns | - | ns |
| **2D-Gelatin** | ns | ns | ns | ns | ns | - |
| | **% of cell population expressing CD105** | | | | | |
| | **0S-P** | **2S-P** | **3S-P** | **4S-P** | **10S-P** | **2D Gel** |
| **0S-P** | - | ns | ns | ns | ns | * |
| **2S-P** | ns | - | ns | ns | ns | ns |
| **3S-P** | ns | ns | - | ns | ns | ns |
| **4S-P** | ns | ns | ns | - | ns | ns |
| **10S-P** | ns | ns | ns | ns | - | ns |
| **2D-Gelatin** | * | ns | ns | ns | ns | - |
| | **% of cell population expressing ALDH** | | | | | |
| | **0S-P** | **2S-P** | **3S-P** | **4S-P** | **10S-P** | **2D Gel** |
| **0S-P** | - | ns | ns | ns | ns | ns |
| **2S-P** | ns | - | ns | ns | ns | ns |
| **3S-P** | ns | ns | - | ns | ns | ns |
| **4S-P** | ns | ns | ns | - | ns | ns |
| **10S-P** | ns | ns | ns | ns | - | ns |
| **2D-Gelatin** | ns | ns | ns | ns | ns | - |
| | **% of cell population expressing α-SMA** | | | | | |
| | **0S-P** | **2S-P** | **3S-P** | **4S-P** | **10S-P** | **2D Gel** |
| **0S-P** | - | ns | ns | ns | ns | * |
| **2S-P** | ns | - | ns | ns | ns | * |
| **3S-P** | ns | ns | - | ns | ns | ** |
| **4S-P** | ns | ns | ns | - | ns | * |
| **10S-P** | ns | ns | ns | ns | - | * |
| **2D-Gelatin** | * | * | ** | * | * | - |